IRON Butterfly

Human Powered Aircraft

Human Powered Aircraft for Sport

AOE 4066 - Virginia Polytechnic Institute and State University
Final Report: Spring Semester – May 5th, 2008

Dr. Kevin Kochersberger	*Faculty Advisor*
Brian Wheeler	*Project Manager*
Ryan Catlett	*Lead Engineer*
Ryan Adams	*Structures*
Horace Botts	*Structures*
Alex Goryachev	*Propulsion*
Nathan Knotts	*Structures*
Jason Powell	*Propulsion*
Nick Vozza	*Propulsion*

Table of Contents

1. Executive Summary

The Virginia Tech Human Powered Aircraft Group is presently in the third year of designing and advancing the development of an aircraft aimed at winning one of the current Kremer Prizes. After two years of preliminary and detail design, the project is in the building and testing phase.

This report details the current design of the entire aircraft. This is a compilation of work from all three teams. The document begins with a brief orientation to the project including an introduction to the Kremer Prize. The body of the report is split into three distinct sections. The first section overviews the entire, current design of the aircraft. The second section is devoted to explaining the construction and prototyping that has taken place throughout the project. The third section details the testing of components. The report concludes with a brief status report and an overview of the team's administrative details.

2. Introduction

2.1 HPA Background

The catalyst for most human-powered aircraft (HPA) activity for the past 40 years or so has been the Kremer Prizes offered by the Royal Aeronautical Society (RAS). The competitions have dictated the design criteria for most HPA's since the advent of the prize in 1959. The first successful HPA was Paul MacCready's Gossamer Condor, which won the first Kremer Prize in 1977, 18 years after the prize had been introduced. Many of the early HPA attempts were based on emulating sailplanes. MacCready changed the direction and expanded on the concepts used in hang-gliders to create the first successful HPA.

MacCready also won the next Kremer Prize only two years later in 1979 with the Gossamer Albatross, which crossed the English Channel. Five years later the RAS offered a new prize based on aircraft speed, the rules for which allowed ten minutes of energy storage by the pilot prior to the flight. There were two main competitors for the speed prize, MacCready and a group of students from MIT. The MIT group successfully flew their entry, Monarch, to win the prize.

There have been several successful HPA's not associated with the Kremer Prize, including MIT's Chrysalis and Daedalus. The designs of many of the successful HPA have several similar characteristics. The first and very important similarity is the pilot seating position. In all but the Condor, the pilot is seated in a recumbent position. This position proves to be much better for power production than the upright position. Another important similarity is the aft tail on all but the two Gossamer aircraft. With the exception of Chrysalis, which was a biplane, all other HPA's have high and generally straight wings. All HPA's except Daedalus have had ailerons. They were cut from Daedalus because its mission required almost no turning, resulting in a small weight reduction.

There are currently three Kremer prizes available, each for a monetary prize. The first is the Kremer International Marathon Competition, which challenges the competitor to fly a 26 mile marathon course in less than an hour. The second competition is the Kremer Human-Powered Aircraft for Sport Competition stressing maneuverability. The competition goal is to design a Human-Powered Aircraft that could be used in an Arial Sporting event around an equilateral triangular course of 500m on each side. The third competition is limited to universities in the UK. [1]

2.2 The Kremer Prize for Sport

2.2.1 Human-Powered Aircraft for Sport Competition

The overall goal of this project is the completion of the Human-Powered Aircraft for Sport challenge hosted by the Royal Aeronautical Society. The purpose of this challenge is to bring forth the creation of a sport from this class of airplane. A reward of £100,000 will be presented to the first entrant that is capable of demonstrating flight that meets of the requirements of the competition. [Appendix A]

The aircraft requirements for this prize are:

- The aircraft has to operate safely at low altitudes, close to the ground, and be well disposed to kit production.
- Flown by one individual that uses muscular power for propulsion.
- No batteries or electric cells can be used to store energy for propulsion.
- No lighter than air gasses can be used to generate lift.
- The entire aircraft must be stored in a trailer with a maximum length of 8 meters.
- No part of the aircraft can be discarded on or after takeoff.

2.2.2 Competition Course

The Human-Powered Aircraft has a specific course that must be adhered to in order to successfully complete the competition. [Appendix A] This course is displayed in the Figure 2.2.2. The course may be anywhere in the UK, either over land or water, such that it meets the following criteria:

- The course is an equilateral triangle 500m on each side.
- The course shall be flown both clockwise and counter clockwise.
- The mean wind speed during flight will not be less than 5 m/s.
- The wind speed will not drop below 5 m/s for more than 20s during flight or the flight will be void.

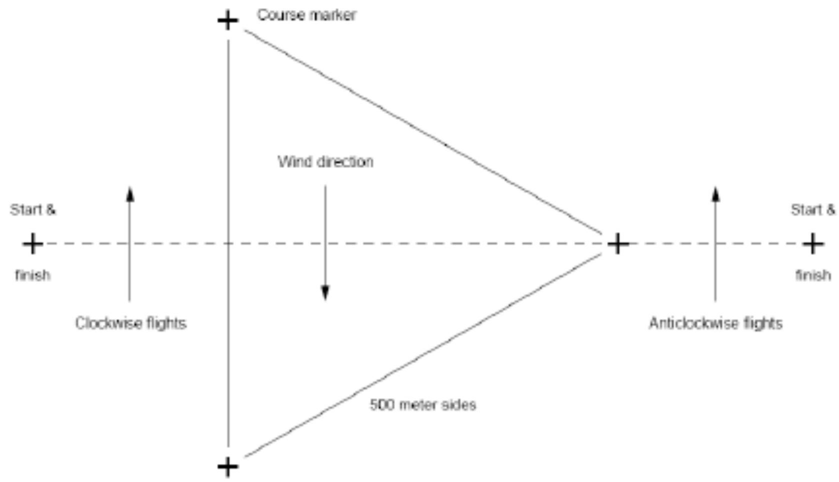

Figure 2.2.2: Kremer Prize for Sport Competition Course Diagram

2.3 Previous Project Development

Because this project is currently in its third year of development, this team must study and understand thoroughly what previous teams have accomplished. The current team was required to pick up where our predecessors left off, while still keeping in mind that previous designs may need to be tweaked or perhaps changed all together. The following sections will give a brief description of the previous project development. Final Reports of the two previous teams can be found in Appendix C and Appendix D.

2.3.1 2005-2006 HPA Team

The Fall of 2005 was the year that the Human Powered Aircraft Group was formed and began conceptual design on an aircraft to eventually compete for the Kremer prize. To properly begin conceptual design, constraints were defined based on the rules for the competition and a mission analysis, which determined how the aircraft and pilot would need to perform during flight. Next, the team considered several conceptual design sketches and ranked them using a design matrix. Two of the top designs were considered for further analysis; a monoplane and a box-wing configuration.

Aerodynamically, the team found that the box-wing configuration was the better of the two options. Using the design constraints, the wing area was selected. They then concentrated on researching airfoils that would perform the best for the wing and tail surfaces with minimal drag.

Structurally, the team considered each of the two concept configurations by building and testing simple models. After finding the box-wing configuration was superior, finite element analysis was performed to optimize the design. Basic structural design such as number of struts and gap width between wings were also analyzed to minimize drag.

The first year's team began some preliminary design regarding the propulsion system. After researching previous HPA's a basic drive train was designed that resembled that of a bicycle. Pilot positioning was also researched and an optimal position was chosen. The team also designed a propeller for use with a variable pitch mechanism in order to provide the optimal propeller pitch at different flight conditions.

The latter half of the year was consumed with constructing and testing a quarter scale model of the aircraft. The model was built primarily to test and validate the dynamic stability and control of the aircraft. The wing structures were constructed with some built-in deflection in order to make the wing perform like the full-scale aircraft. The model was scaled so that it would behave dynamically similar to the full-scale model.

Below is a simple computer model that shows how the first year's team envisioned the HPA.

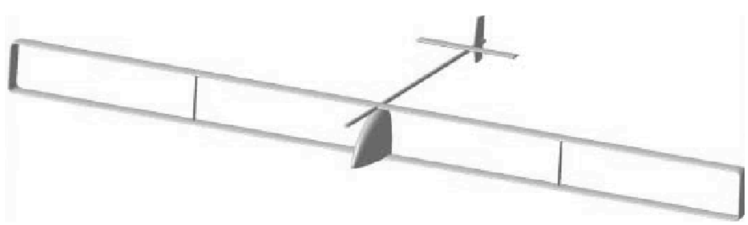

Figure 2.3.1: Computer model of 1st teams design

More information on the first year's progress is referenced in Appendix D.

2.3.2 2006-2007 HPA Team

The second year HPA team picked up where the first year's team left off, and focused the entire first semester in further developing the quarter scale model. Many problems existed with the model in the first year, as documented by the flight test videos and reports. Because of this, the team performed many aerodynamic and stability and control analyses to help provide them with a blueprint for model modifications. Other structural analysis was also performed using computer simulations to help modify the existing design.

After performing this analysis, there were four major concerns the team had regarding the model. These were replacing the original carbon fiber fuselage, addition of guy wires, construction of a new elevator, and the addition of landing gear. Upon completion of these design and construction issues, the second year team began testing the quarter scale model. The flight tests were much improved from the previous year and resulted in the model performing several 360^{o} turns.

Although much of the conceptual design and some detailed design was completed by the previous team, the 2006-2007 team focused their detail design on optimizing the structural aspects of the aircraft, and performing detailed aerodynamic design. In the second semester, along with continued detail design, the second year team began construction of a full-scale prototype with the hope of beginning flight-testing in the spring of 2007. With full-scale construction in mind, the team also began to acquire funds and workspace during the second semester.

In terms of the design, the team reached their goals of finalizing the spar, strut and airfoil design, while continuing to improve the overall detailed design of the aircraft. The team did not, however, complete construction of the full-scale prototype. Multiple wing sections have been built and tested, but the construction processes have not yet been perfected. More information on the second year's progress is referenced in Appendix C.

2.4 Mission Objectives

The team has begun testing two important aspects of the design: propeller efficiency and wing structural integrity. Structural testing has shown discrepancies from the ANSYS predictions made by last year's team. Much of the recent work has been aimed at understanding and resolving these issues. To measure propeller efficiency, a propeller and a testing device were built. The team has performed some preliminary testing. Concurrently, part of the team has worked towards the finalization of the general cockpit design, and a preliminary variable pitch mechanism for the final prototype.

3. Prototype Design

3.1 Aerodynamics

3.1.1 Lift to Drag Analysis

To gain a better understanding of how the wing of the aircraft should perform, an analysis of the lift to drag ratio was performed using AVL software [2]. Lift and drag coefficients were calculated for a range of angles of attack to determine the maximum lift-to-drag ratio, and the results were plotted in Figure 3.1.1. As seen in the graph, the useful range of angle of attack for the current design ends at approximately seven degrees. A 15% stall margin on $C_{L,max}$ was employed for these calculations. Based on these calculations, the maximum lift-to-drag ratio of 29.98 occurs at an angle of attack near 6°.

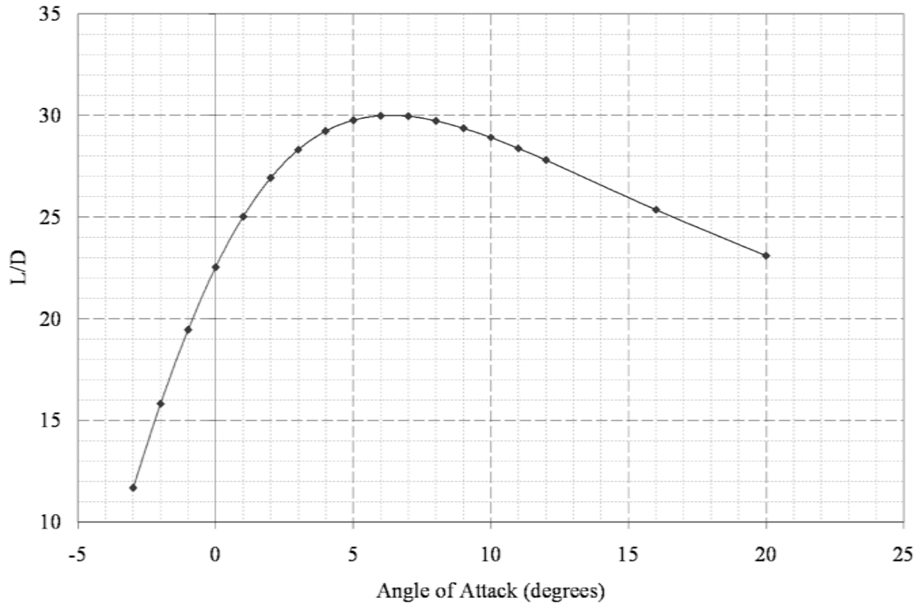

Figure 3.1.1: Effect of angle of attack on lift over drag

3.1.2 Takeoff Speed

To further enhance the understanding of the performance of the aircraft design, a takeoff speed calculation was done. A value of 1.5 for the maximum lift coefficient was previously obtained using a 15% stall margin. Using this value, other parameters from the aircraft's design, and atmospheric conditions, the stall speed can be calculated as shown below:

$$V_{\text{stall}} = \sqrt{\frac{2 \cdot W}{\rho_{\infty} \cdot S \cdot C_{L,\max}}} \quad (3.1.2\text{-}1)$$

From this stall speed, it is generally accepted that the takeoff speed would be somewhat higher than the stall speed, so the equation below is used to calculate the takeoff speed:

$$V_{TO} = 1.2 \bullet V_{stall} \quad (3.1.2\text{-}2)$$

After performing these calculations for a wing surface area of 180 ft2, aircraft weight of 215 lb and a density of 0.002377 slugs/ft3, a stall speed of 17.65 mph was obtained. For this stall speed, the takeoff speed of the aircraft was calculated as 21.18 mph. This takeoff speed is close to the design cruise speed of 24.5 mph.

3.1.3 Cockpit Airfoil

To minimize the total drag on the aircraft, an aerodynamic cowling must be chosen for the cockpit. The cowling shape must fit two basic constraints: drag minimization and fitting a human body inside in a semi-recumbent position. An appropriate design would take into account the length and width of each individual airfoil in the series that would comprise the cowling as it pertains to the two constraints mentioned above. For example, the shape of the human body inside the cowling would affect the maximum width and its position along the airfoils chord. The characteristics of the three most promising airfoil configurations are displayed in Table 3.1.3. The decision was made to use the Van de Vooren airfoil with a 17 percent thickness and a 44° trailing edge. The reason for this decision was to make a compromise between the chord length, the thickness, and the drag that each would add. The final airfoil shape is shown in Figure 3.1.3.

Table 3.1.3: Airfoil comparison chart.

Re = 1.68e6 Density = 1.55 kg/m^3 D = 8 ft viscosity = 0.0183 C_p V = 24.5 mph M = 0.0321				
Airfoil	**C_d**	**Chord [ft]**	**S [ft^2] (5 ft Gap)**	**Drag [lb]**
Van de Vooren 17%t 44deg trailing (created in javafoil)	0.0058	8.349	41.744	0.360
NPL EQH series 16%thick at 38%chord	0.00451	10.297	51.487	0.346
Van de Vooren 15%t 50deg trailing	0.00669	7.603	38.014	0.379

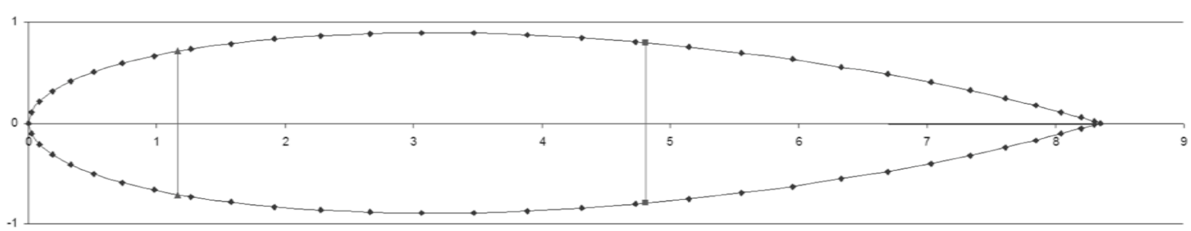

Figure 3.1.3: Van de Vooren 17% thickness, 44° trailing edge angle

The cockpit airfoil is designed to be lofted minimize drag and reduce excess material. The details of this design have yet to be determined.

3.1.4 Cockpit Drag and Sideslip Angle

Drag was a basic consideration of cockpit cowling design. Further consideration was given to how sideslip angle would affect cockpit drag. Analysis was done to determine the increase in power required because of the sideslip induced extra drag. Figure 3.1.4 shows the relationship between the power required and the sideslip angle of the aircraft. The red line is a reference to the power required of the aircraft at no sideslip, and the blue curve displays the power required of an aircraft in a sideslip condition. The drag on the cockpit in a sideslip condition could cause problems for the final competition aircraft when flying a triangular course with relatively high winds requiring crabbing into the wind.

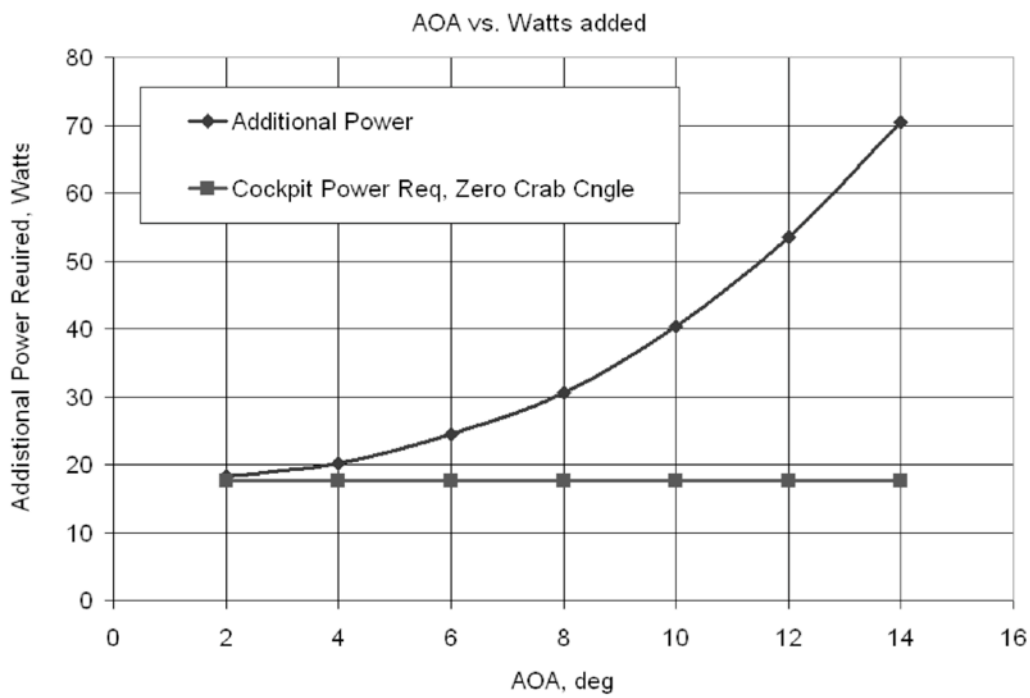

Figure 3.1.4: Sideslip angle vs. addition Watts required

3.1.5 Wingtip Stall

Through analysis of the mission model, it was determined that in a 150 ft. radius turn, the airflow over the inner wing tip would only be 19.8 mph compared to 24.5 mph at cruise. Based on the lift distribution from AVL, the C_L required at the tip was 0.71 and did not exceed the $C_{L,max}$ of the airfoil and therefore does not stall.

3.1.6 Lift Distribution

The lift distribution shown in Figure 3.1.7 was used in the spar design analysis. This lift was calculated for cruise speed of 24.5 mph at cruise angle of attack.

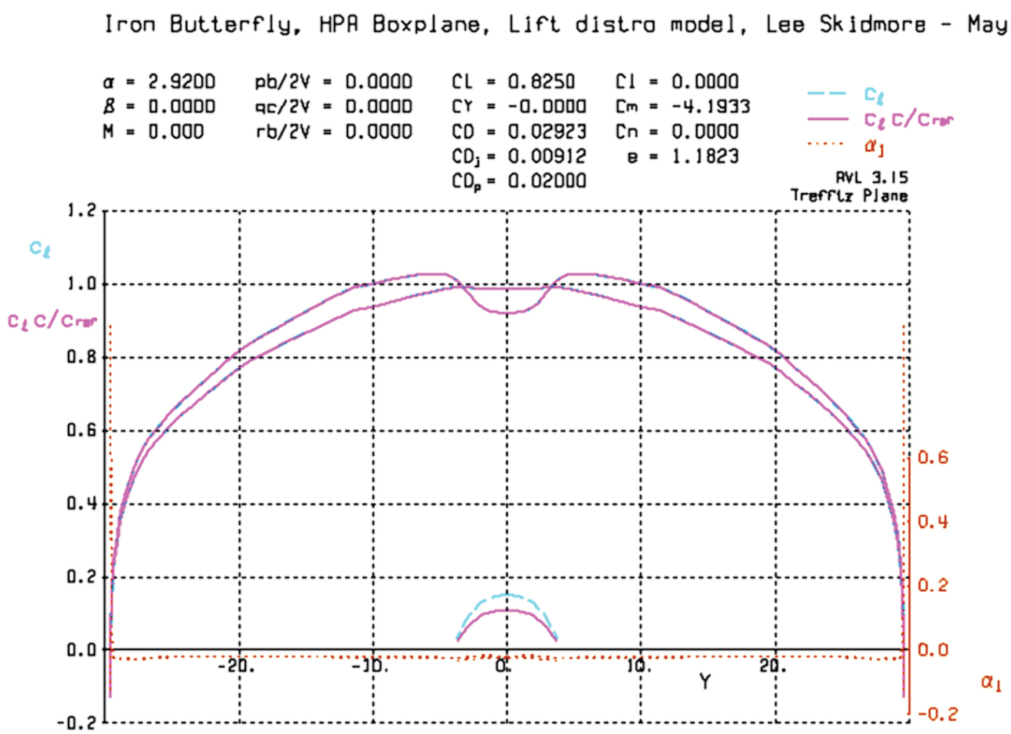

Figure 3.1.6: AVL lift distribution at 2.92° angle of attack

3.1.7 Landing Sink Rate

The sink-rate for a full glide landing was calculated in order to determine the landing load placed on other aircraft components, specifically the wings. Based on a glide ratio of 20 and cruise speed of 24.5 mph a full glide landing will have sink rate of 1.22 mph at a 2.86° angle glide slope.

3.1.8 Spar Placement

The aerodynamic center was determined to be nearly 23 percent chord for the airfoils employed in the design; however, because of size limitations the spar was positioned at 25 percent chord. In the first wind tunnel test, a strong negative pitching moment was observed on the wing and was verified in XFOIL. Further analysis in XFOIL revealed that a better placement for the spar was at 35.6 percent chord because there is a zero pitching moment for cruise conditions at this point. Furthermore, the strongest pitching moment noticed within the flight envelope is less than the constant pitching moment observed at the aerodynamic center. This pitching moment range was compared to both Daedalus and to Musculair; Iron Butterfly's pitching moment falls just in between these two successful human powered aircraft.

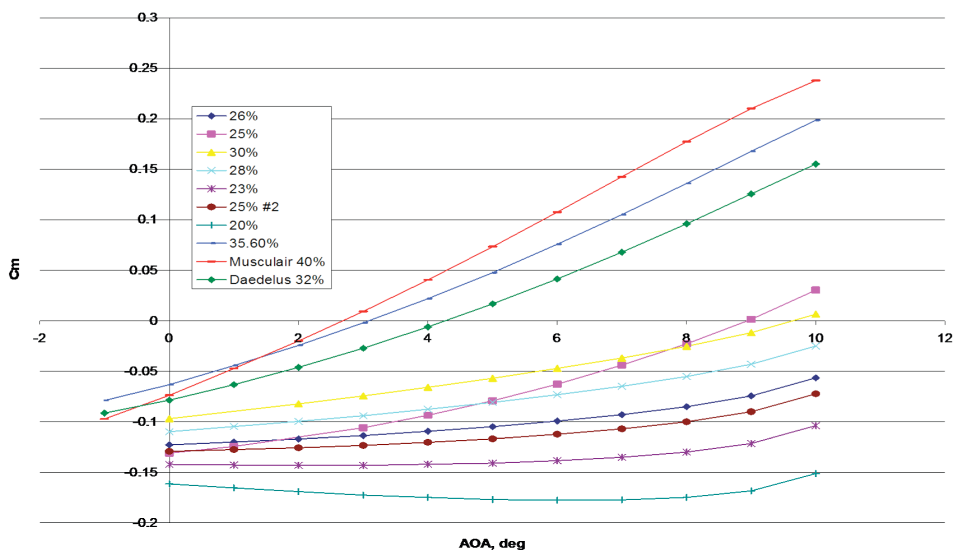

Figure 3.1.8: Spar Placement

3.1.9 Sensitivity of Power Required to C_{D0}

The highest uncertainty in the design of Iron Butterfly is the power required, mostly due to the parasitic drag term, C_{D0}. Parasitic drag is very difficult to estimate for a complete aircraft. In addition, the drag is affected by the smoothness of the DuraLar® skin covering. If the covering is not taut, then the drag will increase due to creases or ripples. Figure 3.1.10 shows the power required for a range of realistic parasitic drag coefficients. The blue horizontal line on the graph represents the maximum power that can be output by a human for 3.5 to 4 min. This line gives an upper bound on the C_{D0} of the aircraft, approximately 0.02. The blue vertical line is the C_{D0} value determined by the 2005-2006 team. The green vertical line is the updated C_{D0} value obtained from work that was performed in the Fall 2006. The vertical red line is the C_{D0} value that was obtained from the fuselage drag being added to the previous drag analysis. The 2007-2008 team found it necessary to add guy wires to improve the wing structure. The new value for C_{D0} is shown by the orange line corresponding to an increase in C_{D0} of 0.0006.

As more parts of the aircraft are finalized and corresponding C_{D0} values are found, the margin of power required versus power available will keep decreasing. So far, the power required is still in the region that can be delivered by the pilot; however, it could grow prohibitively large. If all intersections of aircraft parts are not properly faired, the drag could be too great to fly the aircraft for the required amount of time.

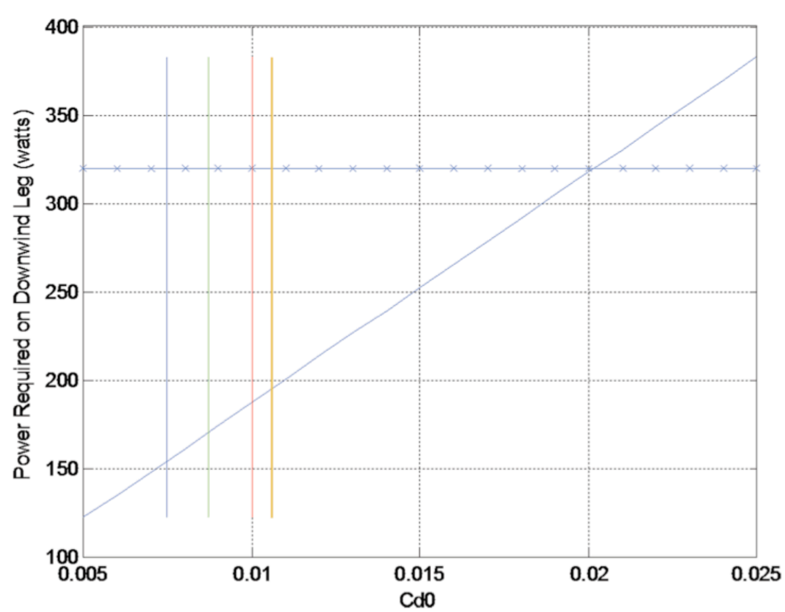

Figure 3.1.9: Power Required vs. C_{D0}

3.2 Stability and Control

3.2.1 Tail Design Method

The vertical tail geometry defined in the first year of the project was designed based on the vertical tail volume coefficient, V_v, that the team had chosen to be 0.05, and Roskam's tail area equation (Equation 3.2.1-1). In addition, a rotation angle of 8° was set as a constraint by the 2005-2006 team to prevent a tail strike from occurring during takeoff. Based on the geometry of the aircraft, the bottom of the tail surface would have to be constrained to be 2.14 ft or less below the tail boom.

$$S_{vt} = \frac{S_{wing} \cdot b_{wing} \cdot V_v}{L_{bom}} \qquad (3.2.1\text{-}1)$$

The 2005-2006 team decided that the tail area was divided so that ¼ of the total area was located below the tail boom with the remaining ¾ of the area located above. Taper ratios were added, producing the tail as seen in Figure 3.2.1-1, which had an overall aspect ratio of 5.6.

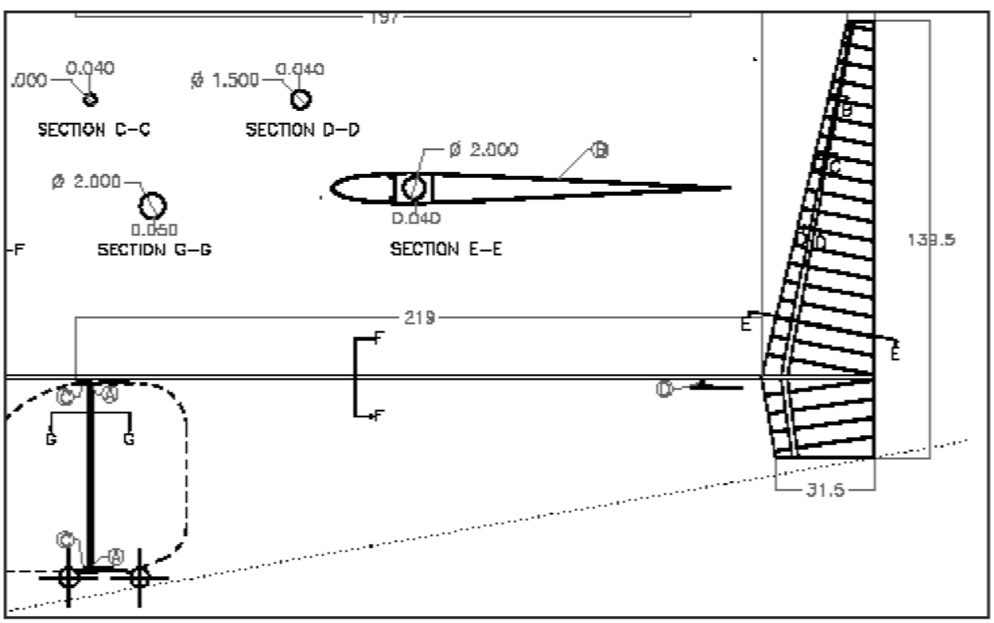

Figure 3.2.1-1: Vertical tail as of May 2006.

Because so much of the tail area lies far above the tail boom, and thus far above the CG of the aircraft, any rudder movement creates an additional rolling moment opposite the direction in which the aircraft is attempting to turn. This moment, depending on the total tail area and the length of the tail boom, can be in excess of 40 ft-lb. The primary goal of the design of the vertical tail was to minimize this rolling moment by placing as little tail area as possible above the tail boom while keeping the boom length and total tail surface area low. This design should save weight, minimize drag, and create a robust surface that would be easy to manufacture.

Initially, a MATLAB code was written that varied tail boom lengths and used equation 3.2.1-1 to minimize the offset of the center of the vertical tail span about the tail boom. This code was written assuming a fuselage height of 6.2 ft at the wing quarter-chord (includes cockpit and landing gear) and using the 8° minimum rotation or "flare" angle. The code was run at 14 aspect ratios ranging from 1 to 8. The output of the code can be seen in Figure 3.2.1-2.

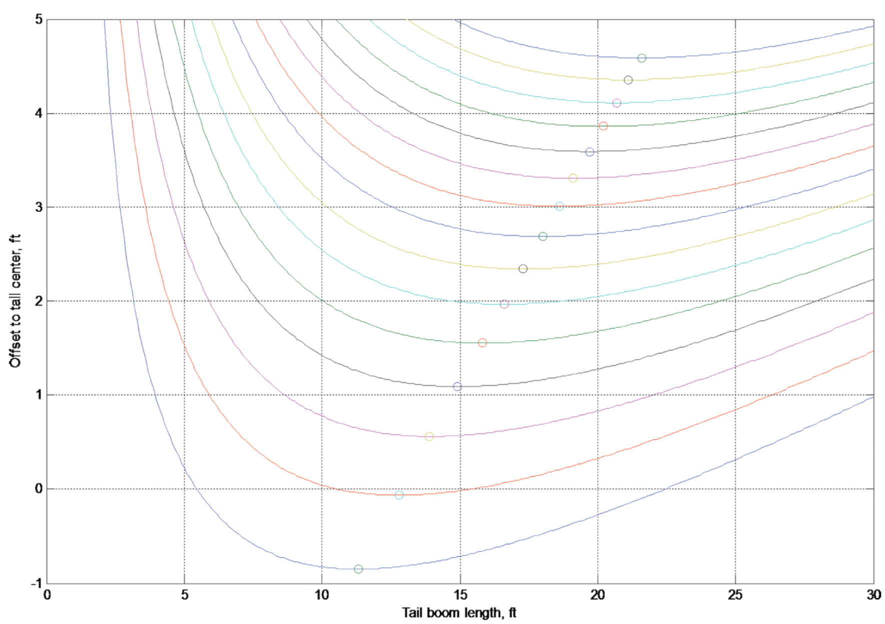

Figure 3.2.1-2: Tail boom length versus offset of tail center at multiple aspect ratios (the bottom blue line represents an aspect ratio of 1 and increases upward to an aspect ratio of 8 while the minimum points are delineated with circles)

For a single aspect ratio, the circle is the lowest tail offset possible for a given aspect ratio. This point occurs at a single tail boom length. These curves effectively gave the team 15 different tails with varying aspect ratios whose geometries have been optimized in terms of tail boom length and amount of area offset below the tail boom. These 15 vertical tail characteristics are shown in Table 3.2.1-1

Table 3.2.1-1: 15 Tails optimized for offset at varying tail boom lengths and aspect ratios

Aspect Ratio	Area [ft^2]	Chord [ft]	Span [ft]	Offset [ft]	Span Below Boom [ft]	Boom Length [ft]
1.00	52.43	7.24	7.24	-0.85	4.47	11.3
1.50	45.76	5.52	8.29	-0.06	4.21	12.8
2.00	41.86	4.58	9.15	0.56	4.01	13.9
2.50	38.85	3.94	9.86	1.09	3.84	14.9
3.00	36.49	3.49	10.46	1.55	3.68	15.8
3.50	34.62	3.14	11.01	1.97	3.54	16.6
4.00	33.13	2.88	11.51	2.34	3.41	17.3
4.50	31.77	2.66	11.96	2.69	3.29	18
5.00	30.68	2.48	12.39	3.01	3.18	18.6
5.50	29.83	2.33	12.81	3.31	3.10	19.1
6.00	28.88	2.19	13.16	3.59	2.99	19.7
6.50	28.13	2.08	13.52	3.86	2.90	20.2
7.00	27.41	1.98	13.85	4.11	2.81	20.7
7.50	26.87	1.89	14.20	4.35	2.74	21.1
8.00	26.21	1.81	14.481	4.58	2.66	21.6

Given these 15 options, each with pre-defined dimensions, the team analyzed the choices in AVL to determine the rolling moment and hinge moment in yaw in a 5° and 10° sideslip condition. This is where an effort to optimize for control was attempted. A small rolling moment was desirable. In addition, the yaw hinge moment needed to be minimized to reduce the force on the actual hinge and that needed to actuate the rudder.

The dynamic response of each surface was also evaluated in terms of the transient response of the aircraft in a 10° sideslip condition. Given that each turn was estimated to take roughly 8 seconds, this span of time on the transient response curve was considered to be the most important. The curve is not completely representative of the actual response of the aircraft in that the only factor that was changed in each case was the yaw damping coefficient, $C_{n\beta}$. All other factors remained the same. The response curve is shown in Figure 3.2.1-3, in which each curve is plotted at a $C_{n\beta}$ of either 0.12, 0.15, or 0.19. A comparator aircraft, Musculair II, reported a $C_{n\beta}$ value of 0.15. This was used as an initial, "ballpark" target. The graph showed that higher roll acceleration was achieved with a lower $C_{n\beta}$ as long as the sideslip condition lasted no longer than roughly 10 seconds. Because of the estimated turn duration of 8 seconds, it was determined that a lower $C_{n\beta}$ was desired.

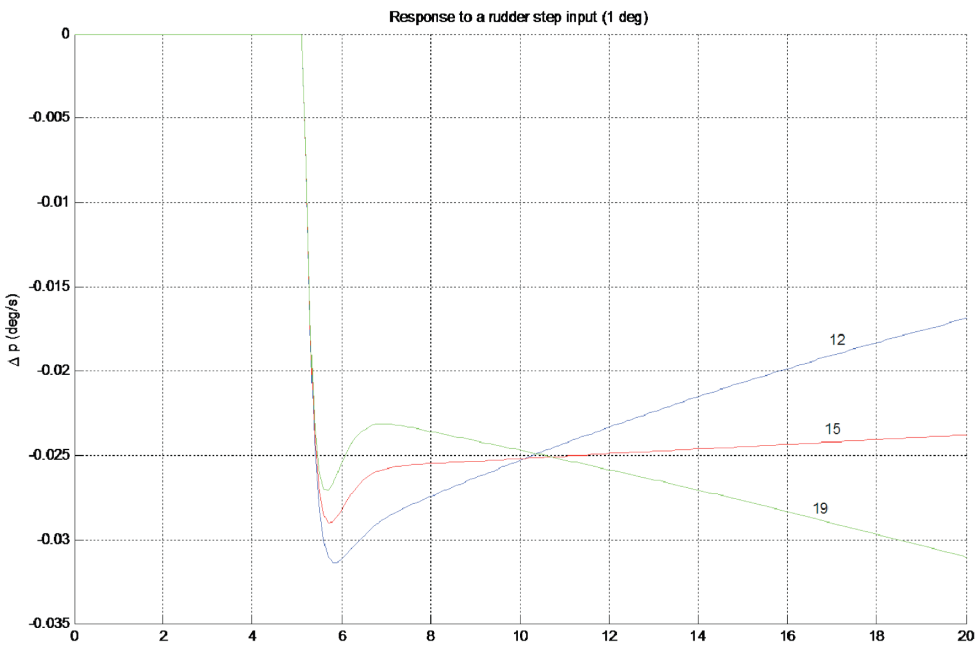

Figure 3.2.1-3: Transient Response of Tail Surface at the three values of $C_{n\beta}$

An additional consideration was the induced drag (drag induced by lift) produced by each surface. Induced drag is calculated using Equation 3.2.1-2 in which C_L is the lift coefficient, *AR* is the aspect ratio of the surface planform, and *e* is Oswald's efficiency factor. Because the induced drag is inversely dependent on the aspect ratio and due to time constraints, the team sought only to evaluate the tail geometries based on their aspect ratios rather than their calculated induced drag. Thus, surfaces with higher aspect ratios, all other conditions being equal, would produce low induced drags than surfaces with lower aspect ratios.

$$C_{\mathrm{di}} = \frac{C_L^2}{\pi \cdot e \cdot AR} \qquad (3.2.1\text{-}2)$$

In order to take structural efficiency into account, a structural efficiency factor was assigned to each surface. The equation for this is shown in Equation 3.2.1-3, in which l_{above} is the span of the tail above the boom and l_{below} is the span of the tail below the boom. The values 0.7 and 0.3 were assigned based on the fact that surfaces with longer wingspans are more susceptible to structural deformation. While excessively large chords are open to deformation, generally longer spans are more of a concern.

$$n_{\text{struct}} = \frac{0.7}{l_{\text{above}}} + \frac{0.3}{l_{\text{below}}} \qquad (3.2.1\text{-}3)$$

Lastly, a manufacturability factor was assigned to each surface, based on Equation 3.2.1-4.

$$n_{\text{man}} = 0.7\frac{c_{\text{min}}}{c} + 0.3\frac{b_{\text{min}}}{b} \qquad (3.2.1\text{-}4)$$

In the manufacturability equation, c represents the chord of the tail in question while c_{min} is assigned the smallest chord length out of the 15 tails being examined, in this case 1.8 ft. This concept applies in the same way to span, b, in which b_{min} is 7.2 ft. Here, it was assumed that surfaces with larger chords are more difficult to manufacture than those with longer spans. If a span needs to be lengthened, a longer spar and more ribs are used. If the chord needs to be lengthened, there is a point at which secondary support structure, such as an aft spar, becomes necessary.

Finally, all of these factors were assembled in a comparative matrix so that the performance of each surface could easily be evaluated relative to the other surfaces. Based on the observation that the optimum for each category occurred at either the very lowest aspect ratio or the very highest aspect ratio, a compromise between these two extremes was sought. Given that the roll moment during sideslip for each surface was negative and that the margin between them was small, this did not factor as importantly as the aspect ratio and weight, for example. Ultimately, the 3.5 AR geometry was chosen as the best compromise between the seven categories.

Table 3.2.1-2: Tail Geometry Comparative Matrix

AR	Weight	Roll Moment [ft-lb]	Yaw Moment [ft-lb]	Structural Efficiency	Manufacturability	C_{n_beta}
2.0	6.98	-10.18	4.50	0.21	0.51	0.120
2.5	7.30	-10.46	5.16	0.19	0.54	0.135
3.0	7.61	-10.69	5.69	0.18	0.57	0.149
3.5	7.88	-10.90	6.13	0.18	0.60	0.160
4.0	8.13	-11.09	6.49	0.17	0.63	0.170
4.5	8.38	-11.24	6.79	0.17	0.66	0.178
5.0	8.59	-11.39	7.05	0.17	0.69	0.185
5.5	8.78	-11.53	7.28	0.17	0.71	0.191
6.0	9.00	-11.72	7.48	0.17	0.74	0.196

At this point, a leading and trailing edge taper ratio of 2.5 was used to approximate constant downwash along the span and for structural efficiency. The leading and trailing edges were tapered such that the spar remained at a constant ¼ chord location along the span for ease of manufacturing and construction. The surface is shown below in Figure 3.2.1-4.

AR	3.5
Area (ft^2)	34.6
Chord (ft)	3.14
Span (ft)	11
V_v	0.05
Span Below Boom (ft)	3.5
LE and TE Taper Ratio	2.5

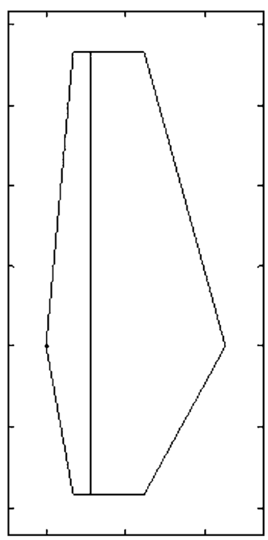

Figure 3.2.1-4: Vertical Tail (Leading Edge left)

Because the design of the horizontal tail was less critical than the vertical tail, the tail boom length was already defined during the design of the vertical surface. Roskam's equation provided a horizontal tail area of 9.5 ft^2. Three different aspect ratios, 9.5, 6.98, and 5.34, were evaluated in terms of induced drag and estimated weight. As was the case with the vertical surface, a compromise between the highest aspect ratio and lowest weight surfaces was chosen considering that the margin between the two highest aspect ratios is smaller than that between the two lowest while the margin between the two lowest weights is smaller than that between the two highest. The horizontal surface comparative matrix is shown in Table 3.2.1-3. Therefore, the 6.98 aspect ratio surface was chosen. In addition, a leading and trailing edge taper identical to the vertical tail were used. This finalized surface is shown in Figure 3.2.1-5.

Table 3.2.1-3: Comparative Matrix for Horizontal Surface

Chord [ft]	AR	Weight [lb]
12	9.50	8.26
14	6.98	7.22
16	5.34	6.43

AR	6.98
Area (ft^2)	9.5
Span	14
V_h	0.5
LE and TE Taper Ratio	2.5

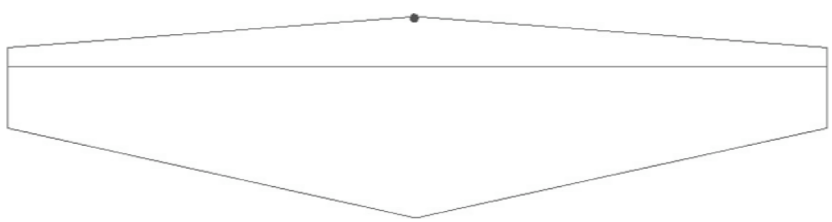

Figure 3.2.1-5: Horizontal Tail (Leading Edge top)

3.2.2 Aileron Design

With low speeds, large wingspans, and extreme light weight, HPA's are difficult to turn. Apparent mass, resulting from additional energy needed to accelerate the body of air around the wing of the airplane, significantly affects the effective rolling inertia of extremely light aircraft. The apparent mass can be modeled as the mass of a circular cylinder of air around the wings. For the Gossamer Condor, the apparent inertia in pitch and roll are 140% and 440%, respectively, of the actual moments of inertia [6]. The model for this aircraft was developed based on these estimates.

A measure of the importance of the roll damping caused by the apparent mass effect may be characterized by the damping time constant defined by Eq. (3.3.2-1)[3].

$$\tau_{roll} = \frac{\dot{\phi}}{\ddot{\phi}} \approx \frac{24 I_{roll}}{\rho V b^3 \bar{c} m} \quad (3.2.2\text{-}1)$$

Where the roll rate is $\dot{\phi}$, the roll inertia is I_{roll}, and the lift curve slope is m.

The ineffectiveness of ailerons for primary roll control may be seen by considering a single degree of freedom model in principle coordinates. The equation of motion is:

$$I_x \dot{p} = L_v v + L_p p + L_r r + \Delta L_c \quad (3.2.2\text{-}2)$$

Where the control is applied through Δ Lc. In the simplest case, when v = r = 0, the effect of a step aileron deflection is a simple first order system. The steady state roll rate for a step aileron deflection may be expressed as

$$p_{ss} = \frac{2 V C_{l_{\delta a}} \delta a}{C_{l_p} b} \quad (3.2.2\text{-}3)$$

From Equation 3.2.2-3, it is found that roll rate of 10 deg/sec at an aileron deflection of 15 deg, $C_{l,\delta a}$ must be at least 0.47. Table 3.2.2-2 shows estimates of $C_{l,\delta a}$ for different aileron sizes. The table indicates that for any realistic aileron size, inherent roll damping prevents turning at the desired roll rate. For this reason, it was determined that yaw-roll coupling was required.

Table 3.2.2-2. $C_{l,\delta a}$ estimates for various aileron sizes.

Length (ft)	% Chord	$C_{l_{\delta a}}$
15	40	0.311
30	40	0.430
15	50	0.351
30	50	0.485
15	60	0.380
30	60	0.520
24	60	0.470

Further problems such as aileron control reversal complicate the roll problem. For these reasons the Gossamer Condor, Daedalus, and Monarch relied on secondary roll generated through yaw-roll coupling [3]. For the Iron Butterfly, the primary roll control system utilizes yaw-roll coupling through deflection of the rudder. The roll control is supplemented through deflection of ailerons. The ailerons were designed to occupy the outboard 15 ft of the 30 ft semi-span, hinged at 70% chord.

A control scheme was developed based on 15 deg aileron deflection and 8 deg rudder deflection. A six degree-of-freedom dynamic model was developed and used to verify the ability to turn with the specified control system. Figure 3.2.2-2 indicates the roll response of this scheme. The figure illustrates that a peak roll rate of approximately 11 deg/sec occurs initially, which diminished with time. Also plotted in Figure 3.2.2-2 is the bank angle time response corresponding with the step deflection. The desired 15 deg bank angle is acquired within 1.6 sec.

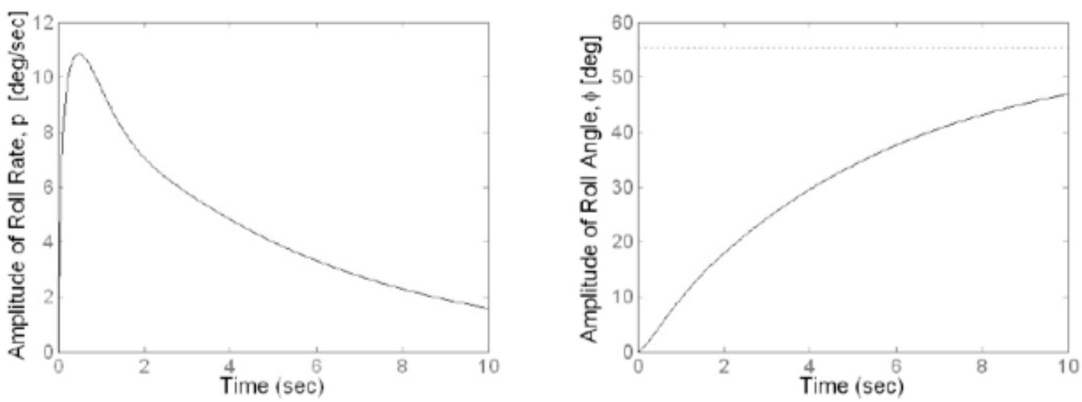

(a) Roll Rate p.　　(b) Roll Angle ϕ.

Figure 3.2.2-2. Response of Iron Butterfly to Aileron-Rudder Step

3.3 Structures

3.3.1 Mass Analysis

Careful mass allowance of all parts of the final design is considered extremely important. In order to ensure that each component is designed and built so that the total aircraft does not exceed weight limits, a strict mass allowance guide must be designed and followed. The previous HPAG teams have made estimates for this purpose. Several components, such as joints and the propeller, have been manufactured and the weights of these components have been updated based on measurements. The current mass allowance is shown in Table 3.3.1.

Table 3.3.1: Current Mass Allowance

Component	Weight (lb)
Spars	17.3
Struts	3.7
Ribs and skin	3.5
Joints	3.5
Tail boom	21.7
Propeller	2
Drive train	3.2
Cockpit frame	5
Vertical tail	7.9
Horizontal tail	7.2
Pilot	140
Total	215

This list is not exhaustive, but does represent the major components of the aircraft. It will be important to revise the mass allowance as components of the design are fabricated and become a reality. Ongoing analysis should continue as the design becomes more detailed. This analysis should guide material selection and weight optimization of the full-scale aircraft.

3.3.2 Spar and Strut Configuration

A schematic and summary of the current spar and strut configuration for this box-wing aircraft can be seen in the following Figure 3.3.2 and Table 3.3.2.

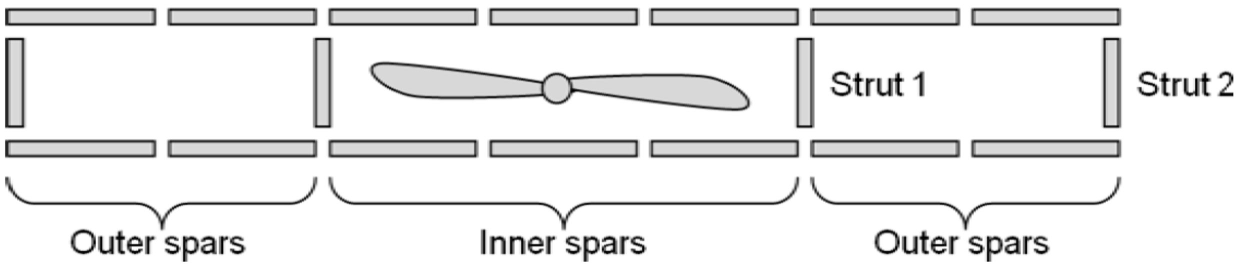

Figure 3.3.2: Spar and Strut Configuration

Table 3.3.2: Spar and Strut Configuration

	Material	Total Length (ft)	OD (in)	Wall Thickness (in)	Weight (lb)
Inner Spars	AL 6061-T6	48	2	0.028	9.8
Outer Spars	Carbon Fiber	72	1.75	approx. 0.015	approx. 7.5
Strut 1	Carbon Fiber	10	1.5	approx. 0.05	approx. 3.0
Strut 2	Carbon Fiber	10	1	approx. 0.02	approx. 0.7

All structural members of the design are cylindrical thin-walled tubes of either aluminum or carbon fiber. Aluminum was chosen for the inner spars because structural analysis [Appendix C - Section 5.4.3] shows that readily available tubes closely met the design requirements. This allows for the obvious advantage of buying the members instead of having to fabricate them.

Other components of the main structure will have to be fabricated by the team. Aluminum of the desired thicknesses called for by the design has not been found. As a result, the best current option is to fabricate the necessary outer spars and both sets of struts out of carbon fiber.

Theoretically, carbon fiber has a superior strength to weight ratio when compared to aluminum. The size of the benefit, however, is varied based upon the construction methods employed in fabrication. As an initial estimate, the carbon fiber structural members should be built to the dimensions of the aluminum members that would be required to meet the design. They should then be analyzed through structural testing to understand what changes can be made to the wall thicknesses to minimize the weight of each member while still meeting the load requirements.

Employing the current method for constructing carbon tubes should yield reliable components. It should be noted that the outer dimension of all struts and spars should remain unchanged as to not require changes to the rib construction method.

Some points of connection between the spars and struts will need to be non-permanent so the aircraft can be disassembled as required by the prize rules. Other connections could be permanent, hopefully easing assembly and providing added structural integrity. A comprehensive description explaining which joints should be permanent has yet to be established.

3.3.3 Rib Design

Comparison of multiple airfoils was performed in the early stages of this project. The DAE series of airfoil designed by Drela was chosen for its low C_d and C_m values as well as favorable boundary layer behavior.

An extensive process of construction, testing, and comparison of multiple rib designs has been performed. The results have concluded in a completed rib design for the 240 necessary ribs throughout the wings of the aircraft.

Given the weight allowance for all of the ribs throughout the aircraft, each rib would have to weigh less than 3 grams. The material selected is Expanded Polystyrene Foam (EPS). The team currently has a large quantity of the material which was donated by a local manufacturer, ThermaSteel Corporation. Figure 3.3.3-1 shows the final rib design.

Figure 3.3.3-1: Final Rib Design

The programs XFOIL and ANSYS were then used to analyze the airfoil. The analysis used the following properties for EPS foam: Young’s Modulus (E) of 250 psi and Poisson’s Ratio of 0.103. The balsa cap strips were not examined as they would take most of the load and therefore would not show the stresses around the cutouts. Figure 3.3.3-2 shows the pressure distribution, followed by the stress and deflection of the airfoil at cruise speed and angle of attack.

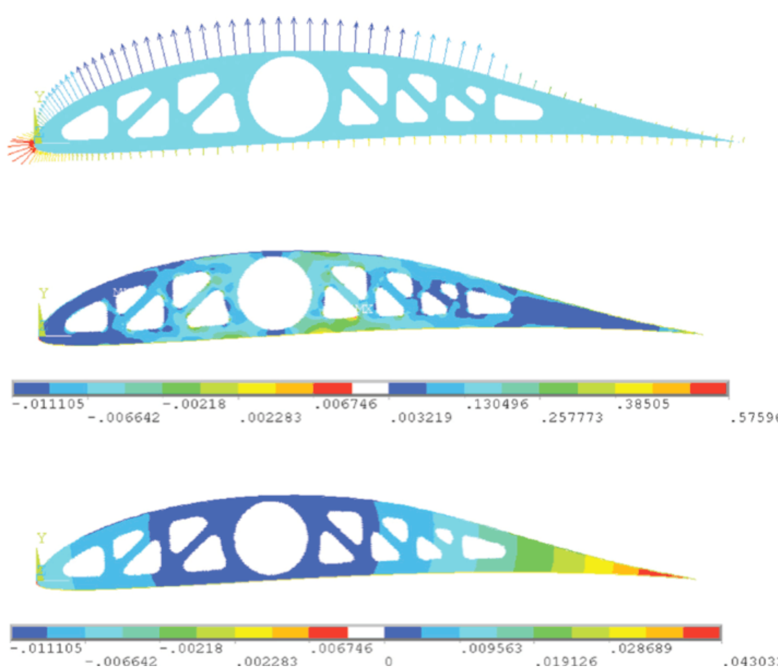

Figure 3.3.3-2: Pressure Distribution, Stress Distribution, and Deflection of the Final Rib Design at Straight and Level Flight

With the analysis completed, it was found that the rib design would be more than adequate structurally. Figure 3.3.3-3 shows both the DAE 11 and DAE 21 ribs with the final truss structure and spar-hole location along with ailerons.

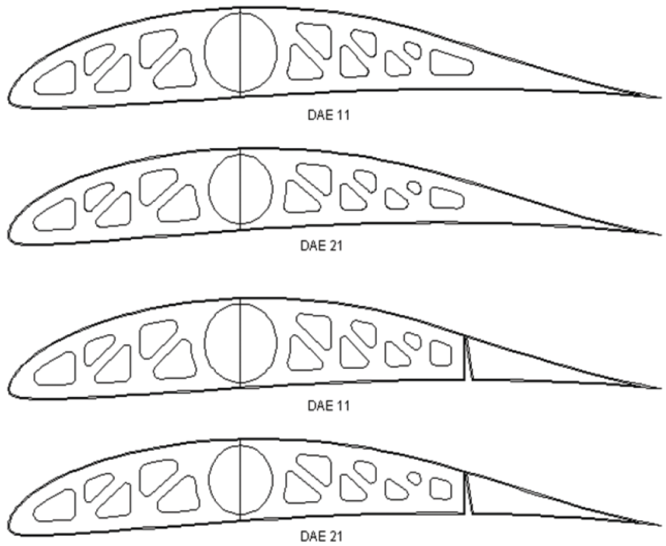

Figure 3.3.3-3: DAE series of airfoils to be used on the aircraft

3.3.4 Joint Design

A joint and balsa plug will be located at every location throughout the aircraft where a spar and/or strut meet. This requires straight, T, and L joints throughout the structure. Each joint connection will need to tightly fit around the spar or strut. Balsa plugs are being employed to deter crimping at the ends of the tubes.

The team is currently using bi-directional carbon fiber as the construction material for these joints. Strength to weight optimization is an iterative process, but through structural testing it has been found that a 2-3 layer straight joint and a 4-5 layer T joint are sufficient. Figure 3.3.4 provides a view of completed T and straight joints.

Figure 3.3.4: Spar and Strut Configuration

The construction method for both of these joints has been established. A method for the L joints needed at the tips of the aircraft has not been completed. It is thought that this process will be quite similar to the method used in T joint construction.

A scheme for non-permanently connecting the joints to the spars or struts has not been finalized, however, pinning the joints with a hollow metal dowel or devising a slotted alignment process has been considered. The final connecting scheme must consider the 30 minute assembly and disassembly requirement of the Kremer Prize. The final option will also need to pass structural testing.

3.3.5 Ailerons

Several requirements were established for determining an adequate aileron design. The ailerons would have to be lightweight and resistant to deformation during flight. They would also need to attach to the main wing without significant added structure and weight. Additionally, they would need to evenly and predictably actuate by a mechanism controlled by the pilot.

Each aileron will be located on the outer 18 feet of the bottom wing. The ailerons are divided into 9 ft sections which are separated at the dihedral change, located 10 ft from the wing tip. The aileron shape will be formed by 28 ribs evenly spaced along the length of the control surface. These ribs will be the same design as the ribs of the main wing. A wind tunnel test, described later in this report, has been performed on the basic aileron design. Further construction and testing of wing sections incorporating the ailerons will finalize the design. It is thought that at least four points of actuation will be needed in order to maintain the aileron shape and deter deformation. Figure 3.3.5-1 gives a view of the current configuration.

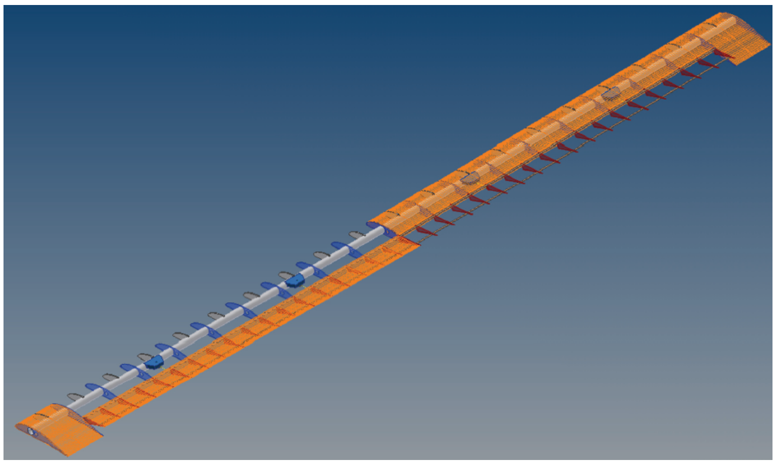

Figure 3.3.5-1: Aileron Placement on the Outer Wing

Due to the significant expected deflection of the wings during flight, the decision to pursue electronic servo control of the ailerons was made. The aileron system has been prototyped, constructed, and tested; however a definitive design has not been established. The Royal Aeronautics Society approved the use of battery control surfaces because it does not supplement propulsive power. A closer view of the aileron system is available in Figure 3.3.5-2.

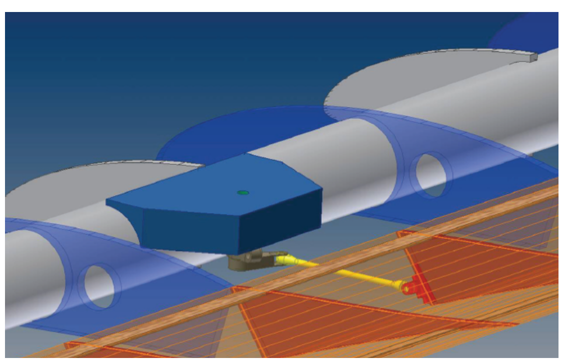

Figure 3.3.5-2: Close-up of Aileron Design

3.3.6 Guy Wire Addition

Full scale structural testing of the inner box wing, simulating straight and level flight, failed until a diagonal guy wire was added to the structure. A wire from the base of the cockpit to the top corner of each of the first struts has been added to the design.

The wire that is currently being used is 200 lb test Spectra fishing line that is 1 millimeter in diameter. The wire's addition allowed for a successful simulation of straight and level flight on one of the inner box wing sections.

The added drag of the proposed wires was found to be 0.15 pounds and the corresponding increase in required power is 7.4 W. While not desirable, the wires' addition is currently considered acceptable due to the successful testing of the structure and conservative parasitic drag estimates of the aircraft. Continued testing should determine the effectiveness of the addition of the wire to the structure.

It should be noted that structural improvements to the T-joint design, such as the addition of a fillet, could potentially allow for successful structural testing. This could eliminate the need for guy wires. Again, additional structural testing would be required.

3.3.7 Cockpit Force and Moment Determination

Calculations were performed to determine the loading of the cockpit caused by various forces throughout the airplane. Moments exerted on the cockpit by the tail boom are extensive due to the handling requirements imposed by the Kremer Prize competition course.

There are three significant moments applied to the cockpit by the horizontal and vertical tail through the tail boom. These are the pitching moment caused by deflection of the horizontal tail, a yawing moment caused by deflection of the vertical tail, and a rolling moment due to a large portion of the vertical tail being above the tail boom.

Based on a distance of 16.5 feet for the length of the tail boom, and a flight speed of 24.5 ft/s, the lifting forces for both the vertical tail were calculated using AVL and multiplied by distance to convert to torques. This analysis showed a yawing moment of approximately 640 ft-lbs and a pitching moment of at least 820 ft-lbs.

A rolling moment of approximately 86 ft-lbs associated with deflection of the vertical tail was also found. More information regarding the analysis of the vertical tail, and efforts to minimize this effect, can be found in Appendix D - Section 5.5.

Within the cockpit, the two primary forces will be the force of the pilot pedaling and the weight of the pilot. The design pedaling force was determined using an output condition of 310 watts at 45 RPM pedaling frequency, giving a safety factor of more than 2 compared to design flight RPM of 90. Using standard bicycle component sizing to determine the pedal arm size and gear size, the worst case pedaling load was estimated to be approximately 85 lbs, applied forward at the front structural member and rearward at the seat. A 2:1 gear ratio is used between the pedaling gear and the propeller shaft. A diagram of this analysis is given in Figure 3.3.7-1

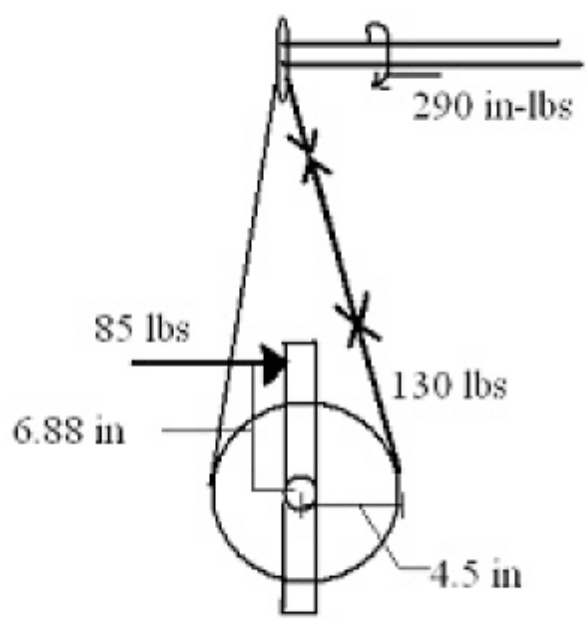

Figure 3.3.7-1: Diagram of the pedaling forces at 310 Watt output power and 45 RPM

The final load considered in this analysis is the pilot's weight, which will be approximately 140 lbs. A diagram showing the placement of all these loads is given in Figure 3.3.7-2.

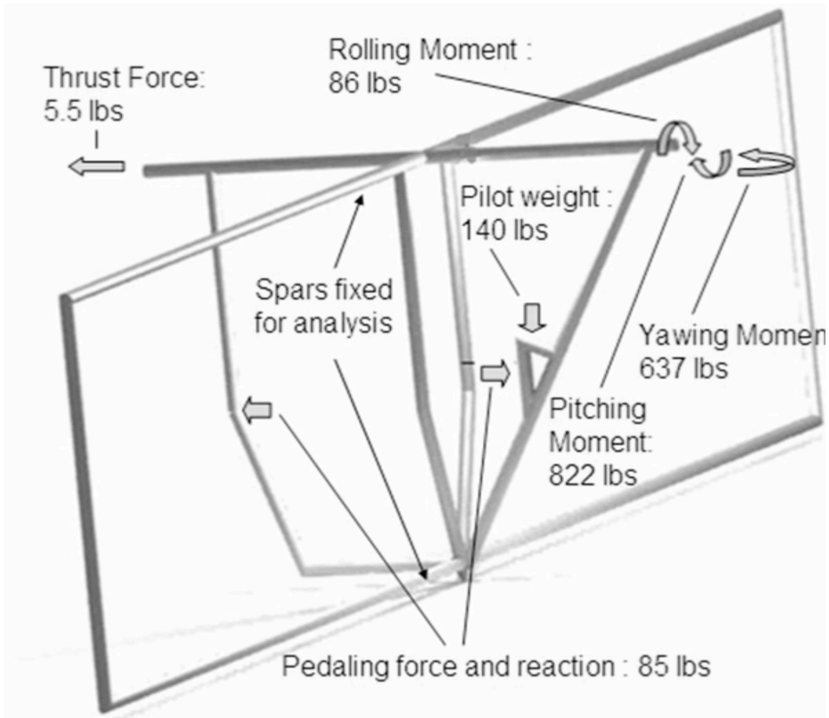

Figure 3.3.7-2: Cockpit loads used in structural analysis.

3.3.8 Cockpit Structural Configuration

The design of a cockpit includes consideration of ergonomics, structures, aerodynamics, and drive train integration. The basic shape of the structure is therefore much a result of non-structural constraints, and its development is discussed in other sections of this report. It is from these non-structural foundations that the structural optimization process began.

Figure 3.3.8-1: Cockpit design based on aerodynamic, ergonomic, and drive train constraints

As a preliminary structural material, it thought that the 2 inch diameter aluminum tubing the team already has would be the easiest to use for the frame. To connect the structural elements, each joint will be reinforced by carbon fiber wrapping. This is the easiest approach due to the customizability of the composite material and its high strength to weight ratio. Cathodic corrosion problems are caused by aluminum to carbon fiber contact, which would be an issue with these permanent joints. To combat this, a thin layer of 0.75 oz fiberglass will act as the first layer of wrap, before the structural carbon fiber wrapping is applied.

To determine the feasibility of the preliminary design, a finite element analysis was performed in COSMOSWorks using beam elements. This analysis assumes structurally perfect joints, and testing of the structure will be required to ensure sufficient strength of these carbon fiber structures. The stress results are given in Figure 5.1.8-2.

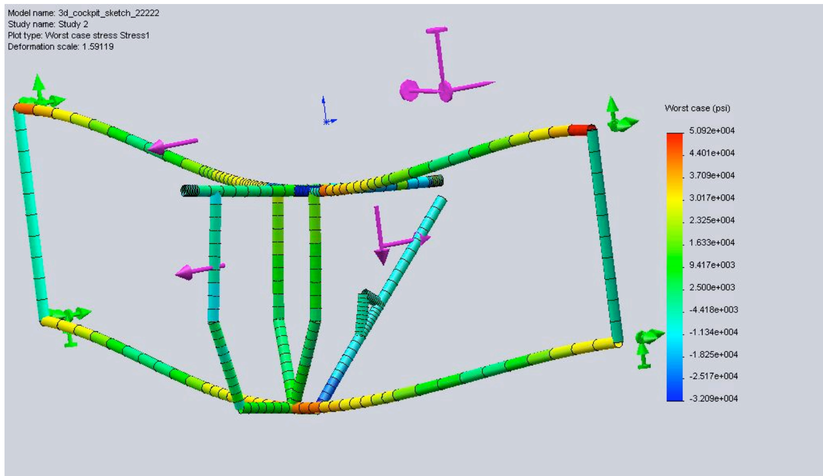

Figure 3.3.8-2: COSMOSWorks structural model

This analysis indicates a few problematic areas which must be further pursued. The red areas are those that exceed the yield stress for the 6061 aluminum. It is currently thought that these areas can be reinforced with additional carbon wrapping, while some of the lower stressed areas can use smaller diameter aluminum. The present calculated weight of the basic cockpit structure is 6.1 lbs, based on all structural members being 2 inch diameter, 0.032 inch wall aluminum tubing.

Work remains before the cockpit structure is fully optimized. As experiments are performed using the PVC mockup, it is likely that the geometry of certain parts of the model will be required to change. Further finite element analysis should be performed to determine the effect of adding structural wires to carry part of the internal loads. Based on the stress results obtained for the current model, it should be very feasible to trim the weight of the inner cockpit structure below 5 pounds by reducing the structure in low stress areas and carefully considering the load paths of the overall structure.

3.3.9 Tail Boom Design

The tail boom connects the wings and fuselage to the tail and the propeller. The distance from the wing to the tail is 16 ft 7 in, with an additional 4 ft from the wing to the propeller. The tail boom must be strong enough to carry the loads of the tail while being lightweight. These loads are given in Table 3.3.9.

Table 3.3.9: Worst case scenario of bending moments experienced by tail boom

Load Description	Quantity
Pitching moment, from elevator deflection	820 lb-ft
Yawing moment, from rudder deflection	640 lb-ft
Rolling moment, from rudder deflection	86 lb-ft
Thrust tensile force, from propeller	5.5 lb

The tail boom also must have very little deflection under load so as not to affect the control response of the tail surfaces through elongation or contraction of the control lines. In order to accomplish these structural requirements, the team has chosen a carbon fiber tail boom. Due to the variability of material properties obtained in composite wet lay-ups, strengths were simply estimated assuming a conservative strength estimate equal to that of aluminum 6061. A tail boom of the thickness required for aluminum should still weigh only 65% of an aluminum structure. This sample piece should be tested to confirm its strength properties, and can be made stronger by adding layers as required.

The preliminary calculations suggest that the tail boom must have an inner diameter of 4 in. The initial tail boom test section will be composed of 3 layers of bi-directional carbon fabric: two layers of 0/90 degree fabric, and one outer layer of 45/45 degree sleeve. The target weight of the tail boom is 21.7 lb.

3.3.10 Tail Design

Major characteristics of the design include a maximum takeoff rotation angle of 8º and an assumed fuselage height of 6.2 ft. The current design also calls for the tail to be placed 16 ft 7 in behind the main wing.

The construction method for both surfaces is in need of finalization, though the team is currently expecting to use a method similar to that of the main wing. This would include foam ribs, balsa or foam leading and trailing edge stock, and Dura-lar® skin. The spar for both surfaces will most likely be a unidirectional carbon tube of roughly 0.5 to 0.75 in. diameter. The design of the hinge used to attach both surfaces to the tail boom is in need of completion, though the team plans to use an external hinge that will be manufactured such that each surface does not rotate about its own spar.

3.3.11 Wind Gusting

The design requirement that differentiates the current Kremer Prize from the previous ones is the inclusion of an average 11 mph wind speed throughout flight. This will result in wind gusts, requiring the final aircraft to be designed to operate over a significantly larger range of load factors than previous HPA's.

The following equations were used to determine the load factors placed on the aircraft due to both vertical and horizontal wind gusts.

Vertical gusting: $$n_z = 1 + \left(\frac{\frac{1}{2}\rho V C_{L\alpha} S U}{W} \right)$$ U = gust velocity

Horizontal gusting: $$n_z = \left(\frac{\frac{1}{2}\rho (V+U)^2 C_{L\alpha} S}{W} \right)$$ U = gust velocity

Table 3.3.11-2 provides the expected load factors for the listed gust velocities at straight and level cruise conditions defined in Table 3.3.11-1.

Table 3.3.11-1: Conditions for Straight and Level Flight

	Straight and Level Flight	Units
ρ	0.002377	lb sec^2/ft^4
V (freestream)	24.5	mph
V_0	35.93	ft / s
C_l	0.8	
c	1.5	ft
b	60	ft
S	180	ft^2
W	215	lbs

Table 3.3.11-2: Load Factors for Horizontal and Vertical Wind Gusts

Vertical Gust (mph)	U (ft/s)	n_z	Horizontal Gust (mph)	U (ft/s)	n_z
1	0.68	1.020	1	0.68	1.067
2	1.36	1.039	2	1.36	1.107
3	2.05	1.059	3	2.05	1.148
4	2.73	1.078	4	2.73	1.190
5	3.41	1.098	5	3.41	1.232
6	4.09	1.117	6	4.09	1.275
7	4.77	1.137	7	4.77	1.319
8	5.45	1.156	8	5.45	1.364
9	6.14	1.176	9	6.14	1.409
10	6.82	1.195	10	6.82	1.455
11	7.50	1.215	11	7.50	1.502
			12	8.18	1.549
			13	8.86	1.597
			14	9.55	1.646
			15	10.23	1.696
			16	10.91	1.747
			17	11.59	1.798
			18	12.27	1.850
			19	12.95	1.903
			20	**13.64**	**1.956**

As apparent from the table, the final aircraft must have a large enough factor of safety in order to withstand the unavoidable presence of wind gusts. The range of acceptable wind gusts will have to be determined. Further structural analysis and testing should incorporate larger load factors based on these results.

3.4 Propulsion

3.4.1 Propeller Design

The propeller was optimized for a thrust required of 5.5 lb at 180 RPM and 24.5 mph. The thrust required of 5.5 lb is from a pessimistic drag estimate with a small factor of safety. By designing for a slightly higher power than what is expected, the propeller is capable of handling increased power input from the pilot. In previous HPA projects, the propeller responded poorly to an increase in power input from the pilot resulting in poor acceleration. To begin the propeller design, the vortex propeller theory from E. Eugene Larrabee was used. The propeller was optimized by inputting the design into XROTOR, a program developed by Mark Drela at MIT.

Although efficiency of the propeller was very important in designing it, constraints were also set so that it could be manufactured with the tools available to the team. The main structural constraint set was that the airfoil thickness at the root and 2 ft from the root be great enough for a 0.25 in diameter tube to fit inside the airfoil. This was set so that the main spar which transmits the load from the propeller to the propeller hub, and allows the pitch of the blades to change, be able to fit inside the propeller. From this constraint, a minimum chord was found that corresponded to the thickness required to fit the 0.25 in tube. Once the constraints were set, the propeller designed was iterated for a range of propeller radii and section CL in order to obtain the most efficient propeller possible. For each radius iteration, the propeller was initially sized using Larrabee's method, and then input into XROTOR to iterate the section CL of the propeller. Through the use of these two programs, a propeller with a tip radius of 4.59 ft, a section CL of 0.7, and an efficiency of 92.27 percent was calculated. The 3-D CAD model of the propeller is shown in Figure 3.4.1.

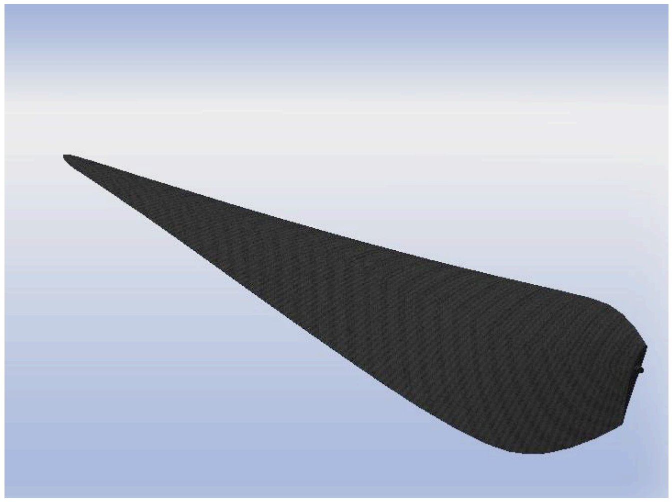

Figure 3.4.1: Initial Propeller Design CAD Rendering

3.4.2 Variable Pitch Mechanism

The Kremer prize mission profile states that there must be a head wind or a tail wind present. Because of the very strict flight regime of the aircraft, the thrust must be adjusted in order for the aircraft to keep the relative airspeed in the designed range. There are two possible ways to increase or decrease the thrust of the propeller: change the RPM of the propeller or change the pitch of the propeller. Chaning the RPM would move the power output of the pilot away from its optimum value. Therefore a variable pitch mechanism should be incorporated to provide the pilot with a way to change thrust while keeping his power output at an optimum level.

In designing a variable pitch mechanism, simplicity, cost, and weight of the mechanism should be considered. The two most popular designs are the pinion-gear type and the pushrod type, as most commonly seen on RC airplanes, shown in Figure 3.4.2-1.

Figure 3.4.2-1: Pinion-Gear VPM (left) and Pushrod VPM (right)

The pinion-gear design would involve a series of gears to transmit the control from the propeller to the pilot, which would increase the weight of the aircraft significantly and complicate the drive shaft assembly. Furthermore, the small inner diameter of the driveshaft constrains the gear size, thus creating a large load on the teeth of the gears.

The pushrod type design would be easier to implement, due to the fact that the control is transmitted through pushrods, which can be made lightweight and cost effective. Furthermore, the load will be transmitted linearly through the pushrods, which serve as a more practical load carrying structure then the gear teeth.

The current design, enclosed in a 4 inch carbon fiber housing, is shown in Figure 3.4.2-2.

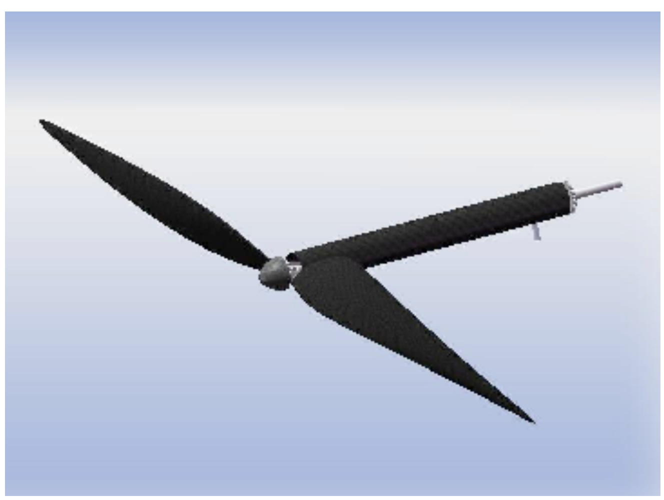

Figure 3.4.2-2: CAD Rendering of Final Assembly

The motivation for this design is to build a cost effective proof of concept for the variable pitch mechanism, which can be adapted to the cockpit test stand for further testing. The mechanism that will be implemented on the flying prototype will be much lighter, with custom made parts.

In the rear end of the assembly, there is an actuator lever for changing the pitch of the propeller, and a drive gear for power transmission to the propeller. Each operates independently of the other. The detail of the mechanism can be seen below in Figure 3.4.2-3.

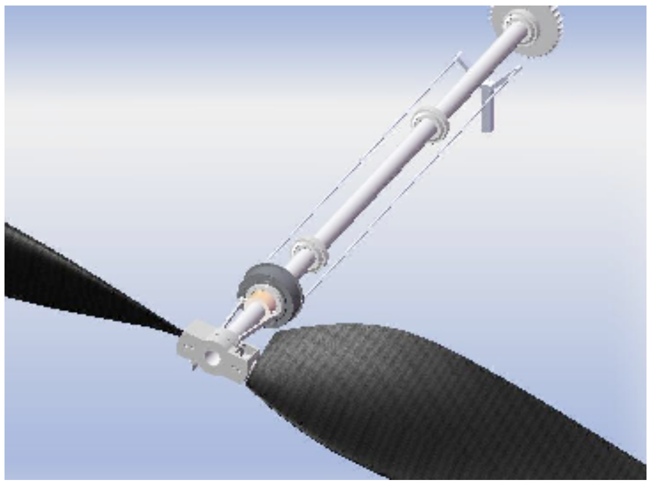

Figure 3.4.2-3: CAD Rendering of the Variable Pitch Mechanism

The two control rods attach the actuator lever to the isolator bearing, which can be seen in detail in Figure 3.4.2-4.

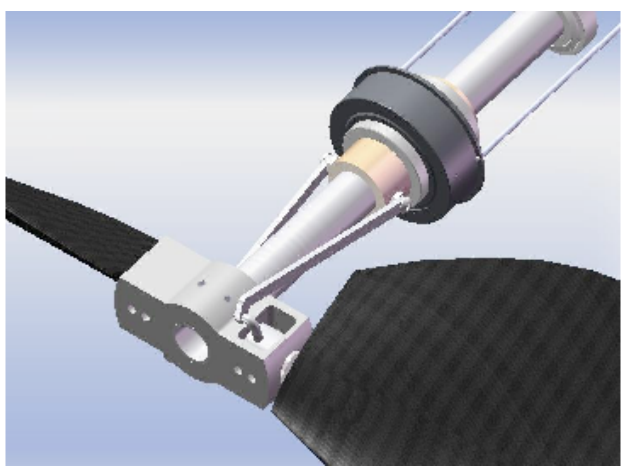

Figure 3.4.2-4: CAD Rendering of the Control Rods and Isolator Bearing in Detail

The isolator bearing isolates the rotation of the shaft from the linear motion of the variable pitch mechanism. The rotational part of the isolator bearing is attached to a brass bushing that slides up and down the shaft, while also rotating with the shaft. The propeller pitch is controlled by two lever arms that rotate the propeller blades inside the main hub. On the final aircraft, the 4 inch diameter carbon fiber housing enclosing the assembly will be attached to the airframe. There will also be a nosecone fitted to the front of the assembly to reduce drag. The actuator lever will be located inside the cockpit along, minimizing drag.

3.4.3 Pitch Control Mechanism Details

In order to determine the forces required to change pitch of the propeller blade, it is necessary to obtain sufficient pitching moment data for the propeller. However, obtaining the moment coefficient for a single blade is very hard to do due to various aero-elastic effects that arise from gyroscopic forces on the propeller, as well as deformations due to drag on the propeller.

Given set geometry constraints and pitch angle, the propeller thrust is directly proportional to the square of the relative velocity of propeller blade (not accounting for stalling of the propeller, since the operating RPM is well below the stall RPM). The pitching moment of the blade is also directly proportional to the square of the relative velocity of the propeller with the same set of constraints. Judging from the low thrust output and RPM of the propeller (as compared to a piston engine aircraft propeller), the moment should be sufficiently small. Furthermore, the design of the prop allows for maximum pitch change of +/– 10 degrees. This is due to the fact that the sections of the prop will produce negative thrust at pitch angles outside that range. Given the size constraint of the 4-inch diameter housing that encloses the variable pitch mechanism, the 20° pitch change of the prop corresponds to 0.7 inch travel of the connector rods. That small distance can be used in a lever setup, which would provide the necessary force to actuate the prop.

From these factors, it was determined that the forces that are required to change the pitch of the prop are negligible, and the actual magnitude can be varied through the pilot-system linkage design. The only requirement on the system is that it has the ability to lock at a given position, so that the pilot does not have to apply a continuous force to keep the propeller at a certain pitch.

Another possibility is an electrical control systems consisting of a hobby aircraft servo, and a analog PID controller. The 2005-2006 team estimated that the maximum weight for the servo/controller system is 20 grams.

The design of the pilot control system is left for future teams. It is dependant on the placement of controls inside the cockpit, which has not yet been determined.

3.5 Cockpit Design

3.5.1 Pilot Positioning

The research that was done by previous teams showed that the optimum power stroke of the human leg to be between 90 degree and 175 degree knee angle (Figure 3.5.1). This corresponds approximately to a distance of 34 and 42 inches from hip to the pedals for a pilot with a height of 70 inches. Positioning tests also showed that a seat angle of 30 degrees provided an optimal position with good visibility.

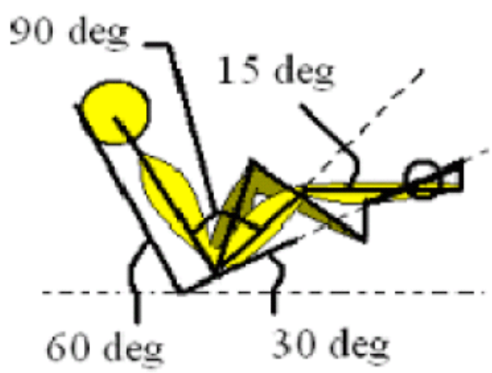

Figure 3.5.1: Pilot Positioning

3.5.2 Pilot Center of Gravity

The aircraft is designed with its center of gravity at 0.4 mean aerodynamic chord (MAC) and centered vertically between the two wings [Appendix D - Section 4.3.1]. Because of the significance of the pilot's weight, the center of gravity of the pilot must correspond to the CG of the airplane.

3.5.3 Drive Train

The easiest way to transfer power from the pilot to the propeller is through a chain. A strong and light plastic chain will be used help minimize weight. A custom pedal assembly will have to be designed to minimize additional weight. A chain system will need to be tested for strength and efficiency on the cock pit mockup (Section 3.5.5). There is concern that the chain may be prone to slipping off the gear. A gearbox may be necessary if the chain design becomes too problematic to implement.

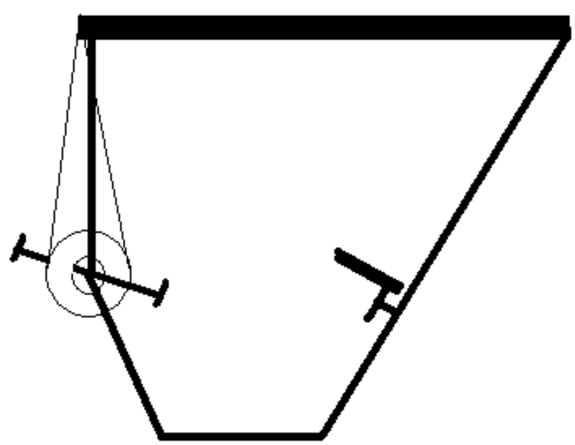

Figure 3.5.3: Chain Drive Train

3.5.4 Pilot Controls

The aircraft's primary controls consist of two side by side control sticks, placed in front of the pilot. Control inputs from the pilot will be transferred to the control surfaces, or to a potentiometer, using a pull-pull control line system. A control system mockup, shown in Figure 3.5.4, has been constructed. This prototype will be used in the PVC cockpit mockup to determine ideal positioning.

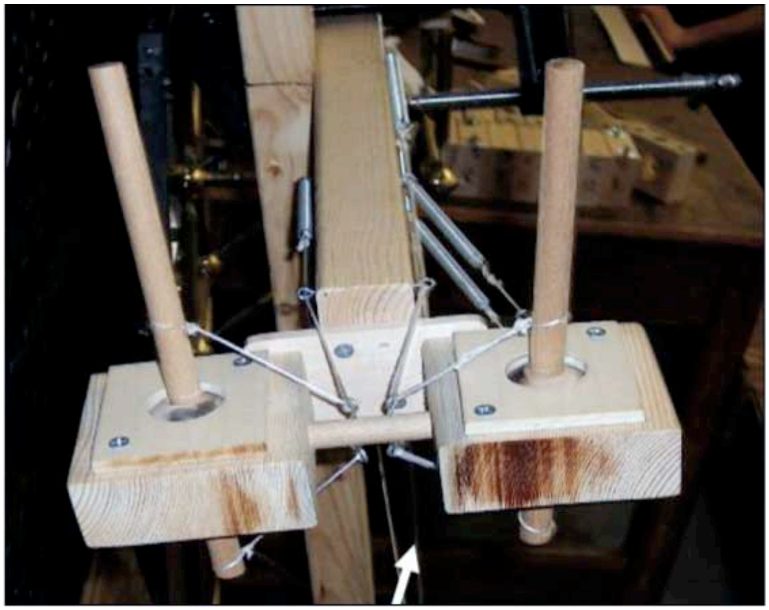

Figure 3.5.4: Two-Stick Control System

3.5.5 Mockup

A full-size PVC mockup of the cockpit was built with a purpose of testing the ergonomics (Figure 3.5.5). PVC was chosen as the material due to the ease of construction and also the ability to support the weight of the pilot.

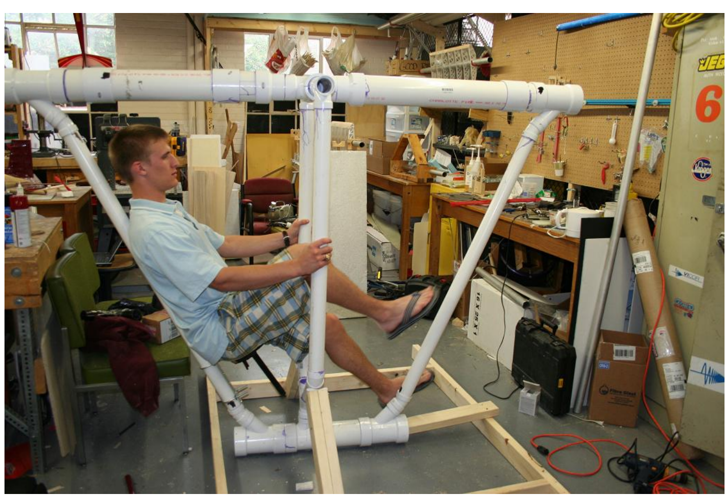

Figure 3.5.5: Full-Size PVC Cockpit Mockup.

Preliminary ergonomic seat testing showed that a bicycle seat would be most efficient for pedaling, however, pilot's stability becomes a concern. Testing using the PVC mockup will allow different seats to be compared for pilot stability and range of motion.

Since this structure can support the weight of the pilot, the drive train can be tested on this mockup. This structure can also facilitate the preliminary construction of the controls and the cockpit cowling.

3.6 Landing Gear

The following landing gear design for the prototype aircraft is based on previous HPA's landing gear and the successes of the model. The prototype's landing gear will be in a bicycle configuration with possible wing-mounted wheels. Bicycle gear can be found on most successful HPA's. The setup includes one large main wheel close to the pilot, which carries most of the loads, with a smaller wheel at the front of the fuselage for longitudinal stability.

Although previous HPA's do not have any landing gear in the wing, they had high wing configurations and therefore there was less of a possibility of a wing tip striking the ground during taxi, takeoff, or landing. Since the team's box plane design has a lower wing, which is close to the ground, the probability of a tip strike is higher. A tip strike would be extremely detrimental due to the fragile nature of the design. In order to avoid this, small wheels could be mounted either at the wing tips or at a semi-span wing strut-spar joint. Further analysis is required on the position and loads carried by the landing gear. A possible configuration is shown below in Figure 3.6.

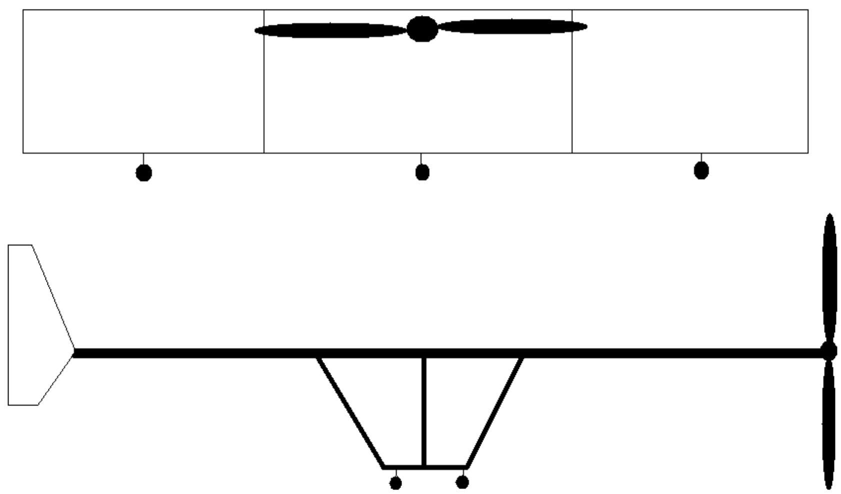

Figure 3.6: Wheel Placement on the Aircraft

4. Prototype Construction

4.1 Airfoil and Wing Construction

The rib, airfoil, and wing construction is made up of the following materials: aluminum spars, foam, balsa ribs, epoxy, and Dura-Lar. The completed ribs are slid onto the spar and the trailing edges are aligned to ensure the pitch of each rib is equal. Then, the ribs are epoxied to the spar in six inch increments. Once the ribs are in place, the leading and trailing edges are also epoxied to the ribs. Finaly, the ribs are covered with Dura-Lar® and shrunk to keep the skin taught using a heat gun. All the components of the wing are held together using epoxy. For further information regarding wing construction refer to Section 5.8.1 of the 2006-2007 report.

4.2 Rib Construction

Construction of the airfoils is done using a hotwire foam cutter to shape the foam and then using epoxy to adhere the balsa cap strips to the foam. The hotwire foam cutter works by heating a nickel-chromium wire to a point where it vaporizes foam as it is passed through. Using laser-cut stainless steel templates to ensure proper shape, the hotwire is guided along these templates through a large foam block to create the initial rib shape. This large rib is then sliced into 0.25 in thick ribs. A different template is then used to secure the balsa cap strip while simultaneously removing sections of the rib that are not structurally critical. A complete rib is displayed in the following image:

Figure 4.2: Competed Rib Sections Aligned on Aluminum Spar

4.3 Aileron Construction

Aileron construction is very similar to airfoil and wing construction. The only major difference is that the mold used to cut out the inner truss section is slightly modified. Once each rib is constructed, the end of the airfoil is cut to create the aileron section. The ribs are then attached to the spar, as described in Section 4.1. Before the aileron section is attached to the rest of the rib, the remote electrical servo is mounted. Lastly, the aileron is attached to the rest of the rib with a hinge made of packing tape. For further information regarding aileron construction refer to the Section 5.8.2 of the 2006-2007 Report.

4.4 Composite Joints

Because of the long wingspan of this aircraft, combined with limited material lengths and transportation constraints, removable joints were required to attach the aircraft's pieces. It was determined that making these from composite materials would result in the most straightforward construction, along with a high strength to weight ratio. Three types of joints are required for this aircraft: T-joints connect two spar sections with the inner vertical struts, straight joints connect co-linear spar sections, and L-joints connect the outer spar with the outer strut. The first two joints have been constructed and tested. No construction work has begun on the L-joints, but their construction process will likely be similar to that of the T-joints. All joints are made with carbon fiber for its high stiffness to weight ratio, and use balsa wood plugs inside the aluminum to reduce stress concentration. Further consideration is required to determine a method for easily attaching and disconnecting the tubing sections from the joints.

4.4.1 T-joints

The first construction method for making the T-joints utilized a foam mold into which a wax plug was cast. A picture of this mold is given in Figure 4.4.1-1. Once the wax hardened, the carbon fiber joint was laid over this plug, which was later melted out. This method resulted in strong joints, but the poor dimensional stability of the wax required tremendous sanding of the joints for compatibility with the tubing sections.

Figure 4.4.1-1: Female T-joint molds for casting wax centers

To improve the accuracy of the joint dimensions, a new process was designed. This method retained the wax casting for the center fillet section and used actual aluminum tubing as the outer portions of the center, ensuring a reliable dimensions of the joint. To create the wax center, a fiberglass mold was made similar to the previous foam molds, with open ends allowing it to clasp over the aluminum tubing. This mold is pictured in Figure 4.4.1-2. More information on the design of this method and the construction of the fixtures is provided in Appendix B – Section 3.2.2. To prevent the epoxy and carbon fiber lay up from sticking to the aluminum tubes, mold release, followed by a layer of heat shrink PVC, was applied.

Figure 4.4.1-2: Final T-joint lay up jig, with fiberglass mold for casting wax center.

Once the wax is cast, the fiberglass mold is removed, while leaving the aluminum tubes in the jig. The T-joints are then created by covering the wax and aluminum with 5 layers of 5.8 oz/yd^2 carbon fiber. Each layer is composed of several carbon fiber strips that are sized to cover the various geometries, with some overlapping to ensure a solid structure. The straight portions of the joint are then covered with heat shrink tubing, and the entire lay up is vacuum bagged. The resulting T-joints are shown in Figure 4.4.1-3.

Figure 4.4.1-3: Completed T-joints and straight joints

4.4.2 Straight joints

Constructing the straight joints is a straightforward procedure; these joints connect two spars of the same diameter, so only one aluminum tube is needed. A section of the aluminum tube is prepared with a wax mold release agent, and is then covered in a layer of heat shrink tubing. Four layers of 5.8 oz/yd^2 bi-directional carbon fiber are then wrapped over the heat shrink tubing, and a second layer of heat shrink is applied over the lay up. Starting at one end, a heat gun is used to shrink PVC tubing. As the tubing shrinks, the heat is moved along the lay up, squeezing out excess epoxy towards the opposite end.

4.5 Composite Spars

The design inherited at the beginning of the year for the outer spars and the struts of the aircraft involved an intensive and dangerous process of chemically etching aluminum. The required wall thickness of the outer spars and struts given by force determination and analysis on the structure was found to be so thin that an available vendor could not be found to provide the material. As a result, the decision to chemically etch the aluminum spars was made in order to drastically reduce the weight of the members and remove unnecessary material from the structure. Further detail of the etching process can be found in Appendix C – Section 5.8.3.

The process was not as reliable as first thought, yielding uneven etching and a lack of the ability to ensure proper etching inside of the spar. Due to this, and the safety risks involved, the current team decided to change the design to carbon fiber spars and struts.

A method of wet carbon fiber lay-ups is anticipated. This method consists of laying carbon fiber over a mandrel covered in thick monokote, which is then covered in heat shrink tubing. The monokote layer allows the carbon fiber to be removed from the mandrel once it has cured. The heat shrink tubing ensures a smooth and uniform finish of the outer surface while compressing the carbon fiber as it cures. The method is currently producing reliable results, but has not been specifically tailored to each tubes dimensions.

Initially all of the dimensions of both the outer spars and struts will remain the same as the etched aluminum dimensions. This decision was made based on the knowledge that the weight difference between aluminum and carbon fiber wet lay-up components is negligible. However, the carbon fiber components should be roughly 30% stronger than the aluminum counterparts.

An important dimension for these components is the outer diameter. It will need to remain the same in order for the airfoil shape and construction method to remain unchanged. Through trial fabrications, this should be achievable. Until testing dictates otherwise, the overall weight and dimensions of the components should remain the same, while their strength increases.

4.6 Propeller Construction

A propeller was constructed based on the CAD model of the XROTOR optimized design in a multiple step process using composite construction techniques. Two positive male propeller plugs were first cut from machining foam with a CNC mill. Once the basic shapes were cut, they were repeatedly painted and sanded until the entire surface was smooth. These plugs are shown in Figure 4.6-1.

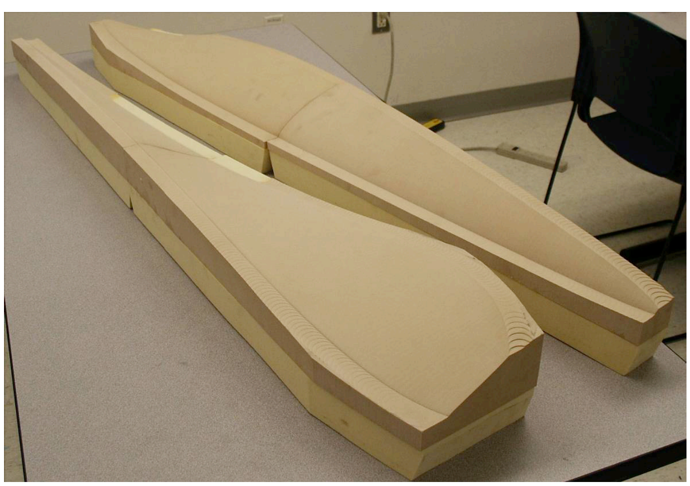

Figure 4.6-1: CNC machined male propeller plugs before final finishing

From the foam plugs, a pair of female fiberglass molds was constructed. To construct these, the plugs were first waxed and prepared with PVA mold release film. They were then coated with a layer of thickened epoxy to act as a smooth surface for the molds. Once the epoxy was tacky, two layers of 6 oz/yd^2 fiberglass were applied. The fiberglass was then covered with a layer of peel-ply release fabric to give a coarse surface. After curing overnight, the release fabric was removed, and the surface was sanded with 120 grit sandpaper to ensure a good mechanical bond between the fiberglass layers. Finally, four layers of fiberglass chopped strand mat were laid up with more epoxy, a layer of peel-ply release and a layer of breather cloth were put on, and the entire assembly was vacuum bagged. Photographs of this process are provided in Figures 4.6-2 and 4.6-3.

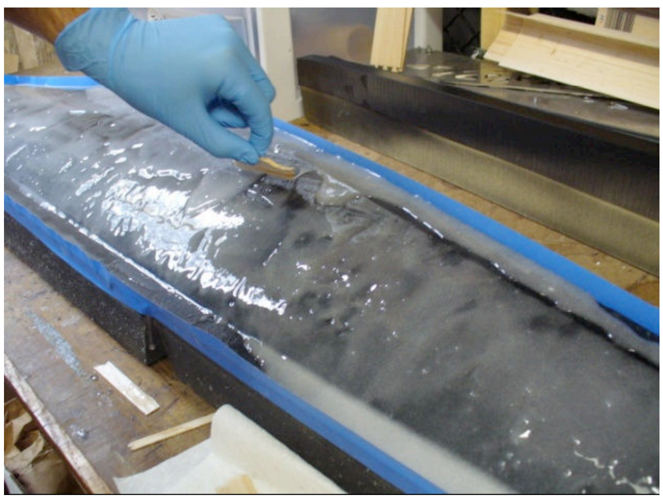

Figure 4.6-2: Thickened epoxy being applied to propeller plug

Figure 4.6-3: Propeller mold in vacuum bag

The completed molds were cleanly removed from the plug without damage. After wet sanding the surface lightly with 320 to 600 grit sandpaper, the release surface of the mold was extremely smooth.

To expedite the testing schedule, it was decided to intentionally overbuild the propeller for testing to ensure that it would function. Based on some preliminary experience with carbon fiber pieces, it was predicted that creating propeller shells out of 2 layers of 5.7 oz/yd^2 carbon would give sufficient strength.

With the molds complete, the layup of the shells was a straightforward process. The mold was prepared in a similar way to the plug; epoxy was spread onto the mold surface, and the two layers of carbon fiber fabric were laid onto the surface and impregnated with more epoxy. The peel-ply and breather cloths were then applied, and the piece was vacuum bagged. To attach the propeller to the shaft, a ¼ inch carbon fiber spar was used. This was in turn connected to the propeller through 4 1/8 inch plywood ribs, made from the existing CAD model of the propeller.

When the shaft and ribs assembly was glued together, it was placed into one of the propeller shell halves, and the entire assembly was connected together using thickened epoxy applied on the edges. The flanges of the completed propeller blades were trimmed, but due to the extremely limited surface area of the seam, the remaining bond between the two shells was extremely weak. To remedy this, a layer of 0.75 oz/yd^2 fiberglass was applied over the seam. To return the propeller to a smooth aerodynamic shape, it was then necessary to apply Bondo glazing putty over the surface and sand back down. The final propeller can be seen in Figure 4.6-4.

Figure 4.6-4: Complete prototype propeller

4.7 Variable Pitch

Several parts were ordered for the construction of the variable pitch mechanism, however there are a few parts that have to be custom made from aluminum. Time constraints did not allow machining of these parts.

The shaft and isolator bearings were assembled and shown below in Figure 4.7. The construction of the variable pitch mechanism is left to the next year's team. A full CAD package is available, complete with all the hardware and McMaster catalog part numbers.

Figure 4.7: Isolator Bearing Attached to Shaft

4.8 Tail Boom Construction Considerations

The tail boom construction and testing procedure has not begun, but much of the process has been planned. An eight-foot mandrel and ten feet of 45/45° carbon sock have been purchased. Thicker Mylar has also been purchased to facilitate release of the layup. Due to the team's lack of expertise with stress analysis of carbon fiber, a first guess of the required layup will first be constructed, which will be tested to the required loads with a simply supported beam test. This first test structure will be constructed with two wraps of the 0/90 bi-directional 5.8 oz/yd^2 carbon fabric, and one layer of 15.1 oz/yd^2 carbon fiber 45/45° sleeve. Peel ply will be used as the final layer of the lay up underneath PVC heat shrink tubing to allow a surface to which more layers of carbon fiber can be attached if testing shows this necessary. The first section will be just under eight feet in length to serve as the top of the cockpit. More sections, or one longer section, will be required to serve as the full length of the tail boom.

5. Testing

5.1 2006-2007 Testing

5.1.1 Quarter-Scale Model Testing

During the Fall Semester in 2006, a quarter-scale model of the HPA design was tested. The main goal of the test was to confirm the aerodynamic properties of the aircraft for feasibility. The model also needed to prove the effectiveness of the elevator, rudder, and ailerons. Although the model was intended to fly the complete course as set up by the Kremer Prize regulations, a suitable testing site was not found. However, the model proved that the configuration of the control surfaces was adequate for stability and control. Further quarter-scaled model information is available in the 2006-2007 Final Report.

5.1.2 Wind Tunnel Testing

In the previous year, wind tunnel testing was performed in Virginia Tech's Open Jet wind tunnel and was used to observe airflow over a 3 ft test wing section. The test section seated in the wind tunnel can be seen in the following figure. The objective of the testing was to ensure that:

1. The flow over the wing stayed attached
2. The Dura-Lar® covering held its shape and stayed taut
3. The leading edge did not deform during aerodynamic loading
4. The spar location induces no pitching moment

Figure 5.1.2: Wind Tunnel Testing

The test procedure used during this experiment was as follows. The wing was secured into the wind tunnel, running at 24.5 mph. A yarn stick was used to check flow attachment at various points along the airfoil. To measure pitching moment, the airfoil was allowed to freely rotate in its holders.

After testing it was concluded that the Dura-Lar® was a sufficient covering material. It did not deform or flap during the test. The yarn showed an attached flow going over the wing as expected. The spar location, however, was found to be insufficient; a strong pitch down moment was created indicating that the spar would need to be located further back.

5.1.3 Aileron Testing

A three-foot test section of the wing containing an aileron was constructed and tested in the Virginia Tech Open Jet Wind Tunnel last year. The purpose of the aileron test was to determine:

1. How many aileron actuators would be necessary to effectively deflect the aileron
2. What structural reinforcements will allow constant deflection across the aileron
3. Is the selected actuator strong enough to deflect the aileron uniformly

In the test section, an electronic servo was used for actuation of the aileron. The complete aileron test section can be seen in the following figure.

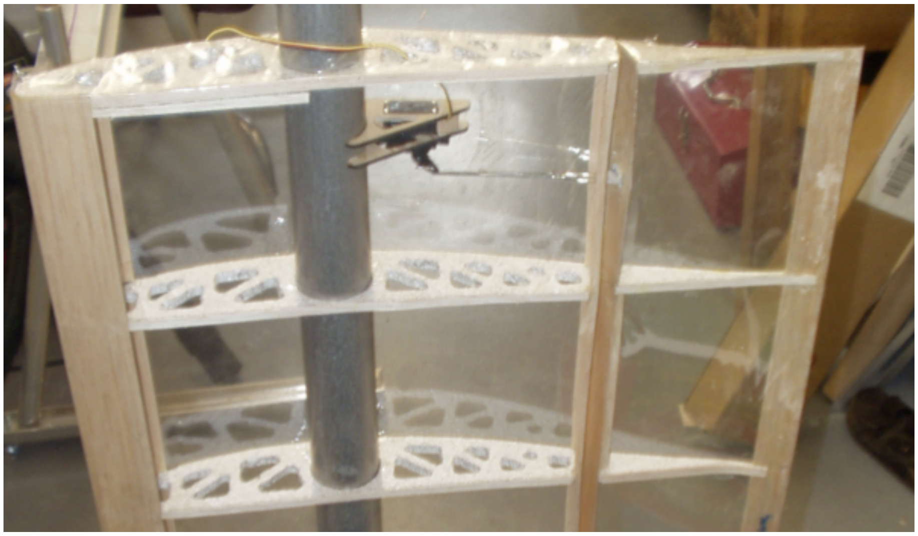

Figure 5.1.3: Aileron Testing

It was predicted that using four actuators on each aileron would provide sufficient deflection. After testing, it was concluded that four actuators spaced evenly throughout the aileron would provide sufficient power and allow even deflection, confirming the prediction.

5.1.4 Spanwise Testing

A 10 ft wing section was constructed with the intent of measuring spanwise deflection to validate the ANSYS models. This wing was constructed out of DAE 11 ribs and a 2.0 in outer diameter aluminum spar. The ribs, leading edge, trailing edge, and covering were attached exactly as they will be done on the final wing. A measuring stick was attached to the tip of the wing so that deflection measurements could be obtained while the wing was moving at flight speed. Once the wing was constructed, a mounting plate was created to attach the wing to the roof rack of a team member's car. The test was performed in an empty parking lot where a ¼ mile strip of open flat pavement was available. Several tests were then completed with varying speeds and angles of attack. The wing section can be seen attached to the car in figure below.

Figure 5.1.4: Spanwise Testing

After the flight testing was completed, it was found that the camera mount was not secure enough to get reliable deflection measurements. However, it should be noted that, qualitatively, the wing performed very well at all conditions tested.

5.2 Wing Testing

5.2.1 Inner Box Wing

The team designed a test for the wing structure that would simulate straight and level flight. The structure being tested is the inner 12-foot section of the box-wing. A distributed load is placed on the structure and moment arms with tip loads to simulate the outer 18 feet of wing section. Figure 5.2.1-1 is a picture of the ¼ scale model which highlights the specific area being tested. The major reasons for running this test was to validate 2006-2007 year's design, test composite joints, and investigate any unforeseen problems relating to construction and/or design.

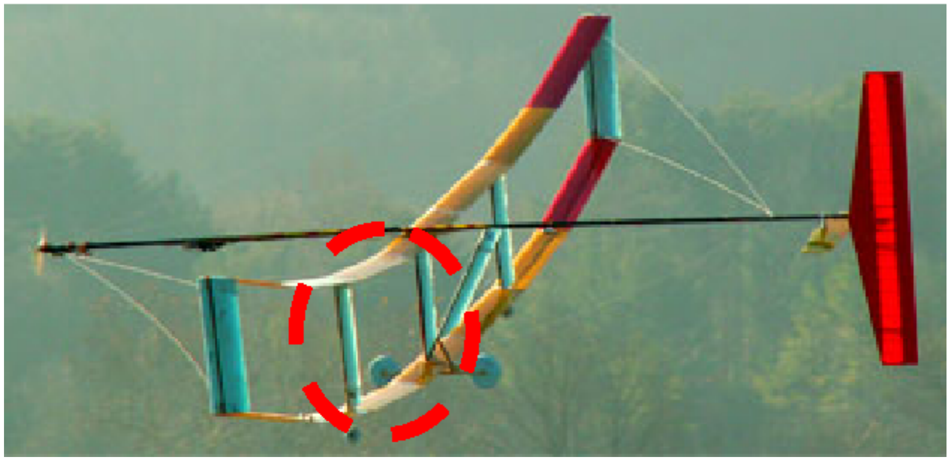

Figure 5.2.1-1: Box Wing Test Area

The lift distribution given by AVL for straight and level flight was used to calculate the necessary loads to apply to the structure. The lift distribution is provided in Figure 5.2.1-2.

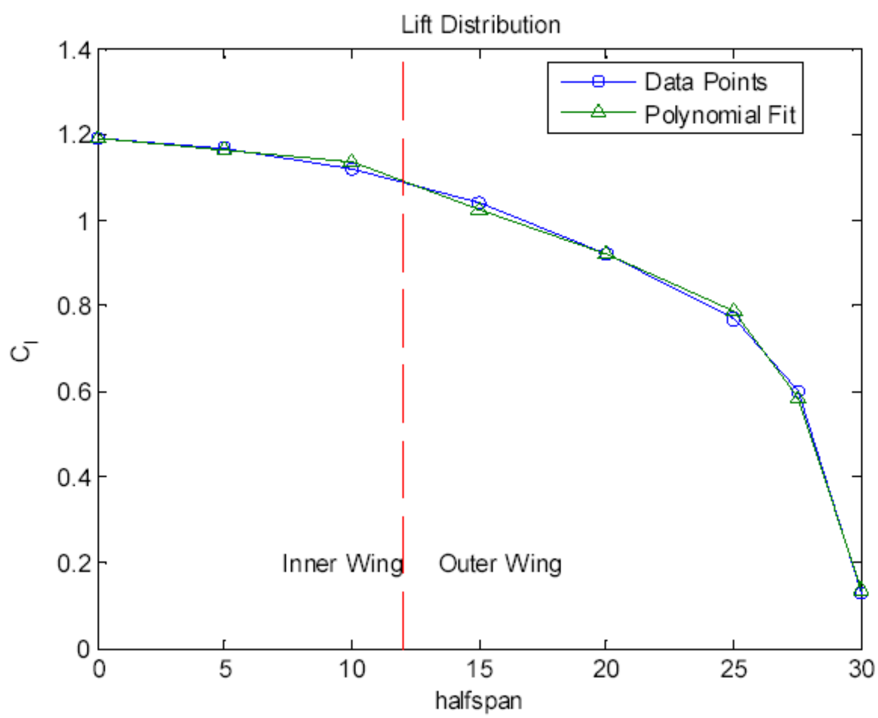

Figure 5.2.1-2: AVL Lift Distribution

The red dashed line denotes the location of the first strut. This point indicates the division of the inner and outer section of the wing. As previously stated, the inner section is to be tested and the outer section is to be simulated. This lift curve was integrated to find the total lift, moment and shear for both sections. The lift on the inner section of the wing can be approximated with a constant distributed load applied directly to the structure. The necessary moment and shear force of the outer wings that needs to be simulated was obtained from the lift curve. The following table provides this information.

Table 5.2.1-1: Applied Load

Inner Applied Load	**0.8 lb placed every 6 inches**
Outer Shear Force	24.7 lb
Outer Moment	183.5 lb-ft

The weight of the moment arms was used to determine their necessary lengths and the tip load that would need to be applied on each for proper simulation of the outer wing section. The following table gives the loads applied to the structure.

Table 5.2.1-2: Wing Moment Load Information

Inner Distributed Load	**0.8 lb placed every 6 inches**
Applied Tip Load	13.1 lb
Moment Arm Length	10.1 lb

In order to perform the deflection test, there was a great deal of design and construction for the test apparatus itself. The first phase of the design was the mast, which would house the spars and act as the location of the cockpit. This rig was constructed of two 12 ft 4x4's standing vertically with 2 inch holes drilled through them 5 feet apart. Inside these holes are carbon sleeves which provide a uniform point of contact for our spars to slide into. The rig also has several 2x4 braces which give it stability and a plumb mast.

The next phase of the experiment was to design and construct the several components that were used for connections, loads, and other aspects of the test. A 1-foot long carbon fiber joint connects the 4 ft and 8 ft spar sections. At the end of the test section, there is also a carbon fiber T-joint, which connects the two spars to the strut. Detailed descriptions of the carbon fiber construction methods are found in the Fall 2007 Final Report.

At each carbon joint there is also a cylindrical balsa plug inserted inside the aluminum; this includes the carbon sleeves inside the mast. The last stage of designing the experiment was reproducing the lifting loads that will be applied to the aircraft in straight and level flight. On the 12 ft spar sections, plastic bottles, filled with water, are hung every six inches along the aluminum tubes to simulate the distributed lifting load. Moment arms were designed to apply the moment at the T-joint caused by the lift acting on the outer 18 ft of the wing. These arms consist of a 2 ft aluminum insert to fit inside the T-joint. The inserts are then bolted to two wooden 1x3s, cut to 10 feet. At the end of these moment arms, tip loads are hung by string to simulate a moment. This entire setup is shown below in Figure 5.2.1-3.

Figure 5.2.1-3: Box Wing Test Configuration

Although the first deflection test did not give the desired results based on the 2006-2007 team's design, it did give good experimental data regarding structural integrity of the aircraft. After the entire distributed load on the inside of the wing was applied, deflection was measured as the bending moment was incremented. The ANSYS model from the 2006-2007 team indicated that the deflection at the T-joint during straight and level flight should be approximately 20 inches. During the actual experiment, the wing began to fail before the entire moment could be applied. The wing failed at the root of the top spar due to stress concentration, resulting in the failure of the bottom spar at a distance of 4 ft from the root. The T-joints also began to fail due to the large moment acting on them. As shown by the following table, the deflection was 25 3/8 inches when a 152.6 ft-lb moment was applied.

Table 5.2.1-3: Moments and Corresponding Deflections

Moment applied at T-joint (ft-lb)	Measured deflection (in.)	Theoretical deflection (in.)
0	6.75	-
52.06	15.125	-
102.35	19.75	-
152.63	25.375	-
183.51 (Straight and Level)	-	20

Because of these failures, the team felt the need to make some minor adjustments to the design and construction of the wing and its components. New T-joints were constructed that were thought to be stronger and more durable. A guy wire was also attached diagonally in between the first 12 ft of the box wing. After several iterations of these tests, the team was successful in validating the new wing design during straight and level flight. Concluding, the team is confident that with the implementation of a diagonally placed guy wire and a strong T-joint, the box wing will be strong enough to withstand the lifting loads that will be felt during straight and level flight.

5.2.2 Composite Joints

By using the composite joints in the box wing deflection tests, it was found that T-joints constructed with 4 layers of carbon fiber fail at very near 130 ft-lb of torque applied to the outer arm,, which is representative of the worst-case scenario for the loads experienced in straight and level flight. Joints constructed with 5 layers did not fail at this point. Straight joints were also used in the box wing deflection test. These joints held up to straight and level flight condition loads.

More testing is required before allowing these joints to be used in the flying prototype, which will experience additional forces beyond those of straight and level flight.

5.3 Propeller Testing

5.3.1 Propeller Efficiency Testing Overview

The propeller efficiency, η_p, is calculated as a ratio of the output power over the input power.

$$\eta_p = P_{out}/P_{in} \quad (5.3.1\text{-}1)$$

Power output is found by multiplying the output thrust, T, by the free stream velocity, V_0.

$$P_{out} = TV_0 \quad (5.3.1\text{-}2)$$

Input power is measured by multiplying the input torque, Q, by the propeller RPM, ω.

$$P_{in} = Q\omega \quad (5.3.1\text{-}3)$$

Testing the propeller statically will not provide sufficient thrust and efficiency data to determine the quality of the propeller design. The propeller needs to be subjected to airflow of known velocity to be able to quantify its efficiency. Since the propeller is too large of a diameter to fit into any available wind tunnel, a movable test rig had to be implemented to be able to generate airflow onto the propeller. A dynamometer was also designed and built to measure the efficiency numbers.

The best concept for the propeller test vehicle was determined to be a three-wheeled tricycle. The two wheels, along with the propeller mast, are mounted in the front of the vehicle to ensure that the propeller would have direct access to the air stream. The mast was designed to accommodate a 9-foot diameter propeller. Steering was taken and modified from a scrapped downhill boxcar. The vehicle also includes a laptop mount for data acquisition. Below is a picture of the completed tricycle.

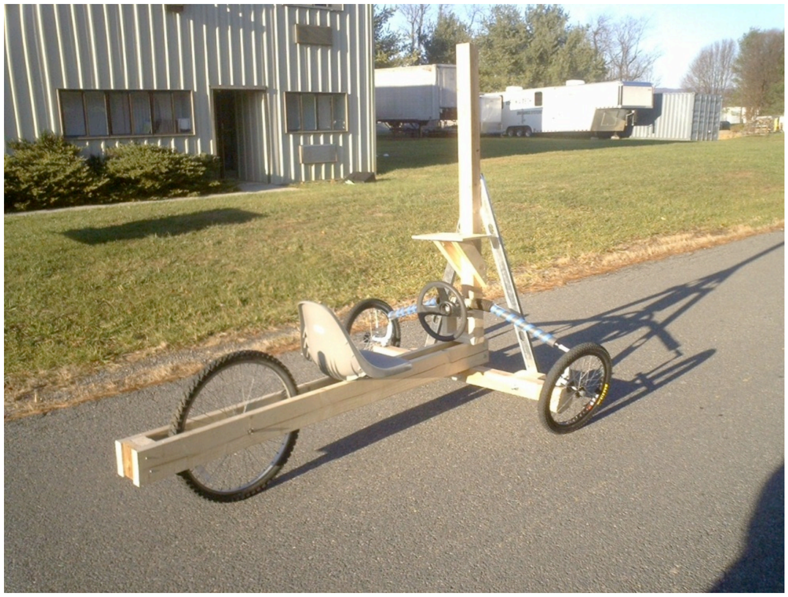

Figure 5.3.1: Completed Propeller Test Vehicle

5.3.2 Dynamometer Overview

To determine the efficiency of the propeller, a measurement device was developed. A dynamometer (dyno) is a force and moment balance able to measure mechanical loads. A dyno isolates thrust and torque, making it possible to measure their values. Figure 5.3.2 shows the complete dynamometer.

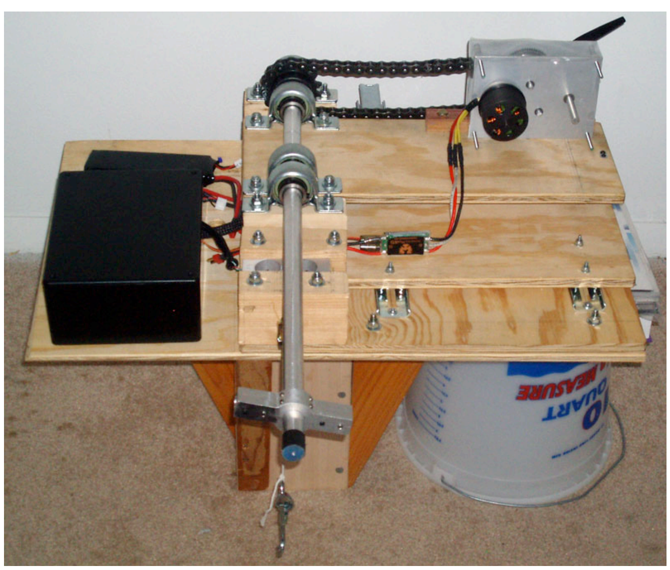

Figure 5.3.2: Finished Dynamometer

The motor used to power the propeller is mounted on a board that is free to rotate through the use of four mounted ball bearings. A load cell prevents the board from rotating and directly measures the downward force, F. Through calibration, the input torque, Q, can be directly measured.

Using this configuration, any inefficiency from the motor or gearbox will be bypassed. This entire assembly is mounted on two linear ball bearing sliders, allowing it to slide freely in the direction of thrust. As before, a load cell will prevent the dyno from sliding and will provide a direct thrust measurement.

5.3.3 Dynamometer Electronic System

In order for the propeller to produce any thrust, it must be powered by some outside source. Byron Price, a member from last year's team, developed the Supplementary Power Source (SPS) as an independent research project. [5] The SPS is a combination of a battery powered brushless motor and gearbox. The SPS was developed as a system to provide power for the flying prototype in order to enable flight testing without the need for a professional athlete, and will be used to power the propeller for testing.

The selected motor is the Mega Motors RC 41/30/15. It is powered by two PolyQuest PQ4S-3100N 4-cell Lithium Polymer (LiPo) batteries wired in series, providing a voltage of 22.2V at up to 30A. Through this combination, the motor is able to produce up to 600W, much higher than that of any human. Figure 5.3.3-1 shows the motor and battery combination.

Figure 5.3.3-1: Battery and Motor Choices

The motor spins at a high rate (~20,000 RPM). For the motor to power the propeller at the desired 180 RPM, a reduction gearbox was designed and built. The gearbox construction consists of two 4”x5.5” aluminum plates and six steel gears. Through the combination of gears, a final reduction of 114:1 is achieved from the motor to the propeller. The first four gears are connected to ¼” steel rods while the final two gears are connected to a 5/16” steel rod. These diameters have enough torsional stiffness to withstand any applied torques required to rotate the propeller. The gearbox construction is pictured below in Figure 5.3.3-2.

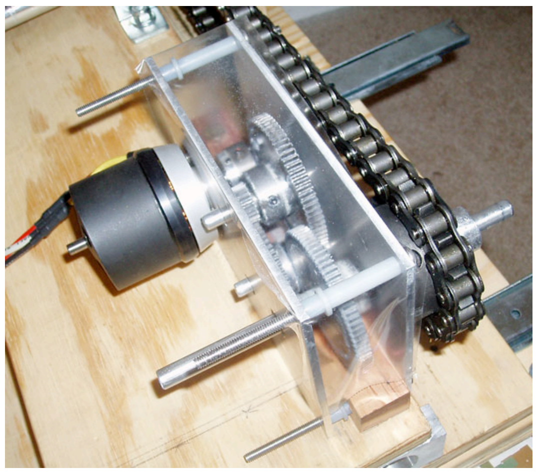

Figure 5.3.3-2: Gearbox Assembly

A 1:1 chain drive connects the gearbox with the propeller shaft. The ANSI 40 steel chain is driven by two 15 tooth sprockets with a ¾” bore. A chain drive was chosen over a belt drive to reduce the tension on the gearbox drive shaft.

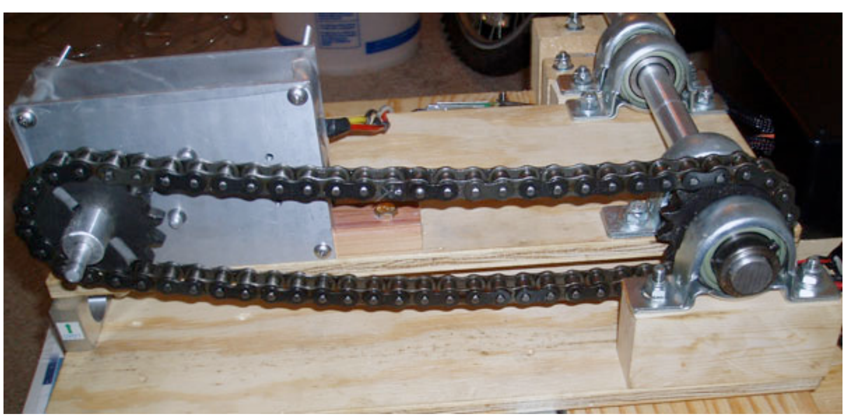

Figure 5.3.3-3: Gearbox Chain and Sprocket Combination

More detail is provided in Byron Price's AIAA paper, Development of a Supplementary Power Source for Human Powered Aircraft. [5]

The speed of the motor and subsequently, the propeller, will need to be varied from its off position to its peak velocity. To change the RPM of the motor, the input voltage must be varied. The motor controller chosen by the team is the Castle Creations Phoenix HV-45, a brushless motor controller capable of handling up to 45A of current. The input to the Phoenix is a Pulse Width Modulation (PWM) signal, corresponding to an output voltage. By sending different PWM signals to the Phoenix, the motor's speed can be changed. The PWM signals must be generated by some device. The Mini SSC II is a digitally controlled PWM generator. These two devices are pictured in Figure 5.3.3-4.

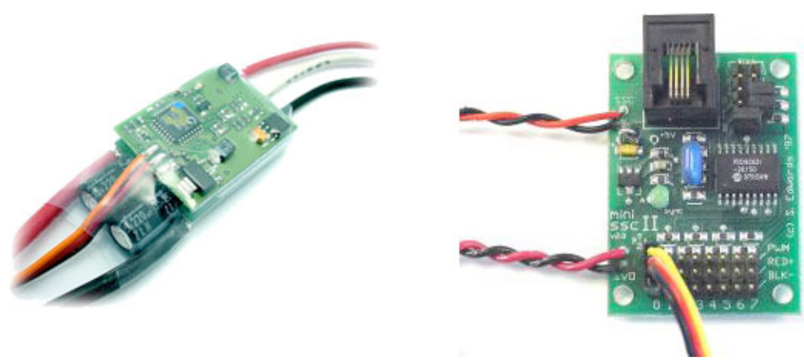

Figure 5.3.3-4: Castle Creations Phoenix HV-45 (Left) Mini SSC II (Right)

Ultimately, the dynamometer has been developed as a means of collecting data. To measure efficiency, four pieces of information must be known: thrust, torque, propeller RPM, and velocity. All four sensors will be powered by a single 5V battery. The two forces, thrust and torque, will be measured by two load cells. The design thrust is 5.5 lbs and the design torque is 15 lbs/ft. Two load cells were purchased from Elane Load Cells, one with a capacity of 10 lbs, and the other with a capacity of 20 lbs. The output signal of each load cells are too weak to be directly measured and they are therefore connected to an INA125P amplifier circuit.

A Hall Effect sensor will measure the RPM of the propeller. The chosen sensor was the Melexis US5781 Unipolar Hall Switch. A magnet will be attached to the propeller shaft. The following figure shows the specific load cells and Hall Effect sensor that the team will be using.

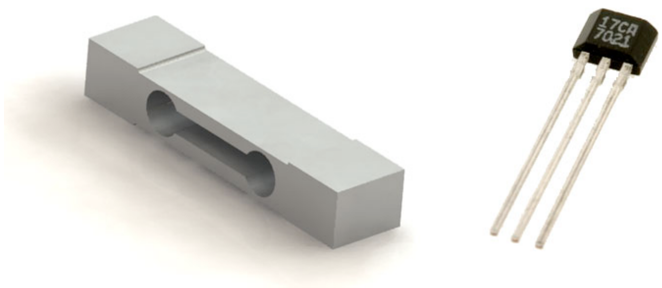

Figure 5.3.3-5: Load Cell (Left) Melexis US5781 (Right)

The USB GPS BU-353 will provide the velocity measurement for the tricycle. The BU-353 outputs standard NMEA 0183 sentences and is able to measure velocity accurately to 0.2 mph. The test setup requires that the testing be performed on a still day to insure that wind speed and air speed are similar. To further reduce possible errors, the test will be run in two opposing directions.

Figure 5.3.3-6: GPS BU-353

The USB NI-6009 is an 8 channel data acquisition board that will be used for all data collection and is pictured below in Figure 5.4.3-7.

Figure 5.3.3-7: USB NI-6009

The NI-6009 is on loan from the AOE department. Each of the three sensors produce analog signals that will be digitized by the NI-6009. The NI-6009 is able to record data at up to 48 kHz with 14 bits (1mV), providing the resolution needed to make accurate measurements. To record the data, a LabView 8.2 VI has been written to interface with the NI-6009.

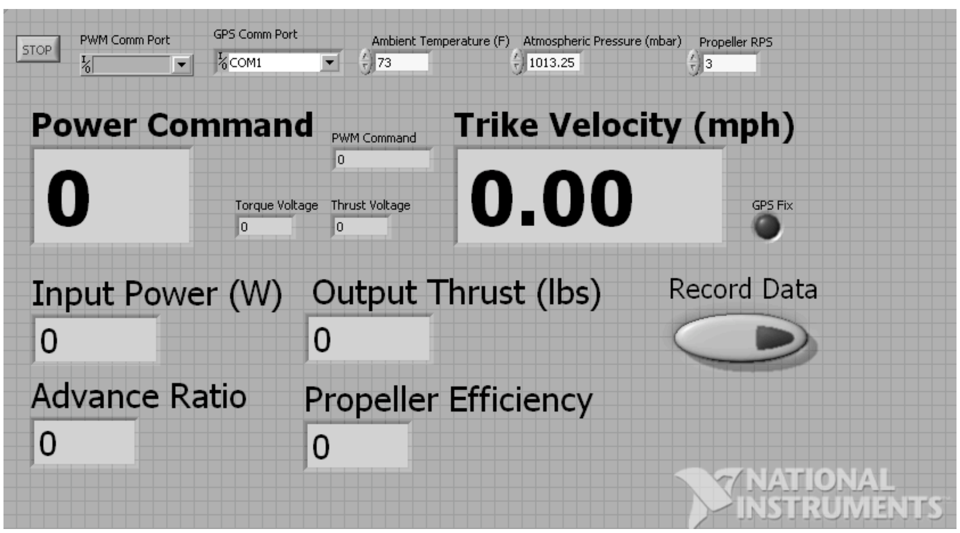

Figure 5.3.3-8: LabView 8.2 VI for Data Acquisition

The VI records the four input sensors and plots each individually. Each measurement, and the calculated efficiency, is recorded at 1000 Hz. Ten times a second, the efficiency is averaged and recorded into a spreadsheet file that can later be plotted by Excel or MATLAB. In addition to recording the sensor inputs, the VI will also command the motor speed by sending commands to the Mini SSC II through a serial port.

A simple LabView VI was created to calibrate the two load cells. To calibrate the load cells, known weights are loaded onto the system and the corresponding output voltage is measured and recorded. By doing this over a range of loads, a force to voltage relation is found. One-pound water bottles were used as known weights.

To calibrate the thrust cell, a pulley is used to translate the vertical load from the water bottles to a horizontal thrust force. The initial load is zero pounds and is increased in one-pound increments to eight pounds. This entire process is done several times to achieve a statistical average and to minimize error in the measurements. Similarly, the torque load cell is calibrated by locking the motor in place and loading the end of a 2' moment arm with water bottles. This configuration is shown below in Figure 5.3.3-8.

Figure 5.3.3-8: Load Cell Calibration

The results of the calibration are depicted below in Figure 5.4.3-9. The results appear to be highly linear with some variance. This linearity means voltage measurements should produce very accurate load measurements.

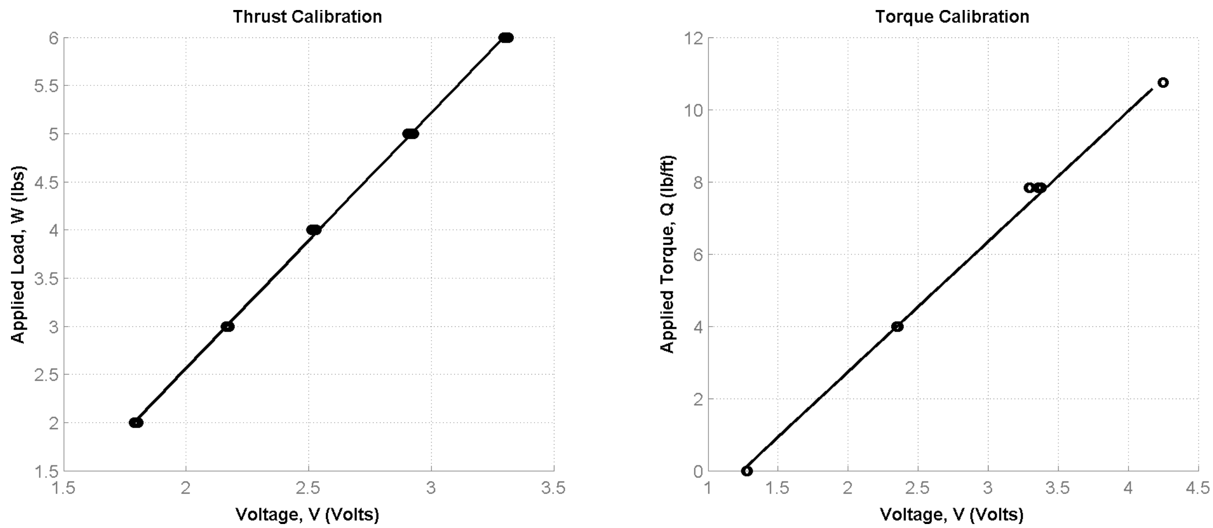

Figure 5.3.3-9: Calibration Results

5.3.4 Electronics Flow Chart

Figure 5.3.4 visualizes how the electrical components will integrate together.

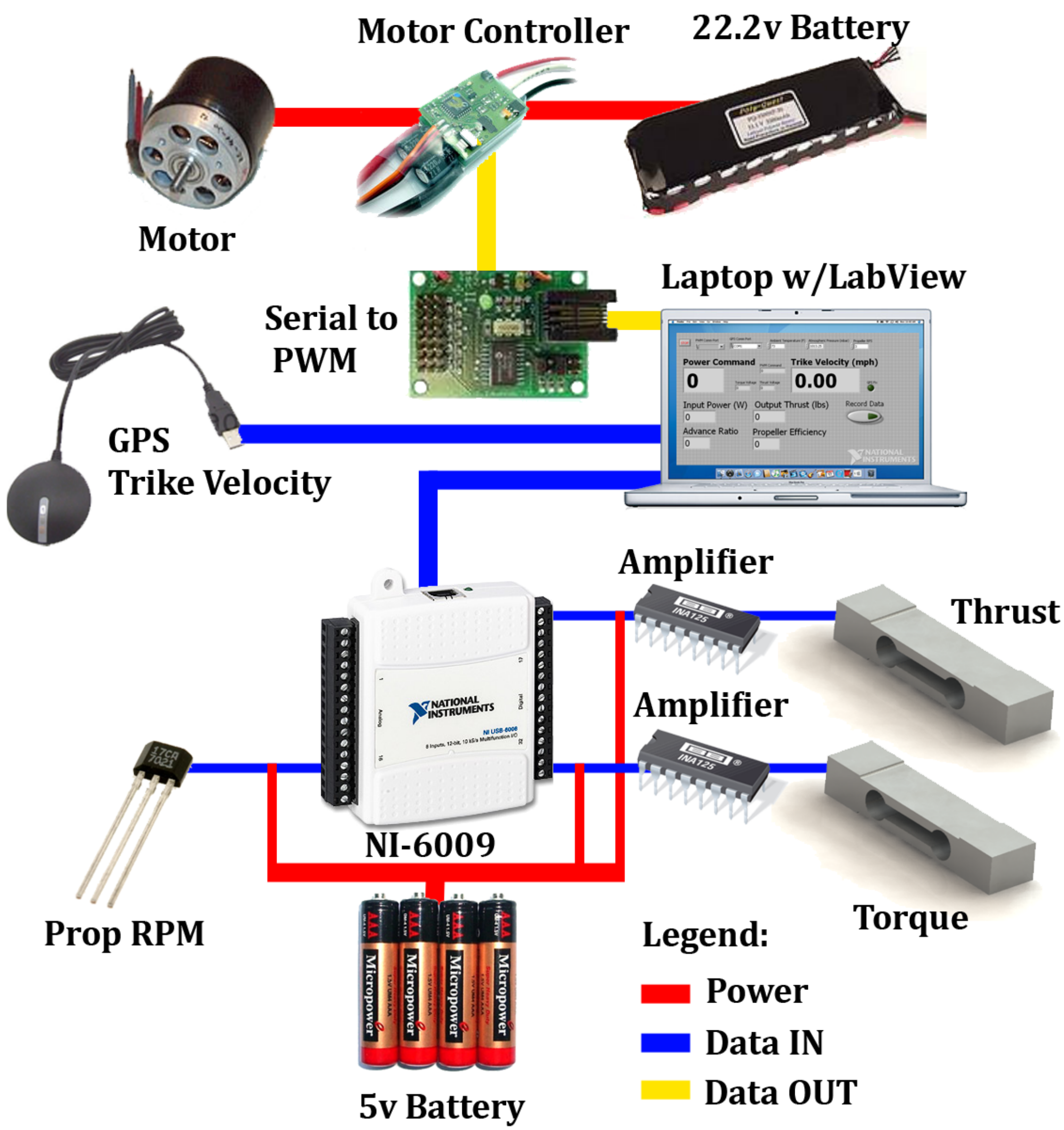

Figure 5.3.4: Electronics Flow Chart

5.3.5 Propeller Attachment and Alignment

A fixture was required to attach the blades to the propeller shaft. An aluminum collar was designed during the Fall of 2007 to accomplish this, which would be attached to both the shaft and the blades with set screws. This piece was machined this semester, and has been shown to work successfully through preliminary propeller testing. This piece is shown in Figure 5.4.5-1. To eliminate the stress concentrations associated with the set screws pressing against the carbon shaft, aluminum sleeves were machined and epoxied onto the portion of the shaft protruding from the propeller blades.

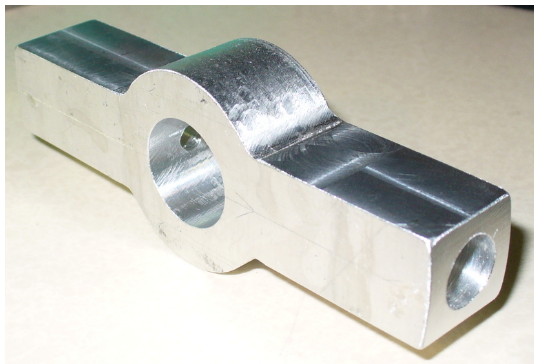

Figure 5.3.5-1: Propeller attachment collar before being drilled for set screws

In order to establish the optimal pitch of the propeller for a given airspeed, several pitch angles must be tested. Due to the complex geometry of the propeller blade, a method must be established to accurately measure the pitch of the blade with respect to a reference angle.

A removable clamp, into which the base of an $^1/_8$ inch diameter, 2 foot long carbon rod can be inserted, is positioned along the root chord of the blade. A second rod is placed at the front of the propeller shaft along the shaft's axis through the use of a wooden adaptor. This setup is shown in Figure 5.3.5-2. By measuring the distance between these two rods and performing a simple set of trigonometric calculations, the pitch angle can be measured more accurately. The measured distance for several pitch angles is provided in Table 5.3.5.

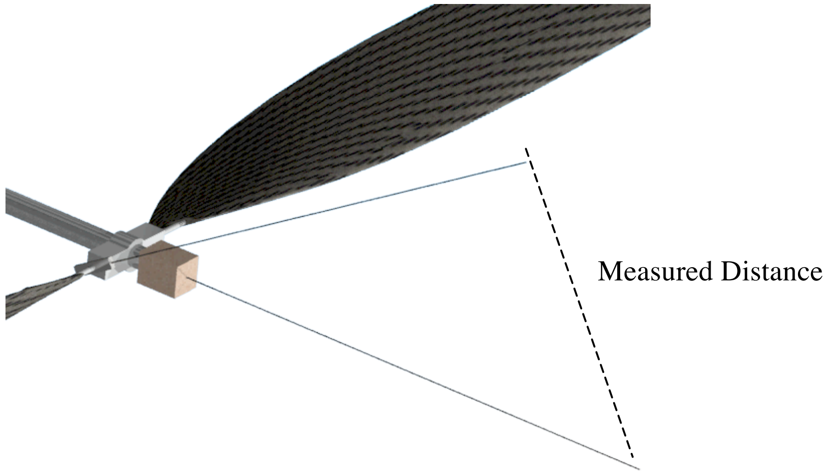

Figure 5.3.5-2: Model of propeller alignment tool

Table 5.3.5: Tabulated Geometric Relations

Measured Distance (in)	Pitch angle (°)	Root Chord Angle from Horizontal (°)
29.990	-10	29.58
29.835	-9	28.58
29.683	-8	27.58
29.533	-7	26.58
29.387	-6	25.58
29.244	-5	24.58
29.105	-4	23.58
28.969	-3	22.58
28.838	-2	21.58
28.711	-1	20.58
28.588	0	19.58
28.470	1	18.58
28.357	2	17.58
28.248	3	16.58
28.145	4	15.58
28.048	5	14.58
27.956	6	13.58
27.870	7	12.58
27.790	8	11.58
27.715	9	10.58
27.648	10	9.58

5.3.6 Testing Specifics

Testing took place near the Autonomous Aerial Vehicle Team's lab along Plantation Rd. This location was chosen because of its proximity to the HPA trailer, its relative seclusion allowing for undisturbed testing, and the straight, level, and long properties of the road.

Testing was performed in the morning to minimize wind. If no or very little wind was present, it could be assumed that the measured ground speed would be equivalent to the airspeed. Atmospheric conditions such as temperature and pressure were recorded so the calculated coefficients would be accurate.

Before testing could commence, all of the necessary components had to be integrated and inspected. The dynamometer, along with the propeller, had to be mounted on top of the tricycle mast. Next, the pitch of the propeller had to be set to its desired value and securely fastened. The laptop was then mounted and all of the electrical components were turned on. Calibration was performed on both load cells using the method described in Section 5.3.3. A test spin ensured the gearbox was properly mounted and all measurement devices were recording data. Finally, both the car and the tricycle were moved to their starting positions and were tied together by a 300 ft rope. This length was chosen to minimize the effects of the wake of the car on the measurements. The figure below shows the complete assembly of the test vehicle.

Figure 5.3.6-1: Full propeller vehicle assembly test spin

Once this was done, the driver of the tricycle initiated the data logging and slowly accelerated the propeller to 150 RPM. This RPM, instead of the design RPM of 180, was chosen due to battery constraints. During this period, the static thrust was measured. The tricycle operator then gave a signal to begin the test procedure. The car driver accelerated slowly to the desired velocity, to ensure a safe ride for the tricycle operator and to prevent the rope from breaking. It was important to achieve a steady velocity so efficiency results could be improved by averaging over a long period of time. This process was done at ground speeds ranging from 6 mph to 15 mph in 3 mph increments. It was intended that this entire process would be repeated for a range of propeller pitch angles. However, due to time constraints, the process was only done for a pitch of 0°.

Figure 5.3.6-2: Tow Testing

5.3.7 Propeller Efficiency Results

Testing was cut short when it was discovered that no thrust data had been measured once the vehicle began to accelerate. This was initially attributed to inertial loading and is depicted in the following figure.

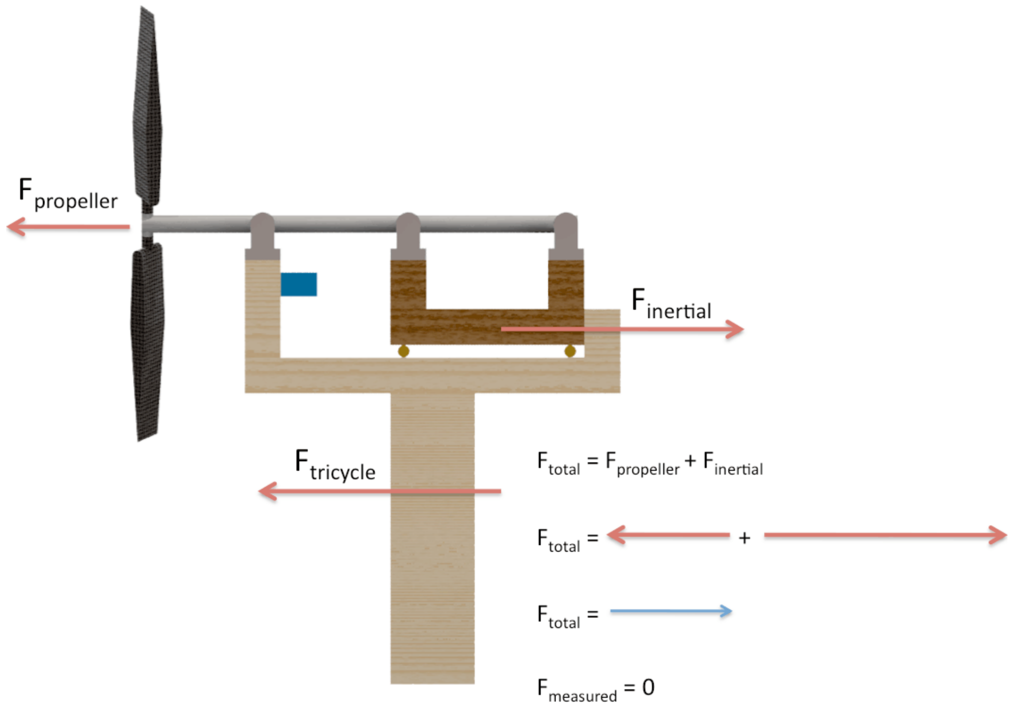

Figure 5.3.7-1: Inertial loading on the prevention of thrust measurements.

Despite running part of each test at a constant velocity and therefore eliminating the inertial load, no thrust measurements were made with the vehicle in motion. There are several potential reasons for this: running below the design RPM didn't produce enough thrust, running at 0° pitch didn't produce enough thrust, small vehicle accelerations were always present leading to further inertial loading, small friction in the linear bearings prevented the rig from sliding, or the propeller simply doesn't perform to it's design. Further investigation will have to be done to determine the cause and find a solution.

Even though no dynamic thrust measurements were taken, static thrust measurements were recorded. The results of this are shown in Figure 5.3.7-2.

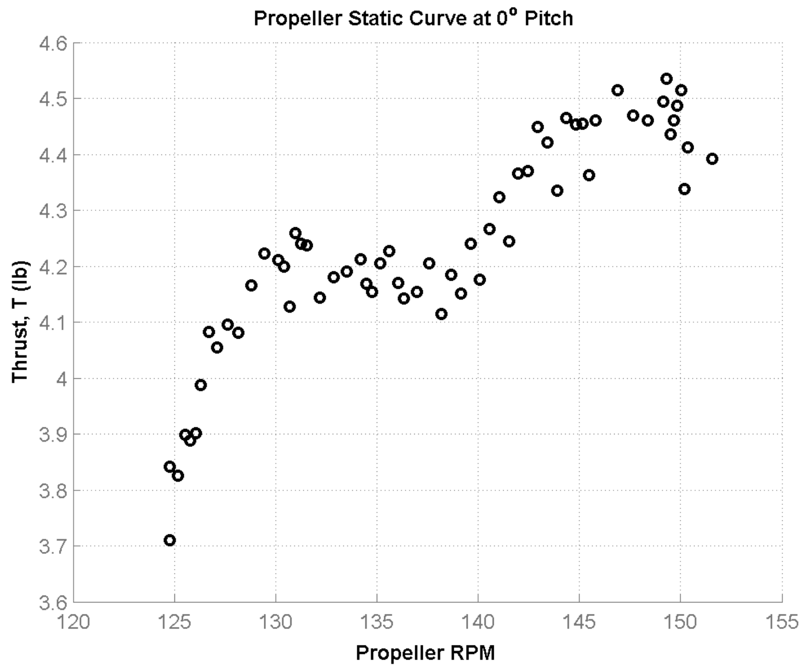

Figure 5.3.7-2: Propeller Static Curve at 0° Pitch

The propeller was able to output a static thrust of 4.5 pounds at 150 RPM, at 0 degree pitch. Another observation is the extreme thrust increase at around 125 RPM. If the thrust continues to increase with RPM at such a rate, it appears that the required thrust of 5.5 lbs at 180 RPM should be attainable. However, extrapolation is not being relied on, and further testing will be required to determine the thrust at higher RPM and various pitch angles.

5.3.8 Efficiency Testing Outlook

Full propeller efficiency curves are still needed for two reasons: to confirm the design of the propeller and to determine the optimal pitch angles at various regimes for use with the variable pitch mechanism. While the dynamometer is unable to collect thrust in it's current state, a few small modifications should allow testing to continue. During one of the torque calibrations, the aluminum output shaft of the gearbox was bent, preventing the gearbox from running reliably past 120 RPM. As seen in Figure 5.3.7-2, this RPM simply doesn't produce enough thrust to ensure contact with the load cell at different ground speeds. This shaft should be replaced with a steel shaft to prevent this from happening again.

Even with an unbent shaft, two Lithium Polymer (LiPo) batteries providing 22 V were unable to spin the propeller at 180 RPM. Adding a third LiPo (33 V) should provide enough power to the motor to achieve 180 RPM. This could cause problems, however, as 4 LiPo batteries overstressed the motor. Another solution is to reduce the gearbox ratio by decreasing the amount of teeth on the gearbox output sprocket.

Various pitch angles should be tested. It is possible that a pitch of 0° is unable to achieve the thrust required while other angles will have more than enough thrust. This can only be confirmed by further testing and will also be beneficial in the design of the VPM.

The tricycle may need modification. Its front wheels are angled inward, creating drag and instability. Fixing this problem will require someone with welding and machining skills. While this is not required, it is highly recommended if heavy testing is to be done.

Once the team becomes familiar with the procedure and equipment, fixing the above problems should be manageable, and further testing should be done.

6. Project Status

6.1 Quarter-scale Model

Once the preliminary design of the aircraft was completed, the past teams constructed a quarter-scale model in order to validate the design. The construction and testing process was iterative, but ultimately successful. Testing of the quarter-scale model proved that a controlled turn performed by an aircraft of the current design is possible. This accomplishment is substantial because of its direct application to the achievement of the Kremer Prize. The quarter-scale model is currently disassembled and lacking major components required for flight. Its purpose has already been served and is not expected to provide further information.

6.2 Prototype

Work from the second and third teams has been focused on constructing and testing components of a prototype of the designed aircraft. An iterative process of design, construction, and testing is still required for almost every aspect of the design. This process has begun for the wing structure, joints, propeller and cockpit of the aircraft. Additional final design and construction methods are still required for many components.

It is expected that construction and testing of prototype components will continue, resulting in the design being reviewed and revised based upon the results. This process will need to continue until a prototype aircraft can be completed.

6.3 Remaining Work

A substantial amount of work remains for the ultimate achievement of winning the Kremer Prize. The detail design of the aircraft is almost entirely complete. The design will need to be continually reviewed and optimized as the prototype is constructed and components are tested.

Work should continue in the areas of the design that have been left by the most recent team. There are areas of immediate concerns, which should yield important results for the entire project. These areas include making improvements to the dynamometer to re-run propeller tests, constructing carbon fiber structural members, and continuing wing loading tests at increased load factors.

Minor revisions to the dynamometer should alleviate the current problems and allow for complete testing of the propeller efficiency. The results of these tests will be invaluable to the design and the project. The propeller must perform as designed for the aircraft to be successful.

The next step in the wing structure aspect of the design is to construct the necessary carbon fiber outer spars and struts. This can also easily extend to constructing the tail boom. All of these products will then need to undergo testing to identify their mechanical properties. Optimization of their design based on weight should then follow with the goal of performing an entire 30 ft half span wing deflection test.

There are several other works in progress that the future teams may finalize. Continued structural analysis and weight optimization of the cockpit should occur. Completion of the prototype variable pitch mechanism is also unfinished. Lastly, a review of the aircraft sizing and weight allowances should be an ongoing task as components of the design are constructed.

Constructing a prototype of the design will be an enormous task, allowing substantial insight to be gained into the necessary methods of construction and detail of the aircraft. This period of the project will also be very exciting as full-scale components become fabricated and integrated and initial flight attempts are made. Successful flying of the prototype will need to occur before components of the final aircraft can be built.

7. Administration

7.1 Funding

The teams from the first two years operated exclusively on donations and sponsorships. This led to a method for recognizing sponsors, which is detailed in the 2006-2007 final report [x]. The third year's team received funding from the Ware Lab and has operated almost entirely from it. As a result, the team did not pursue sponsorship with the same rigor as the past teams. However the acknowledgement of past sponsors and the seeking of new ones will be a necessary occupation of future teams. Continued Ware Lab funding should be strongly pursued as well.

7.2 Facilities

Currently the team shares a bay with the Design Build Fly Team of Virginia Tech in the Ware Lab. The space is required for the necessary construction and testing throughout the project. The current team is investigating the possibility of switching bays with another aerospace design team to receive additional space as construction continues. The details of this arrangement are not presently available.

Additionally, the team maintains a trailer that was generously donated by John Moore, a significant sponsor of the team. The trailer houses large components of the project that would otherwise not fit in the Ware Lab bay. The trailer is ultimately intended for transporting the prototype and competition aircraft as specified in the Kremer Prize requirements. The trailer is currently located at an off-campus research facility on Plantation Road.

7.3 Budget

A definite budget for the construction of a full-scale aircraft has not yet been established. The second year's team proposed that the total cost of construction of a prototype aircraft to be well over eight thousand dollars [Appendix C – Section 7.3]. Through the design and prototype construction phase of this project, a significant amount of this cost has already been accounted for in acquiring materials.

The third year's team received funds from the Ware Lab, which was a first for this project. The Ware Lab appropriated $2800 to the team for the year. The continuation of Ware Lab funding as well as the accruement of supplemental funding through donations or sponsorship will be essential for the continuation of this project. The second year's team left $375.72 in a separate foundation account for this project. The following table lists the current financial balance of the team.

Table 7.3: HPA Balance

	Ware Lab Account	Foundation Account
Balance	$ 1,395.65	$ 375.72

The team from each year has greatly benefited from the generosity of donors and sponsors. This includes materials and facilities vital to the project. The third year's team received a significant donation of carbon fiber from Hexcel Corporation helping to alleviate a major cost of construction. As the project advances, a growing public interest in the project should help in the search for continued sponsorship.

8. Summary

This is the third year of a multi-year design team with the goal of winning one of the current international Kremer Prizes. This report details the overall design of the aircraft as opposed to the individual accomplishments of the current year. The three major sections of the report include the design, construction, and testing aspects of the aircraft. The purpose of this report is to present a comprehensive description of the project so that future teams will have a solid basis for continuing the project.

9. References

1. McIntyre, John. Human Powered Flight Group. March 2007. Royal Aeronautic Society. <http://www.raes.org.uk/cmspage.asp?cmsitemid=SG_Hum_Pow_Home>.
2. Drela, M. ALV Extended Vortex-Lattice Model. Available at http://web.mit.edu/drela/Publie/web/avl/2004
3. M. Drela. "Aerodynamics of Human-Powered Flight". Annual Review of Fluid Mechanics, (22):93–110, 1990.

4. Price, Byron. Development of a Supplementary Power Source for Human Powered Aircraft. Virginia Tech Department of Aerospace and Ocean Engineering. AIAA, 2007.

APPENDIX

Appendix A: Kremer Prize Rules and Regulations

Appendix B: Fall 2007-2008 Final Report

Appendix C: Spring 2007-2008 Final Report

Appendix D: Spring 2006-2007 Final Report

Human Powered Flight

Rules and Regulations
for

THE KREMER HUMAN-POWERED AIRCRAFT FOR SPORT

THE ROYAL AERONAUTICAL SOCIETY

4 Hamilton Place, London, W1V OBQ

Telephone +44 (0)20 7670 4345 Fax +44 (0)20 7670 4349

The Royal Aeronautical Society

KREMER HUMAN-POWERED AIRCRAFT COMPETITION FOR SPORT RULES AND REGULATIONS

The purpose of this competition is to direct interest in Human-Powered Aircraft towards the design for production and ongoing development of aircraft suited to athletic competition. In particular it is necessary to specify and design aircraft able to operate in normal reasonable weather conditions, as encountered in the United Kingdom.

It is anticipated that a Human-Powered Aircraft for Sport will differ in several respects from aircraft previously designed and flown successfully in calm conditions. As a potential sporting event, it is considered important that the general public are informed and develop interest in the progress of this type of Human-Powered Aircraft.

The competition is organised by The Royal Aeronautical Society, Human-Powered Aircraft Group Committee (The Organisers). It is open to entrants worldwide.

The prize of 100,000 pounds will be awarded to the first entrant successfully demonstrating a Human-Powered Aircraft, in accordance with these Rules and Regulations. No other prizes will be awarded by the Royal Aeronautical Society.

Human-Powered Aircraft for Sport (HPAS)

1.1) The HPAS shall be designed with the following attributes:

a) Safe operation at low altitudes near the ground, with a potential for flight at moderate altitudes as the technology evolves.

b) Athletes intending to fly the HPAS can train themselves ab-initio in calm conditions, and progressively fly the aircraft in more typical wind conditions, as specified for the competition.

c) Suitable for small batch production, or for assembly from kit form. Simplicity of the HPAS is important both in minimising first cost and in coping with repair or replacement.

d) Quickly dismantled or assembled from its major components to facilitate transport by road and for storage, and thus for use in sporting events.

1.2) The entrant is required to satisfy the Organisers at the time of entry that the design embraces these attributes in accordance with the Rules.

1.3) For the purpose of this competition, the event in which the HPAS is required to compete is directed at speed around a closed circuit. The event may be staged over land or water, at the discretion of the entrant.

1.4) As a potential sporting event, it is considered important that the general public are informed and develop interest in the progress of HPAS, and accordingly the competition attempts must be open for public observation.

The Aircraft

2.1) The HPAS must meet any Airworthiness Requirement defined for such aircraft, as and when such requirements are established.

2.2) The HPAS shall not use any lighter than air gas for the purpose of generating lift, or as a buoyancy aid.

2.3) The HPAS shall be a fixed wing aircraft. It shall be flown and powered by one person, relying solely on his/her own muscular effort for propulsion. No energy storage device or electric cell may be used for propulsion or lift.

2.4) An onboard source of electric power is permitted for the sole purpose of control, including auto-stabilisation and propeller governing.

2.5) The whole machine shall stow into a roadworthy vehicle supporting a weatherproof container not longer than 8.0 m (26.24 ft) internally.

2.6) No part of the aircraft or its means of launching may be discarded at take-off. The entire aircraft shall complete an attempted official flight without touching the ground.

2.7) No communication or external assistance may be given to the pilot or to the aircraft during the flight.

2.8) The aircraft shall demonstrate its facility to land safely at the completion of each attempted official flight.

The Competition Course

3.1) The course shall be established by the entrant at a place open to the public for observation, within the United Kingdom. The course location, with details of its authorisation for use, including arrangements for the protection of the public, shall be notified to the Organisers, and receive their approval before any flying commences at that location.

3.2) The competition course shall comprise an equilateral triangle (60 degree corners), with side lengths of 500 m (1640 ft). At each corner a clearly visible marker shall be erected. The course shall be defined over an essentially flat surface on land, or over water.

3.3) The Course shall have one leg aligned approximately with the currently prevailing wind direction at the commencement of an attempt. A start and finish line shall be established close to the middle of this side, for clockwise flights. The start and finish line shall be extended beyond the opposite corner of the course, for anti-clockwise flights, (see diagram of the course).

3.4) During each attempted official flight, the wind strength shall be recorded. The mean wind speed measured over the duration of each flight at a height not more than 10m above ground level, shall be shown to be not less than 5.0 m/sec (16.4 ft/sec or 11.2 mph).

3.5) Lighter winds or conditions of relative calm, in which the wind strength is less than 5.0 m/sec (16.4 ft/sec or 11.2 mph) for a period of 20 seconds or more, are unacceptable.

3.6) For the purpose of compliance with 3.4) and 3.5) above, a recording anemometer will be provided by the Organisers, and it shall be set up within the triangular course, and located at a point agreed by the Judges. It will be capable of continuously recording wind speed with an accuracy of 5%, verified by an independent authority in the United Kingdom.

3.7) This recording anemometer will be placed at the disposal of the Judges during each attempted official flight. The Judges will retain the readings for any official flight, and take charge of the recording anemometer, pending its re-verification by the independent authority.

Official Flights

4.1) An entrant wishing to attempt an official flight shall notify the Organisers in advance, giving details of proposed time and location and shall make all necessary arrangements relating to the competition course, the operation of flights, the attendance of the Judges, and observation by the public.

4.2) Upon making an attempt, it will be deemed unsuccessful or official by the Judges. Details of an official attempt must be submitted to the Organisers within an elapsed time of one month, for ratification. Submissions will be treated strictly in order of receipt by the Organisers.

4.3) At the commencement of the proceedings the HPAS shall be removed from its transporter, and assembled ready for flight with crew onboard and ready to start, within an observed time of 30 minutes. The first attempted flight may then commence at the instruction of the Judges, on that day.

4.4) The HPAS shall take-off starting from rest, and may be assisted by not more than two ground personnel. The assistants are permitted only to stabilise the aircraft to the point of take-off. The assistants may not cross the start line.

4.5) The aircraft shall be observed to cross the starting line at a clear height of not less than 5 m (16.4 ft). It shall continue to navigate the course without touching the ground, and to pass entirely clear of each marker outside the triangular course. The flight terminates when observed to cross the finishing line at a height not less than 5.0 m (16.4 ft).

4.6) One circuit of the course shall be flown in each direction, using the appropriate start/finish line as shown in the course diagram. The crew of the aircraft shall be the same person for each flight. He/she may remain on the ground to recuperate between the flights, for a time not exceeding one hour.

4.7) Each flight will be timed by the Competition Judges, observing the nose of the aircraft to cross the start/finish line. Two stopwatches will be used and the recorded times averaged, provided that those times do not differ by more than one second, otherwise the higher time will be recorded.

4.8) Two flights in opposite directions around the course must be completed within a total (for both flights taken together) flying time of 7.00 minutes. The flying speed required to attain this is at least 10 m/sec (about 33 ft/sec or 22 mph).

4.9) Upon successful completion of the two flights, and when the judges are ready, the pilot will leave the aircraft and it shall be dismantled and stowed in its road transporter all within an observed time of 30 minutes.

Competition Judges

5.1) The Judges will be appointed by the Royal Aero Club, in the United Kingdom, who will establish procedures and operate within their practices for judging Kremer Competitions, with such adjustments as they see fit in relation to these Rules and Regulations.

5.2) The Judges will scrutinise and observe all attempts made in the competition and decide whether they are unsuccessful or official in accordance with these Rules. Establishing arrangements with the Judges to attend, in advance of an attempt, will be the responsibility of the entrant.

5.3) The Judges will exercise their powers within the general provisions of the FAI Sporting Code, which includes, amongst other things, provisions covering the use and administration of drugs.

5.4) Compliance with all provisions of these Rules and Regulations in all respects shall be a necessary precondition of any attempt being judged official. The decision of the Judges shall be final and binding upon the entrant.

Entry Procedure

6.1) Entry forms are available from the Organisers, at The Royal Aeronautical Society, Human Powered Aircraft Group, 4 Hamilton Place, London W1V 0BQ. The entry fee to accompany the completed entry form will be 250 presented in Sterling or by equivalent international bank draft.

6.2) The entry shall include a 1/20 scale three-view engineering drawing of the aircraft, depicting it assembled with leading dimensions, and as stowed for transportation.

6.3) The entry must be accompanied by an outline of proposed technical features of the HPAS, including the provisions for control and flight in the wind conditions defined for the competition, estimates of weight, lift and drag, and a prediction of performance.

6.4) Individuals or groups intending to make an entry, are recommended to advise the Organisers at the earliest opportunity as outlined by 6.2) and 6.3) above, to establish that the proposed entry is acceptable in respect of the attributes required of an HPAS.

Limitations

7.1) The Organisers reserve a right to refuse an entry where, for any reason in their opinion, the entry is found to not conform, or to be inadequately defined. If the entry is not acceptable any entry fee, less administrative charges, will be refunded within three months of its receipt. Otherwise the Organisers shall not be liable for any costs whatsoever incurred by an entrant whose entry is refused.

7.2) All entrants enter and participate in the competition at their own risk, and they are entirely responsible for the safety of the aircraft and for any injury caused to any persons (including themselves) or to any property (including the aircraft). The Organisers shall have no responsibility for inspecting or approving the aircraft or the arrangements from the point of view of safety.

7.3) Accordingly the entrant agrees, by entering the competition, to indemnify the Organisers against any claims which may be made against the Organisers by any person in connection with the aircraft or its operation for the purpose of the competition. Such indemnity shall be provided in a sum not less than 5 million, and will additionally indemnify the Ministry of Defence, or other owner of land where the Course is established, to their satisfaction.

7.4) Furthermore the Organisers accept no responsibility, either to the entrant or to the spectators or to other third parties, for the suitability of the course or the safety of persons or property, and the entrant shall bear full responsibility for such suitability and safety, except in respect of the recording anemometer.

7.5) Neither the Organisers, nor the Royal Aero Club shall have any liability to the entrant in respect of any failure of the Judges to attend, or any other act or omission of any Judge.

7.6) The entrant shall be responsible for all costs and expenses incurred by the Judges in carrying out their official business in relation to the competition, and it is for the entrant to make such prior arrangements in this respect with the Judges as the entrant thinks fit.

7.7) In all matters concerning the interpretation of the Rules and Regulations, the decision of the Organisers is final and binding upon the entrant.

7.8) The Organisers reserve a right to terminate the competition at any time in the future as considered appropriate, subject to giving all accepted entrants one years notice in writing.

7.9) The Organisers have no present intention to terminate the competition before 1 January 2010, but if the prize has not then been won, the Organisers reserve a right to apply part or all of the prize fund to reward entrants who have demonstrated significant progress in the development of Human Powered Aircraft for Sport.

Course Diagram

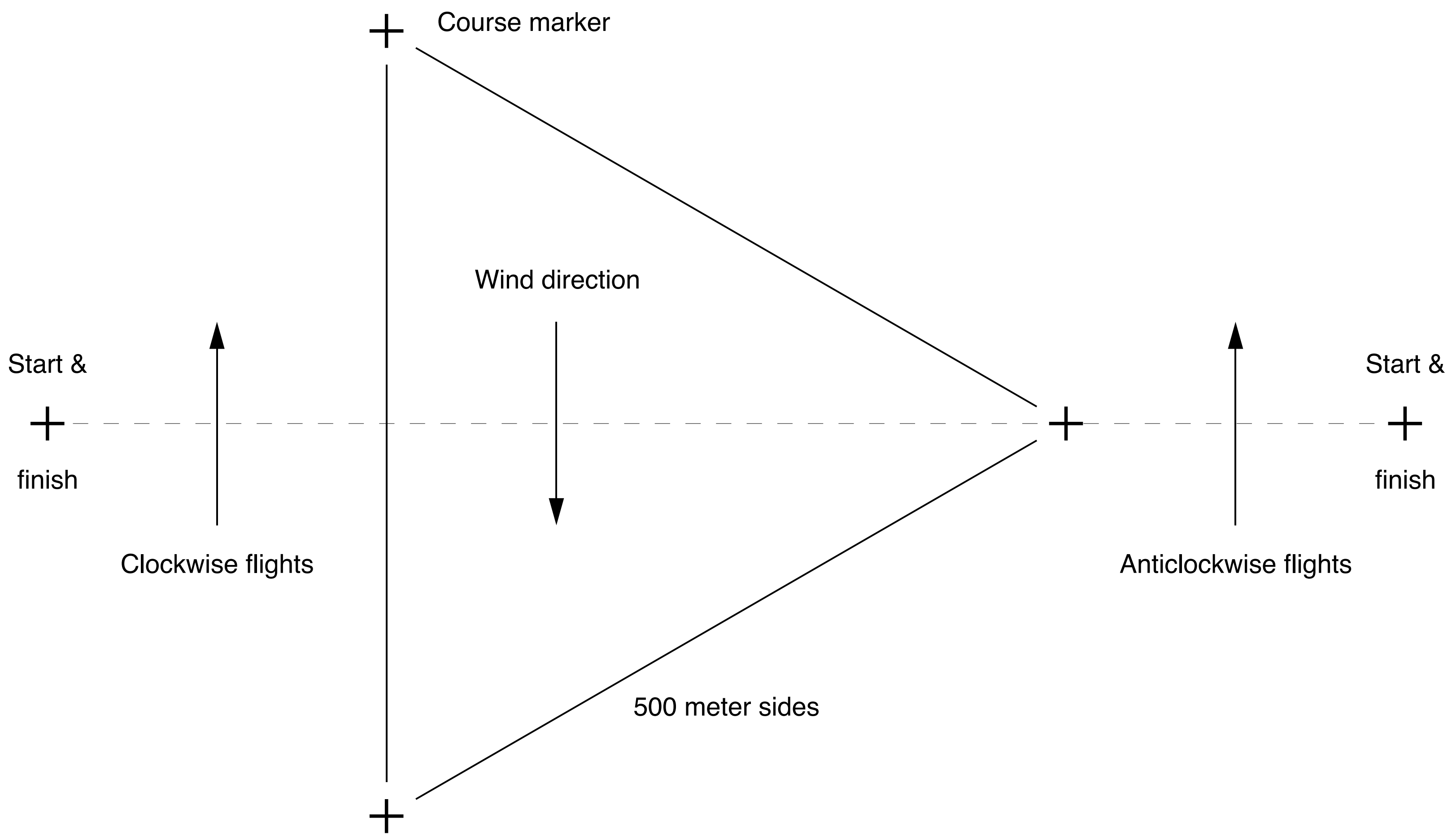

IRON Butterfly
Human Powered Aircraft

Human Powered Aircraft for Sport

AOE 4066 - Virginia Polytechnic Institute and State University
Final Report: Fall Semester – December 12th, 2007

Dr. Kevin Kochersberger	*Faculty Advisor*
Brian Wheeler	*Project Manager*
Ryan Catlett	*Lead Engineer*
Ryan Adams	*Structures*
Horace Botts	*Structures*
Alex Goryachev	*Propulsion*
Nathan Knotts	*Structures*
Jason Powell	*Propulsion*
Nick Vozza	*Propulsion*

Table of Contents

1. Executive Summary

The Virginia Tech Human Powered Aircraft Group is a third year design group attempting to build a flying prototype of an aircraft designed to win one of the current Kremer Prizes. The state of the design is such that most of the current work involves taking a good design and making it real.

This report details the current project state and the team's goals for the remainder of the academic year. A brief orientation to the project is first given, which includes an introduction to the Kremer Prize, a background on what project development has occurred so far, and a brief overview of the present aircraft design. The remainder of the report is focused on the present project development, and is broken down as follows. First, a description is given of the current short term and long term objectives, and how they were chosen. Then a detailed description of the work being done on the propulsion and structures area is provided, followed by a schedule and budget information.

2. Introduction

2.1 The Kremer Prize

In 1959, the industrialist Henry Kremer offered a monetary prize of £50,000 given to any pioneer that could develop a Human-Powered Aircraft that would be able to fly a figure eight course between two markers that were a half of a mile apart as well as remain ten feet above the ground. It wasn't until August 23, 1977, that this initial prize was claimed by Dr. Paul MacCready and his Gossamer Condor piloted by Bryan Allen. The second Kremer prize, which required a Human-Powered Aircraft to fly across the English Channel, was also won by Dr. Paul MacCready. This prize was won on June 12, 1979 for a monetary prize of £100,000 by Dr. MacCready's Gossamer Albatross piloted by Bryan Allen as well. [2] There was a third Kremer prize of £20,000 awarded to a design team from the Massachusetts Institute of Technology for their MIT Monarch B aircraft. The aircraft completed a triangular 1.5 km course in less than three minutes.

There are currently three Kremer prizes available, each for a monetary prize. The first is the Kremer International Marathon Competition, which challenges the competitor to fly a 26 mile marathon course in less than an hour. The second competition is the Kremer Human-Powered Aircraft for Sport Competition stressing maneuverability. The competition goal is to design a Human-Powered Aircraft that could be used in an Arial Sporting event around an equilateral triangular course of 500m on each side. The third competition is limited to universities in the UK. [3]

2.1.1 Human-Powered Aircraft for Sport Competition

The overall goal that our team is striving towards is the completion of the Human-Powered Aircraft for Sport challenge that is hosted by the Royal Aeronautical Society. The purpose of this challenge is to bring forth the creation of a sport from this class of airplane. A reward of £100,000 will be presented to the first entrant that is capable of demonstrating flight that meets of the requirements of the competition. [4] As for aircraft parameters that have to be adhered to:

- The aircraft has to operate safely at low altitudes, close to the ground, and be well disposed to kit production.
- Flown by one individual that uses muscular power for propulsion.
- No batteries or electric cells can be used to store energy for propulsion.
- No lighter than air gasses can be used to generate lift.
- The entire aircraft must be stored in a trailer with a maximum length of 8 meters.
- No part of the aircraft can be discarded on or after takeoff.

2.1.2 Competition Course

The Human-Powered Aircraft has a specific course that must be adhered to in order to complete the competition. [4] This course is displayed in the Figure 2.1.2. The course must be flown anywhere in the UK, either over land or water, such that it meets the following criteria:

- The course is an equilateral triangle 500m on each side.

- The course shall be flown both clockwise and counter clockwise.
- The mean wind speed during flight will not be less than 5 m/s.
- The wind speed will not drop below 5 m/s for more than 20s during flight or the flight will be void.

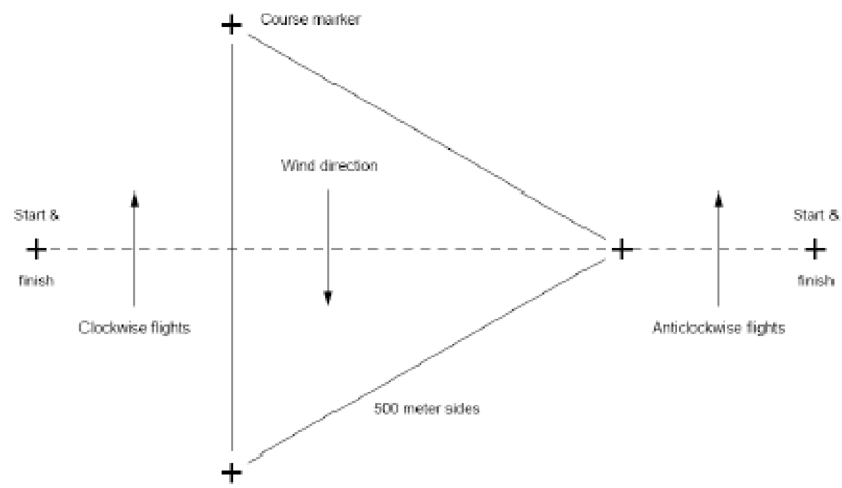

Figure 2.1.2: Kremer Prize for Sport Competition Course Diagram

2.2 Previous Project Development

Because this project is currently in its third year of development, this team must study and understand thoroughly what previous teams have accomplished. The current team must try to pick up where its predecessors left off, while still keeping in mind that previous designs may need to be tweaked or perhaps changed all together. The following sections will give a brief description of the previous project development. Midterm and Final Reports of the two previous teams can be found at http://www.aoe.vt.edu/design/hpa/media.php.

2.2.1 2005-2006 HPA Team

The fall of 2005 was the year that the Human Powered Aircraft Group was formed and began conceptual design on an aircraft to eventually compete for the Kremer prize. To properly begin conceptual design, constraints were defined based on the rules for the competition and a mission analysis which determined how the aircraft and pilot would need to perform during flight. Next, the team considered several conceptual design sketches and ranked them using a design matrix. Two of the top designs were considered for further analysis; the monoplane and box-wing configurations.

Aerodynamically, the team found that the box-wing configuration was the better of the two options. Using the previous design constraints, the wing area was selected. They then concentrated on researching airfoils that would perform the best for the wing and tail surfaces based on minimal drag.

Structurally, the team considered each of the two concept configurations by building and testing simple models. Once the box-wing configuration was found to be superior, they began to perform finite element analysis to try to perfect the design. Basic structural design such as number of struts and gap width between wings were also analyzed with minimizing the drag in mind.

The first year's team began some preliminary design regarding the propulsion system. After researching previous HPA's a basic drive train was designed that resembled that of a bicycle. Pilot positioning was also researched and an optimal position was chosen. The team also designed a propeller for use with a variable pitch mechanism in order to provide the optimal propeller pitch at different flight conditions.

The latter half of the year was consumed with constructing and testing a quarter scale model of the aircraft. The model was built primarily to test and validate the dynamic stability and control of the aircraft. The wing structures were constructed with some built-in deflection in order to make the wing perform like the full scale aircraft. The structure of the model, however, was built overly stiff in order to counteract aeroelastic effects. The model was scaled so that it would behave dynamically similar to the full scale model. The team performed some preliminary flight tests of the model, but ran into several problems which the next team addressed.

Below is a simple computer model that shows how the first years' team envisioned the HPA.

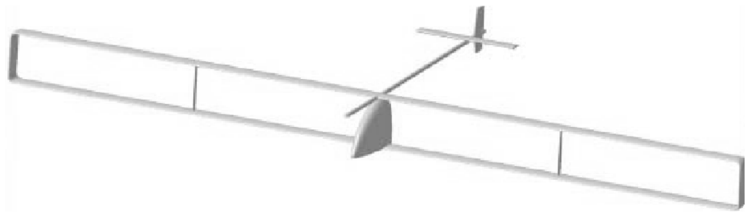

Figure 1.2.1: Computer model of 1st teams design

2.2.2 2006-2007 HPA Team

The second year's HPA team picked up right where the first year's team left off. They focused the entire first semester in further developing the quarter scale model. There were many problems with the model in the first year as documented by the flight test videos and reports. Because of this, the team performed many aerodynamic and stability and control analyses to help provide them with a blueprint for model modifications. Other structural analysis was also performed using computer simulations to help modify the existing design.

After performing this analysis, there were four major concerns the team had regarding the model. These were replacing the original carbon fiber fuselage, addition of guy wires, construction of a new elevator, and the addition of landing gear. Upon completion of these design and construction issues, the second year team began testing the quarter scale model. The flight tests were much improved from the previous year and resulted in the model performing several 360^{o} turns.

Although, much of the conceptual design and some detailed design was completed by the previous team, the 2006-2007 team focused their detail design on optimizing the structural aspects of the aircraft, and performing detailed aerodynamic design. In the second semester, along with continued detail design, the second year team began construction of a full-scale prototype with the hopes to begin flight testing in the spring of 2007. With full scale construction in mind, the team also began to acquire funds and workspace during the second semester.

In terms of the design, the team reached their goals of finalizing the spar, strut and airfoil design, while continuing to improve the overall detailed design of the aircraft. The team did not, however, complete construction of the full-scale prototype. Multiple wing sections have been built and tested, but the construction processes have not yet been perfected.

2.3 Aircraft Design To Date

As mentioned before, much of the design for this aircraft has been finished prior to this year. Below is a picture of the actual quarter scale model in flight. Although, this is not exactly what the full scale prototype will look like, it gives a better understanding of the actual design to date.

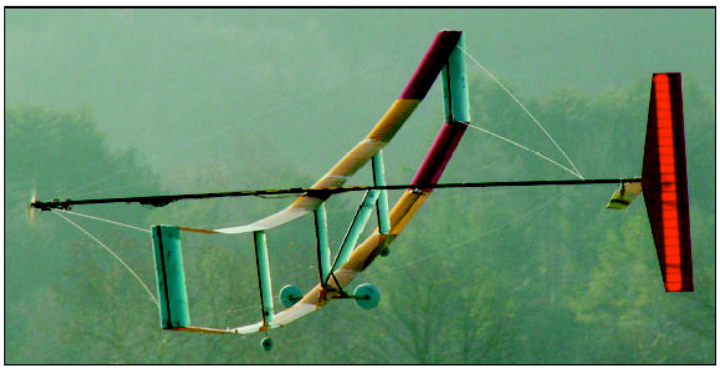

Figure 2.3-1: Quarter Scale Model in Flight

The basic structure of the aircraft is a box-wing with a wing span of 60 feet. The top and bottom spar consists of multiple aluminum tubing sections. This year's team was left with a fairly complete wing spar and strut design. A schematic of the box wing design follows in Figure 2.3-2. Each segment represents a separate circular tube section. Table 2.3 provides the lengths of each section. Each of these spar sections and struts will be connected by carbon fiber joints in a "T", "L", or straight line configuration depending on what pieces are being connected.

Table 2.3: Spar and Strut Configuration

Section	Length (ft)
Outer spars	9
Inner spars	8
Strut 1	5
Strut 2	5

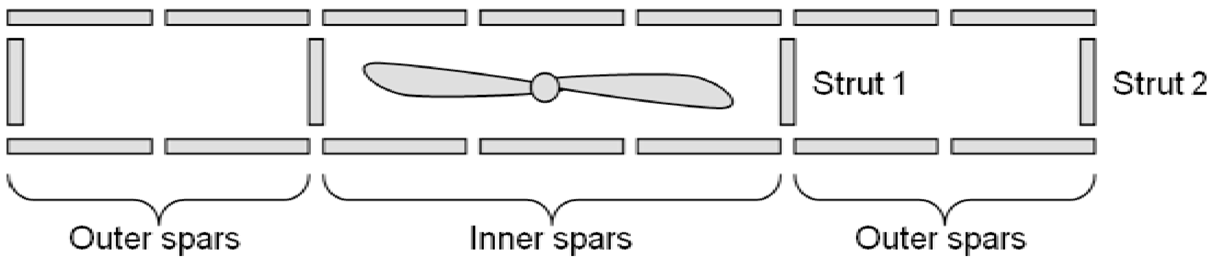

Figure 2.3-2: Spar and Strut Configuration

The actual wing has been designed and is a basic rib and skin configuration. The ribs will be made of foam with balsa surrounding the outside and will be placed every 6 inches across the span of the spars. There will also be balsa at the leading edge and trailing edge to help keep the shape of the wing. The rib configuration will be wrapped in skin made of Dura-Lar ®. It is worth noting that on the outer 18 feet of the wings there will be ailerons for control. This will be discussed later.

Figure 2.3-1 shows the location of the cockpit which is between the wings at the center of the span. The actual cockpit structure has not yet been designed except that it is known that a semi recumbent position is optimum for the pilot when considering pedaling efficiency and freedom of movement. Also, it is likely that the airfoil shape of the cockpit will be a Van de Vooren with 17% thickness and a 44^{o} trailing edge.

The other major structure shown in Figure 2.3-1 is the tail boom. This will be 20 feet 7 inches long and connect the vertical tail with the propeller. This will also connect with the cockpit in the center of the wing. Because of the length and strength requirement of the structure, it will be made of carbon fiber.

The aircraft will be controlled by a simple aileron, rudder, and elevator configuration. The elevator and rudder will be controlled mechanically, but the aileron will be a fly by wire system controlled by servos because of large wing deflections.

2.4 Mission and Objectives

Soon to be added

3. Structures

3.1 Mission Statement

The team spent a significant amount of time deciding what part of the aircraft should be tested first structurally. In order to continue construction on our full scale aircraft the team felt the most important aspect of the design to finalize was the inner box-wing section. This is the reason that we will be structurally testing one half of the inner box-wing section to validate the deflection characteristics when a lifting load is applied. This test will also validate our composite joints which are used to hold our wing sections together. Once the inner wing section is structurally confirmed, the team can continue to design important aspects of the aircraft that have not yet been addressed. These include the design and integration of the cockpit and the tail boom. To do this, two separate goals were laid out. A reliable method of producing t-joints was needed and a detailed method of structurally testing the inner wing section had to be developed.

3.2 T-Joints

3.2.1 T-Joint Development

The present human powered aircraft team inherited a wax casting mold for construction of composite T-Joints. The wax castings constructed using this mold were designed to be wrapped in carbon fiber, and after curing, the wax was to be melted out. The difficulty with this process was the poor dimensional stability caused by the shrinking of the wax. It was therefore necessary to develop a new method which would maintain the filleted shape of the center of the wax castings, while ensuring tight dimensions to allow the spars and struts to fit cleanly into the finished piece.

The new manufacturing method required some new tooling to be developed: A fiberglass mold which would allow the wax centerpiece to be manufactured, and a lay up jig to hold the assembly together when applying the carbon fiber.

The requirements for the actual T-Joints were a precise inner diameter throughout the area where the tubing is inserted, and an approximate copy of the center section for reduced stress concentration. To choose a manufacturing method, several proposed ideas were compared using a simple design matrix:

Table 3.2.1 Design matrix for determining T-Joint manufacturing process

	Difficulty of Making Jig	Cost of Materials	Time to Make Jig	Difficulty of Producing Pieces	Total
Interlocking Machined Metal with Wax Fillets	4	5	5	3	17
Interlocking Machined Metal with Wood Fillets	5	5	5	4	19
Improving Existing Mold with Deeper Machining	3	1	5	2	11
Hybrid Wax/Aluminum Plug	2	2	2	3	10

It was decided that proceeding with a hybrid method using the existing center shape cast from wax and aluminum tubing from the spars and strut as the plug for the cylindrical portions would be the most effective method. This process required both a new mold for casting the wax centers, and a fixture for holding the assembly together while laying up the piece.

3.2.2 T-Joint Construction

It was quickly apparent that the most efficient method of constructing the mold for the wax casting would be making a two piece fiberglass unit which would clamp onto all three tubes. This first required the construction of a plug to give the desired shape. A plug was manufactured using the existing wax mold with short lengths of tubing along the cylindrical regions.

To make a mold of one half this shape, we required a level flange along the center of the plug. To accomplish this, a box was constructed with a cut-out of the correct shape, allowing the plug to be half recessed. Clay was used to fill the gaps between the plug and the wood, and the entire surface was waxed and covered in PVA mold release.

Figure 3.2.2-1: Wax/aluminum hybrid plug and box for creating flange

Figure 3.2.2-2: T-joint plug and first half of fiberglass mold.

With the plug and box complete, one half the fiberglass mold of the shape wax laid up with fiberglass chopped strand mat and epoxy. When this was complete, the plug and the mold half were removed from the box, the entire surface of the remaining plug half and the mold surface were again prepped, and the other half of the mold was laid up.

The lay-up fixture was designed to hold the three aluminum tubing sections level throughout the build process, and to allow all portions of the t-joint to be accessible to allow the carbon to be applied. The fixture was constructed out of 2X4 pieces of wood, and is shown in figure 3.4.2-3.

With the completion of the mold and the fixture, two t-joints have been constructed.

Figure 3.2.2-3: T-joint layup fixture

3.3 Structural Testing

3.3.1 Test Stand

In order to perform a structural test on the inner box-wing section a test stand had to be designed. Preliminary brainstorming told us that we need a device that is rigid at one end and that will allow our box wing to hang in a cantilever configuration. The design that the team has come up with is shown in Figure 3.3.

PICTURE HERE

Figure 3.3: Structural Test Stand

There will be a 2x4 bolted to the wall with 2 in. diameter holes drilled through it. The holes will be 5 ft. apart because that is the designed distance between the box-wing spars. The bottom hole will be at least 3 ft. above the ground to allow for the wing to deflect. There will be another 2x4 with the same hole configuration that is 8 ft. away from the one bolted to the wall. There will be braces connecting the two pieces of wood to keep them as rigid as possible. There will also be removable bolts going through the side of the 2x4s to hold the spars in place once they are fed through the test stand.

3.3.2 Description of Experiment

In performing this experiment we want to simulate the lifting loads applied to the inner box-wing section. We will feed two 12 foot aluminum spars through the 2 in. diameter holes. This will allow 4 feet of spar to hang out of the free end of the test stand structure. These two spars will connect to two 8 foot spars by a straight composite joint. At the end of these spars two composite T-joints will connect the two spars to a vertical strut. This entire 12 foot span is one half of the inner box-wing wing section. Once the structure is in place, we will need to simulate the lifting force on the wing. We will do this by hanging 1 lb. water bottles every six inches across the spar length. At the end of the wing section we will hang a point load that will be equal to the lifting force from the rest of the wing minus the weight of the rest of the wing. This point load is equal to approximately 28 lbs. Once the wing is loaded the wing will deflect. We will measure the deflection relative to its original position which will hopefully validate the structural integrity of our design. According to calculations done by the previous year's teams, the deflection that we hope to observe is about 20 in.

4. Propulsion

4.1 Tricycle Development

4.1.1 Propeller Test Rig Requirements

The sole purpose of the Propeller Test Rig is to validate the design of the propeller and find the propeller efficiency. This is a very high priority because the propeller's power is provided by human stroke. In ideal conditions, the pilot would put out a constant amount of power at all times but translating that power to provide the maximum amount of efficiency requires manipulation of the propeller. The propeller has to be tested at different airspeeds since the power out of the propeller is a function of thrust and velocity.

The test stand is a three-wheeled “tricycle” with a weight maximum of 75 pounds. It needs to be structurally stable, and can accommodate a 140 pound driver. There is implementation of steering and break system, along with a Laptop mount for data acquisition. There is an appropriate clearance required for the mount of the motor, and the position of the propeller.

4.1.2 Propeller Test Rig Construction

The materials used for the construction of the Propeller Test Rig, included non-pressure treated wood.   The dimensions of this wood included boards of wood that were 2x4, 4x4 and 2x6. Other materials included aluminum studs, plywood, a boat seat, salvaged back bike while and break system, various bolts, washers, nuts and screws, and a donated steering and front wheel system from a soap-box car.

Once all of the materials were obtained, construction was underway. First, 2-4x4 pieces of wood were bolted together to form an upside down “T” shape. The 2-2x6 pieces of non-pressure treated wood was bolted to the vertical 4x4 piece of wood forming a reversed “L” shaped. At the end of the L shape, there was a 4x4 piece of scrap wood that served as a space holder until further construction was done on the rear of the vehicle. Moving forward, a steering box was designed and implemented. It was constructed of 4 pieces of 2x4 nailed together and mounted on top of the 2-2x6s flush against the 4x4.   Soon after the steering wheel was mounted to the top of the steering box. Summarizing the remainder of what was competed from a construction standpoint, the front wheel system was inserted into the lateral 4x4 piece of wood with some difficulty. The design difficulties will be addressed in the following section. Following that, there was a laptop stand that was design and built out of one sheet of plywood and 2-2x4 pieces of wood. This was then mounted on to the vertical 4x4 piece of wood. The rear wheel was then attached with a sever amount of difficulty. Following the rear wheel mount, the aluminum supporters where attached to aid the equilibrium of the vertical 4x4 piece of wood. The last piece of construction that was completed was the addition of the boat seat that was attached at the appropriate distance on the 2-2x6 pieces of wood. There was a considerable amount of modify done to the propeller test stand, including trimming off excess wood from the 2-2x6s and removing the 4x4 placeholder at the rear of the 2-2x6 pieces of wood, and replacing it with a modified trimmed piece of 4x4.

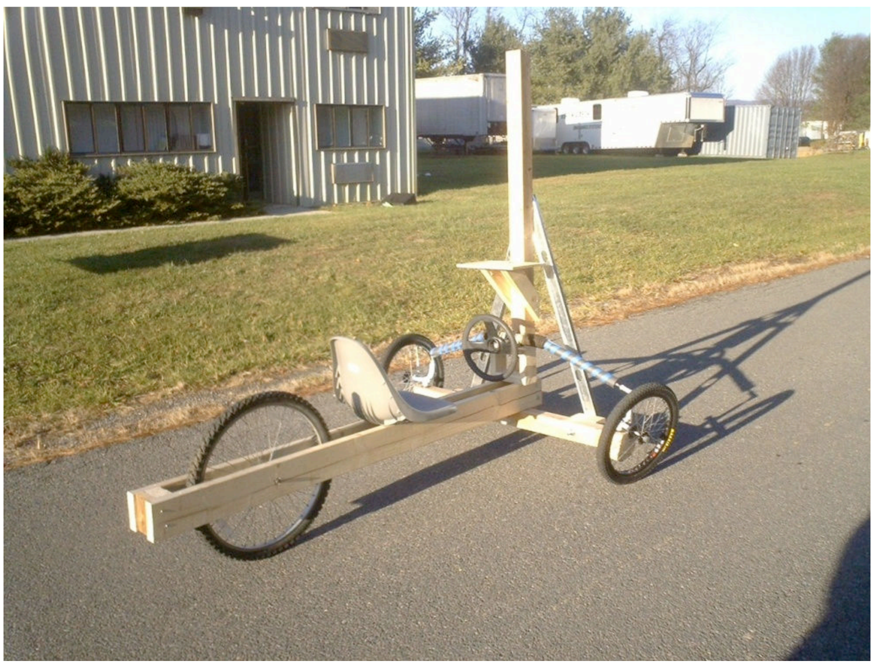

Figure 4.1.2: Propeller Test Stand

4.1.3 Propeller Test Rig Design Concerns

While constructing the propeller test stand, several issues and concerns came up that caused us to alter the design and construction path that we were on. The first was involving the design of the steering box. Initially we assume that we could attach the steering mechanism directly to the 2-2x6 pieces of wood. Once we realized that this wouldn't give us the best designs and appropriate steering ability, there was a multitude of suggestions. Eventually we concluded that the most appropriate and best idea was the creation of a steering box and that was implemented in the current design. Once the steering concerns were addressed, front wheel alignment became the next pressing issue. We had to make sure that the once the wholes where drilled into the lateral 4x4, the orientation of the connecting joint was in its appropriate direction; otherwise the wheel would not perform as expected. Once that was addressed through trial and error, we needed to add a 2x4 block to the bottom of the lateral 4x4 because the spacing was not correct when it came to screwing in the bottom ball bearings. Once that problem was addressed then we moved on to addressing the back wheel. After the back wheel was attached, it was apparent that the wheel was not performing the way that was expected because of the spacing of the rod. This was causing the rear wheel to move in more than the ideal 90-degree location, those given the appearance of wobbling. These in essence caused more drag, and cause the propeller test stand to be unbalanced. What was done to correct this problem was the addition of aluminum spacer to the rod and that was inserted into both of the 2x6 boards to stabilize the wheels. This created a stable test stand and the back wheel then performed as expected. The last design concern dealt with the functionality of the steering system. When the propeller test stand was initially tested, there was an increased drag. This was due to the orientation of the wheels. Initially the wheels angled out which caused an increased amount of drag. To correct this problem, the length of the steering system was shortened considerably until the wheels were angled in. This proved to be the solution the steering problem and caused a smooth and responsive steering system. The last design concern deals with the placement of the rear wheel break. It has been conceptualized that a piece of plywood would be attached to the core 2x6 boards with in reach of the seat. The brake system would be salvaged from the same bicycle that the rear wheel was salvaged from. At this present moment, the brake system has not been attached but it has been designed and the equipment has been prepped for placement.

4.1.4 Propeller Stand Performance

As it has been previously state, the purpose of the propeller test stand will be used to determine the efficiency of the propeller. To perform this task, the test stand will towed up to the appropriate speed, and testing will begin. Initially the propeller will be at zero pitch. Thrust, Velocity, and RPM data will be gathered for this run to serve as reference data. The consecutive runs will be conducted with the propeller pitch incremented by 1 degree for each sequential run. Upon gathering the data, the pitch angle will be mapped as a function of velocity. The reasoning for examining the behavior of the propeller at various pitch settings is to optimize the efficiency for various speeds as the plane is flying through the course. It's easier to optimize the propeller pitch for maximum efficiency with the intent to have the pilot pedal at a constant RPM. A variable pitch mechanism will be discussed later in the report that works hand in hand with the pilot pedaling at constant RPM.

4.2 Propeller Efficiency

4.2.1 Propeller Efficiency Overview

Due to the very narrow design constraints of the Human Powered Aircraft, the flight speed must be maintained at a design speed of 24.5 mph in order for the aircraft to aloft. The propeller was designed to output 5.5 lbs of thrust at 180 RPM, which equates to 270 Watts of prop power. The propeller shape that was generated by XROTOR with those parameters is show in the Figure **PUT FIGURE HERE**, and the airfoil cross-section is shown in figure **PUT FIGURE HERE**.

The estimated propeller efficiency is 92.25%. This would mean that the human would have to provide approximately 300 Watts of power throughout the flight, with increased power for turns and flying into the wind. Considering a college athlete can only provide an average continuous output of 260 Watts, the pilot would have to be a professional cyclist providing a continuous power output at a constant RPM (which was determined to be 90 RPM, the most efficient for a human). This narrow range of human power output at a given rpm places great importance on validating propeller efficiency.

Validating the propeller efficiency will determine whether the propeller will be able to output 5.5 lbs of thrust at 180 RPM. For a propeller of a given diameter, the efficiency varies with airspeed and rpm. The airspeed will change throughout the flight due to wind; however, changing the rpm to bring the prop to maximum efficiency places too much strain on the pilot. The solution to the problem is being able to change the pitch of the prop, which shifts the maximum efficiency of the prop with changing velocity when the RPM's kept constant.

In the flying prototype, a variable pitch system will be instituted to allow for dynamic pitch changes in flight. This could be coupled to a controller based on current airspeed to ensure the propeller operates at maximum efficiency at *all* flight regimes. For more information on the variable pitch system see Appendix A.

4.2.2 Propeller Efficiency Testing

The power supplied to the prop will be achieved through a geared electric motor powered by batteries. The power provided to the propeller will be 320 Watts at 90 RPM, representing the power output of the pilot of the final aircraft. The pitch settings will range from -10 degrees to + 20 degrees (in respect to normal initial position) with 5 degree pitch increments. Upon mounting all the equipment on the tricycle test vehicle, the propeller will be spun statically at the different pitches to determine the pitch setting that will provide the maximum static thrust. Afterwards, the tricycle will be run at an airspeed ranging from 10 mph to 40 mph with 5 mph speed increments with the different pitches for each airspeed to determine the propeller efficiency for each speed. The propeller efficiency, η_p, is calculated as a ratio of the output power over the input power.

$$\eta_p = \frac{P_{out}}{P_{in}} \quad (4.2-1)$$

Power output is found by multiplying the output thrust, T, by the free stream velocity, V_0.

$$P_{out} = TV_0 \quad (4.2-2)$$

Input power is measured by multiplying the input torque, Q, by the propeller RPM, ω.

$$P_{in} = Q\omega \quad (4.2-3)$$

All of the data will be measured with strain gages and RPM sensors, and gathered with LabView.

Afterwards the data will be analyzed to determine if the current design is valid to power the aircraft, or a possible solution that could be implemented in case the prop fails to achieve the required performance. Also, the test will be rerun with more precise pitch setting for a certain air velocity based on interpolation of the gathered data.

4.3 Electronics System

4.3.1 Dynamometer Overview

To measure the efficiency of our propeller, a measurement device had to be developed. A dynamometer (dyno) is a force and moment balance, able to measure mechanical loads. A dyno independently isolates both thrust and torque, making it possible to measure their values. To achieve this, many parts were designed and put together. Figure 4.1 shows a CAD model of the assembled dynamometer.

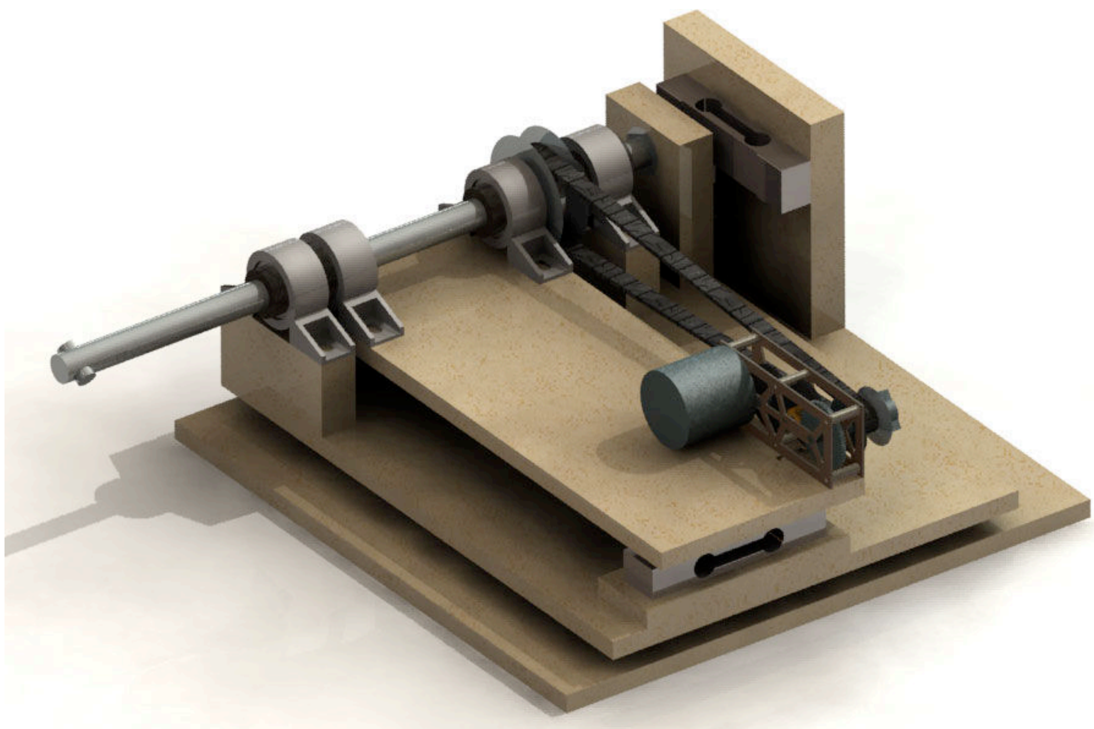

Figure 4.1: Dynamometer CAD Model

A motor is mounted on a board that is free to rotate through the use of four mounted ball bearings. However, preventing the board from actually rotating is a load cell, which will directly measure the downward force, F. Knowing the moment arm, d (1 ft), the input torque, Q, is calculated.

$$Q = Fd \quad (4.1)$$

Using this configuration, any inefficiencies from the motor or gearbox will be accounted for. This entire configuration is mounted on two linear sliders, allowing the dyno to slide freely. As before, a load cell will prevent the dyno from actually sliding and will provide a direct thrust measurement.

The propeller is mounted to the end of the metal shaft shown in Figure 4.1. Since the propeller is over 8 ft in diameter, wind tunnel testing is not possible. Instead, the dyno is mounted on top of a tricycle, with the propeller producing all of the velocity.

4.3.2 Motor and Gearbox

In order for the propeller to produce any velocity, it must be powered by some outside source. Byron Price, a member from last year’s team, developed the Supplementary Power Source (SPS) as an independent research project. The SPS is a combination of a battery powered brushless motor and gearbox. The SPS was developed as a system to provide power for the flying prototype in order to enable flight testing without the need for a professional athlete. However, the SPS will be adopted to suit our needs for efficiency testing.

The selected motor was the Mega Motors RC 41/30/15. It is powered by three PolyQuest PQ4S-3100N 4-cell Lithium Polymer (LiPo) batteries wired in series, providing a voltage of 50.4V at up to 15A. Through this combination, the 41/30/15 is able to produce up to 600W, much higher than that of any human. Figure 4.2-1 shows the motor and battery combination.

Figure 4.2-1: Battery and Motor Choices

The 41/30/15 spins at an incredibly high rate (~10,000 RPM). For the motor to spin the propeller at the desired 180 RPM at the design power, a reduction gearbox was design. Byron Price designed and built a 114:1 reduction gearbox. The final reduction ratio is 57:1, is facilitated by a 2:1 belt and pulley system. The gearbox and pulley is pictured below in Figure 4.2-2.

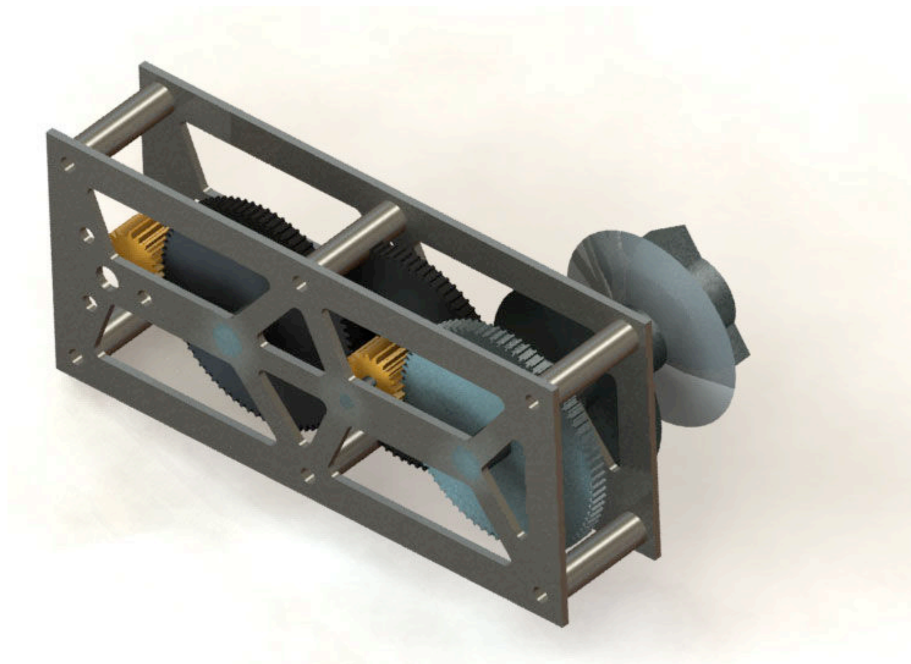

Figure 4.2-2: Gearbox and Pulley CAD Rendering

More detail is provided in Byron Price's AIAA paper, Development of a Supplementary Power Source for Human Powered Aircraft.

4.3.3 Motor Control

To change the RPM of the motor, the input Voltage must be varied. The Castle Creations Phoenix HV-45 is a brushless motor controller able of handling up to 45A of current. The input to the Phoenix is a Pulse Width Modulation (PWM) signal, corresponding to an output voltage. By sending different PWM signals to the Phoenix, the motor's speed can be changed. The PWM signals must be generated by some device. The Mini SSC II is a digitally controlled PWM generator. The SSC is controlled by commands sent through a computer's serial port. These two devices are pictured in Figure 4.3.

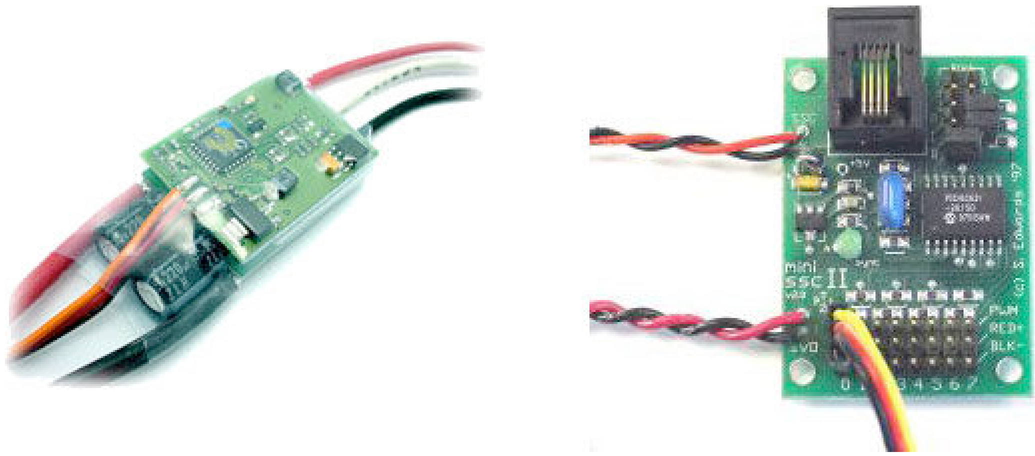

Figure 4.3: Castle Creations Phoenix HV-45 (Left) Mini SSC II (Right)

4.3.4 Input Sensors

Ultimately, the dynamometer has been developed as a means of collecting data. To measure efficiency, four pieces of information must be known: thrust, torque, propeller RPM, and velocity. All four sensors will be powered by a single 5V battery. The two loads, thrust and torque, will be measured by two load cells. The design thrust is 5.5 lbs and the design torque is 15 lbs/ft. Two load cells were purchased from Elane Load Cells, one with a capacity of 10 lbs, and the other with a capacity of 20 lbs. The output signal of the load cells are too weak to be directly measured. To correct for this, each load cell is connected to an INA125P amplifier circuit.

Hall Effect sensors will measure the RPM of the propeller and the velocity of the tricycle. A Hall Effect sensor creates a digital signal when a magnet is detected. By measuring the time between pulse, angular rate (RPM) can be directly measured. The chosen sensor was the Melexis US5781 Unipolar Hall Switch. When By attaching a magnet to the propeller shaft, a Hall Effect sensor can directly measure the RPM. Similarly, a hall effect sensor will be mounted to one of the wheels on the tricycle. The measured RPM of the tricycle is then converted to a linear velocity .

$$V_0 = 2\pi R\omega \quad (4.4)$$

Where R is the radius of the tire and ω is the angular rate (RPM).

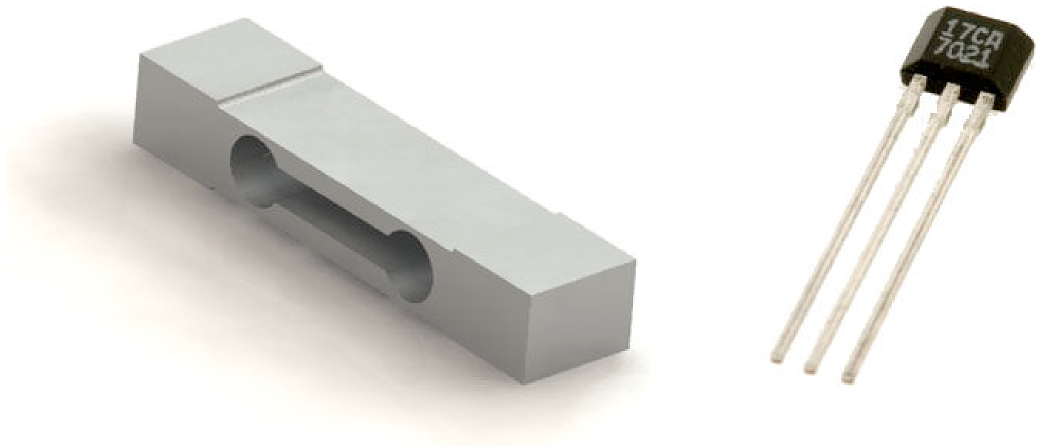

Figure 4.4: Load Cell (Left) Melexis US5781 (Right)

4.3.5 Data Acquisition

The USB NI-6009 is an 8 channel data acquisition board and is picture below in Figure 4.5-1.

Figure 4.5-1: USB NI-6009

The NI-6009 is on loan from the AOE department. Each of the four sensors produce analogue signals that will be digitized by the NI-6009. The NI-6009 is able to record data at up to 48 kHz with 14 bits (1mV), providing the resolution needed to make accurate measurements. To record the data, a LabView 8.2 VI has been written to interface with the NI-6009.

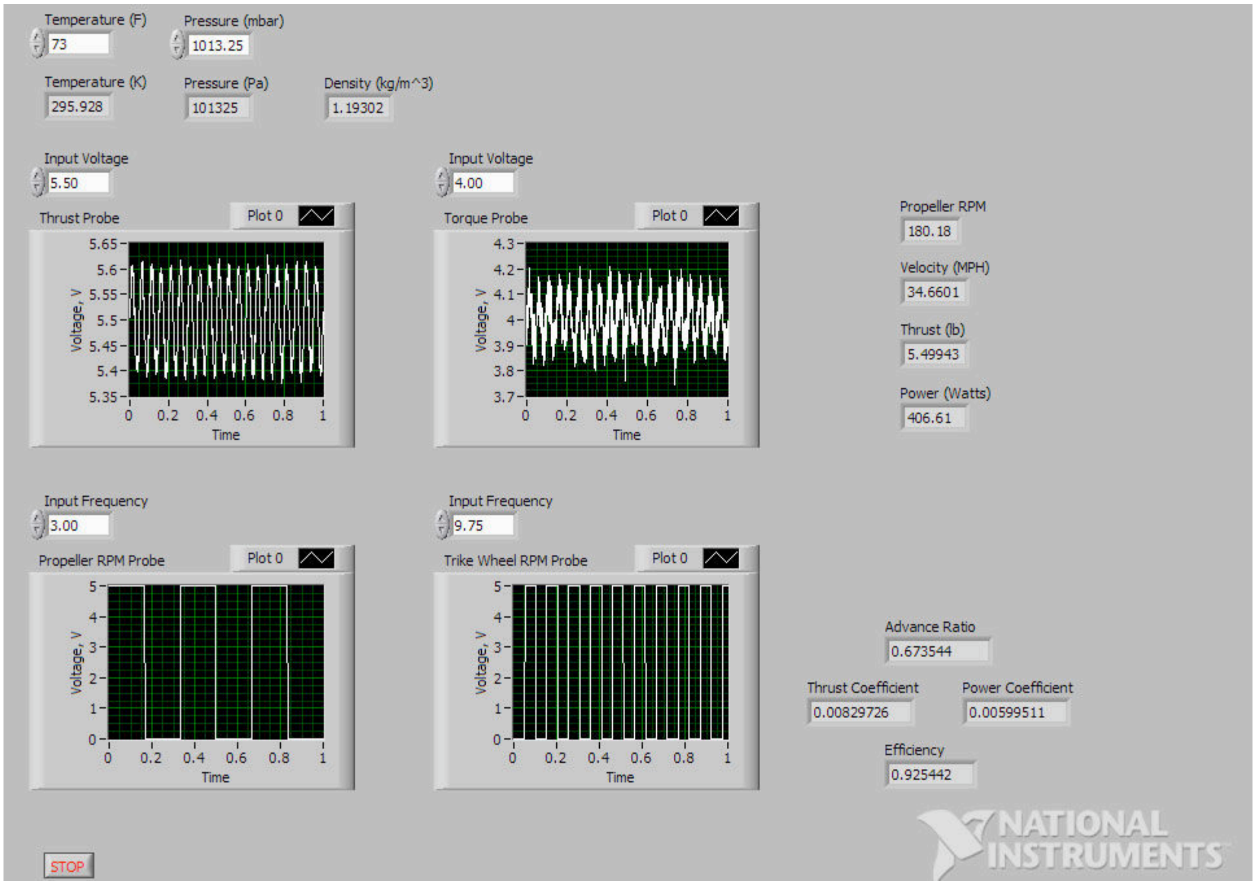

Figure 4.5-2: LabView 8.2 VI for Data Acquisition

The VI records the four input sensors and plots each individually. After each measurement (running at 1000 Hz), efficiency is calculated. Ten times a second, the efficiency is averaged and recorded into a spread sheet file that can later be plotted by Excel or MATLAB. Besides recording the sensor inputs, the VI will also command the motor speed by sending commands to the Mini SSC II through a serial port.

4.3.6 Electronics Flow Chart

Figure 4.6 visualizes the way all of these components will hook together.

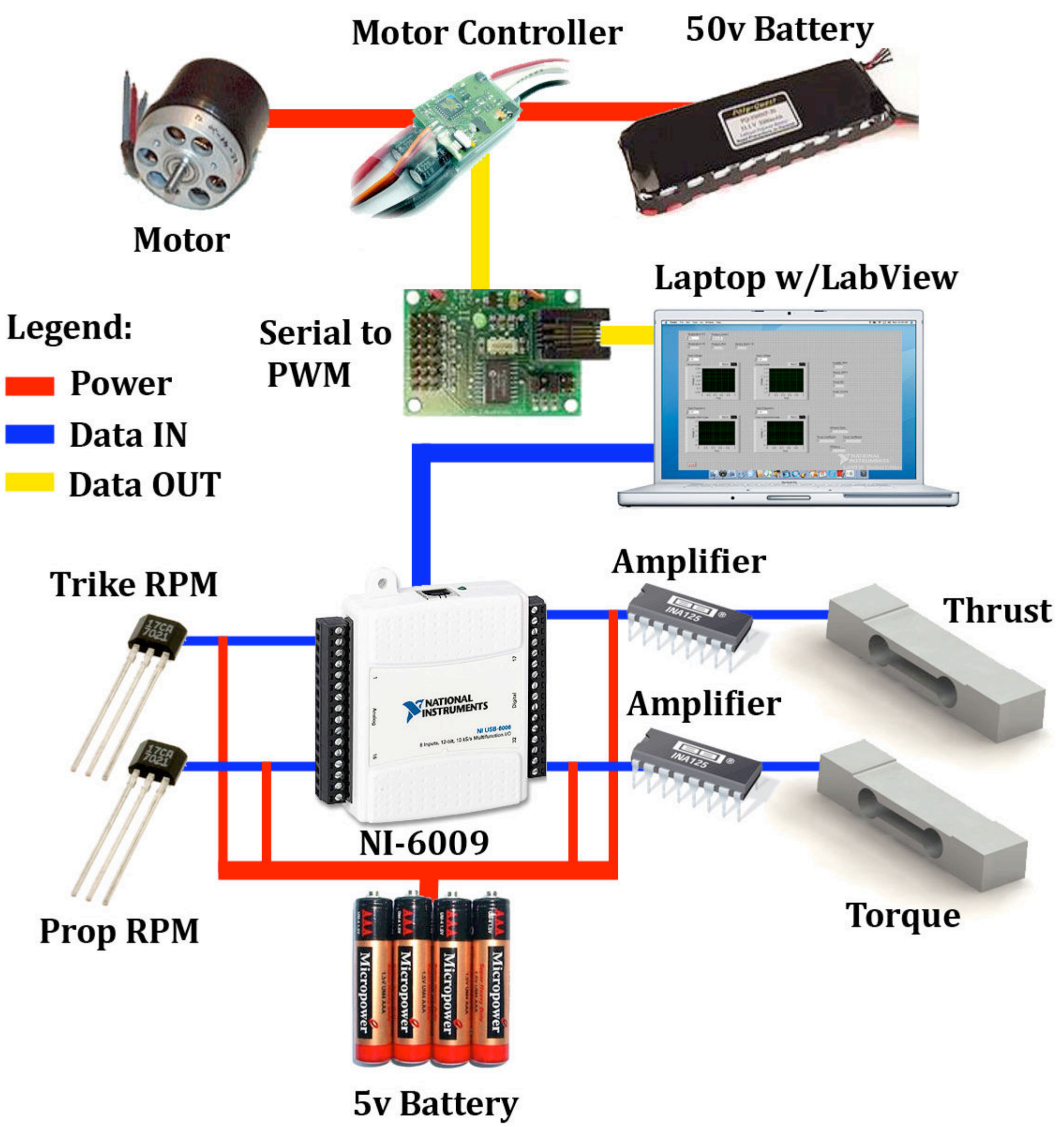

Figure 4.6: Electronics Flow Chart

The four input sensors (2 load cells and 2 Hall Effect) will be powered by a single 5V battery and will be measured by the NI-6009. The NI-6009 is interfaced with the a laptop which will record and plot the data. In addition, LabView will send commands to the Mini SSC II, which will generate PWM commands for the Phoenix motor controller. The Phoenix will receive power from the Lithium Polymer batteries and will generate a Voltage corresponding to the PWM input.

4.4 Propeller Realization

4.4.1 Propeller Construction

A method was required for creating a lightweight propeller from a pair CNC machined plugs created by the previous team. The procedure for making a propeller shell with a shape identical to the plug requires a sturdy female mold to be made. Due to the team's experience with epoxy based composites, it was decided to abandon the polyester resin and gelcoat method suggested by the previous team for creating this piece. The plug was first prepped using several coats of mold release wax, and a thin sprayed layer of PVA film. Once dry, the PVA was coated plug was covered with a layer of West Systems Epoxy thickened with Colloidal Silica, which was allowed to cure for approximately two hours until sticky. The next step was the application of two layers of 6 oz/ yd^2 fiberglass impregnated with epoxy, which was covered with a layer of peel-ply release fabric to give a course surface. Once this was cured overnight, the release fabric was removed, and the surface was sanded with 120 grit sandpaper to ensure a good mechanical bond between the fiberglass layers. Finally, four layers of fiberglass chopped strand mat were laid up with more epoxy, a layer of peel-ply release and a layer of breather cloth were put on, and the entire assembly was vacuum bagged.

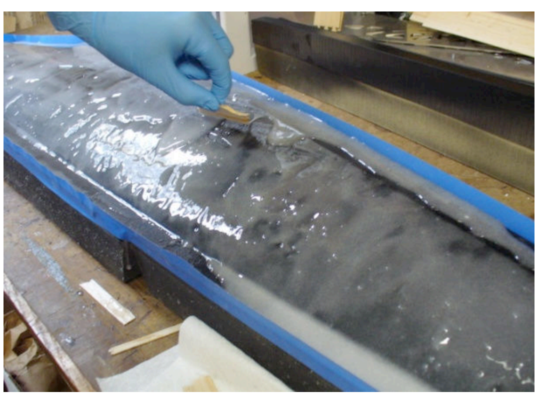

Figure 4.4.1-1: Thickened epoxy being applied to propeller plug

Figure 4.4.1-2: Propeller mold in vacuum bag

The completed molds were quite easily removed from the plug without damage, and after wet sanding the surface lightly with 320 to 600 grit sandpaper, the "good" surface of the mold felt extremely smooth.

To expedite the testing schedule, it was decided to intentionally overbuild the propeller for testing to ensure that it would function, and to save the final design until the prototype nears completion. Based on some preliminary experience with carbon fiber pieces, it was predicted that creating propeller shells out of 2 layers of 5.7 oz/ yd^2 carbon would give sufficient strength. With the molds complete, the layup of the shells was a straightforward process. The mold was prepared in a similar way to the plug, epoxy was spread onto the mold surface, and the two layers of carbon fiber fabric were laid onto the surface and impregnated with more epoxy. The peel-ply and breather cloths were then put on, and the piece was vacuum bagged.

To attach the propeller to the shaft, a ¼ inch carbon fiber spar was used. This was in turn connected to the propeller through 4 1/8 inch plywood ribs, made from the existing CAD model of the propeller. The ribs, after being cut out, were oriented along the shaft using alignment marks from the drawings. When the shaft and ribs assembly was glued together, it was placed into one of the propeller shell halves, and the entire assembly was connected together using thickened epoxy. The flanges of the complete propeller are then trimmed, and any gaps filled.

PICTURE OF COMPLETE PROPELLER HERE

4.4.2 Propeller Collar

The propeller needs some way of connecting to the shaft. Here it is…

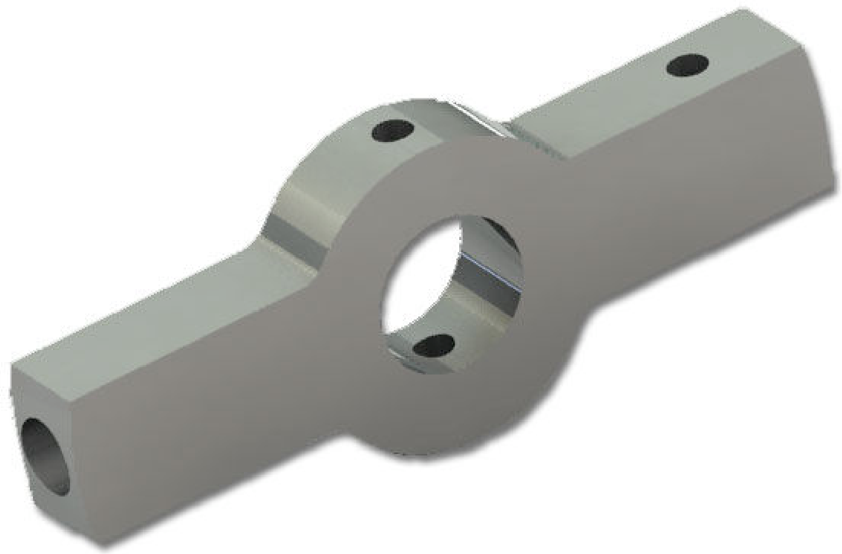

Figure 4.4.2: Propeller Collar

5. Administration

5.1 Schedule

When this project began, over two years ago now, it was planned to be a three year design project culminating in a flying aircraft. From the onset of the semester, this team felt ambitious that this deadline could be held, and planned accordingly.

As the semester progressed the team began to realize the loftiness of our initial goals. The completion of tasks took considerably more effort and time than initially expected. Having realized this, the team revised the schedule and subsequent Gantt charts to a more reasonable pace. Below is the main Gant chart that was presented at the mid-term.

ID	Task Name	Start	Finish
1	Review Existing Design / Previous HPA's	8/20/2007	10/12/2007
2	Setup Team Structure / Wiki	8/30/2007	9/5/2007
3	Plan Project / Select Goals	9/5/2007	10/23/2007
4	Preliminary Construction for Experience	10/4/2007	10/19/2007
5	Complete Inner Box Wing Sections	10/22/2007	12/10/2007
6	Complete Propeller Test Stand/ Test Propeller	10/22/2007	12/10/2007

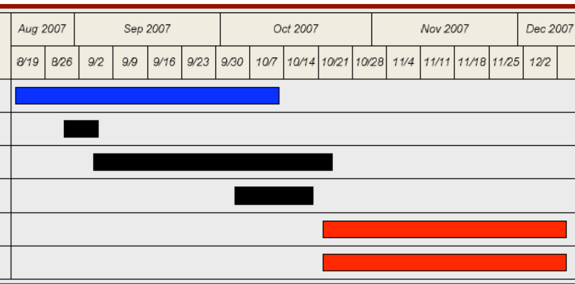

Figure 5.1: Fall Semester Gantt Chart

Revising the schedule this way was helpful for many reasons. The team had to decide what was most significant for progressing onward with the project, instead of simply listing what was not yet completed and setting unreasonable benchmarks. The team now had a set of sensible goals to focus on and address. This allowed small groups to form and concentrate on individual goals.

As can be seen, the two major goals of this semester were to have a tested box wing section and propeller efficiency test completed. Both of these projects are painfully close to completion, however have not been achieved. With an additional week of work the team feels that at a minimum the propeller test would be underway, if not the box wing construction and test as well. These will be immediate concerns at the beginning of the spring semester.

This revision has also helped the team in setting reasonable goals for the spring semester. Again, focusing on the most pertinent aspects of the design that the team truly feels can be accomplished. The following is the Gantt chart for the spring semester.

SPRING CHART (I have my list, but I don't have VISIO. I'll have it tomorrow.)

As mentioned, the completion of the two goals from the fall semester will be primary concerns to begin the semester. The other notable goals will be to further the design and then build a cockpit, to design and begin construction on the drive train system, and to construct and design the tail boom and the way in which it will integrate into the aircraft. The completion of these tasks will be major milestones for the project, and more importantly, ones that the team feels are attainable. While they are not the initial goal of attaining a flying prototype, once completed, they will be important accomplishments to the project and to a future team continuing the project.

5.2 Budget and Sponsorship

A definite budget for the construction of a full scale aircraft has not yet been established. Last year's team proposed the total cost of construction to be well over eight thousand dollars. To an extent, a significant amount of this cost has already been spent or donated. Major purchases still remain; however the current team has had the ability to make its necessary purchases.

This year's team has received funds from the Ware Lab, which is a first for this project. The Ware Lab appropriated $2800 to the team. Last year's team left $375.72 in the account for this project. The team hopes to attract more sponsorship, but is presently able to make necessary purchases.

Preliminary purchases have been made by the team without the need of having to immediately worry about receiving donations. The team has been able to construct some major components of the design with the current materials and available funds. It is hoped that successful demonstration of these components and subsequent experiments will lead to more serious sponsorship. The following is a table of the team's purchases and current financial balance. Receiving donations will most likely be more of a concern in the spring semester.

BUDGET TABLE

A major cost of construction throughout the project will stem from the carbon fiber parts throughout the aircraft. To date, the team has received one significant donation of carbon fiber. While very generous, the team expects to have to purchase more in the coming semester, as well as other construction materials necessary for the project.

The previous year's teams drew upon substantial generosity of sponsors. As the current team, we have tried to continue those relationships with those that have previously helped the team as well as initiate new ones.

6. Summary

7. References

1. Human Powered Aircraft for Sport. AOE 4066 Final Report: Spring Semester. May 2007.
2. 2006. Gossamer Albatross. Wikipedia: The Free Encyclopedia. <http://en.wikipedia.org/wiki/Gossamer_Albatross>.
3. McIntyre, John. Human Powered Flight Group. March 2007. Royal Aeronautic Society. <http://www.raes.org.uk/cmspage.asp?cmsitemid=SG_Hum_Pow_Home>.
4. The Royal Aeronautical Society. 2004. Human Powered Flight: Rules and Regulations for the Kremer Human-Powered Aircraft for Sport. The Royal Aeronautical Society. <http://www.raes.org.uk/cms/uploaded/files/SG_HPAG_sport.pdf>.

Appendix

Appendix A: Variable Pitch Mechanism

The variable pitch mechanism is shown in figure MAKE THIS FIGURE. This is a conceptual design, mostly for representing the actual motion of the system. The range of the pitch change is pretty small (±20 degrees), which is due to the geometry and construction of the propeller.

The propeller has an inherent twist of 80 degrees between the root and chord tips, therefore any change past 10 degrees in any direction will result in negative thrust will be produced at a certain part of the propeller, assuming a non -deforming propeller. However, the propeller IS expected to deform in flight, thus changing the pitch past 10 degrees may correct the deformation and not result in negative thrust being produced.

The main aspect of instituting a variable pitch system is keeping the propeller operating at maximum efficiency with the changing airspeed. The propeller pitch is changed by pivot arms which are connected to a collar through metal rods. The collar rotates with the shaft, but has the ability to slide along the shaft. The rotational motion is isolated at the collar through a ball bearing. The non-rotating part of the bearing is connected to the actuator plate, which will be actuated through a lever or through a servo.

Next semester involves the detailed design of the Variable Pitch System, which involves researching the available components, as well as calculating the loads placed on the components.

Appendix B: Individual Contributions

B.1 Ryan Adams

In the second half of the semester I was part of the team that was primarily responsible for designing and constructing the trike for testing the propeller. I wrote the sections in the report about testing the box-wing, the description of that experiment, and the design/construction of the test stand. For the presentation I put together the 2 slides about the trike.

B.2 Horace Botts

The work that I have done individually since the mid-term status report included work on the construction of the propeller test stand. This construction period was over a span of several weeks with meetings on multiple occasions during the week. I also contributed to the final presentation slides even though I did not present this time. The sections that I wrote for this report include all of the propeller test stand sections.

B.3 Ryan Catlett

Since the midterm, I and group of others have concentrated on the completion of the tricycle test vehicle that we plan to use in our propeller efficiency test. It is complete and waiting for the other pieces necessary for the experiment. I try to be involved in all current team activity. Notably, I have had a hand in the carbon fiber work of fabricating the propeller and T-joints. Additionally, I have been working on designing the test stand for our proposed box wing deflection test. I am the team member primarily responsible for the logistic and administrative work of the team; namely placing purchase orders and handling the budget. The sections that I wrote for this report are the schedule and budget sections.

B.4 Alex Goyachev

B.5 Nathan Knotts

As far as the project goes, my main contributions have been in composites and in data acquisition. I helped create the fiberglass t-joint mold, the fiberglass prop mold, and the 4 carbon fiber propeller blades. I have been solely responsible for the data acquisition board (design, construction, programming, etc.) and I have, on occasion, helped construct the tricycle.

I served as the main editor for the presentation and for this report as well. As far as writing goes, I wrote the Mission and Objectives section (2.4) and the entire Electronics section (4.3).

B.6 Jason Powell

B.7 Brian Wheeler

This semester, I was primarily involved in the composites manufacturing. I taught team members composite techniques and designed most of the processes involved in constructing the different pieces. I also served as “project manager”, which involved ensuring that the team was communicating and that team members did not become alienated. Additionally, I send out newsletters for the project approximately every three weeks.

In this report, I wrote the sections on t-joint development and construction, and on propeller construction.

B.8 Nick Vozza

IRON Butterfly

Human Powered Aircraft

Human Powered Aircraft for Sport

AOE 4066 - Virginia Polytechnic Institute and State University

Final Report Draft: Spring Semester - April 12, 2007

Dr. William H. Mason	Faculty Advisor
Ryan Beach	Project Manager
Reid Doughten	Stability & Controls
Brett Mather	Aerodynamics
Thomas McQuigg	Structures
Michael Parker	Human Factors
Byron Price	Propulsion
Thalia Ruetenik	Structures
Derek Slaughter	Integration

Contents

1. Executive Summary

The goal of the Human Powered Aircraft for Sport Project is to design and build a controllable human powered aircraft (HPA) to win the Kremer Human-Powered Aircraft Competition for Sport. A human powered aircraft is a manned heavier than air vehicle powered only with energy exerted by the pilot, typically through a pedaling motion. The competition requires the aircraft to be flown twice (clockwise and counterclockwise) around an equilateral triangle 500 m on each leg in under seven minutes. In addition, the aircraft will be subject to a constant crosswind during flight. Other requirements for the prize are aircraft specific and include sizing constraints, airworthiness requirements, and power specifications. The purpose of this contest is to inspire the development of an affordable, easily assembled aircraft that could be the basis of a sport in the future [12].

This project is a continuation of a design that began in August of 2005 during which much of the conceptual and preliminary design for the aircraft was completed. The previous year's team developed a quarter-scale model of the final aircraft to validate the overall design. The 2006-2007 team began the school year with testing and development of the quarter-scale model. Model development began with replacement of the original carbon fiber tube fuselage. Analysis was done using advanced modeling techniques in finite element method computer simulations as well as experimentally to find a suitable replacement. Other structural modifications included the addition of guy wires, the construction of a new elevator, and the development of landing gear. Aerodynamic, stability, and control analyses were preformed to predict performance and to guide modifications. A comprehensive flight-testing program was used to validate design changes. The first semester's program concluded with several successful 360° turn flights. The results obtained from these test flights translated to improvements of both the model and full-scale design.

Upon completion of the development and testing of the model, the team focused on development of a full-scale prototype to begin flight-testing in the spring of 2007. While preliminary prototype design was completed by the 2005-2006 team, the present team's accomplishments for fall of 2006 included initial development of an accurate mission model, detailed aerodynamics analyses, cockpit design, and structural optimization.

With full-scale construction beginning spring of 2007, the team has fully realized the need for funding and workspace. Throughout the fall, the team contacted companies and organizations to fill both of these needs. The Virginia Tech Ware Lab agreed to accommodate the team in one of its bays. The HPA team has had success in finding sponsors, several in the form of companies, and some sponsorships from individuals.

During the first half of the spring semester the team has finalized the wing spar design, airfoil design and construction, and further refined the overall aircraft detailed design. The etching process to reduce the wall thickness of the aluminum spar has been tested repeatedly to ensure appropriate results. Four wing test sections have been constructed and placed in the wind tunnel not only to verify aerodynamic properties, but also to test different building methods. The goal was to become prepared to build the final aircraft and the team feels ready to complete the challenge.

2. Introduction

2.1. Human Powered Aircraft Background

Otto Lilienthal, a notable aeronautical pioneer, once said, "To invent an airplane is nothing. To build an airplane is something. But to fly....is everything," [14]. For centuries, it has been the dream of many people to fly self-propelled like birds in the sky. Hundreds of attempts have been made over the course of history, but only recently was the feat accomplished.

HPAs are characterized by their method of propulsion. The aircraft must be propelled by human power alone, which gives rise to the name. The first HPA attempts were based upon sailplane design with a lightweight, large wingspan, and high glide ratios. However, this approach produced aircraft that were too heavy to be effective and design had to be started from the ground up to create a successful HPA. While the concept of creating an aircraft that could be powered by a person was indeed novel, it required a little more innovation to make HPAs a reality.

2.2. The Kremer Prize

In 1959, Henry Kremer offered £5000 to anyone who could make an HPA that could fly a figure eight course [9] thereby establishing the first prize for human powered flight. It was eighteen years before aeronautical engineer Paul MacCready and pilot Bryan Allen met the challenge. On August 23, 1977, the aircraft, Gossamer Condor, was piloted around the figure-eight course to claim the first Kremer prize [8]. Paul MacCready won the second Kremer prize with a second design on June 12, 1979, the Gossamer Albatross, which successfully flew 22.2 miles across the English Channel [15].

There are currently two Kremer Prizes that have not been claimed. The first is the Kremer International Marathon Competition, which challenges the competitor to fly around two turning points at least 4051 m (2.53 miles) apart a total of five times. The complete distance of the course is equal to the length of a standard marathon. The second competition is the Kremer Human-Powered Aircraft Competition for Sport, which is the challenge that this team is attempting to meet. The overall competition goal is to design an HPA that could be used in an aerial sporting event around an equilateral triangular course of 500 m (1640 ft) on each side [12].

2.3. Previous Project Development

This project is a continuation from the previous HPA team at Virginia Tech, which was established in 2005. The 2005-2006 team analyzed the competition rules and performed the conceptual and preliminary design necessary to create a quarter-scale model of the aircraft. Calculations were based on design criteria that would allow the full-scale plane to win the Kremer Prize for Sport Competition.

Over the year, the team designed an aircraft with basic box wing structure, tail boom, fuselage, and tail as shown in figure 2.3-1, shown below. Detailed design of the wing was performed to optimize for correct lift characteristics. A quarter-scale model of the airplane was constructed to validate the aerodynamic and controls calculations [5].

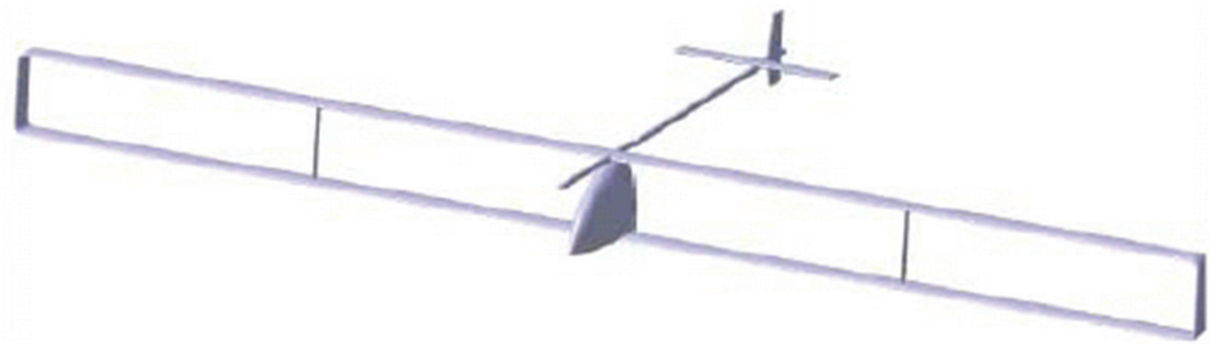

Figure 2.3-1. Computer Model of Previous Team's HPA Design [5]

This approach was used because it would allow the team to test various aspects of the design using the model without risking damage to a much more costly full-scale prototype. The quarter-scale model was flown once in April of 2006 with limited success. Due to a lack of funding and structural design, the fuselage was extremely flimsy, which caused a vibration to occur in the tail boom during flight. This oscillation caused the vertical stabilizer to resonate while moving through the air, causing the plane to be uncontrollable. The flight itself was a success as the model was able to glide and fly under power for short distances even without rudder control.

This quarter-scale model was based upon scaled down dimensions of the full-scale design, which were determined by the team to yield an adequate HPA to meet the competition requirements. However, one should note that the model was designed only to validate the stability and control of the prototype and not the structure. The structural aspects would be too difficult to model, as the components do not scale linearly. The previous team left the current one with a partially working quarter-scale model and conceptual design specifications that can be used to fully design the full-scale prototype. It will be necessary for the current team to complete detailed design of the prototype before beginning construction and then flight-testing.

2.4. Quality Function Deployment Chart

The quality function deployment (QFD) chart was constructed to aid in making decisions about the design of the HPA. Figure 2.4-1 shows the HPA QFD chart for this year's design. It compares the design from the previous year to HPAs built for the other Kremer Prizes. The applicability of the other HPA designs is questionable due to their designs being based on other challenges. To the team's knowledge, there are no other HPAs currently being developed for the Kremer Prize for Sport Challenge. The QFD chart shows that the most significant aspect of the design is the plane's wingspan, followed by thrust and power required for flight. This information will help the team make decisions to best improve the design of the airplane throughout the span of the project.

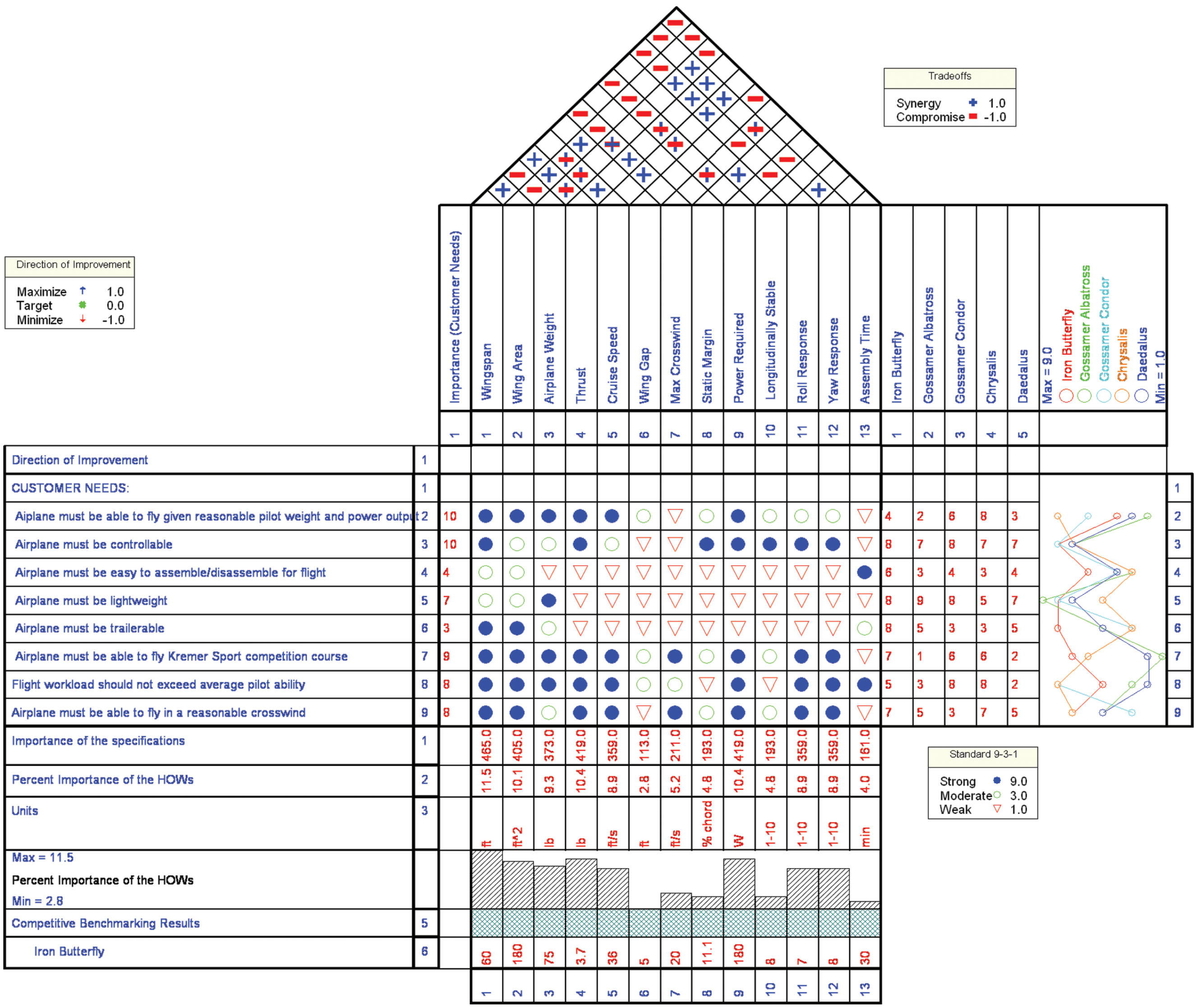

Figure 2.4-1. Quality Function Deployment Chart.

2.5. Report Structure

The remainder of this report will describe the efforts of the 2006-2007 HPA team to design and construct a fully functional HPA. The specific mission will be addressed, followed by developments made in the model and then in the full-scale prototype. The model and prototype sections will be divided into subsections to address the various aspects of design: aerodynamics, structures, stability and controls, integration, human factors, and propulsion as the sections warrant. The subsections will include all relevant data, experiments, and results that apply.

3. Mission and Objectives

3.1. Kremer Prize for Sport

The team's mission is to complete the Kremer Human Powered Aircraft for Sport challenged hosted by the Royal Aeronautical Society. The purpose of this competition is to drive the development of HPA such that in the future it will be possible to create a sport from this class of airplane. An award of £100,000 will be presented to the first entrant capable of demonstrating flight that meets all the requirements in the following section [12]. This challenge has not yet been completed and the team stands a reasonable chance of accomplishing the goal. The rules in their entirety may be found online at http://ourworld.compuserve.com/homepages/j_d_mcintyre/kremer.htm.

3.2. Aircraft Requirements

A section of the competition rules clearly outlines the requirements for the aircraft itself. The aircraft requirements are designed around making a plane that could be used to create a sport. The plane must be able to operate safely at very low altitudes, close to the ground, and the design must be well disposed to kit production. When and if any Airworthiness Requirements are defined for this type of aircraft the requirements must be met. At the time of this report, no such requirements have been created. Then there are several requirements to verify that the plane is human powered. The HPA is to be flown by one person who uses only muscular power for propulsion. There can be no batteries or electric cells used for storage of energy. No lighter than air gasses can be used to generate lift. It must be possible to store the entire plane in a roadworthy trailer with a maximum internal length of eight meters. To ensure practicality, no part of the aircraft may be discarded on takeoff [12].

3.3. Competition Course

The HPA must fly a specified course to complete the competition. This course is shown in Figure 3.3.1. The course may be established anywhere in the United Kingdom, over land or water such that it meets the following criteria:

- The course is an equilateral triangle 500 m (1640 ft) on each side.
- The course shall be flown both clockwise and counterclockwise.
- The mean wind speed during flight will not be less than 5 m/s (11.2 mph).
- The wind speed shall not drop below 5 m/s for more than 20 s during the flight or the flight will be void [12].

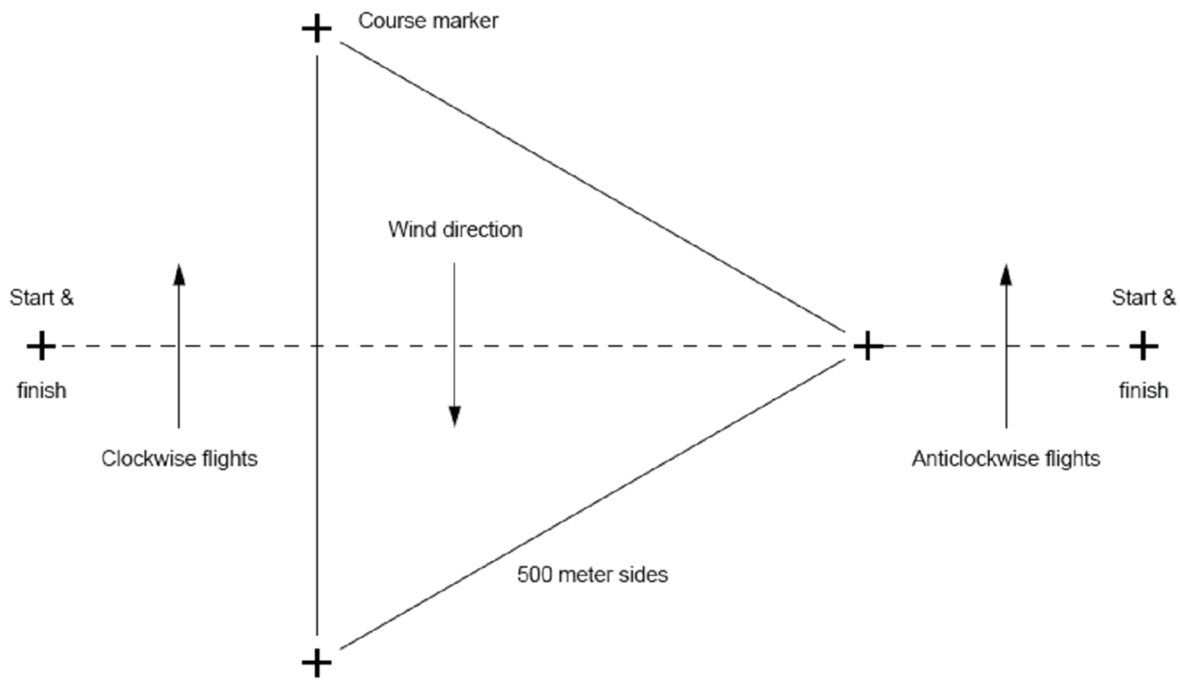

Figure 3.3-1. Competition Course Layout [12].

3.4. Team Objectives

The objectives for the current team have been split up into two categories. One category is the quarter-scale model and the other is the full-scale prototype. The model will be used to validate the prototype so it is imperative that the model fly successfully. With the model flight testing being a success, the team has moved on to prototype development and construction.

3.4.1. ¼ Scale Model Objectives

The initial objective is to make the quarter-scale model flight worthy. This task involves making structural improvements to the initial version of the model. First, a larger constant diameter tube replaced the initial fuselage to reduce oscillation induced by tail flutter. In addition, guy wires were added to torsionally stiffen the wings to reduce aeroelastic effects.

3.4.2. Full-scale Prototype Objectives

Once the aerodynamics, stability, and control response were validated on the quarter-scale model, the detail design of the final model was begun. The ultimate objective is to have a fully functional prototype HPA at the end of the spring semester. "Fully functional" is defined by the ability to sustain controlled flight powered by a human. The prototype may not be able to complete the competition course due to structural limitations. However, the prototype will be useful to the following year's team for finding design flaws and for pilot training while constructing a final competition aircraft.

4. Model Development

4.1. Gantt Chart

The Gantt Chart in figure 4.1-1 shows the progress the team made during the first semester in regards to the quarter-scale model aircraft. Since the team began working on the model, many defects have been corrected and several test flights have been completed. The model has allowed the team to demonstrate adequate flight characteristics and to move forward on designing and constructing the full-scale prototype.

ID	Task Name	Start	Finish	Duration
1	Wing Gap Correction	9/20/2006	10/4/2006	11d
2	Fuselage Analysis	9/18/2006	9/20/2006	3d
3	Fuselage Replacement	9/20/2006	10/4/2006	11d
4	Control Linkage Correction	9/20/2006	10/4/2006	11d
5	Torsional Stiffness Anaylsis	10/16/2006	10/20/2006	5d
6	Torsional Stiffness Correction	10/20/2006	10/25/2006	4d
7	Landing Gear Analysis	10/12/2006	10/18/2006	5d
8	Landing Gear Implementation	11/6/2006	11/10/2006	5d
9	Midterm Design Review	10/11/2006	10/18/2006	6d
10	Minor Adjustments/Repairs	8/22/2006	12/12/2006	81d
11	Stability Analysis	8/22/2006	12/12/2006	81d

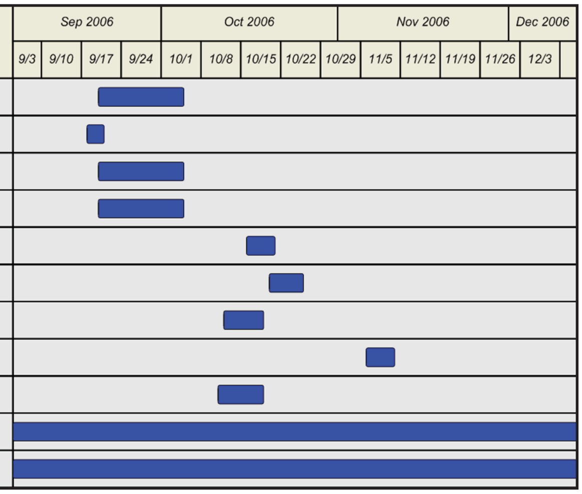

Figure 4.1-1. Gantt chart illustrating accomplishments made on the model.

4.2. Aerodynamics

4.2.1. Wing Gap Reduction

In the original configuration for the quarter-scale model aircraft, the distance between the two wings of the box plane configuration was not fully optimized for performance. With a gap distance that approaches infinity, the induced drag of the box plane configuration is nearly one fourth of that of a monoplane with the same surface area. However, the wing gap could be enlarged to the point where the wing would be prone to flexing and deformation and could negate any performance benefits gained. Therefore, to improve the performance of the model it was necessary to optimize the wing gap. The original gap between the wings on the model was 2.08 ft based on scaling from the design. This translates to an 8.32 ft gap on the full-scale aircraft, which was previously calculated as the optimum. This optimum gap was originally calculated for a given spar strength under the assumption that the struts were rigid members. A more realistic analysis accounted for deformation of the struts, which increased the required strength of the spar. Rather than increasing the size of the spar and thus increasing its weight, the load on the spar was decreased by reducing the wing gap. An analysis of this problem was preformed by the previous year's team in which the optimum gap was determined in terms of induced drag and weight. The results yielded a wing gap of 5 ft for the full-scale aircraft and 1.25 ft for the model [4]. The reconstruction was performed on the model by removing the appropriate length sections from the centers of the carbon fiber struts and endplates. The readjusted struts and endplates were then reconnected using an aluminum joiner and glued into place.

4.2.2. Guy Wire Aerodynamics

Even with the reduction of the wing gap, the wings were still too flexible to perform well aerodynamically. To remedy this problem, four guy wires were attached from each the nose and the tail to the tip of both the top and bottom wing resulting in eight guy wires. Aerodynamic drag analysis of the guy wires was performed in order to determine the additional drag on the aircraft. A value of 1.2 was chosen for the drag coefficient, CD, for the guy wires based on research for the drag on circular cylinders operating at a low Reynolds number [8]. An estimate for the total drag added by the guy wires was then determined using the dimensions of the guide wires at sea level conditions. Interference drag caused by the wake of the guy wires was assumed to be negligible. According to this computational analysis, it was shown that the guy wires would add no more than 0.3 oz of drag. This additional drag was considered acceptable in comparison to the benefits of the added torsional stiffness that the guy wires would provide.

4.3. Stability and Control

4.3.1. Design Requirements for Model and Full-scale Prototype

The design and evaluation of the inherent stability and control response of the quarter-scale model were continued relative to the requirements set forth by the 2005-2006 HPA team as follows:

Static requirements:

- The aircraft exhibit at least 5% longitudinal stability.
- No more than 8° elevator deflection should be needed to trim in stall.
- The center of gravity (CG) should be placed at 0.4 mean aerodynamic chord (MAC) and centered vertically.
- No more than 5° rudder deflection should be needed to land in 11.3° crosswind.
- No more than 9° rudder deflection should be needed to sustain a 15° banked turn.

Dynamic requirements:

- The aircraft should be stable in all modes except spiral.
- The spiral mode time-to-double amplitude must be less than 10 sec [5].

4.3.2. Predicted Model Performance

With much of the preliminary design work already complete, including tail surface sizing and deflections necessary to exact a controlled turn and crosswind landing, most of the focus of the 2006-2007

HPA team has been placed on validating these calculations with a fully functional quarter-scale model of the HPA aircraft. This has led to a unique design approach for both the model and the prototype, one that has been guided almost entirely by the weekly flight performance of the model and the problems it uncovers. Table 4.3.2-1 provides the static margin, control deflections in stall and turn conditions, and time to bank for a controlled turn as given by the 2005-2006 final report [4].

Table 4.3.2-1. Untested control parameters of model.

Static Margin	0.14
Trim in Stall δe [degrees]	6
Turning δa [degrees]	10.8
Turning δr [degrees]	7.93
Turning β [degrees]	2.15
Roll Rate pss [degrees/s]	8.3

4.3.3. Vertical CG Study

The first change made to the model was a decrease in the wing gap from 2.09 ft to 1.29 ft to correct an error in the calculations preformed by the previous year's team. The updated model was reevaluated in AVL, which resulted in a new static margin of 0.111 MAC [4]. In addition, the elevator deflection to trim in stall changed to 2° from 6°.

Problems with vertical CG and thrust-line placement during initial flight-tests on October 3 prompted further investigation into the effect of a varying vertical CG on static margin, $C_{m\alpha}$, and $\delta_{e,trim}$. Using AVL, the vertical location of the CG was varied between 4 in above center and 4 in below center, yielding deceivingly linear trends. As was discussed in the 2005-2006 final report, the variance of $C_{m\alpha}$ with vertical CG is not actually linear, although AVL assumes a linear relationship when solving for the pitching moment. The same principle applies to the elevator trim required. Despite this fact, the results obtained during the study were considered sufficient to help determine importance of placing the CG of the model as close to the center of the wings as possible.

Figure 4.3.3-1 shows the relationship between vertical CG location and static margin at three different angles of attack. As the CG progresses above the center point, as was the case with the model during the October 3, 2006 flight-tests, the neutral point moves forward relative to the CG thus decreasing longitudinal stability. The same trend is evident in the relationship between $C_{m\alpha}$ and CG location. However, during the October 3, 2006 tests, the pitch-up moment created by the below-CG thrust-line was far stronger than any initial pitch-down tendency of the aircraft so the destabilizing effects of the high CG were eclipsed by the thrust-line moment.

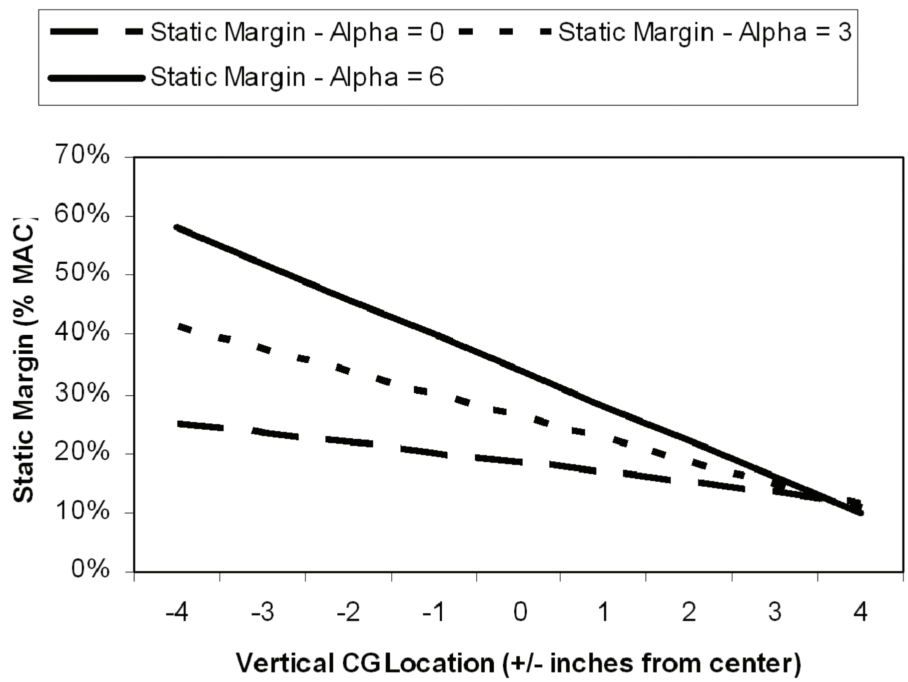

Figure 4.3.3-1. Variance of Static Margin with Vertical CG Location on the ¼ Scale Model.

It is also interesting to note that the elevator deflection needed to trim decreased with increasing vertical CG location at nonzero angles of attack (for practical purposes, the trim deflections at 0 degree angle of attack were constant and assumed to be zero). This trend is shown in Figure 4.3.3-2.

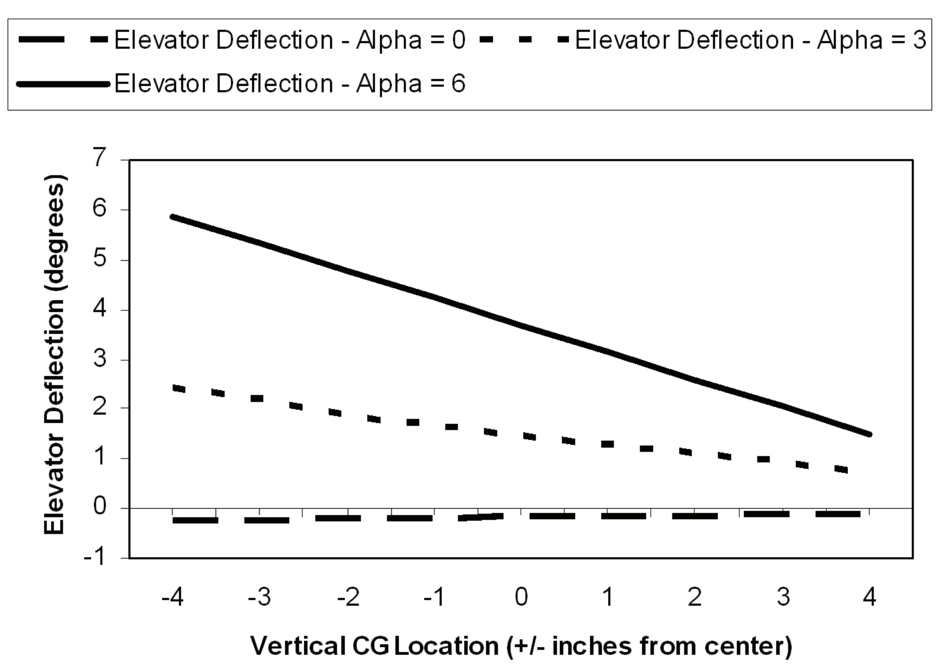

Figure 4.3.3-2. Variance of Static Margin with Vertical CG Location on the ¼ Scale Model.

4.3.4. Turning Mechanics

The turning ability of the aircraft as predicted by the 2005-2006 team was characterized by coupled aileron and rudder input, primarily because the bank angle needed for a coordinated turn could not be achieved by the ailerons alone. According to table 4.3.2-1, an aileron deflection of 10.8° and a rudder deflection of almost 8° should induce a sideslip angle of 2.15° and a roll rate of 8.3°/s for the quarter-scale model. While these predictions could not be directly validated by the model, general control inputs and the resulting aircraft response were observed during flight-testing to determine if controlled turns would even be possible given similar aileron and rudder inputs. The radii needed to sustain a turn at a cruise speed of 16.5 ft/s at bank angles of 5°, 10°, and 15° were calculated to assist the pilot in performing properly controlled turns. These calculations were made using a 15° rudder deflection with no aileron deflection in hopes of establishing a safe, upper limit for control input and subsequent radii needed for a turn. The recommended turn radii as told to the pilot are shown in table 4.3.4-1.

Table 4.3.4-1. Recommended Turn Radii for Given Bank Angles.

Bank Angle [degrees]	Radius [feet]
φ = 15	35-40
φ = 10	55-60
φ = 5	95-100

It was also noted that the required C_L for each of the turns was approximatly 1.1. Given that C_{Lmax} occurred at roughly 1.4, this left a stall margin of only 0.3. Thus, it was also recommended that the pilot keep the angle of attack as low as possible to avoid mid-turn stall.

During the subsequent flight-testing, several successful turns were completed using rudder-only input, aileron-only input, and aileron/rudder coupling. This validated not only the ability of the aircraft to sustain a controlled turn, but also showed that the roll moment induced by the ailerons was much more effective than previously considered. Tight radius, controlled turns induced only by aileron deflection with little to no altitude loss were performed successfully at bank angles near 15°. Rudder-only turns were also completed; though they required larger turn radii as well as more time to complete the turn. The most effective turns, however, were performed with simultaneous aileron and rudder control, a principle, which will be carried over to the full-scale prototype.

Exact inputs for both aileron and rudder needed to complete the course will be calculated using a six degree-of-freedom simulation based on derivatives calculated using AVL [4]. Accurate control inputs, however, will only be obtained through trial and error during eventual flight-testing of the full-scale prototype, in which the calculated inputs will serve only as an initial guide.

4.4. Structures

Over the first half of the fall 2006 semester, the primary goal of the team was to improve on the quarter-scale model designed and built by the 2005-2006 HPA team. The idea was that major structural improvements could readily be analyzed and implemented. These changes were necessary to achieve more desirable flight characteristics. With an improved aircraft, a better validation of the team's design could be achieved and greater weight given to the results of flight-tests.

The structural analysis and reconstruction of the quarter-scale model involved three major phases. These phases were fuselage reconstruction, wing skin analysis, and guy wire analysis. These phases will be discussed in the following sections.

4.4.1. Fuselage Reconstruction

A major problem with the original design of the quarter-scale model was the presence of rudder flutter that caused oscillations of the carbon fiber tube fuselage. These oscillations were attributed to an undersized, tapered fuselage tube that rendered the rudder control lines useless. ANSYS 10.0 was used to predict the deflection of the original 0.28 in diameter tube as well as the deflections of two alternate designs considered viable and readily available [1]. These two designs included a 0.55 in diameter carbon fiber tube and a 1.5 x 1.5 in balsa box structure. Table 4.4.1-1 shows the material properties of these three designs.

Table 4.4.1-1. Physical properties of fuselage candidates.

Material	Carbon Fiber (Original)	Carbon Fiber (New)	Balsa
Density [slug/in^3]	0.0019653	0.0019653	0.00015722
Length [ft]	5	5	5
Cross Section	Circle	Circle	Square
Dimension [in]	0.28 Dia.	0.55 Dia.	1.5 x 1.5
Modulus of Elasticity [GPa]	102	102	102

Of the designs, ANSYS 10.0 predicted that the larger carbon fiber tube was best choice of the two new alternatives. An experimental test was used to verify these predictions. Figure 4.4.1-1 shows the test apparatus. For the experimental test, a 60 in test section was held parallel to the ground and fixed only at one end. At the opposite end, various loads ranging from zero to two pounds were applied. The deflections of the rod caused by these loads were then recorded and compared. Table 4.4.1-2 compares the experimental results with the predictions given by ANSYS 10.0. Experimentation showed that ANSYS 10.0 predicted the correct response of the rod, thus providing validation of the analysis.

Table 4.4.1-2. Deflection analysis verification for the thick carbon rod.

Load [lb]	Experiment Results [in]	Predicted Results [in]
0.125	0.438	0.416
0.250	0.875	0.832
0.500	1.688	1.664
1.000	3.375	3.328
2.000	6.688	6.655

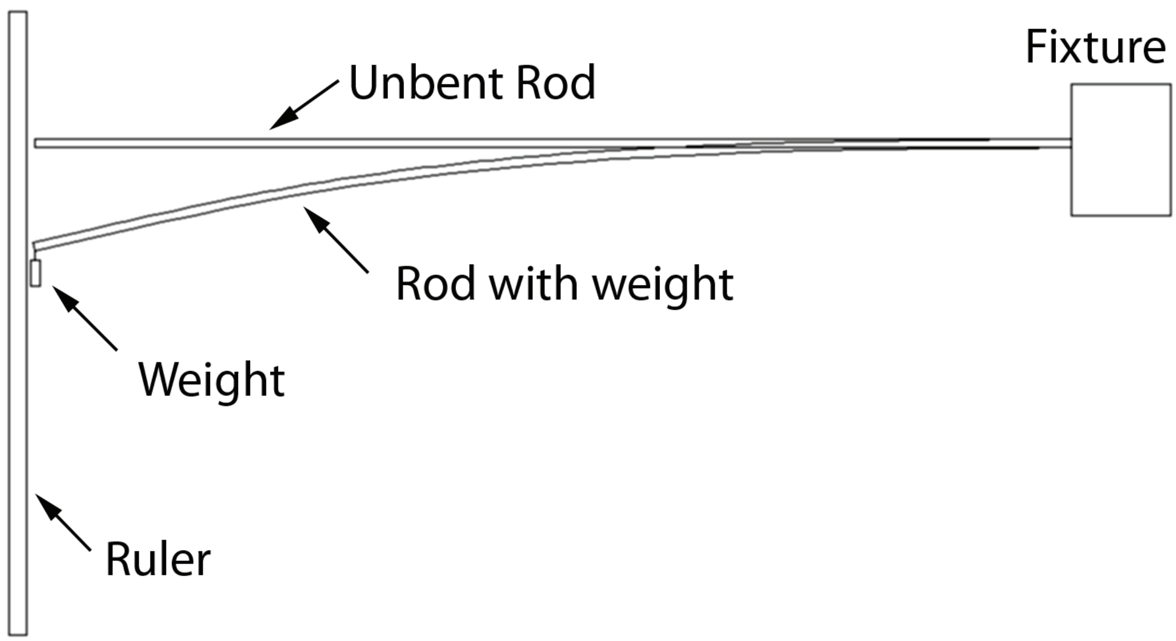

Figure 4.4.1-1. Static loading test on 0.55 in diameter carbon fiber rod.

The vibration analysis of the tail section of the fuselage rod involved finding the natural frequency of the thicker carbon fiber rod. This frequency was then compared to the natural frequency of the original carbon fiber rod. By increasing the natural frequency of this major part of the fuselage structure, the vibration would be naturally damped. The natural frequency of each rod was determined by equation 1,

$$f = \frac{\sqrt{\dfrac{12 \cdot E \cdot I}{L^3 \cdot m_c}}}{2\pi} \quad \textbf{(4.4.1-1)}$$

where, f is the natural frequency, E is elastic modulus, I is the cross section moment of inertia, L is the length of the rod, and m_c is the tip mass of the beam, or rod in this case. Determination of the natural frequency showed that the larger rod used had the added benefit of a significantly larger natural frequency of 5.7 Hz. This frequency is a 67% increase over the natural frequency of the smaller rod.

4.4.2. Wing Skin Analysis

Analysis of the effectiveness of different wing skin materials was the first of two analyses done to try to improve wing torsion stiffness. The wing's lack of adequate stiffness under torsion was considered a likely cause of inadequate roll control from the model's ailerons. At the time, it was thought that a stiffer skin material might provide a valuable increase in wing torsional stiffness and warrant re-covering the wing structure.

Figure 4.4.2-1 shows the test rig used during this experimental analysis. Three identical balsa frames were constructed, and three different skin materials were used to cover them: a sample of the current wing covering, Micafilm, another sample of Micafilm with fiberglass reinforcement tape and a more popular skin choice among model aircraft builders, Monokote®. These frames were then subjected to identical torsion loadings.

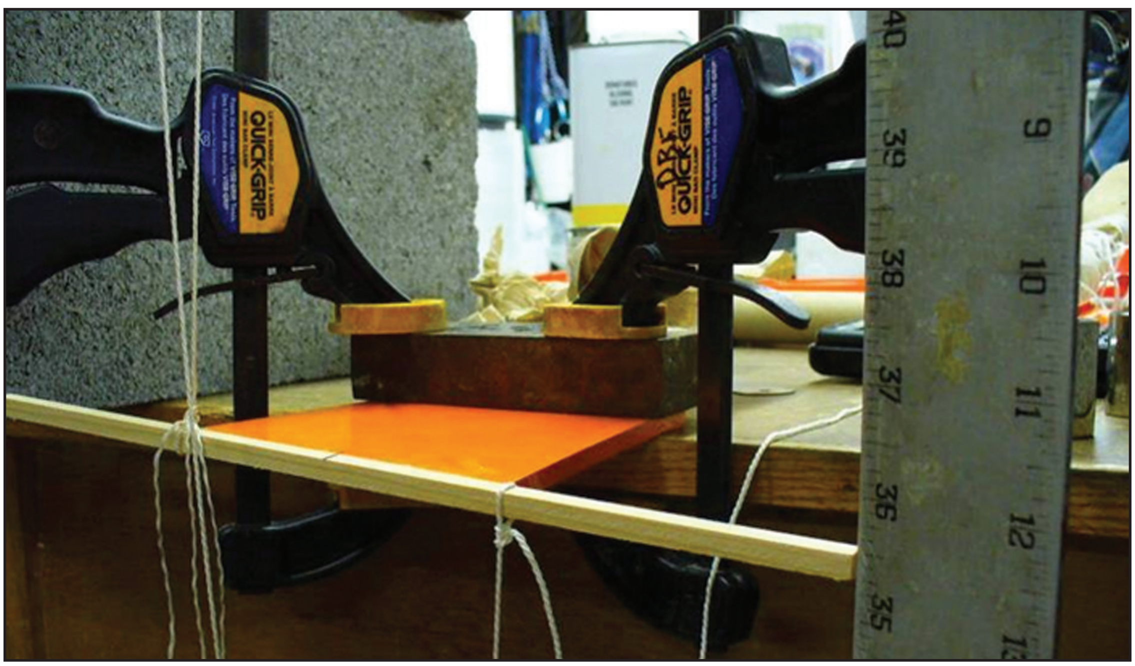

Figure 4.4.2-1. Wing skin torsion loading test rig and Monokote® covered balsa test frame.

It was shown during the above test that none of the materials provided significant improvements in overall torsional stiffness. Table 4.4.2-1 shows the results of all three tests. These results showed that re-covering the wing with a stiffer skin would not be a solution to the wing stiffness problem. Another solution would have to be found.

Table 4.4.2-1. Results of wing skin torsion test.

Weight [oz]	Torque [oz-in]	Micafilm	Monokote©	Micafilm with Tape
		Deflection Angle [deg]	Deflection Angle [deg]	Deflection Angle [deg]
0	0	0	0	0
22.7	51.1	1.19	1.19	1.19
44.66	100.5	2.39	2.39	3.58
73.64	165.7	4.17	4.76	5.95

4.4.3. Guy Wire Analysis

The application of guy wires to the quarter-scale model was considered the next viable option for improving torsional stiffness of the wing. One reason for this decision was the widespread use of guy wires in previous human powered aircraft designs. A major consideration in guy wire design is the additional drag. As discussed in the previous aerodynamic section it was found that the drag caused by the guy wires at the Reynolds number at which the model was flying was acceptable. An additional concern was the ability of the wire to withstand any loads encountered in flight and to resist stretching under loading. These two factors were not expected to be difficult to meet for the model. However, structural and aerodynamic analysis will be needed for applying guy wires to the final aircraft.

4.4.4. Guy Wire Application

As stated, it was expected that adding guy wires to the quarter-scale prototype would offer significant improvements to torsional stiffness of the wing. Two requirements were placed on any potential materials considered for use as guy wires. First, they had to be strong enough to resist any sustained loads in flight and hard landings. Second, they had to offer resistance to stretching.

Goldberg Flying Line was chosen for use as the guy wires. It was readily available, fit the required strength criterion, and was already in use in the model aircraft world. Four guy wires were attached to both the forward and aft most section of the fuselage boom and connected to the top and bottom wingtips. This resulted in eight guy wires used in the aircraft. Figure 4.4.4-1 shows the guy wire configuration of the quarter-scale model. It was immediately observed that the guy wires offered significant improvement in torsional stiffness of the wing. However, experimental data was then used to verify this conclusion.

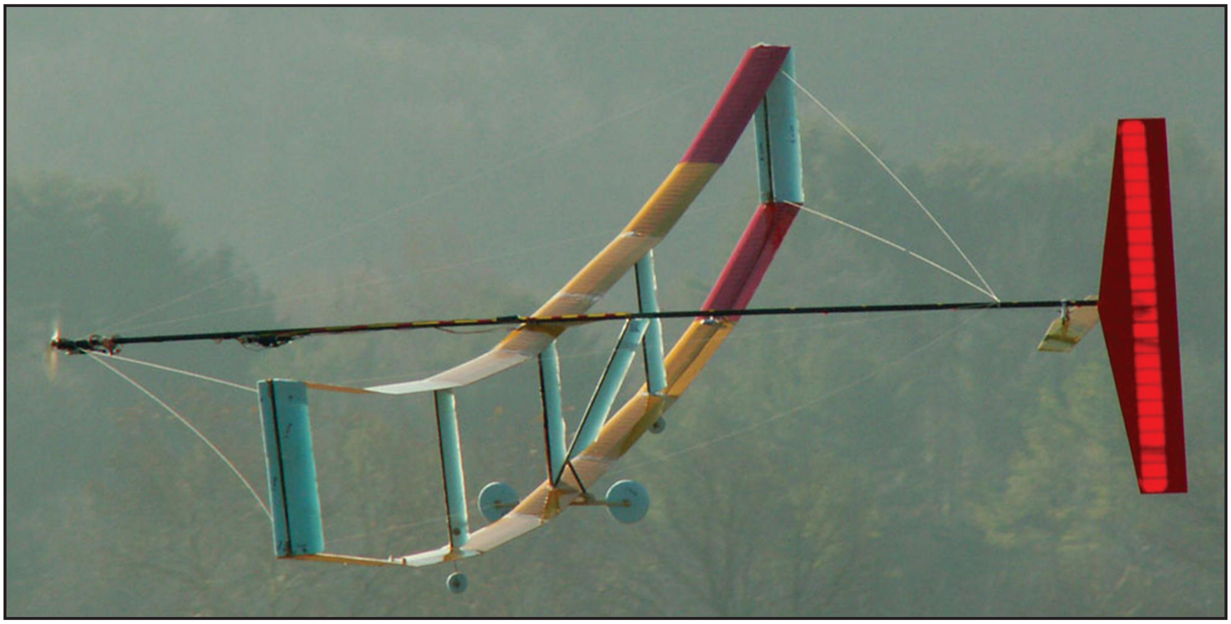

Figure 4.4.4-1. Quarter-scale model with guy wires.

The stiffness of the wing experiencing a torsional load was measured experimentally with and without guy wires. Figure 4.4.4-2 shows the device used to apply a given torque. Table A-1 (Appendix A) shows the results of the tests with wires and without wires. Figure 4.4.4-3 graphically shows the response of the wing to an applied torque. These results show that a much stronger force is required to achieve the same angle of twist for the wing with wires than the wing without wires. Figure 4.4.4-3 shows that the guy wires double the force required to obtain a given deflection.

Figure 4.4.4-2. Torsion testing of the wing.

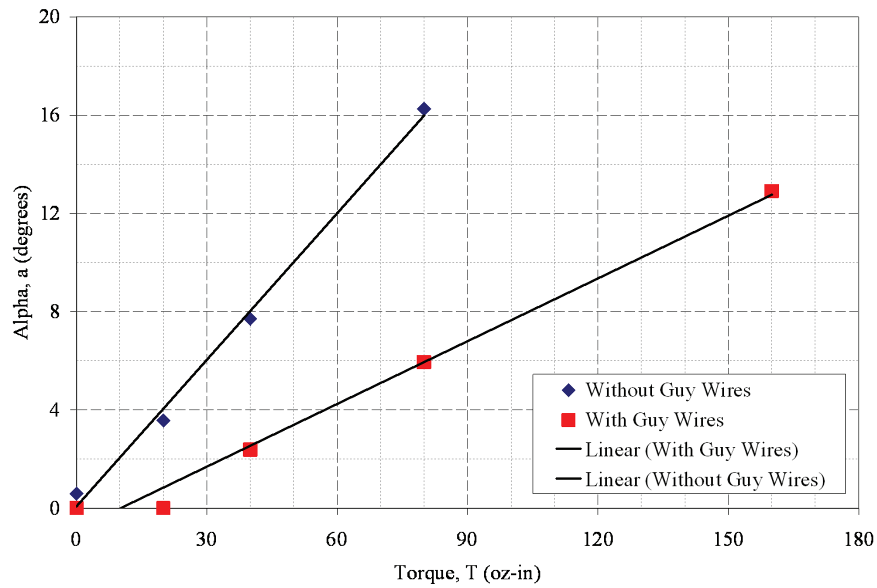

Figure 4.4.4-3. Graphical depiction of wing torsion test results.

4.4.5. Revised Control Surfaces

The construction of the elevator in the quarter-scale model was overly robust and therefore contained weight. Since this control surface never sustained any type of damage during test flights, the decision was made to rebuild the elevator as a balsa frame instead of the full balsa sheeting and basswood spar with which it was originally constructed. To construct the new elevator, shaped ribs were cut to match the airfoil of the original elevator. The aerodynamic changes to the elevator by its reconstruction were only those caused by sag of the Monokote® covering, which were considered to be negligible for such a thin airfoil. This reconstruction reduced the weight of the elevator surface by approximately 1 oz. and allowed for the removal of the ballast from the nose of the model, reducing the total weight of the model by another 0.35 oz. This resulted in a total weight reduction of approximately 1.35 oz. Another benefit of removing weight from the nose and from the elevator was the downward shift of the vertical center of gravity. Originally, the center of gravity was built higher than it was designed. The weight reduction from the top of the aircraft shifted the vertical center of gravity closer to the midpoint between the two wings.

4.5. Propulsion

4.5.1. Electronic components

The radio components were chosen for the model to keep the lowest weight possible while being able to perform as required to fly the model. The receiver chosen was the Hitec Electron 6 because it is the lightest six-channel, dual-conversion receiver available. Since each wing has an independent servo, six channels are necessary to control the airplane. Dual conversion specifies how the radio signal is processed and is much less susceptible to interference than a single conversion receiver. The previous year's team selected the servos by calculating the aerodynamic loads on the tail and then finding the smallest servos capable of supplying this torque [5].

To select the battery and motor, ElectriCalc [11] was used and wind tunnel tests were conducted. First, an appropriate size speed control was selected that could handle the loads with a factor of safety. Then the battery pack was selected based on the initial power requirements from the drag estimate and a desired run time. The run time was selected to be greater than 10 min, so battery life was not a concern during flight test. Once this was selected, the smallest motor that output the required power with the battery selected was chosen using ElectriCalc. This completed setup was then tested in a wind tunnel to verify ElectriCalc results and select the propeller. Testing and verification of the battery and motor were preformed by the previous year's team. The radio configuration determined from analysis of the aerodynamic loads and power requirements is displayed in Table 4.5.1-1.

Table 4.5.1-1. ¼ Scale Radio Configuration

Component	Type	Weight	Dimensions	Description/Specification
Receiver	Hitec Electron 6	0.6 oz	1.8″ x 0.9″ x 0.6″	6 channel dual conversion receiver, positive shift for Airtronics
Tail Servos	Hitec HS-81	0.58 oz	1.17″ x 0.47″x 1.16″	Stall Torque (4.8 V): 36.10 oz-in
Aileron Servos	Hitec HS-55	0.28 oz	0.89″ x 0.45″x 0.94″	Stall Torque (4.8 V): 15.27 oz-in
Speed Control	Phoenix 25	0.6 oz	1.08 x 0.91 x 0.16″	Brushless Motor Speed Control, 5-10 cell NiCD, 25 Amp continuous
Motor	Axi 2204/54	0.91 oz	1-3/32″D x 1-1/32″L	Max Efficiency 77%, Max current 7.5 Amps, 2-3 cell Li-Poly
Battery	ThunderPower 2cell 1320mAh	2.06 oz	2-1/2 x 1-1/4 x 1/2″	17 Amp maximum continuous, 20 Amp peak
	Total Weight	5.03 oz		

4.6. Landing Gear Design

The original landing gear on the model consisted of a main skid on the bottom of the fuselage, with two outrigger wire skids attached to the inboard strut between the two wings. After the first flight-test, the need for a more reliable and more effective landing gear solution was assessed. The previous solution was ineffective as a skid and caused the plane to stop abruptly on touch down, resulting in large landing loads on the airframe. It was determined that a better landing gear would be beneficial to the survival of the airplane. The key requirements for the landing gear were that it must be very lightweight, be able to operate in grass, provide longitudinal and lateral stability on the ground, and be able to handle loads induced during landing. Three different options were then compared to determine the best solution. The first option was a traditional main gear attached to the fuselage, which is similar in configuration to many model aircraft and general aviation aircraft with fixed gear. The second alternative was a bicycle gear attached to the fuselage with longer outrigger wires on the wings for lateral stability. The third option was to place the landing gear directly on the wings for better stability and landing load capacity via single wheels in place of the current outrigger wires. Placing the landing gear on the wings would decrease landing loads due to the wing being half the weight of the aircraft.

When compared, the bicycle gear was determined to be the best option. The main gear option was determined to have no longitudinal stability, which is necessary to prevent tail-strike and reduce pilot workload on landing. In addition, with the landing gear on the fuselage with no outriggers, the landing loads imposed on the wing would be much higher. The landing gear on the wings, although the best for handling the landing loads, would be less longitudinally stable, as well as heavier and more difficult to implement. The bicycle design was determined to be the best option because it had both lateral and longitudinal stability, and the outriggers better distributed the landing loads. A comparison of these concepts can be seen in table 4.6.1-1.

Table 4.6.1-1. Comparison of Landing Gear Configurations.

Alternative	Reliability	Ease of Construction	Weight	Wing Landing Loads	Total
Percentages	0.2	0.15	0.3	0.35	1
Traditional Main Gear on Fuselage	1	0	0	-1	-0.15
Bicycle with Longer Outrigger Wires	0	0	0	0	0
Landing Gear on Wings	-1	-1	-1	1	-0.3

The bicycle landing gear was then constructed and attached to the aircraft to test the design. The wheels were constructed of half-inch thick blue foam cut into circles five inches in diameter with thin plywood wheels hubs three-quarter inches in diameter used to distribute the load from the axle over a greater area of foam. The landing gear struts were constructed out of spruce dowel rods, as they were strong and light, and then lashed to the fuselage. The axle used was a small steel wire. Through flight-testing results, the design was modified so that the struts were no longer angled down from the fuselage, but angled horizontally in order to save weight and increase the strength of the landing gear. In addition, 2 in in diameter wheels were added to the outriggers to reduce the risk of the skid catching on the grass and reduce the rolling friction of the landing gear system. These revisions improved the landings of the aircraft; however, the landing gear struts were not strong enough to take the landings. The final revision of the landing gear was to make the struts out of a harder dowel rod.

Overall, the landing gear performed well. The bicycle configuration provided the required longitudinal stability, while the outriggers provided the lateral stability. The landing gear also performed its main objective in reducing the landing loads on the structure, reducing structural failures and repairs. In addition, the landing gear also was lightweight, adding less than 1.5 ounces to the total plane weight.

4.7. Flight-testing

Flight-testing of the quarter-scale model began with the continued philosophy of the 2005-2006 HPA team, which proposed that the model could validate the flight stability and control response of the aircraft. In the 2005-2006 final report, it was noted that the quarter-scale model could provide drag data, L/D estimates, and validation of control response. When flight-testing began under the guidance of the 2006-2007 HPA team, the primary focus was evaluation of the model's control response. The highest priority was thus evaluation of the model's ability to make a controlled, full 360° turn. Implicit in this was validation of the lateral and directional control response to aileron and rudder inputs and any inherent coupling between the two. In addition, flight-tests were planned in which L/D estimates could be determined based on glide slope estimates extracted from flight video and photos. However, the drag of the model was considered unrepresentative of the final aircraft due to the presence of the guy wires, absence of a fuselage pod, and other small protrusions from the fuselage. Thus, no drag estimates were made.

Pending modifications and improvements to the model after the April 30, 2006 flight attempts, the first flight-tests conducted by the 2006-2007 HPA team took place on October 3, 2006. These modifications and improvements include:

- The wing gap was reduced from 2.09 ft to 1.29 ft
- The tapered fuselage carbon tube was replaced with a larger, constant-diameter carbon tube to reduce flexibility
- The pull-pull wires controlling the rudder were replaced with a push-rod to reduce the amount of play in the system and establish reliable rudder control
- The motor was mounted such that the thrust line ran through the center of the wing gap (the optimum CG location)

Initial flight-tests were performed on October 3, 2006 at 8:30 am. Prior to flying, the model was weighed at 54 oz and balanced such that the CG was located at 40% MAC and 3.5 in down from the top wing. During the five flight attempts, the model was unable to demonstrate flight in either glide or powered conditions. When powered, the aircraft exhibited a strong pitch-up moment during launch, which resulted in an immediate stall. No amount of down trim on the elevator could correct the pitch problem. It was determined that the location of the thrust line relative to the vertical CG location was the primary cause of the pitch moment and required that the CG be lowered and the thrust line be corrected such that it ran through the actual CG location rather than the design CG location. This repair was made prior to the second set of test flights. In addition, the tail surfaces were realigned to the vertical and horizontal planes and guy wires were added.

The second set of tests flights took place on October 26, 2006. The flight plan included a straight-and-level glide test, a powered straight-and-level flight-test, and a powered flight with a controlled turn. The glide test was unsuccessful and resulted in only minor damage. The first powered test exhibited true controlled flight lasting 17 s at full throttle (41 W). Next, the aircraft successfully performed a coordinated, right turn using primarily rudder with only slight aileron input. The total flight time was 26 s. A fourth flight-test was performed in which another coordinated turn was attempted but at only approximately 75% throttle (27 W). Upon entering the turn at the lower throttle setting, the inner wing stalled almost immediately and the aircraft subsequently crashed. As a result, it was apparent that the power required during turns was higher than originally thought. At the field, the electric power ranged from 27 W to 41 W.

As indicated by previous analysis of the model, the required power was 3.8 W. It should be noted that this figure was meant to be indicative of the total propulsive system; however, this power output is difficult to measure during flight-tests. All power levels measured at the field were representative of only the battery power. If the total propulsive efficiency was taken into account, the power required by the aircraft would generally be less than the power measured at the battery. For example, the 41 W of full throttle would translate into only about 10 W of power required by the aircraft. Because the aircraft could not fly with much less than the power available at full throttle, this validated the previously mentioned analysis.

The third set of flight-tests occurred on November 9, 2006, and consisted of two glide tests and a short powered flight. The two glide tests were reattempted such that the model was launched at full throttle, which would later be reduced to zero power when the aircraft exhibited stable, wings-level flight. During both flights, the aircraft stalled and crashed before attaining stable flight; thus, no useful data was extracted. A third test flight was attempted in hopes of performing a powered, controlled turn, but the aircraft crashed due to stall after only a brief flight. The stall occurred primarily due to the aircraft porpoising because of inadequate elevator control. It was determined that the resistance in the elevator servo horn connection was preventing the surface from rotating freely with each servo arm movement, thus resulting in unwanted and inaccurate elevator deflections for given stick inputs. This problem and minor damages were addressed prior to the next set of test flights.

Tests continued on November 14, 2006, on which five flight-tests were conducted. Again, a glide test was attempted with a powered launch but soon made a forced landing due to an onset of flutter on the empennage. It was determined that the flutter was most likely caused by a combination of propeller downwash flow and play in the rudder connection. The rudder connection was subsequently tightened.

Four separate attempts were then made to perform a controlled 360° turn. The first of these flights ended abruptly when the aircraft hit a telephone pole shortly after takeoff. As discussed in Section 4.3, the recommended turn radii were calculated based on varying bank angles, which, in turn, are achieved with varying rudder and aileron input. Thus, in subsequent tests, the amount of rudder and aileron deflection used to induce a turn was varied to qualitatively validate these calculated trends. Of the subsequent three flights made, all resulted in controlled turns with varying rudder and aileron input. While the turn radii could not be directly measured, it was evident that the radii used for yaw-only turns dramatically increased from the radii needed when the ailerons were used to induce small bank angles (less than 15°). In addition, successful turns were made using the ailerons without any rudder input. This exceeded performance expectations for the model as the ailerons were not expected to induce a significant roll moment by themselves due to roll damping.

The most recent test flights of the model took place on November 28, 2006, and consisted of two flights. In the first flight, the aircraft performed a full 360° all-aileron turn. In the second, the aircraft was unresponsive to control input roughly ten seconds after takeoff, banked left, and crashed. It was hypothesized that a gust of wind rendered the control surfaces unresponsive, induced stall on the left wing, and caused the aircraft to crash.

4.8. Model Development Summary

In summary, testing of the quarter-scale model proved that a controlled turn performed by an aircraft of the current design is possible, though highly dependent on the power provided by the motor. However, it is of note that the turns may be induced and possibly fully sustained through use of the ailerons as the primary control mechanism.

5. Prototype Development

5.1. Gantt Chart

The Gantt chart in figure 5.1-1 shows the tasks that have been completed in the first half of the spring semester along with the tasks that must be completed during the second half in order to finish the prototype. This is a strenuous schedule to follow but the team feels that it will be worthwhile to complete the prototype for the next year's team. In the first half, methods were created for building the significant parts of the airplane. The next half of the semester will consist of using those methods to construct the fully working prototype.

ID	Task Name	Start	Finish	Duration
1	Rib Testing	1/16/2007	3/14/2007	42d
2	Chemical Etching Testing	1/16/2007	3/14/2007	42d
3	Dura-Lar Testing	2/26/2007	2/28/2007	3d
4	Midterm Design Review	2/27/2007	3/1/2007	3d
5	Majority Material Acquisition	3/1/2007	3/14/2007	10d
6	Spring Break	3/2/2007	3/12/2007	7d
7	Spar Location Testing	3/12/2007	3/16/2007	5d
8	Midterm Report	3/13/2007	3/16/2007	4d
9	Aileron Test Section	3/13/2007	3/16/2007	4d
10	Chemical Etching	3/16/2007	4/2/2007	12d
11	Rib Cutting	3/16/2007	5/1/2007	33d
12	Right Top Outer Wing	4/2/2007	4/18/2007	13d
13	Propeller Design	4/2/2007	4/10/2007	7d
14	Final Report Draft	4/9/2007	4/12/2007	4d
15	Propeller Construction	4/12/2007	4/24/2007	9d
16	AIAA Regional Conference	4/13/2007	4/17/2007	3d
17	Advisory Board Presentation	4/19/2007	4/19/2007	1d
18	Top Left Outer Wing	4/18/2007	4/25/2007	6d
19	Final Presentation	4/24/2007	5/3/2007	8d
20	Final Report	4/24/2007	5/3/2007	8d
21	Top Middle Wing	4/25/2007	4/30/2007	4d
22	Bottom Middle Wing	4/30/2007	5/3/2007	4d
23	Tail Boom	4/30/2007	5/10/2007	9d
24	Bottom Left Outer Wing	5/4/2007	5/11/2007	6d
25	Tail (Vertical/ Horizontal)	5/7/2007	5/10/2007	4d
26	Graduation	5/14/2007	5/14/2007	1d

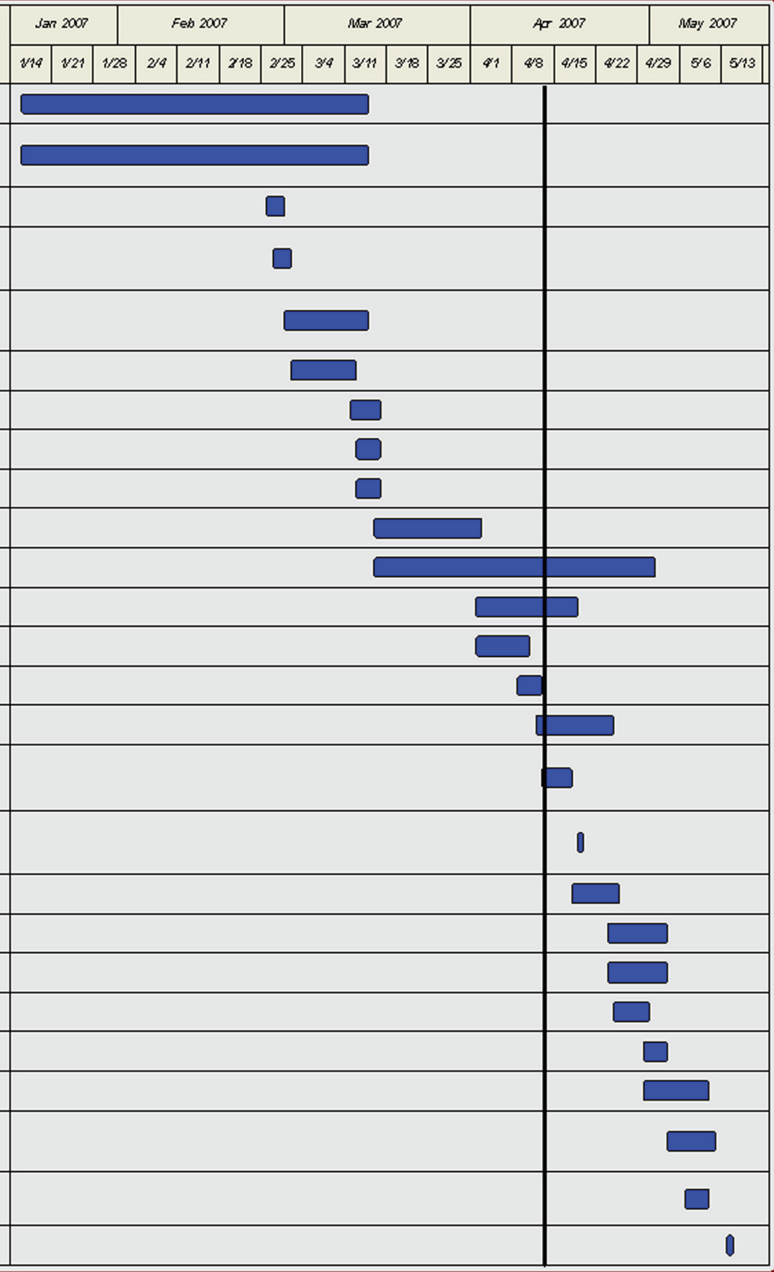

Figure 5.1-1. Gantt chart illustrating accomplishments and future plans for the prototype

5.2. Aerodynamics

5.2.1. Lift to Drag Ratio Analysis

To gain a better understanding of how the wing of the aircraft should perform, an analysis of the lift to drag ratio was performed using AVL software [3]. Lift and drag coefficients were calculated for a range of angles of attack to determine the maximum lift-to-drag ratio, and the results were plotted in figure 5.2.1-2. As can be seen in the table A-2 in appendix A, the useful range of angle of attack for the current design ends at approximately seven degrees. A 15% stall margin on $C_{L,max}$ was employed for these calculations. Based on these calculations, the maximum lift-to-drag ratio of 29.98 occurs at an angle of attack near 6°.

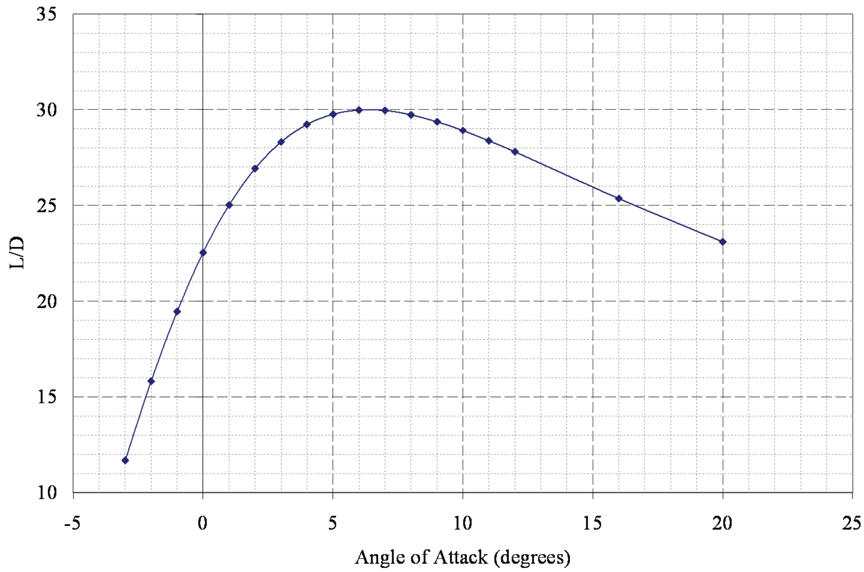

Figure 5.2.1-2. Effect of angle of attack on lift over drag

5.2.2. Take-off Speed

To further enhance the understanding of the performance of the aircraft design, a takeoff speed calculation was done. A value of 1.5 for the maximum lift coefficient was previously obtained using a 15% stall margin. Using this value, other parameters from the aircraft's design, and atmospheric conditions, the stall speed can be calculated as shown below [13]:

$$V_{\text{stall}} = \sqrt{\frac{2 \cdot W}{\rho_\infty \cdot S \cdot C_{L,\max}}} \quad \textbf{(5.2.2-1)}$$

From this stall speed, it is generally accepted that the takeoff speed would be somewhat higher than the stall speed, so the equation below is used to calculate the takeoff speed [13]:

$$V_{\text{TO}} = 1.2 \cdot V_{\text{stall}} \quad \textbf{(5.2.2-2)}$$

After performing these calculations for a wing surface area of 180 ft2, aircraft weight of 215 lb and a density of 0.002377 slugs/ft^3, a stall speed of 17.65 mph was obtained. For this stall speed, the takeoff speed of the aircraft was calculated as 21.18 mph. This takeoff speed is close to the original design cruise speed of 22.5 mph. The design cruise speed has since been increased due to a previous calculation error and is now 24.5 mph, which gives a significantly wider range of operation from the takeoff speed.

5.2.3. Cockpit Airfoil

To minimize the total drag on the aircraft, an aerodynamic cowling must be chosen for the cockpit. The cowling shape must fit two basic constraints of drag minimization and fitting a human body inside in a semi-recumbent position. To shape the cowling a series of airfoils would be considered. An appropriate design would take into account the length and width of each individual airfoil in the series that would comprise the cowling as it pertains to the two constraints mentioned above. For example, the shape of the human body inside the cowling would effect the maximum width and its position along the airfoils chord. The characteristics of the three most promising airfoil configurations are displayed in table 5.2.3-1. The decision was made to use the Van de Vooren airfoil with a 17 percent thickness and a 44° trailing edge. The reason for this decision was to make a compromise between the chord length and thickness and the drag that each would add. The final airfoil shape is shown in figure 5.2.3-1.

Table 5.2.3-1. Airfoil comparison chart.

Re = 1.68e6 Density = 1.55 kg/m^3 D = 8 ft viscosity = 0.0183 C_p V = 24.5 mph M = 0.0321				
Airfoil	**C_d**	**Chord [ft]**	**S [ft^2] (5 ft Gap)**	**Drag [lb]**
Van de Vooren 17%t 44deg trailing (created in javafoil)	0.0058	8.349	41.744	0.360
NPL EQH series 16%thick at 38%chord	0.00451	10.297	51.487	0.346
Van de Vooren 15%t 50deg trailing	0.00669	7.603	38.014	0.379

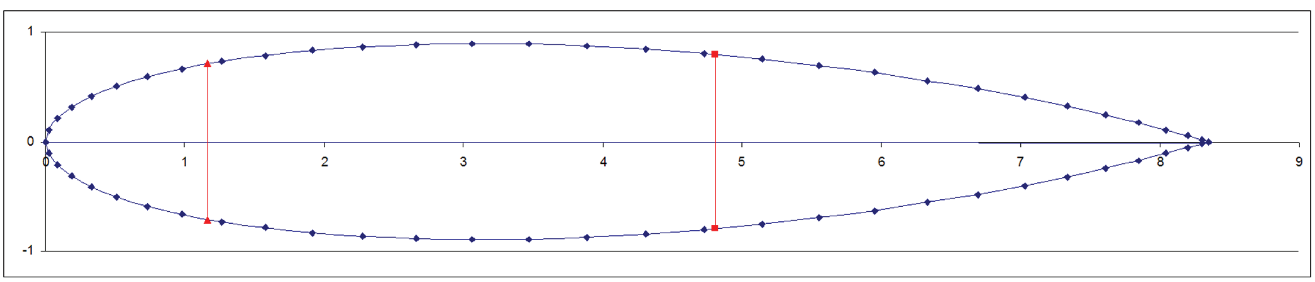

Figure 5.2.3-1. Van de Vooren 17% thickness, 44° trailing edge angle

5.2.4. Cockpit Drag and Sideslip Angle

Drag was a basic consideration of cockpit cowling design. Further consideration was given to how sideslip angle would affect cockpit drag. Analysis was done to determine the increase in power required because of the sideslip induced extra drag. Figure 5.2.4-1 shows the relationship between the power required and the sideslip angle of the aircraft. The red line is meant to be a reference to the power required of the aircraft at no sideslip to show the difference between this and an aircraft in a sideslipped condition as displayed in the blue curve. The drag on the cockpit in a sideslip condition could cause problems for the final competition aircraft when flying a triangular course with relatively high winds requiring crabbing into the wind.

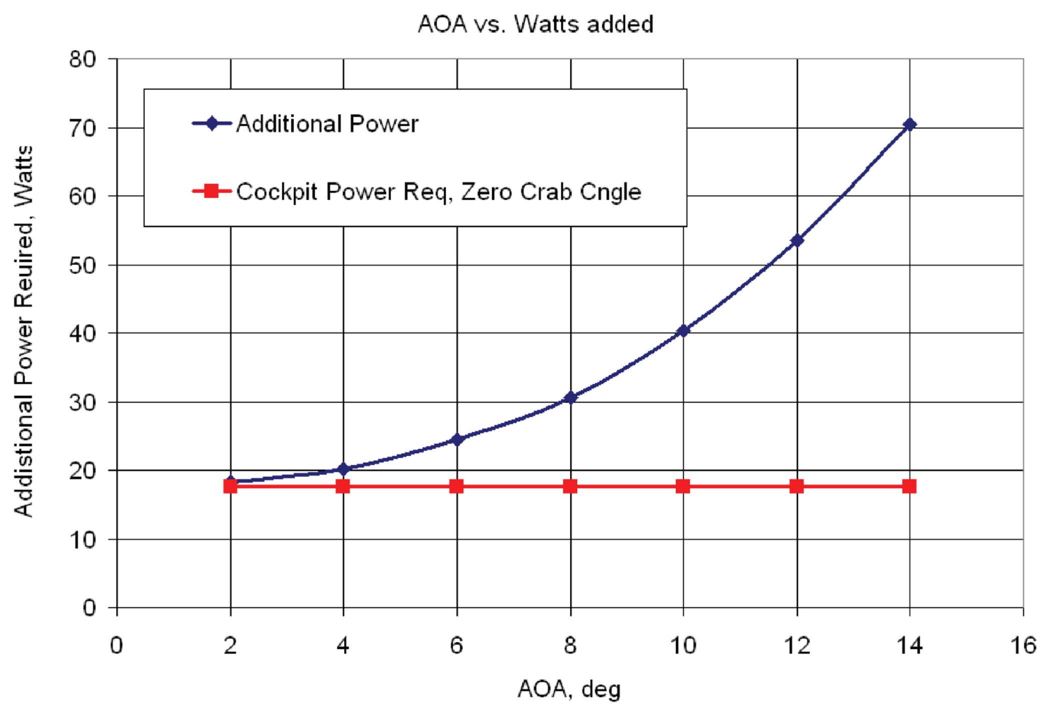

Figure 5.2.4-1. Sideslip angle vs additional watts required.

5.2.5. Cockpit Tapering

to be completed later

5.2.6. Wingtip stall

In analysis of the mission model, it was determined that in a 150 ft. radius turn the airflow over the inner wing tip would only be 29 ft/s compared to 35.9 ft/s at cruise. For this reason, it was considered necessary to ensure that the inner wingtip would not experience stall condition during the turn. Based on the lift distribution from AVL the C_L required at the tip was 0.71 and did not exceed the C_{Lmax} of the airfoil and therefore does not stall.

5.2.7. Lift Distribution

The lift distribution shown in figure 5.2.7-1 was used in the spar design analysis. This lift was calculated for cruise speed of 24.5 mph at cruise angle of attack.

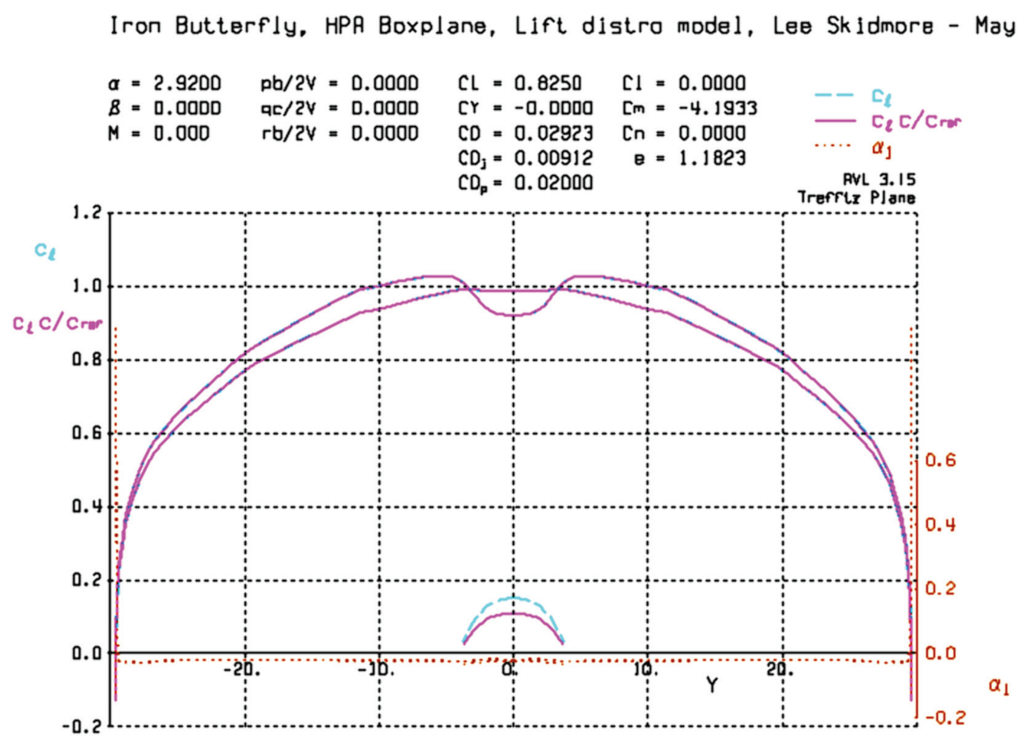

Figure 5.2.7-1. AVL lift distribution at 2.92° angle of attack.

5.2.8. Landing Sink Rate

The sink-rate for a full gliding landing was calculated in order to determine the landing load placed on other aircraft components, specifically the wings. Based on a glide ratio of 20 and cruise speed of 24.5 mph a full glide landing will have sink rate of 1.22 mph at a 2.86° angle glide slope.

5.2.9. Spar Placement

The aerodynamic center was determined to be nearly 23 percent chord for the airfoils employed in the design, however, because of size limitations the spar was positioned at 25 percent chord. In the first wind tunnel test, a strong negative pitching moment was observed on the wing and was verified in Xfoil. Further analysis in Xfoil revealed that a better placement for the spar was at 35.6 percent chord because there is a zero pitching moment for cruise conditions at this point. Furthermore, the strongest pitching moment noticed within the flight envelope is less than the constant pitching moment observed at the aerodynamic center. This pitching moment range was compared to both Daedalus and to Musculair and Iron Butterfly's pitching moment falls just in between these two successful human powered aircraft.

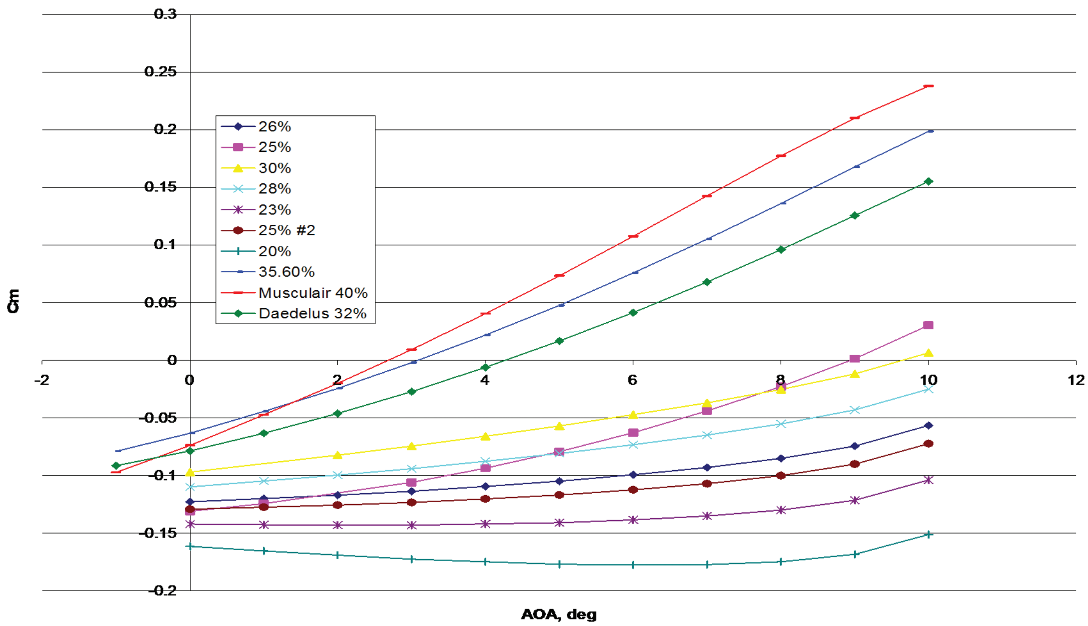

Figure 5.2.9-1. Spar Placement.

5.2.10. Sensitivity of Power Required to C_{D0}

The highest uncertainty in the design of Iron Butterfly is the power required, mostly due to the parasitic drag term, C_{D0}. Parasitic drag is very difficult to estimate for a complete aircraft. In addition, the drag is affected by the smoothness of the DuraLar® skin covering. If the covering is not taut without creases or ripples, then the drag will increase. Figure 5.2.10-1 shows the power required for a range of realistic parasitic drag coefficients. The blue horizontal line on the graph represents the maximum power that can be output by a human for 3.5 to 4 min. This line gives an upper bound on the C_{D0} of the aircraft, approximately 0.02. The blue vertical line is the C_{D0} value determined by the 2005-2006 team. The green vertical line is the updated C_{D0} value obtained from work that was performed in the Fall 2006. Finally, the vertical red line is the C_{D0} value that was obtained from the fuselage drag being added to the previous drag analysis. As more parts of the aircraft are finalized and corresponding C_{D0} values are found, the margin of power required verses power available keeps decreasing. So far, the power required is still in the region which can be delivered by the pilot; however, it could grow prohibitively large. If the covering is not taut and smooth and if all intersections of aircraft parts are not properly faired, the drag could be too great to fly the aircraft for the required amount of time.

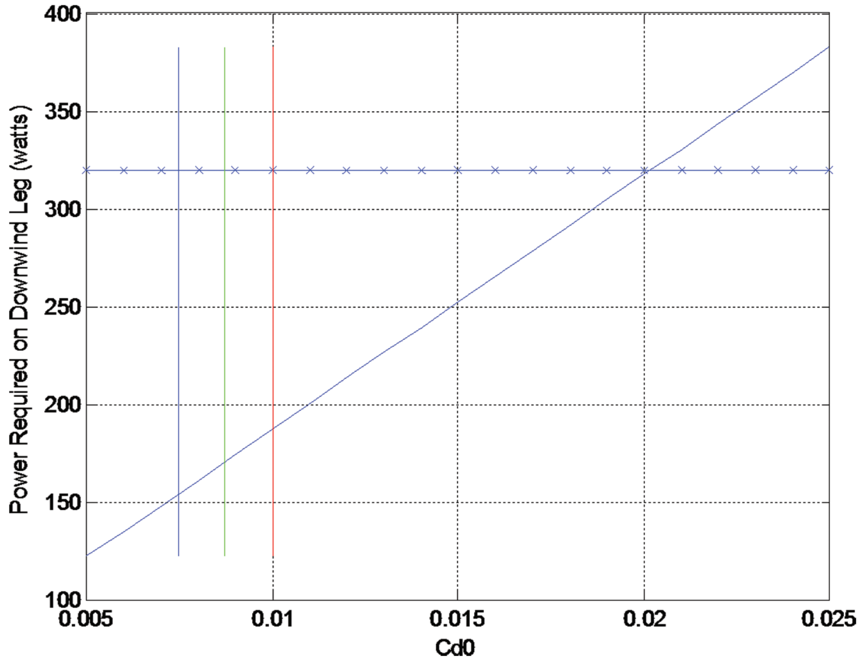

Figure 5.2.10-1. Power Required versus C_{D0}.

5.3. Stability and Control

5.3.1. Tail Design Method

The vertical tail geometry defined in the first year of the project was designed based on the vertical tail volume coefficient Vv, that the team had chosen to be 0.05, and Roskam's tail area equation (Eq. 1). In addition a rotation angle of 8° was set as a constraint by the 2005-2006 team to prevent a tail strike from occurring during takeoff. Based on the geometry of the aircraft the bottom of the tail surface would have to be constrained to be 2.14 ft or less below the tail boom.

$$S_{\text{vt}} = \frac{S_{\text{wing}} \cdot b_{\text{wing}} \cdot V_v}{L_{\text{bom}}} \tag{5.3.1-1}$$

The 2005-2006 team also decided that because of the asymmetry of the tail about the tail boom and the limited time available the tail area was divided so that ¼ of the total area was located below the tail boom with the remaining ¾ of the area located above. Taper ratios were added, producing the tail as seen in figure 5.3.1-1, which had an overall aspect ratio of 5.6.

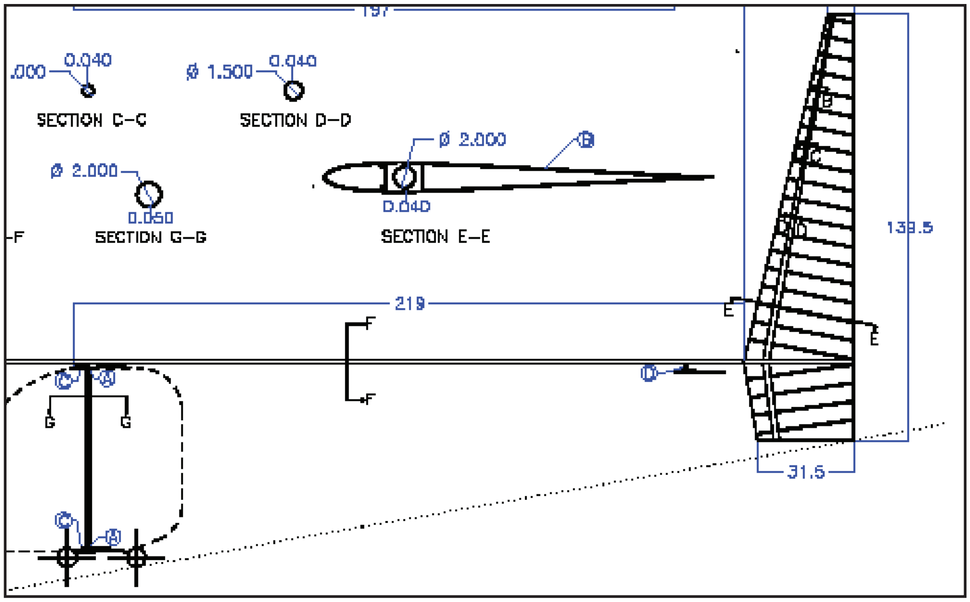

Figure 5.3.1-1. Vertical tail as of May 2006

Because so much of the tail area lies far above the tail boom, and thus far above the CG of the aircraft, any rudder movement creates an additional rolling moment opposite the direction in which the aircraft is attempting to turn. This moment, depending on the total tail area and the length of the tail boom, can be in excess of 40 ft-lb. The primary goal of the design of the vertical tail was to minimize this rolling moment by placing as little tail area as possible above the tail boom while keeping the boom length and total tail surface area low. This design would save weight, minimize drag, and create a robust surface that would be easy to manufacture.

Initially, a MATLAB code was written that varied tail boom lengths and used equation 5.3.1-1 to minimize the offset of the center of the vertical tail span about the tail boom. This code was written assuming a fuselage height of 6.2 ft at the wing quarter-chord (includes cockpit and landing gear) and using the 8° minimum rotation or "flare" angle. The code was run at 14 aspect ratios ranging from 1 to 8. The output of the code can be seen in figure 5.3.1-2.

The output showed that, for a single aspect ratio, the minimum point is the lowest tail offset possible for a given aspect ratio. This point occurs at a single tail boom length. These curves effectively gave the team 15 different tails with varying aspect ratios whose geometries have been optimized in terms of tail boom length and amount of area offset below the tail boom. These 15 vertical tail charateristics are shown in table 5.3.1-1.

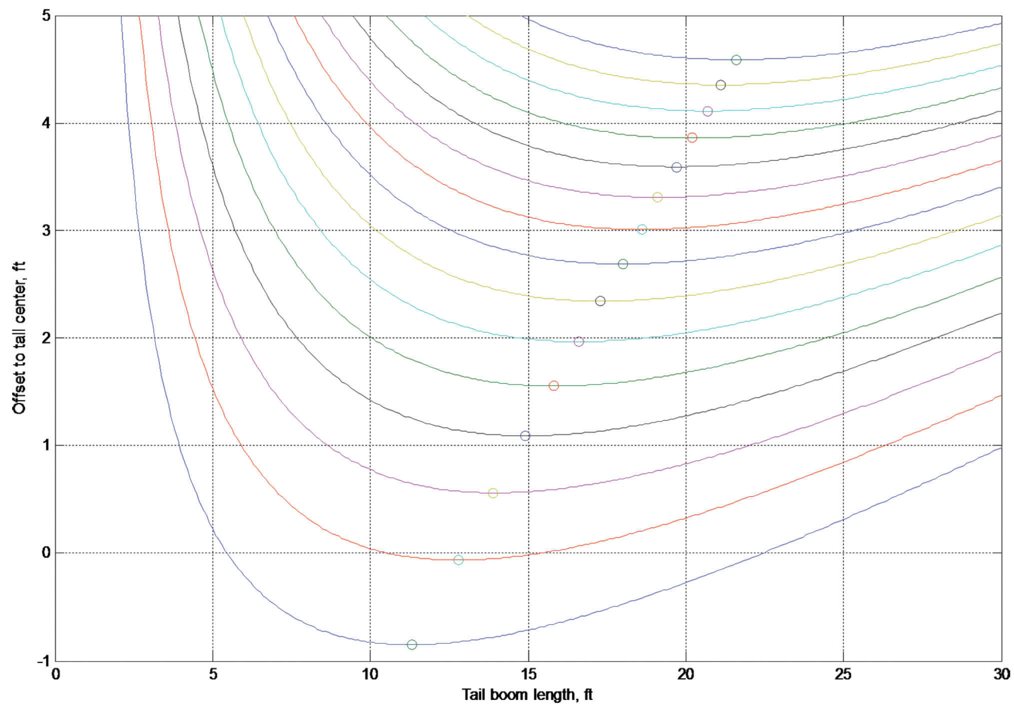

Figure 5.3.1-2. Tail boom length versus offset of tail center at multiple aspect ratios (the bottom blue line represents an aspect ratio of 1 and increases upward to an aspect ratio of 8 while the minimum points are delineated with circles)

Table 5.3.1-1. 15 Tails optimized for minimum offset at varying tail boom lengths and aspect ratios.

Aspect Ratio	Area [ft^2]	Chord [ft]	Span [ft]	Offset [ft]	Span Below Boom [ft]	Boom Length [ft]
1.00	52.43	7.24	7.24	-0.85	4.47	11.3
1.50	45.76	5.52	8.29	-0.06	4.21	12.8
2.00	41.86	4.58	9.15	0.56	4.01	13.9
2.50	38.85	3.94	9.86	1.09	3.84	14.9
3.00	36.49	3.49	10.46	1.55	3.68	15.8
3.50	34.62	3.14	11.01	1.97	3.54	16.6
4.00	33.13	2.88	11.51	2.34	3.41	17.3
4.50	31.77	2.66	11.96	2.69	3.29	18
5.00	30.68	2.48	12.39	3.01	3.18	18.6
5.50	29.83	2.33	12.81	3.31	3.10	19.1
6.00	28.88	2.19	13.16	3.59	2.99	19.7
6.50	28.13	2.08	13.52	3.86	2.90	20.2
7.00	27.41	1.98	13.85	4.11	2.81	20.7
7.50	26.87	1.89	14.20	4.35	2.74	21.1
8.00	26.21	1.81	14.481	4.58	2.66	21.6

Given these 15 options, each with pre-defined dimensions, the team analyzed the choices in AVL to determine the rolling moment and hinge moment in yaw in a 5° and 10° sideslip condition. This is where an effort to optimize for control was attempted. A small rolling moment was desirable, if not a slight moment in a direct proverse to the yawing direction during a turn (which would require a majority of the tail area be located below the aircraft CG). In addition, the yaw hinge moment needed to be minimized to reduce the force on the actual hinge and to minimize the stick force needed to actuate the rudder.

The dynamic response of each surface was also evaluated in terms of the transient response of the aircraft in a 10° sideslip condition. Given that each turn was estimated to take roughly 8 seconds, this span of time on the transient response curve was considered to be the most important. The curve is not completely representative of the actual response of the aircraft in that the only factor that was changed in each case was the yaw damping coefficient, $C_{n\beta}$. All other factors remained the same. The response curve is shown in figure 5.3.1-3, in which each curve is plotted at a $C_{n\beta}$ of either 0.12, 0.15, or 0.19. A comparator aircraft, Musculair II, reported a $C_{n\beta}$ value of 0.15. This was used as an initial, "ballpark" target. The graph showed that higher roll acceleration was achieved with a lower $C_{n\beta}$ as long as the sideslip condition lasted no longer than roughly 10 seconds. Because of the estimated turn duration of 8 seconds, it was determined that a lower $C_{n\beta}$ was desired.

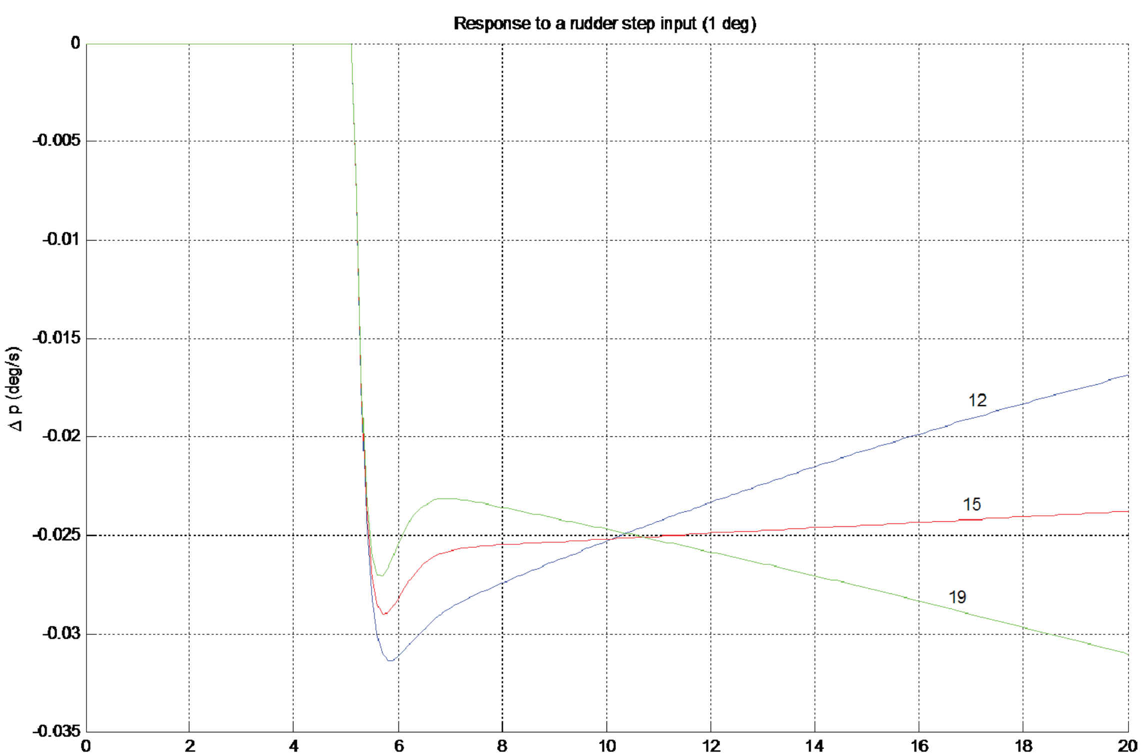

Figure 5.3.1-3. Transient Response of Tail Surface at three values of $C_{n\beta}$.

An additional consideration was the induced drag (drag induced by lift) produced by each surface. Induced drag is calculated using equation 5.3.1-2 in which C_L is the lift coefficient, AR is the aspect ratio of the surface planform, and e is Oswald's efficiency factor. Because the induced drag is inversely dependent on the aspect ratio and due to time constraints, the team sought only to evaluate the tail geometries based on their aspect ratios rather than their calculated induced drag. Thus, surfaces with higher aspect ratios, all other conditions being equal, would produce low induced drags than surfaces with lower aspect ratios.

$$C_{\mathrm{di}} = \frac{C_L^2}{\pi \cdot e \cdot A\,R} \tag{5.3.1-2}$$

In order to take structural efficiency into account, a structural efficiency factor was assigned to each surface. The equation for this is shown in equation 5.3.1-3, in which l_{above} is the span of the tail above the boom and l_{below} is the span of the tail below the boom. The values 0.7 and 0.3 were assigned based on the fact that surfaces with longer wingspans are more susceptible to structural deformation and, while excessively large chords are open to deformation, generally longer spans are more of a concern.

$$n_{\mathrm{struct}} = \frac{0.7}{l_{\mathrm{above}}} + \frac{0.3}{l_{\mathrm{below}}} \tag{5.3.1-3}$$

Lastly, a manufacturability factor was assigned to each surface, based on equation 5.3.1-4.

$$n_{\mathrm{man}} = 0.7\,\frac{c_{\mathrm{min}}}{c} + 0.3\,\frac{b_{\mathrm{min}}}{b} \tag{5.3.1-4}$$

In the manufacturability equation, c represents the chord of the tail in question while c_{min} is assigned the smallest chord length out of the 15 tails being examined, in this case 1.8 ft. This concept applies in the same way to span, b, in which b_{min} is 7.2 ft. Here, it was assumed that surfaces with larger chords are more difficult to manufacture than those with longer spans because, in general, increasing spar length is easier than increasing rib length. If a span needs to be lengthened, a longer spar and more ribs are used. If the chord needs to be lengthened, there is a point at which secondary structure, an aft spar for example, becomes necessary.

Finally, all of these factors were assembled in a comparative matrix so that the performance of each surface could easily be evaluated relative to the other surfaces. In addition, the 15 original tail geometries had been narrowed down to a more viable 9 geometries. Based on the observation that the optimum for each category occurred at either the very lowest aspect ratio or the very highest aspect ratio, a compromise between these two extremes was sought. Given that the roll moment during sideslip for each surface was negative and that the margin between them was small, this did not factor as importantly as the aspect ratio and weight, for example. Ultimately, the 3.5 AR geometry was chosen as the best compromise between the seven categories.

Table 5.3.1-2. Tail Geometry Comparative Matrix

AR	Weight	Roll Moment [ft-lb]	Yaw Moment [ft-lb]	Structural Efficiency	Manufacturability	C_{n_beta}
2.0	6.98	-10.18	4.50	0.21	0.51	0.120
2.5	7.30	-10.46	5.16	0.19	0.54	0.135
3.0	7.61	-10.69	5.69	0.18	0.57	0.149
3.5	7.88	-10.90	6.13	0.18	0.60	0.160
4.0	8.13	-11.09	6.49	0.17	0.63	0.170
4.5	8.38	-11.24	6.79	0.17	0.66	0.178
5.0	8.59	-11.39	7.05	0.17	0.69	0.185
5.5	8.78	-11.53	7.28	0.17	0.71	0.191
6.0	9.00	-11.72	7.48	0.17	0.74	0.196

At this point, a leading and trailing edge taper ratio of 2.5 was used to approximate constant downwash along the span and for structural efficiency. The leading and trailing edges were tapered such that the spar remained at a constant ¼ chord location along the span for ease of manufacturing and construction. The surface is shown below in figure 5.3.1-4.

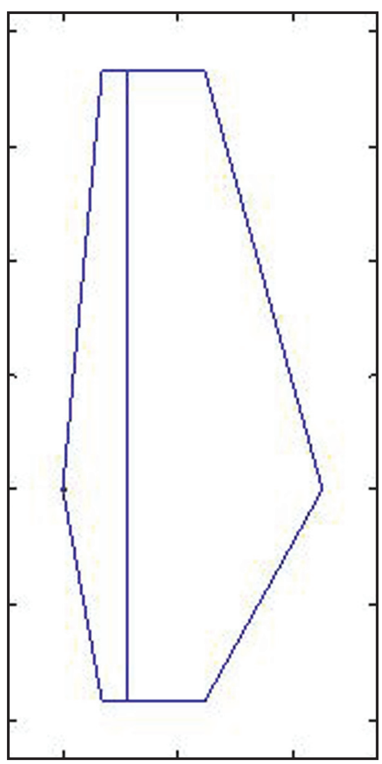

Figure 5.3.1-4. Vertical Tail (Leading Edge left).

Because the design of the horizontal tail was less critical than the vertical tail, the tail boom length was already defined during the design of the vertical surface. Roskam's equation provided a horizontal tail area of 9.5 ft^2. Three different aspect ratios, 9.5, 6.98, and 5.34, were evaluated in terms of induced drag and estimated weight. As was the case with the vertical surface, a compromise between the highest aspect ratio and lowest weight surfaces was chosen considering that the margin between the two highest aspect ratios is smaller than that between the two lowest while the margin between the two lowest weights is smaller than that between the two highest. The horizontal surface comparative matrix is shown in table 5.3.1-3. Therefore, the 6.98 aspect ratio surface was chosen. In addition, a leading and trailing edge taper identical to the vertical tail were used. This finalized surface is shown in figure 5.3.1-5.

Table 5.3.1-3. Comparative Matrix for Horizontal Surface

Chord [ft]	AR	Weight [lb]
12	9.50	8.26
14	6.98	7.22
16	5.34	6.43

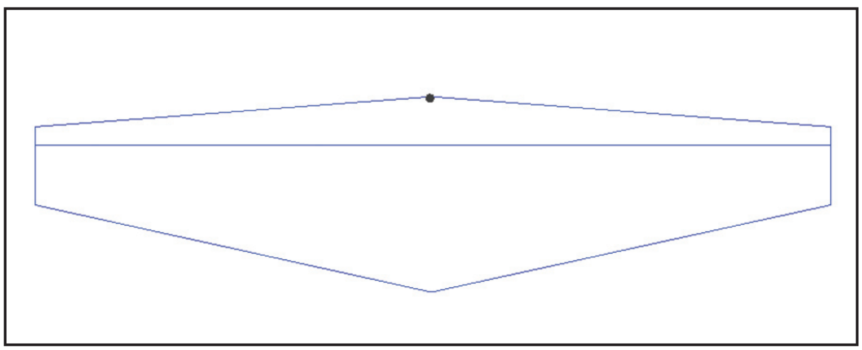

Figure 5.3.1-5. Horizontal Tail (Leading Edge top).

Looking ahead, the construction method for both surfaces is need of finalization, though the team is currently expecting to use a method similar to that of the main wing. This would include foam ribs, balsa or foam leading and trailing edge stock, and Dura-lar® skin. The spar for both surfaces will most likely be a unidirectional carbon tube of roughly 0.5 to 0.75 in. diameter. The design of the hinge used to attach both surfaces to the tail boom is in need of completion, though the team plans to use an external hinge that will be manufactured such that each surface does not rotate about its own spar. Testing is currently underway for both the hinge and surface construction method.

5.4. Structures

5.4.1. Mass Analysis

Careful mass allowance to various parts of the final design is considered extremely important. In order to ensure that each component is designed and built so that the total aircraft does not exceed weight limits, a strict mass allowance guide must be designed and followed. The previous HPAG team made a rough estimate for this purpose. This original allowance is shown in table 5.4.1-1. An ongoing analysis is being conducted to further extend this mass allowance guide to a more detailed level. In the future, this analysis will be used to guide material selection and construction of the full-scale aircraft. In addition, it will be continually studied for various ways of optimizing the weight allocation and reducing the total weight of the final aircraft.

Table 5.4.1-1. Original mass allowance [4].

Component	Weight (lb)
Wing Spars and Struts	25.30
Tail boom	21.70
Rudder Spar	1.6
Elevator Spar	0.80
Wing Ribs/Secondary Structure	1.56
Tail Secondary Structure	0.50
Fuselage Frame	5.00
Covering	2.00
Prop	2.00
Drive Train	3.13
Miscellaneous Hardware	5.00
Pilot	148.00
Total	215.00

First, a more detailed material list was constructed. This list mostly focuses on wing structures for two reasons. One, this structure is farthest along in the design phase and two, it will probably be the most time consuming to construct and therefore must be started before other parts of the aircraft. This material list is provided in table 5.4.1-2. This material list will be continually updated as part of the effort to optimize the materials and construction method used to create this aircraft.

Table 5.4.1-2. Current detailed material list [2, 5, 6, 10].

Part	Material	Density [lb/in^3]
Spar	6061-T6 Aluminum	0.098
	Carbon Fiber	0.054
Ribs	Styrofoam	0.001319
	Balsa	0.0056
Skin	**Material**	**Area Density [lb/in^2]**
	Monokote® (clear)	0.000091875
	Mylar©	0.000100434
	Micafilm (clear)	0.000034375
	Ultracote	0.0000575

Several observations can be made from this list. Corrugated paper was added to the list without a known density. This material was used in previous HPAs for leading edge definition; however, there is not much public material information on this product [7]. Four types of skin material were analyzed. All of them have different pros and cons in areas of material mass (per unit area), strength, price, and availability. Most of these factors will need to be examined in later analyses but from this table it can be determined that Ultracote, an alternative to Monokote®, provides the lightest material to act as skin for the wing.

These materials were then used in an analysis of various material scenarios to try to verify the original mass allowance. During analysis of the total wing structure, for example, the weight needed was found to be 28.86 lb; this is approximately the original weight allotment. This analysis is an ongoing effort. The purpose of this optimization will be to try to reduce the total material needed, and thus the weight of the aircraft.

5.4.2. Wing Spar Preliminary Analysis

There were several simulations used to test the validity of different wing spar structures. The first set of analyses were conducted to determine the best material to use for the wing spar. The two most applicable materials were aluminum and carbon fiber due to their high strength to weight ratio. Sample cross sections were taken for tubes made from each material and then analyzed in ANSYS to determine how much the wings would deflect under an elliptical load distribution [1]. Table 5.4.2-1 summarizes the physical characteristics used in the analysis.

Table 5.4.2-1. Material Property Summary.

Material	Aluminum [Al 6061-T6]	Carbon Fiber [Roll Wrapped Rod]
Modulus of Elasticity [psi]	10e6	14.8e6
Poisson's Ratio	0.3	0.3
Density [lb/in^3]	0.098	0.054

Modeling of the prototype wing structures was performed using ANSYS Classic 10.0 to verify the results found by the previous year's team and to further optimize the wing for this year [1]. The cross sections tested are listed in table 5.4.2-2. The previous year's team described the aluminum tube dimensions used [4]. Figure 5.4.2-1 shows a sample output of from ANSYS with the deformed wing structure and the maximum deflection.

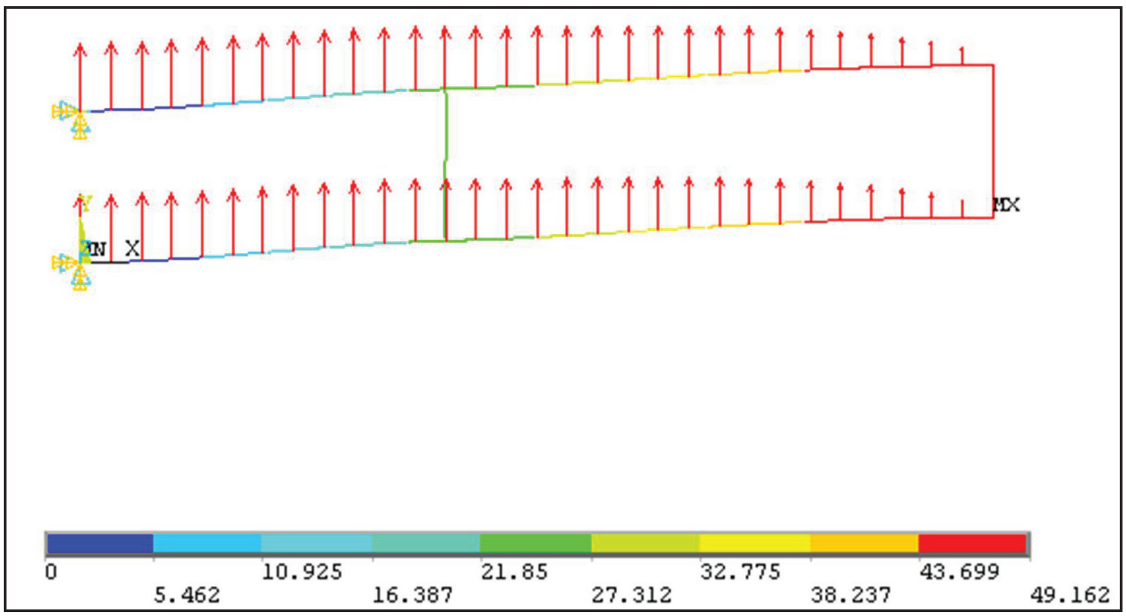

Figure 5.4.2-1. ANSYS deflection model of the wing structure showing elliptical load distribution.

The tip deflections for each material and tube cross section are summarized in table 5.4.2-2. From the deflections, it was determined that a carbon tube of reasonable weight would not have a small enough deflection to serve for the wing spar. The spar size with the least deflection was the aluminum tube with the two inch outer diameter; however, it was also the heaviest spar.

Table 5.4.2-2. Tube Cross Section Properties

Sect.	Mat.	OD [in]	ID [in]	Area [in^2]	Iyy, Izz [in^4]	Weight [lb]*	Tip Deflection [in]**
1	Alum	2.000	1.960	0.1244	0.0609	17.56	49.162
2	Alum	1.500	1.460	0.0929	0.0254	13.12	117.48
3	Carbon	0.715	0.625	0.0947	0.0053	13.37	337.94
* Total weight of spar structure (60 ft. span biplane: 120 ft. total)							
** Distributed load applied at 30 points along upper wing structure							

In determining which spar size would be desirable, there were many factors to consider such as tip deflection and weight. Of the spars analyzed, the most reasonable spar had an outer diameter of 2 in and an inner diameter of 1.96 in. However, constructed in this manner the spar would be extremely susceptible to buckling because of the thinness of the wall. In addition, the etching process used to manufacture the required wall thickness increased the chance that the material would contain defects. The least amount of etching required was considered to be optimal.

5.4.3. Final Spar Analysis

The final spar analysis was performed using a method similar to the preliminary analysis except the lift distribution was not assumed to be elliptical and the spars could be different sizes along the span. The lift distribution was derived directly from the lift coefficients from AVL. Figure 5.4.3-1 shows the spanwise lift coefficients created by the wing when the angle is at an angle of attack of 4.0°.

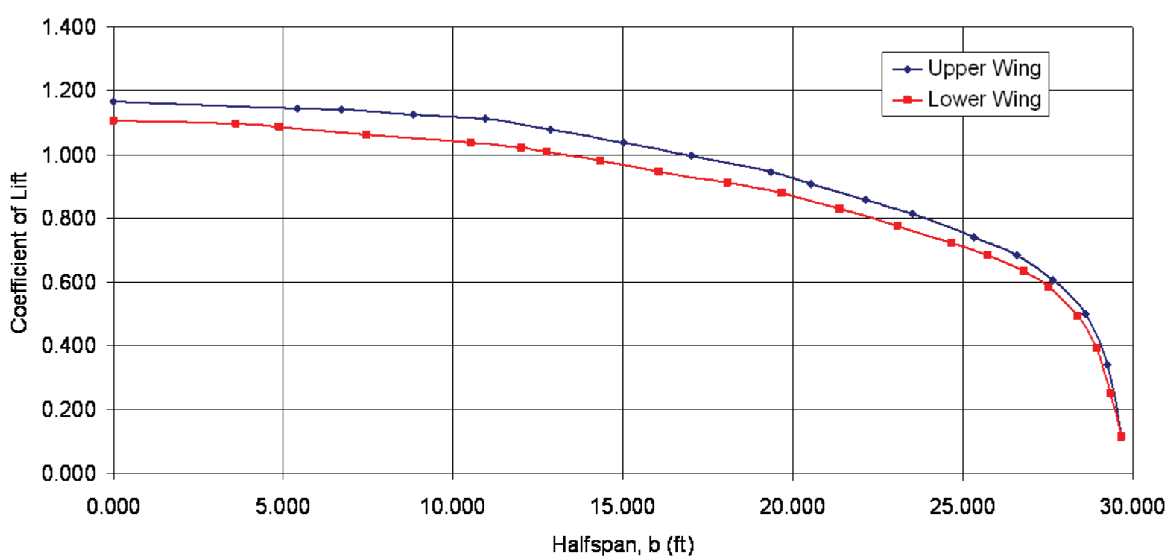

Figure 5.4.3-1. Spanwise lift distribution from AVL.

The lift coefficients were used to calculate the lift on the wing at each rib, spaced six inches apart. Figure 5.4.3-2 shows the lift at cruise speed of 24.5 mph as applied to the ANSYS model.

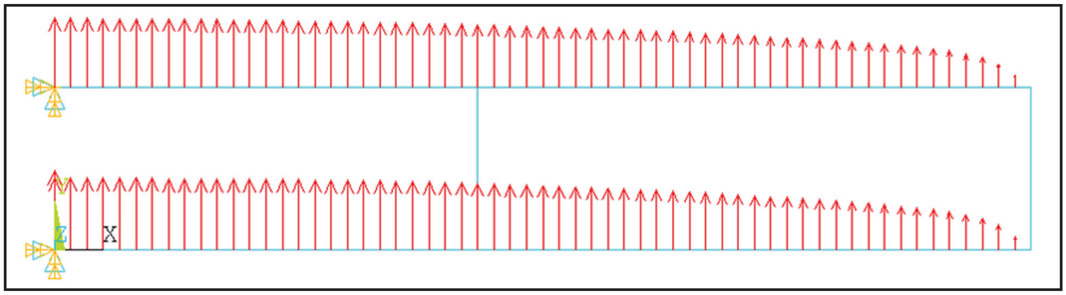

Figure 5.4.3-2. Lift forces applied to ANSYS model.

Initial spar sizes were selected based on the preliminary analysis. Size cases were run to try to minimize the stress on the overall structure. After several cases it was decided that changing the spar size at the strut may reduce the stress. This design would be desirable because a heavier spar could be used near the root where the stress is typically greater while a smaller spar could be used on the outboard sections where the stress is less to save weight. The different cases were analyzed with ANSYS to show the total stress on the spars. Figure 5.4.3-3 is an ANSYS plot of the total stress on each part of the wing structure. The stress is graphed perpendicular to each member. The figure shows the maximum stress to be 21311 psi which is well below the yield strength of 6060-T6 aluminum, the type of aluminum the team plans on using. Figure 5.4.3-3 shows the stress for the final spar design at cruise speed and cruise angle of attack. Therefore, the final spar design should have a factor of safety of 1.8 while at cruise.

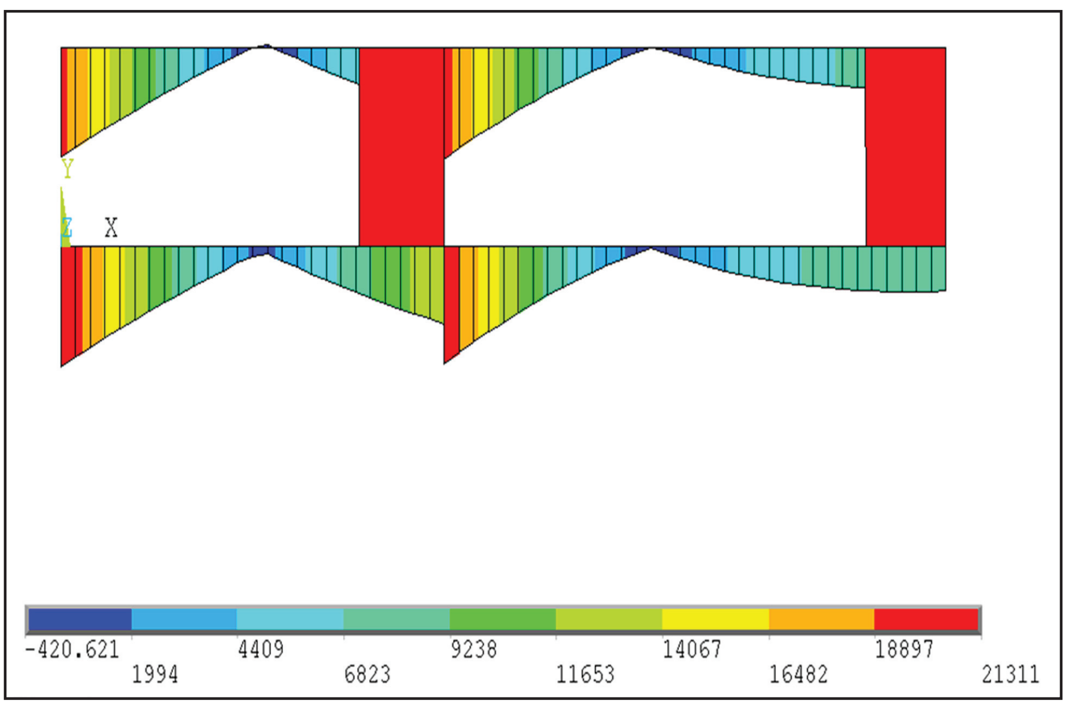

Figure 5.4.3-3. Stress distribution on final spar design at cruise.

In addition to checking the stresses in the spar, the wing deflection along the span was also examined. Figure 5.4.3-4 shows the deflection of the final spar design with the same load conditions as applied in figure 5.4.3-3.

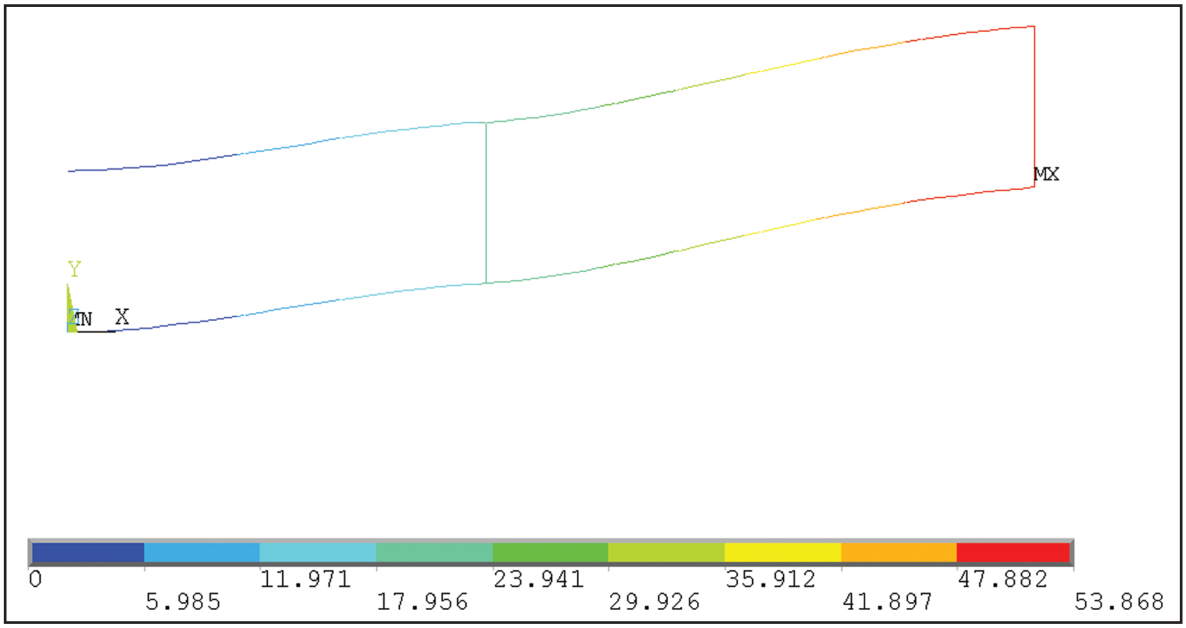

Figure 5.4.3-4. Wing deflection at cruise.

The result of this analysis was the final spar design which is summarized in table 5.4.3-1.

Table 5.4.3-1. Final wing spar sizes.

Section	Mat.	OD [in]	Wall [in]	ID [in]	Area [in2]	Iyy, Izz [in4]	C [in]	Length [ft]	Weight [lb]
Strut I	Alum.	1.50	0.056	1.388	0.25404	0.066314	0.750	10	2.97
Strut 0	Alum.	1.00	0.020	0.960	0.06158	0.007395	0.500	10	0.72
1	Alum.	2.00	0.028	1.944	0.17347	0.084339	1.000	48	9.74
2	Alum.	1.75	0.016	1.718	0.08716	0.032762	0.875	72	7.34
							Total	**140**	**20.78**

The next stage in the analysis was to see how the wing would react to gust loads. Load cases were run from a gust of 2 mph to 10 mph. In addition, the loading of the wing while in a turn was examined to check that the wing would not fail while the plane was in a turn. Table 5.4.3-2 summarizes the wing characteristics in each load case.

Table 5.4.3-2. Final wing load case summary.

Case	Velocity [mph]	Gust [mph]	Tip Deflection [in]	Max Stress [psi]	Factor of safety
Cruise	24.5	0	53.87	21311	1.877
Cruise	26.5	2	64.01	25321	1.580
Cruise	28.5	4	74.94	29646	1.349
Cruise	30.5	6	86.67	34285	1.167
Cruise	32.5	8	99.19	39239	1.019
Cruise	34.5	10	112.52	44507	0.899
Turn	24.5		72.06	28339	1.411

The table shows that it would be unsafe to fly the prototype in competition conditions where a gust of wind could easily reach 8 mph and cause the wing to fail. This is the main reason that next year's team will have to build another aircraft possibly using carbon fiber spars. With the current design, the airplane should be able to fly well in calm conditions.

5.4.4. Aileron Preliminary Design

In previous analysis, the team determined that the length of the control surface on each wing would be 18 ft and that they would extend from the tips inward. Further analysis of the surfaces and the control forces needed was done using AVL to determine percentage of the wing chord the ailerons will need. The preliminary design included aileron construction and attachment to the wing. In addition, the method of aileron actuation was addressed.

Several conditions were established as requirements for an adequate aileron concept. The ailerons would have to be lightweight, but resistant to deforming forces during flight. They would also need to be effectively attached to the main portion of the wing without considerable extra structure, again to limit weight. Finally, they would need to be evenly and predictably actuated by some form of mechanism connected to the pilot's controls.

Figure 5.4.4-1 shows the results of this conceptual design. It represents the outer 20 ft of the bottom wing of Iron Butterfly. The aileron, 18 ft in total length, is divided into 9 ft sections, separated at the dihedral change which will be located 10 ft from the wing tip. The aileron shape will be formed by 28 ribs evenly spaced along the length of the control surface. These ribs will be constructed of Expanded Polystyrene (EPS) foam and capped using balsa, the same design as the wing ribs. Balsa strips will connect the ribs and prohibit longitudinal deformation of the aileron shape. Final sizing of the balsa strips is pending ongoing testing of wing test sections.

The ailerons will then be covered in 0.001 in thick DuraLar® covering, the same covering used on the main part of the wings. The ailerons will be hinged to the wing using a strip of either clear lightweight tape of high adhesive ability, or a strip of DuraLar® with appropriate adhesive. This hinge will cover the entire 18 ft length of the aileron to ensure adequate hinge strength, that the aileron is not allowed to twist, and that the aileron will have even deflection along its length. Again, further testing of wing sections incorporating this aileron design will help us finalize this design.

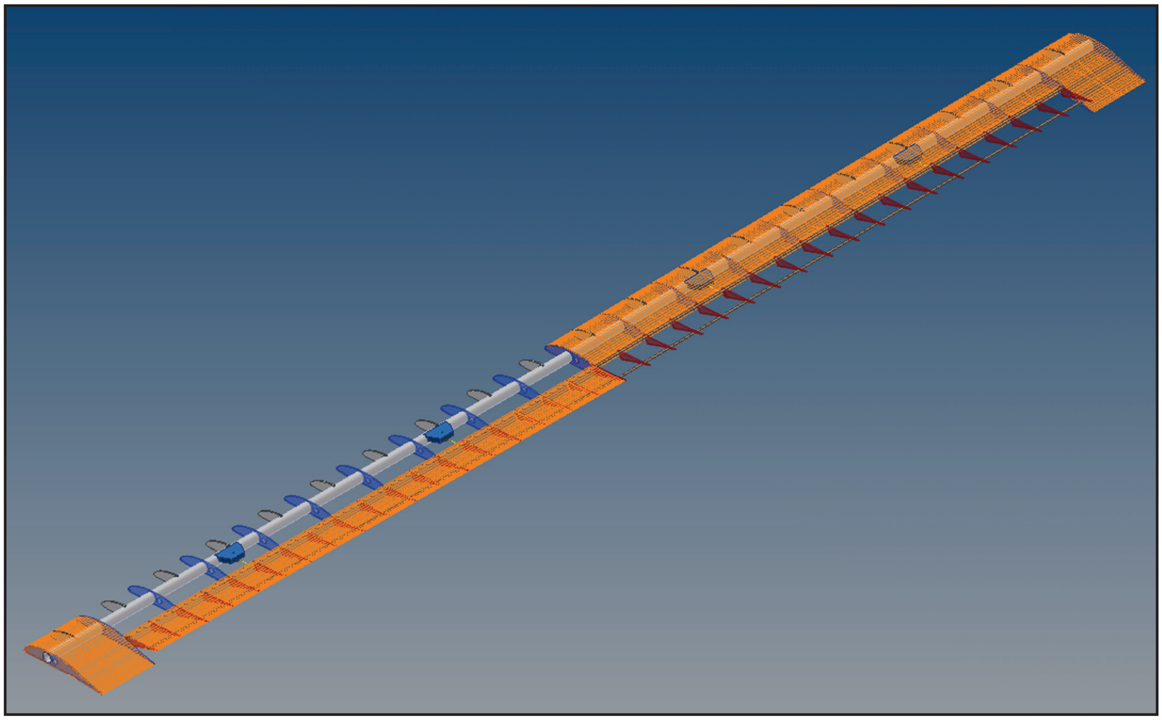

Figure 5.4.4-1. Outer 20 ft of lower wing section.

An important component of this preliminary aileron design was that of the aileron mechanization device. We determined that at least four devices would be needed per aileron, two for each aileron section, to ensure even actuation across the control surface. This was due to the extreme length of the control surfaces. It was also determined that the control wires connecting the actuation device to the controls would need to run through the wing structure, as opposed to above or below it, to avoid the excess drag the wires would cause.

Figure 5.4.4-2 shows the actuation device as conceived by the team. The device consists of four primary components. The first is the mounting block. Likely to be constructed of balsa wood, the mounting block would be connected directly to the aluminum spar. The control wire connection point swivels on a pin extruding from the bottom of the mounting block. The desired actuation will be done through a pull-pull control scheme (two wires will be used; when one is pulled the aileron will actuate one way, when the other is pulled the aileron will actuate in the opposite direction). The wires will connect at the control wire connection point securely and then continue past the actuation device to the next.

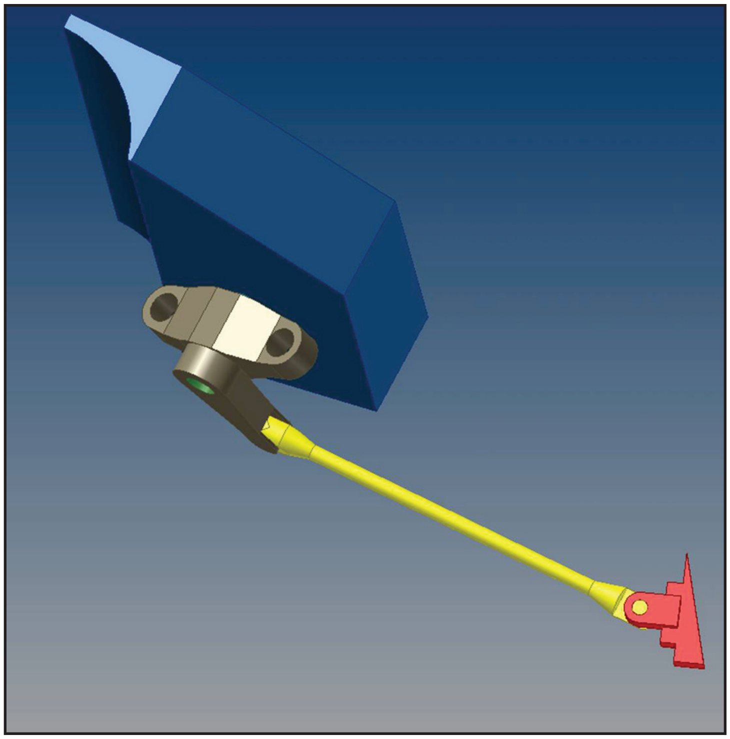

Figure 5.4.4-2. The aileron actuation device.

The third important component of the actuation device is the push rod. This rod, roughly 3 in long, will transfer the pull of the wires to the pushing and pulling of the ailerons. Finally, the aileron connection bracket will mount directly to an aileron rib. This will ensure that the actuation device acts on the most structurally sound portion of the aileron. It will also mean that no extra structure will be required to attach the aileron actuator to the aileron. This in turn will keep the weight of the control surface to a minimum. Final design of the aileron actuation device will focus on final sizing, connection adhesives, and a material list.

Figure 5.4.4-3 shows the actuation device connected to the main part of the wing structure. It should be noted that one important potential problem with this actuation system is the uneven actuation of the ailerons due to slack in the control wires between actuation devices. Special attention will be made to construction and installation of the control actuators to insure that proper control deflection is achieved.

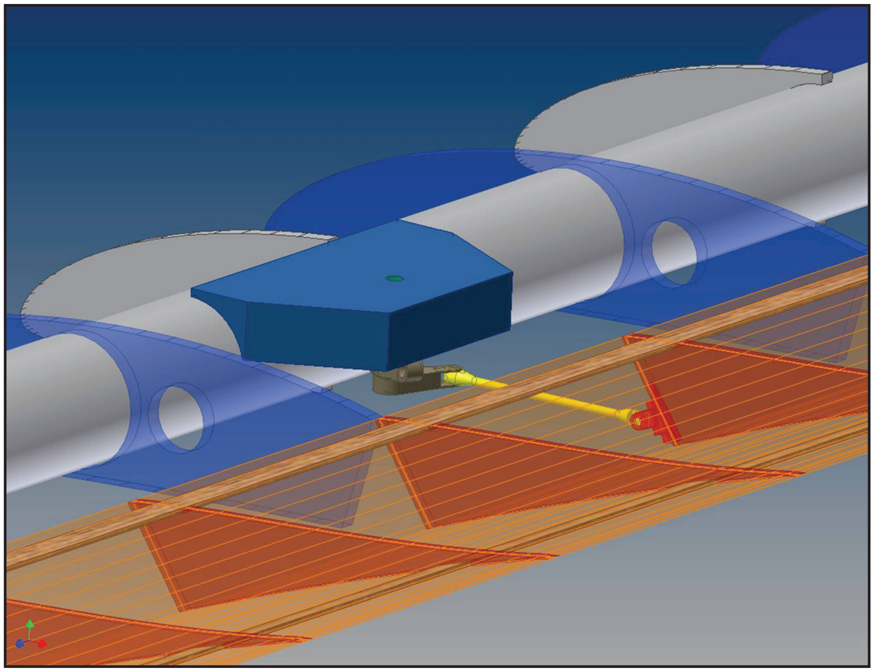

Figure 5.4.4-3. Aileron actuator installed on the wing section.

5.4.5. Rib Design

Rib design testing this semester has led to a final, complete design. This design occurred in two phases. In the first phase, previous HPA ribs were surveyed for construction materials and techniques. In addition, alternate conceptual rib designs were devised. Several of these concepts were constructed and tested. This initial testing including a very basic assessment concerning the best choice for rib construction and manufacturing. At this conclusion, rib design proceeded to the second phase. Again, several ribs were constructed, tested and compared. Manufacturability was also considered, that is the ease of which we would be able to construct the 240 ribs which are necessary to complete construction of the Iron Butterfly. Lastly, an assessment was made to determine the final rib choice. Both phases of rib design will be detailed in this report section.

When phase one began it was determined that the total weight of all 240 ribs must be between 3 and 4 lb. This necessitated that individual rib weight be under 3 g. Such a low rib weight would require lightweight materials and efficient construction techniques. The primary material considered in wing construction was foam; the type of foam would be determined later. Foam can be very strong for its weight, can be easily manufactured, and had already shown to be a good rib material choice based upon previous HPA successes, such as McCready's Gossamer Albatross. Other key materials and adhesives identified by the team were carbon fiber, fiberglass, epoxy, cyanoacrylate glue, and balsa wood. In addition, non-essential material might actually be removed from the interior of the rib to create a truss-like structure, further reducing weight. Four primary preliminary designs were then decided upon.

First, the primary candidate for our rib design was that used by the Gossamer Albatross. The Albatross' successes were such that we felt that their rib design would be a great place for us to start our own designs. The albatross rib consisted of a foam core reinforced by balsa cap strips, a carbon fiber truss inlayed on the outside of the rib and a Kevlar wrapping to strengthen the trailing edge of the rib. Figure 5.4.5-1shows a constructed prototype rib of the Albatross' type.

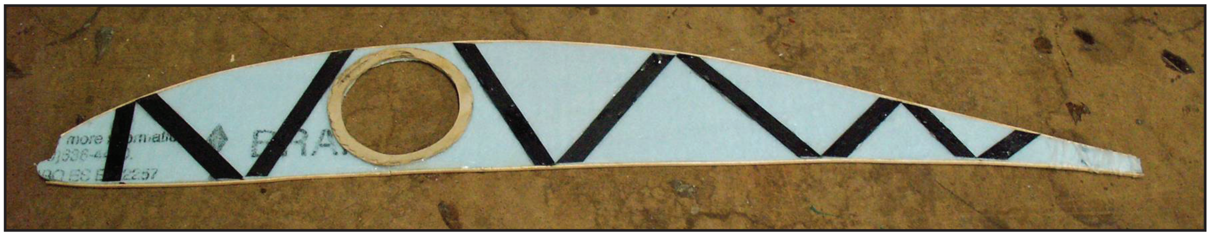

Figure 5.4.5-1. Gossamer Albatross type rib concept.

A thicker all foam rib was then considered because the current design did not require the strength per rib that Gossamer Albatross's rib needed. Our design's short wing chord and the smaller displacement between each rib eliminate the need for such strength. In order to achieve weight savings, non-essential material was removed from the interior of the foam core. Varying material removing patterns were considered. Figures 5.4.5-2 and 5.4.5-3 show two examples of prototype all foam ribs. One benefit immediately perceived to be gained by use of only foam was manufacturing simplicity. The time required to construct an all foam rib was significantly shorter than the time required to construct a Gossamer Albatross rib.

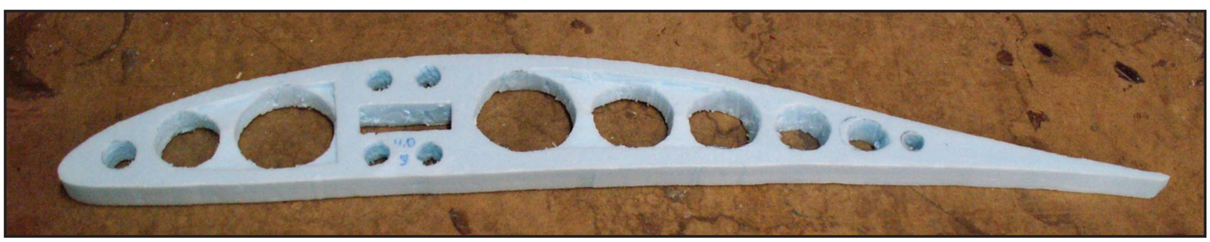

Figure 5.4.5-2. Early version of the all foam rib concept.

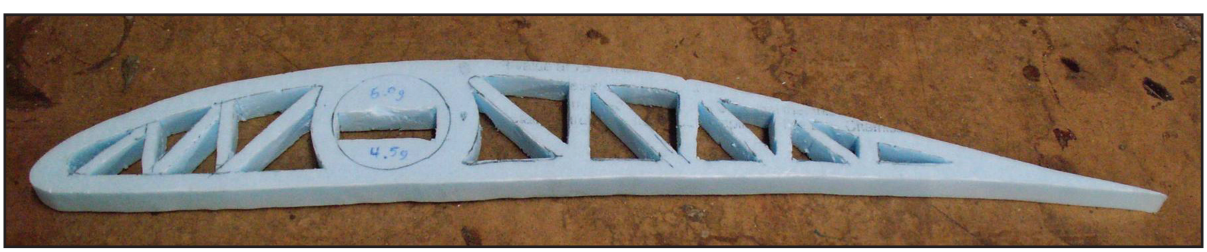

Figure 5.4.5-3. Later version of the all foam rib concept with more defined interior truss.

Two further preliminary rib concepts were briefly considered including an all balsa core rib. Again it was found that a rib made of entirely one material was very desirable in terms of manufacturability. A problem found with the all balsa rib was that it was not nearly as strong per weight as foam, at least for the size. A wider rib would be desirable because it would give more definition to the wing itself. Finally, a composite fiberglass concept was considered. No serious effort was give to construct a prototype fiberglass rib. The reason for not manufacturing and testing this final prototype was that it was immediately conceived that it would require too much excess time per rib to construct. In addition the materials necessary would be much heavier then that required of the all foam ribs and several offshoots of the Albatross design that were already showing promise.

With a great deal of new insight into rib design and manufacturing, we decided that a preliminary assessment of the results of the design to this point was necessary. The point of the preliminary assessment would be too limit the focus of this ongoing design process and allow us to focus clearly upon the most promising rib designs. The following six criteria were used to assess the merits of the four preliminary rib concepts outlined above: ease of manufacturing, weight, strength, durability/erosion, cost, and deformation. These “figures of merit” were then given the weights shown in table 5.4.5-1.

Table 5.4.5-1. Initial assessment of rib design status.

	Weight	Goss. Albatross	All Foam	Balsa/Carbon Fiber only	Fiberglass Majority
Ease of manufacturing	20	15	20	10	5
Weight	30	20	20	20	8
Strength	10	10	10	10	10
Durability	10	8	8	5	2
Cost	20	15	20	10	5
Deformation	10	5	2	7	10
Total (out of 100)	100	73	80	62	40

Using the above criterion, each rib concept was evaluated using lessons learned in construction and informal strength testing. The assessment confirmed what was already very clear to us: the all foam and the Gossamer Albatross concepts were the best two concepts. They were related close enough in terms of construction that we decided to pursue both concepts. It was our hope that the final rib design would closely resemble a combination of the positive attributes of these two designs.

During phase two of rib design, the following final rib concepts were determined to meet the initial requirements of this design process outlined above. Figure 5.4.5-2, actually an early version of the all foam rib concept, shows the rib concept entitled “All Foam Revision 2” for the purposes of the final evaluation. Even though it was an early concept, during strength testing it actually showed great resistance to deformation. In addition, the weight saving sections cut from the interior in the form of circles were much quicker and easier to construct qualitatively than a trust structure. Figure 5.4.5-4 below shows the second design considered in this final assessment, an all foam rib reinforced with a carbon fiber truss structure. This was a slight departure from the original Gossamer Albatross concept in that it left out the balsa caps and Kevlar® wrapping at the trailing edge. This made the concept easier to construct and considerably lighter. It was later determined in testing that the balsa caps were actually the much more desirable external portion of the Albatross concept when compared to the carbon fiber truss.

Figure 5.4.5-4. All foam rib with inlayed carbon fiber truss for support.

The all balsa rib was included in this final design assessment for comparison only. It was determined very clearly in final testing that the all balsa rib could not be constructed to perform as well as the all foam rib for the same weight , though it was somewhat easier to manufacture. With both of these conclusions, it was easy to recognize the all balsa rib simply wouldn't compete with the all foam version and its alternate versions. Figure 5.4.5-5 shows a sample all balsa rib. Finally, an all foam rib with balsa caps was considered as the fourth and final viable candidate to be assessed in this design process. Figure 5.4.5-6 shows this rib concept, which would become our final rib design.

Figure 5.4.5-5. All balsa rib.

Table 5.4.4-2 below shows the results of the final analysis. It includes the use of the same figures of merit and their weights as the initial assessment. Concept A is the all foam rib with circular cuts of material, Concept B is the foam with carbon fiber truss structure, Concept C is the all balsa rib, and Concept D is the all foam rib with balsa caps. As noted above, the rib test section with all foam interior with balsa caps was determined to be the best rib design available to the team. It is also important to note that the team decided to use Expanded Polystyrene Foam (EPS) when the material became available to us in abundant qualities from a nearby manufacturer, ThermaSteel Corporation. In figure 5.4.5-6 you will note the difference in color and texture that this new foam has compared to the pervious blue foam insulation previously used. The EPS was also significantly lighter then the blue foam, but with efficient application of the balsa caps we still achieved a rib design with negligible loss of stiffness.

Table 5.4.5-2. Final assessment of rib designs.

	Weight	Concept A	Concept B	Concept C	Concept D
Ease of manufacturing	20	16	5	20	14
Weight	30	30	20	10	25
Strength	10	2	6	10	6
Durability	10	4	6	8	8
Cost	20	20	5	15	18
Deformation	10	2	6	10	8
Total (out of 100)	100	74	48	73	79

Figure 5.4.5-6. Final rib design.

Once the final rib design was chosen, it was analized in ANSYS. Coefficients of pressure from Xfoil were used to determine the amount of pressure around the outside of the foil. This analysis was important in determining whether the truss structure would hold the loads to which the rib would be subjected. Figure 5.4.5-7 shows the pressure distribution applied to the rib.

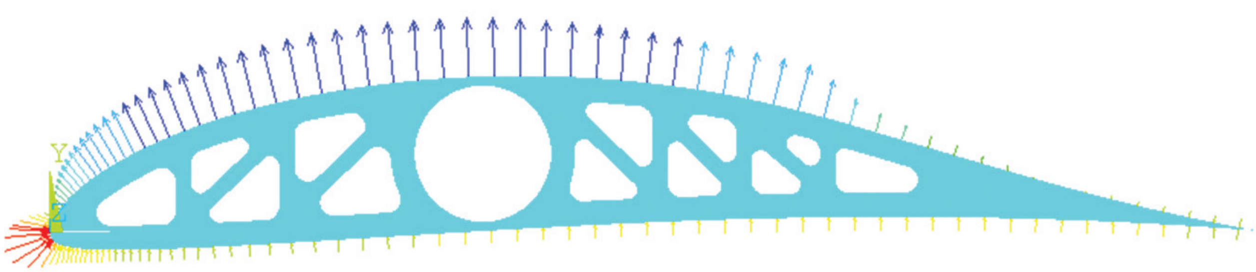

Figure 5.4.5-7. Airfoil pressure distribution.

The analysis used properties for EPS foam: modulus of elasticity of 250 and poisson's ratio of 0.103. The balsa cap strips were not examined as they would take most of the load and therefore would not show the stresses around the cutouts as well. Figure 5.4.5-8 shows the stress (psi) exerted on the airfoil at cruise speed and angle of attack.

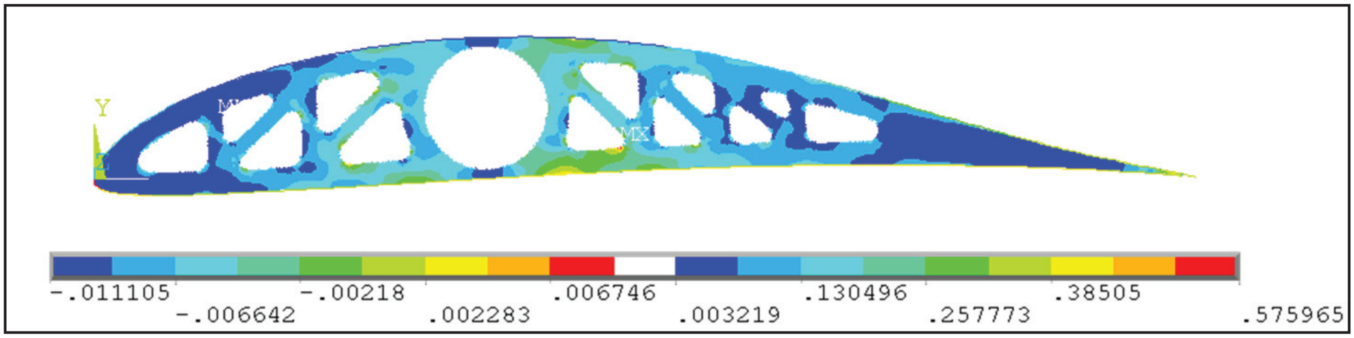

Figure 5.4.5-8. Airfoil stress distribution at cruise speed.

The next item examined was the deflection of the airfoil under the same load case. Figure 5.4.5-9 shows the deflection of the foam under cruise loads. Even without the balsa strips the deflection is very small so the completed ribs will be extremely strong.

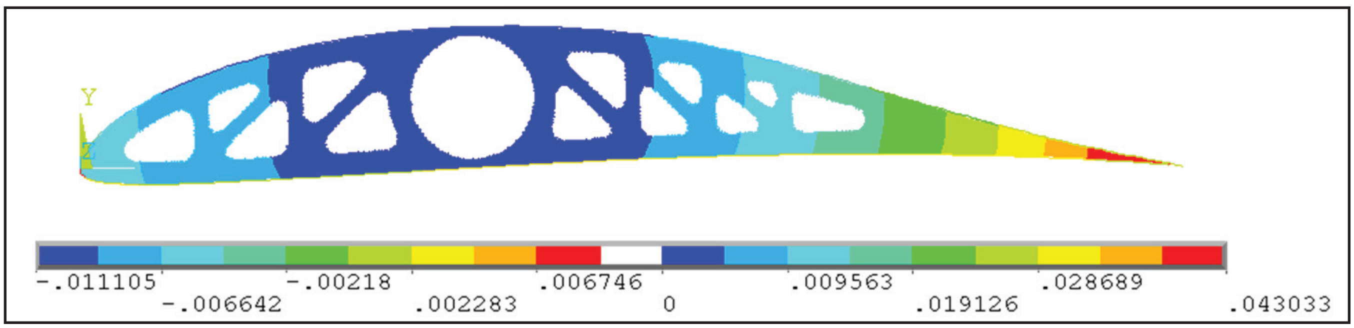

Figure 5.4.5-9. Airfoil deflection at cruise speed.

With this analysis completed, it was found that the rib design would be more than adequate structurally. Figure 5.4.5-10 shows both the DAE 11 and DAE 21 ribs with the final truss structure and spar hole location along with ailerons.

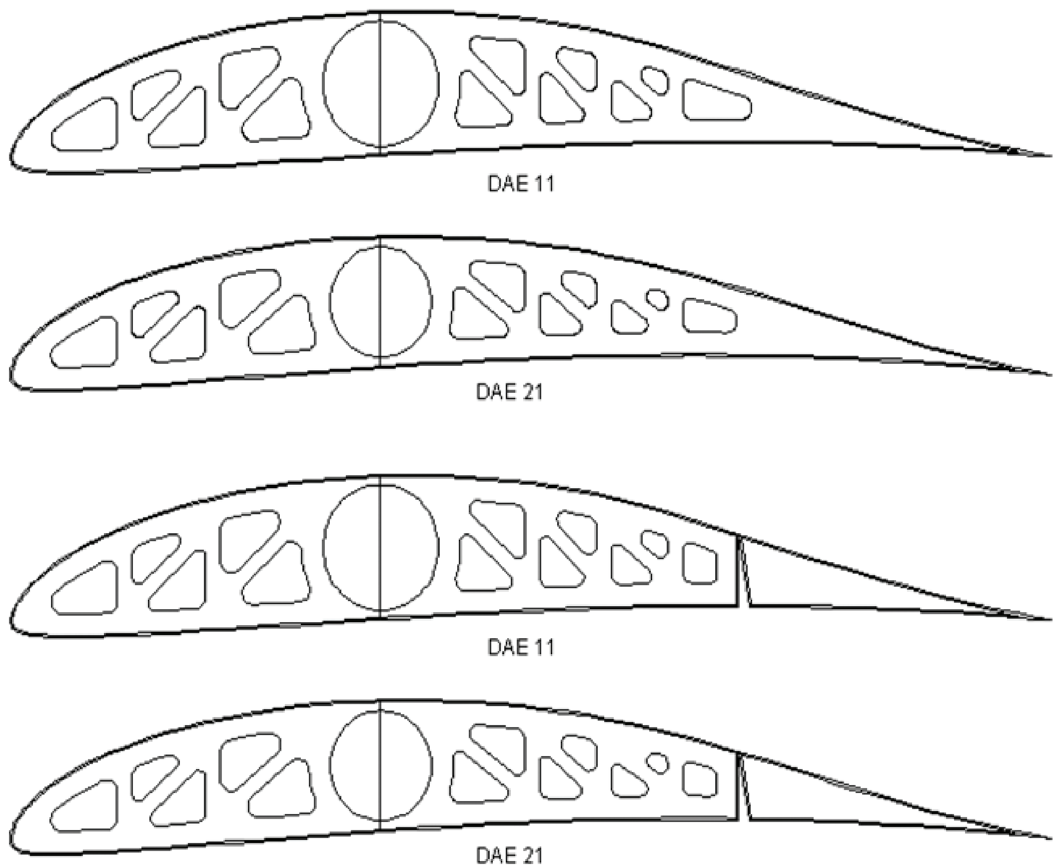

Figure 5.4.5-10. Final rib design summary.

5.5. Propulsion

In order to better analyze and predict the performance of the plane on the course, a mission model was developed. The 2005-2006 team performed a mission analysis and constructed a simple mission model to determine the bank angle and flight speed required to complete the course in time. From this analysis, the flight speed and bank angle determined were used as the criteria upon which the aircraft was designed [5]. However, while reviewing the previous year's mission model and writing the one for this year, it was determined that an error concerning the orientation of the course had been made. When this error was corrected, an increase in the flight speed of 2 mph from 22.5 mph to 24.5 mph was necessary in order to complete the course in the allotted time. The results of the new code can be seen in figure 5.4-1, while the results of the old code are shown in figure 5.5-2. In both figures, the diagonal hash line marks the maximum flight time limited by the competition rules, and the star marks the decided operating point. A flight time of 6.3 min, instead of the maximum course time of 7 min, was used to decide the speed and bank angle at which to fly so that a factor of safety would be included.

This change will lead to an increase in power required, as well as a possible redesign of the aircraft to better optimize the design. Currently this decision has yet to be made, as the error in the mission model is a recent development.

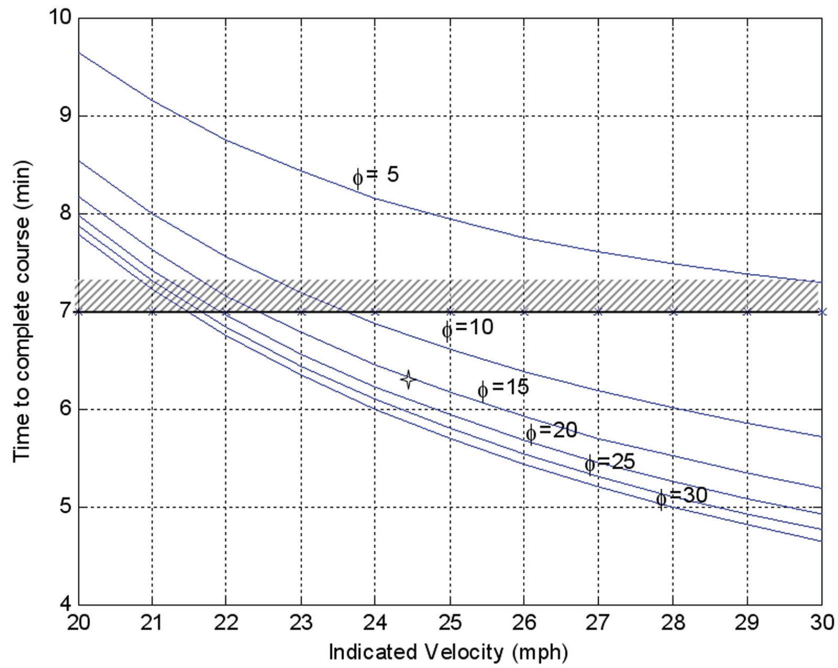

Figure 5.5-1. Time to complete full course vs. airspeed from the new mission model

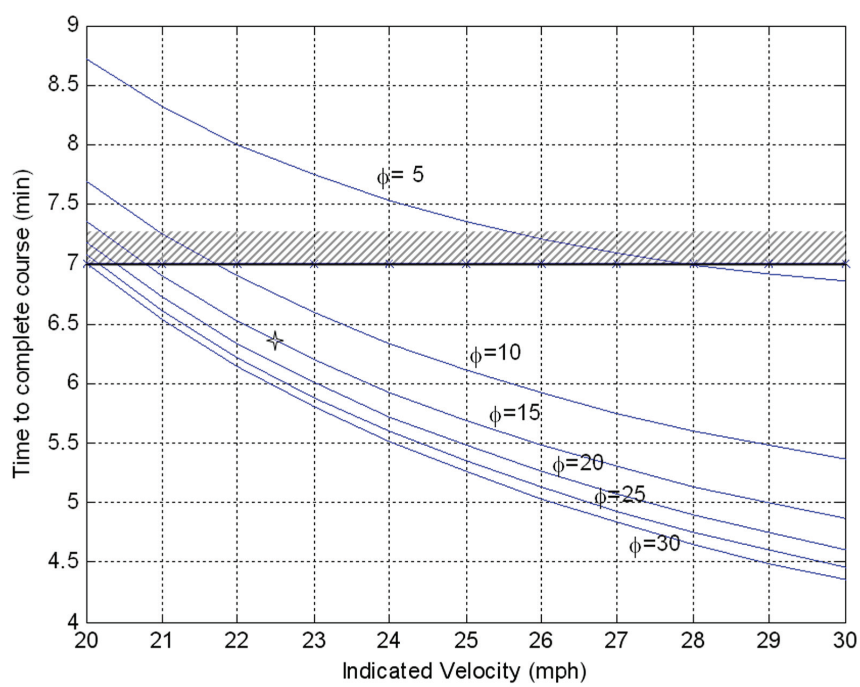

Figure 5.5-2. Time to complete full course vs. airspeed from the old mission model.

In addition to checking last year's numbers, the new mission model was written in order to expand on last year's work and incorporate power required analysis. Power required analysis was based on aerodynamic numbers generated from the design last year [5]. The results for the downwind leg, which is currently representative of the power required on all straight legs of the course, can be seen in figure 5.5-3.

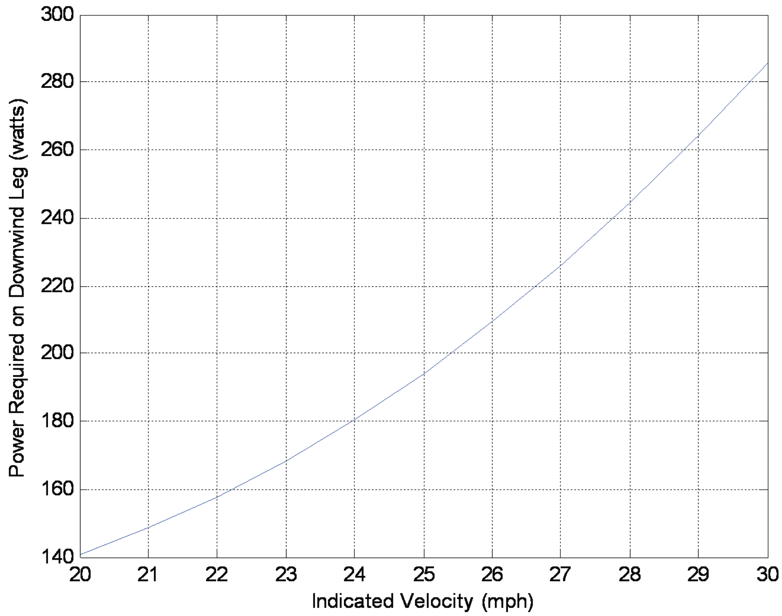

Figure 5.5-3. Power required versus airspeed on the straight legs of the course

The power required as a function of airspeed and bank angle can be seen in figure 5.5-4. These values do not account for the constantly changing sideslip angle in the turn.

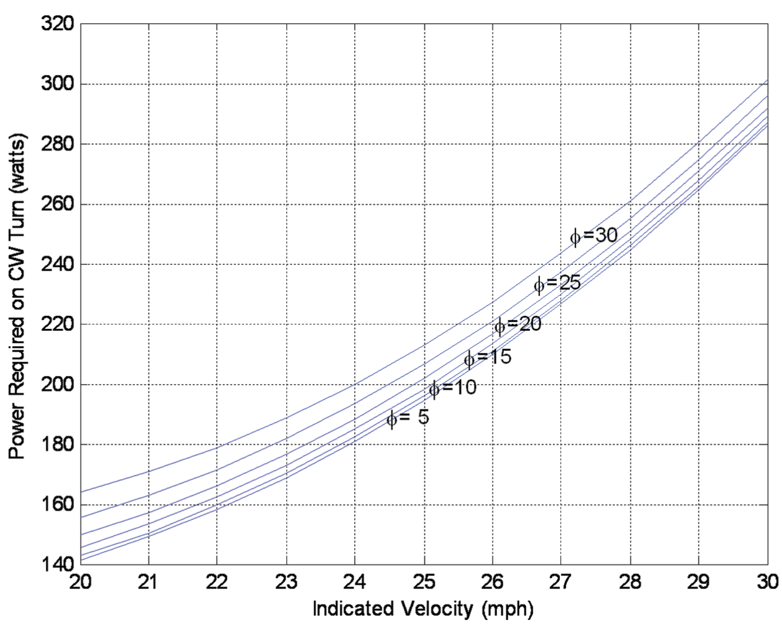

Figure 5.5-4. Power required versus airspeed and bank angle in the turns of the course.

Further analysis, through varying the inputs, showed that the power required is highly sensitive to the aerodynamic numbers, especially C_{D0}. Since quality power required information is contingent upon accurate values of C_{D0}, it is important to carefully derive C_{D0}.

Currently the mission model incorporates only power required. For future work, it is planned to include analysis of structural load and control response. The purpose of including these additional parameters is to optimize this analysis by making it more representative of actual flight. The final mission model should represent the actual flight well and be a robust tool by which to optimize the design.

5.6. Cockpit Design

5.6.1. Pilot Position

Much progress has been made on cockpit design since the beginning of the semester. In the opening weeks of this semester pilot position was discussed. The team considered two positions: fully upright, as in a traditional bicycle, and semi-recumbent, where the pilot would be in a seated, slightly reclined position. There were three main criteria to meet when deciding on the pilot's position: efficiency, visibility, and freedom of movement of the pilot's arms and hands. After completing research regarding the efficiency of each position, two references stated that in both positions the pilot could produce the same amount of power [16, 17]. Thus, the decision became dependent on the visibility and freedom of movement alone. A cockpit mockup was constructed and the two positions were compared. It became evident that the semi-recumbent position would allow better freedom of motion while pedaling, as the arms would not be needed to support the rider, and the visibility would be increased because vision would not be as impaired by the forward cockpit support. A rendering of the cockpit layout can be seen in figure 5.6-1.

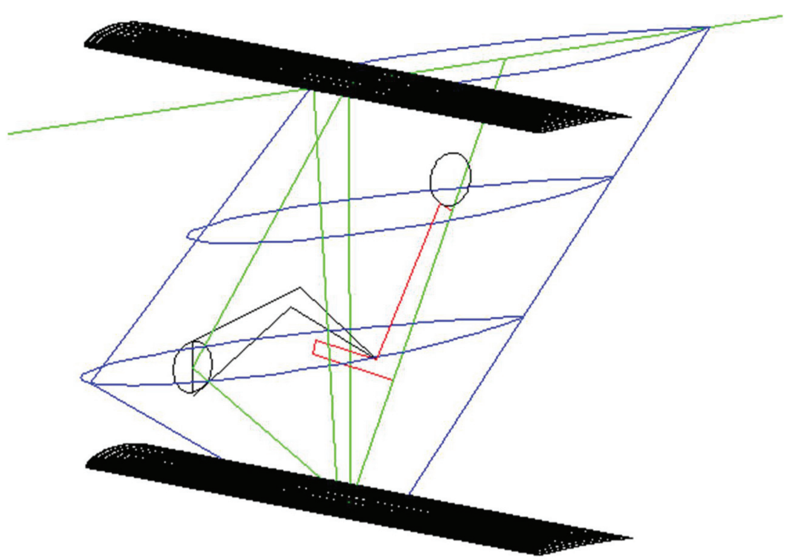

Figure 5.6-1. AutoCAD rendition of full-scale cockpit. Green lines are load-bearing structures, blue lines are the outer skin of the cockpit, red lines are the chair, and black lines represent the pilot. The bold, black objects are the wings of the aircraft.

5.6.2. Pilot Center of Gravity

Since the pilot will be a large portion of the weight of the final aircraft, it is important to know the center of gravity (CG) of the pilot in the semi-recumbent position. To find the CG, anthropometric measurements of the pilot's body parts were taken. These weight and length measurements were entered into a set of equations to find the location of the CG for each part; then, these locations were used to determine the overall CG of the pilot [18]. The position of the CG, measuring from the hip joint, is 11.4 in forward and 8.75 in up.

5.6.3. Drive Train

Another issue regarding cockpit design is the drive train, which will transfer power from the pilot to the gear driving the propeller. The team is looking into the use of a slightly elliptical chain ring because of its potential to deliver up to a 12 percent increase in efficiency. This increase is caused by the elliptical shape of the chain ring, which takes advantage of the natural motion of the leg while pedaling. Essentially, the elliptical chain ring allows the chain to be moved further during the more powerful part of the pedal stroke, translating into higher power output. The ideal eccentricity of the ellipse is between 1.05 and 1.2, and the ideal position of the chain ring occurs when the major axis of the ellipse is placed 75 degrees ahead of the crank arm. The team is planning on testing two chain rings to find the best position and eccentricity for our application in the HPA.

In order to transfer power from the rotating cranks to the gear driving the propeller, a chain must be used. In this design the chain must rotate 90 degrees between the drive gear and the propeller gear. The most suitable chain that meets the needs is a polyurethane chain that is both strong and light. Polyurethane chain was previously used in Gossamer Condor.

5.6.4. Pilot Controls

Once the HPA lifts off the ground, it must be controlled. The main controls will be placed directly in front of the pilot and will consist of two side by side control sticks. The left stick will control the rudder while the right still will control the elevator and ailerons. Control inputs from the pilot will be transferred to the control surfaces using a pull-pull control line system. A control system mockup is shown in figure 5.6.4-1.

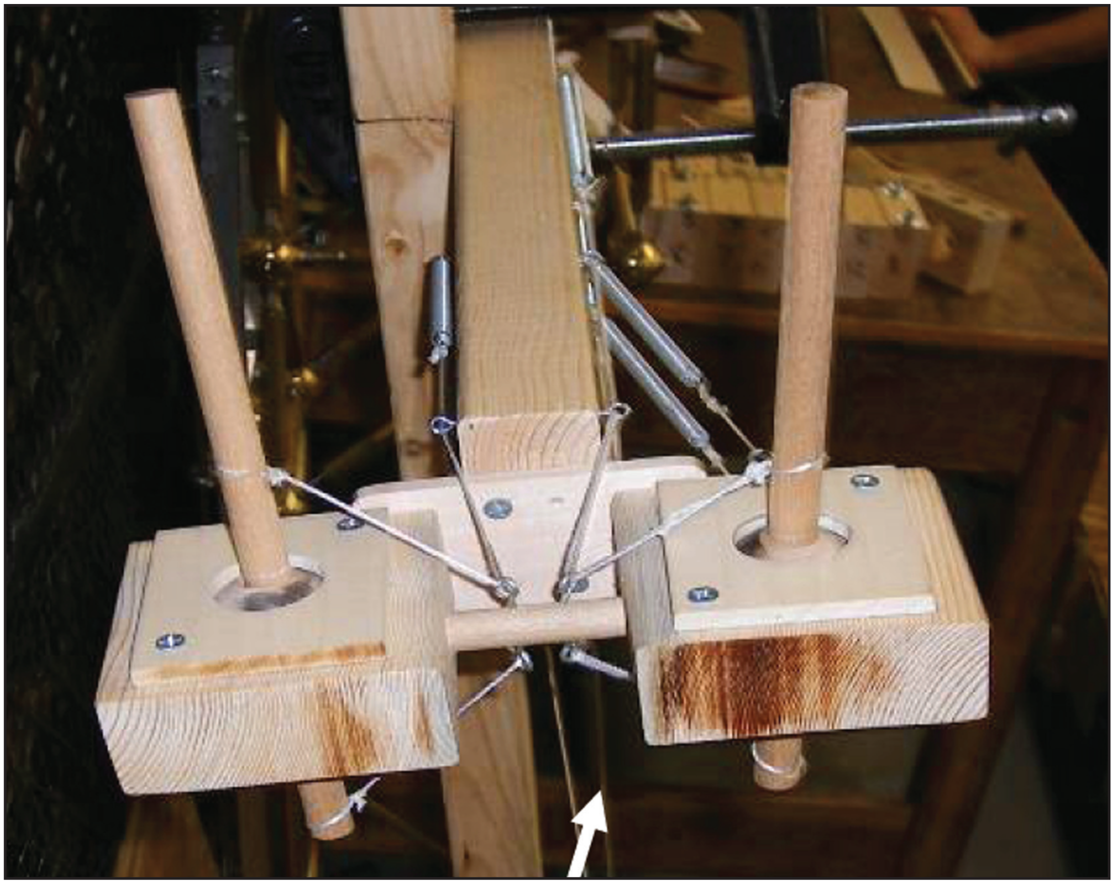

Figure 5.4.6-1. Control System Mockup.

5.7. Landing Gear

The following landing gear design for the prototype aircraft is based on previous HPAs landing gear and the successes of the model. The prototype's landing gear will be in a bicycle configuration with possible wing-mounted wheels. Bicycle gear can be found on most successful HPAs. The setup includes one large main wheel close to the pilot, which carries most of the loads, with a smaller wheel at the front of the fuselage for longitudinal stability. Although previous HPAs do not have any landing gear in the wing, they had high wing configurations and therefore there was less of a possibility of a wing tip striking the ground during taxi, takeoff, or landing. Since the team's box plane design has a lower wing, which is close to the ground, the probability of a tip strike is higher. A tip strike would be extremely detrimental due to the fragile nature of the design. In order to avoid this, small wheels could be mounted either at the wing tips or at a semi-span wing strut-spar joint. Further analysis is required on the position and loads carried by the landing gear.

5.8. Propeller

The propeller used in this design was initially designed by the previous year's team. However, as the flight speed increased from 22.5 mph to 24.5 mph this year, the prop had to be re-optimized. The propeller was optimized for a thrust required of 5.5 lb at 180 rpm and 24.5 mph. The thrust required of 5.5 lb is from a pessimistic drag estimate with a small factor of safety. By designing for a slightly higher power than what is expected, the propeller is capable of handling increased power input from the pilot. In previous HPA projects, the propeller responded poorly to an increase in power input from the pilot resulting in poor acceleration. The rotational speed of the propeller was determined previously based on the best efficiency rpm for a human. To optimize the propeller design, the vortex propeller theory from E. Eugene Larrabee was used to determine the original configuration of the propeller. The propeller design was then input into XROTOR, a program developed by Mark Drela at MIT, to further optimize the propeller.

Although efficiency of the propeller was very important in designing it, constraints were also set so that it could be manufactured with the tools available to the team. The main structural constraint set was that the airfoil thickness at the root and 2 ft from the root be great enough for a 0.5 in diameter tube to fit inside the airfoil. This was set so that the main spar which transmits the load from the propeller to the propeller hub, and allows the pitch of the blades to change, be able to fit inside the propeller. From this constraint, a minimum chord was found that corresponded to the thickness required to fit the 0.5 in tube. Once the constraints were set, the propeller designed was iterated for a range of propeller radii and section C_L in order to obtain the most efficient propeller possible. For each radius iteration, the propeller was initially sized using Larrabee's method, and then input into XROTOR to iterate the section C_L of the propeller. Through the use of these two programs, a propeller with a tip radius of 4.46 ft, a section C_L of 0.6, and an efficiency of 92.18 percent was designed. The 3-D CAD model of the propeller is shown in Figure 5.8.1.

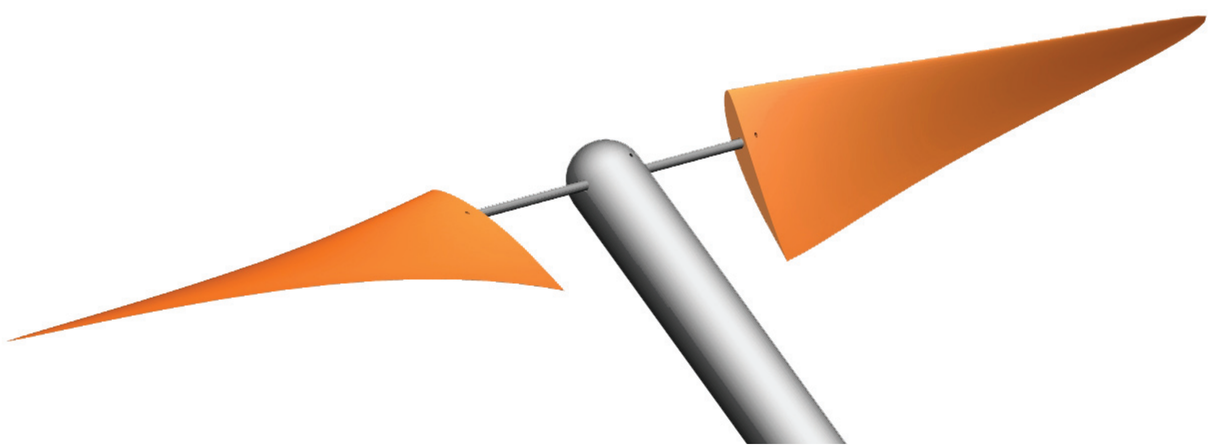

Figure 5.8-1. 3-D Model of Propeller for Iron Butterfly.

5.8. Construction

5.8.1. Airfoil and Wing Construction

Construction of the airfoils is done using a hotwire foam cutter to shape the foam and then using epoxy to adhere the balsa cap strips to the foam. The hotwire foam cutter works by heating a nickel-chromium wire to a point where it vaporizes foam as it is passed through.

Using laser-cut stainless steel templates to ensure proper shape, the hotwire is guided along these templates through a large foam block to create the initial rib shape. This large rib is then sliced into 0.25 in thick ribs. A different template is then used to secure the balsa cap strip while simultaneously removing sections of the rib that are not structurally critical. A completed rib can be seen in figure 5.8.1-1.

Figurew 5.8.1-1. Rib & Wing Assembly.

Once the ribs are completed they are slid onto the aluminum spar. The trailing edges are aligned to ensure the pitch of each ribs is equal. Then, the ribs are epoxied to the spar in six inch increments. This spacing can be seen in Figure 5.8.1-1 above. Once the ribs are in place, the leading and trailing edges are also epoxied to the ribs. Then, the covering is attached to the ribs starting at the leading edge of the airfoil and carefully adhered along the upper surface of the wing until the trailing edge is reached. This is then repeated along the lower surface of the airfoil. A heat gun is used to shrink the Dura-Lar® to make it taut across the ribs.

5.8.2. Aileron Construction

The aileron was first constructed as a three foot test section for use in the Virginia Tech Open Jet Wind Tunnel. Construction took place in three phases: rib construction, section construction, and covering and attachment. Construction of the test section would prove to validate the design as part of the effort to move forward with full scale prototype construction.

Rib construction is outlined above. This is where the basic aileron construction starts. The key difference in between aileron rib construction and normal rib construction is the molds used to cut out the interior truss section. The sections had to be slightly modified to make room for the aileron section. Once the balsa caps strips are adhered with epoxy and the truss is formed the rear [get number from Derek] % of the chord is cut off from rest of the aileron. 10 degrees of freedom is cut from between the two sections also. This is to allow for the appropriate deflection.

Section construction also begins normally. Ribs, minus the aileron sections are glued to the aluminum spar with epoxy. A strip of $^1/_{32}$ in. thick balsa is then epoxied to the rear of the of the ribs where the aileron sections were removed. The strip was used to create stability at the end of the ribs. Next the section was covered with DuraLar. Construction of the aileron section was slightly more complex. Another strip of balsa needed to be applied to the cut end of the aileron ribs. This was done by laying the strip of balsa on a table and then gluing the ribs with epoxy. A balsa strip was also used for the trailing edge much like a standard rib section. The completed aileron section was then covered with DuraLar.

Attachment is slightly complex. Before covering, the servo needed to be mounted to the spar. As of this writing, the it had not been decided whether a remote electrical servo was going to be used or a manual pilot-operated actuator. The servo must be anchored to the aileron. Once this is done a hinge is made with packing tape. This completes of attachment of the aileron to the wing section.

5.8.3. Aluminum Spar Tube Etching

The spar of the aircraft is composed of two different size aluminum tubes. The inboard 24 ft of wing uses aluminum tube which has a 2 in outer diameter and a 0.028 in wall thickness. The remaining outboard sections of wing use a smaller 1.75 in outer diameter tube with a .016 in wall thickness. Although the 2in tube can be purchased in the required thickness, the 1.75 in tube cannot. The 1.75 in tube is available with a wall thickness of 0.035 in. In order to obtain this wall thickness the aluminum tube must be milled down. However, traditional mechanical milling will not work to reduce the wall thickness for several reasons. First, the material must be removed from the inside of the tube to preserve the outer diameter. Second, the tube sections are 9 ft long, much longer than most machining lathes' working length. Lastly, the required wall thickness of 0.016 in is fragile, and damage incurred while machining is very likely. Since mechanical machining is not a viable option, the tubes are to be chemically milled to the appropriate wall thickness.

Chemical milling of aluminum is done by subjecting it to a heated solution of sodium hydroxide (NaOH) in water, which slowly etches away the aluminum. First, small samples of aluminum tubing were used to characterize the rate of milling with respect to NaOH concentration and solution temperature. Once the etching process was better understood, several different methods of etching the aluminum tube were tested. These methods included pumping NaOH solution through the aluminum tube, sealing an end of the tube and filling the inside with sodium hydroxide solution, and immersion of the entire tube into a bath of NaOH solution.

The first method tested was the use of a pump to circulate the sodium hydroxide solution through the tube to be etched. The aluminum tube was encased in a 3 in PVC pipe with stand-offs machined from Delrin® to support the aluminum tube. A small drill-powered pump was then used to circulate the solu¬tion through the pipe. However, during a test with water, it was found that the pump did not have enough power to move the water through the pipe with the desired flow rate. As a result, it was decided not to pursue this method of chemically milling, but to test a different method.

Next, sealing an end of the tube and filling it with NaOH solution was tested. For this test, the alu¬minum tube was once again inside of the PVC tube. This was done both to give structural support to the tube and to contain the NaOH if the seal at the end of the tube failed. The end of the tube was sealed with a flexible Latex membrane secured with a pressed on compression ring. When the solution was poured into the vertically oriented aluminum tube, the gas produced from the reaction of the NaOH solution and the aluminum caused the tube to bubble over. The test was aborted and the NaOH solution neutralized. This method was determined to be too much of a safety hazard to pursue further.

The third method tested was the immersion of the aluminum pipe into a bath of NaOH solution. The major problem with this method was finding a coating which could be applied to the tube to prevent the outside from being etched. Several different coatings were tried, including AeroGloss®, rubber latex, and PlastiDip®. The rubber latex was the most promising of the coatings and, if properly sealed at the ends of the tube, would keep the outside of the tube from being etched. The sodium hydroxide solution was held in a trough made from 3 in PVC pipe. The ends of the tube were capped and a valve placed at the end to allow draining of the tube. A sample 2 ft long tube was etched with this method, but it was found that the latex could not be properly sealed at the ends of the tube and the NaOH solution seeped underneath the coating. In addition, several cracks in the latex formed from where the latex was applied to the tube, although this could be corrected with a thicker coating of latex. It was decided that unless a suitable covering for the outside could be found, this method would not be viable.

For the next test, the previously abandoned method of pumping the solution through the aluminum tube was redesigned. This time hose clamps were used to secure PVC hose on either end of the aluminum tube and a larger, more powerful pump was used. In this way the solution could be pumped from a holding tank, through the aluminum tube, and back into the holding tank. Once the etching was complete, acid could be easily circulated to stop the reaction and clean the tube, and then water to clean out the residue. However, when this was tested, the tube did not etch uniformly around the circumference. The bottom of the tube had much more material milled off than the top of the tube. This disparity was due to the gas rising from the bottom of the horizontal tube to the top, displacing the NaOH solution and preventing etching from occurring. In addition, it was difficult for the pump to begin pumping, and switch from pumping NaOH, to pumping acid, to pumping water. To pump easily, the PVC tube had to always be filled with water, and oil had to be frequently circulated through the pump. For these pumping troubles and the non-uniformity of the etch, the method of circulating the NaOH solution with a pump was once again found to be inadequate to chemically mill the tubes.

While work was being done with the pumping system, PVC heat-shrink tubing was purchased to test as a covering for the outside of the tube. This heat-shrink fits around the tube, and when heat is applied shrinks tightly onto the tube. Another test etch was performed with the NaOH bath in the trough using the PVC shrink tubing to cover the outside of the aluminum tube. The ends of the shrink tubing were secured with hose clamps to prevent NaOH from seeping underneath the heat-shrink. This test was conducted with a lower concentration of NaOH solution to reduce the rate of reaction to make the process safer, but with a longer etching time to make up for the decrease in etching rate. The heat-shrink performed very well and did not allow the NaOH to contact the outer surface of the tube. In addition, the etching was very controllable and calm, and most importantly the thickness removed was consistent around the entire circumference of the tube. It was decided from these test results that this method would be the one used for all of the chemical milling.

Currently, etching of the full-size tubes is underway. Half of the tubes necessary to build a complete wing have been etched, with the rest in the process. During full scale etching, several minor problems with the etching process were noted. First, the full scale tube does not etch exactly concentric if it remains in the same orientation in the bath and must therefore be rotated. Rotation of the tube can be done either during etching of the tube, or in between successive etching sessions. Full scale tubes for this project were etched in three 30 minute sessions with the tubes being rotated the proper amount in between sessions to ensure concentric etching. The second problem encountered was the Sodium Hydroxide burning through the PVC shrink wrap and etching the tubes on the outside. Although the PVC was impervious to Sodium Hydroxide, if a tear or pinhole developed in the PVC due to rough handling, the Sodium Hydroxide could get through the shrink wrap. If the hole allowed for the Sodium Hydroxide to contact the aluminum tube, it would heat the area, which would shrink the PVC tubing more and enlarge the hole. To prevent burn-through the tubes were covered with three layers of PVC shrink wrap. In addition the tubes were inspected before and after each etch for tears or pinholes which could let the Sodium Hydroxide through the PVC shrink tubing. If a tear or hole was found, another layer of PVC shrink tubing was added to the area and sealed at each end with PVC electrical tape. Through this careful process only one burn-through developed on one of the tubes. Luckily this was at the end of the tube and can be cut off with the excess tubing. This is possible because the wing sections are 9ft long, but the commercially available tube length is 12ft. Provided precautions are taken to prevent these problems, immersion in a bath is the best way to etch aluminum tubes.

The final chemical etching setup used for full scale etching of the aluminum spar tubes was immersion of the tubes in a bath of Sodium Hydroxide. The solution used was 0.5 lb Sodium Hydroxide to 1 gal water. Commercially available 6 in PVC tubes were cut into troughs to hold the bath. The aluminum tubes were covered with three layers of PVC shrink tubing, which was wrapped with PVC electrical tape at the ends and clamped tight with hose clamps over the electrical tape. Each tube was etched in the solution for 30 min, then submerged in a mild solution of HCl to stop the etching and clean the tubes, and then rinsed with water. The tube thickness was then measured with tubing micrometers, the angle of rotation needed for a uniform etch noted, and the hose clamps rotated the necessary angle. This process was then repeated twice more, with the time in the 3rd bath tailored to achieve the desired thickness. To etch the 1.75 in outer diameter 0.035 in wall thickness 12 ft aluminum tube to the desired wall thickness of 0.016 in the full 30 min duration for each of the three baths is required. Once the tubes were etched to the desired thickness the PVC shrink tubing was removed and the aluminum tubes cut to the required length of 9 ft by cutting 1.5 ft off of each end of the tube with a machining lathe.

5.8.4. Spar Joints

Each 60 ft spar is composed of four 9 ft sections and three 8 ft sections of tube. This is done both due to the available length of aluminum tubes and in order to build dihedral into the wing. Methods for joining aluminum tubes used by previous HPA teams were researched; the method the team is most likely to apply now is the use of a balsa plug epoxied inside the ends of the joining aluminum tubes. For instance, the joints are discontinuities in the structure highlighted by stress concentrations found in analysis. These stress concentrations are the points in the wing structure which are most likely to fail. Balsa plug joints will provide an easily repairable and lightweight solution.

To join the aluminum tubes, a balsa plug is machined to the inner diameter of the aluminum tubes to be joined. Once the plug is made, it is glued into the ends of the aluminum spar. The joint is then reinforced on the outside with Kevlar™ wrappings. The entire assembly, minus the Kevlar™ wrappings, is shown exploded in figure 5.8.3-1.

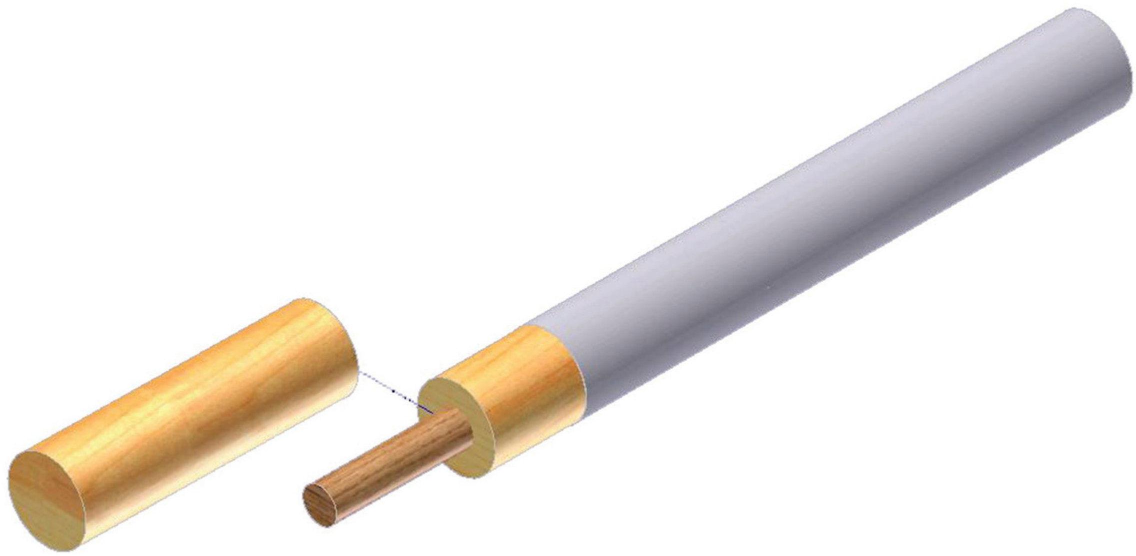

Figure 5.8.3-1. Spar Joint Assembly Exploded

5.8.5. Tail Boom

The tail boom connects the wings and fuselage to the tail and the propeller. The distance from the wing to the tail is 16 ft 7 in, and approximately 4 ft from the wing to the propeller. The tail boom must be strong enough to carry the loads of the tail while being lightweight. The tail must also have very little deflection under load so as not to affect the control response of the tail surfaces through elongation or contraction of the control lines. In order to accomplish these structural requirements, the team decided to construct a carbon fiber tail boom. Through structural analysis, it was determined that the tail boom must have a diameter of 4 in and a wall thickness of 0.036 in. The tail boom is going to be composed of four layers of carbon fiber with a stacking sequence of approximately [+45°,-45°,+45°,-45°]. An analysis for the optimum angle is still being conducted.

To construct the tail boom, the carbon fiber layers will be wrapped around an aluminum tube with the appropriate outer diameter. Once this is completed, PVC shrink tubing will be shrunk on top of the carbon fiber wrapped tube. The purpose of the two tubes is to ensure good bonding between the layers of carbon fiber and to produce a smooth surface finish. The tube assembly will then be placed into a custom built oven to cure. This oven will be constructed from Expanded PolyStyrene (EPS) foam to keep the temperature constant over a long period of time. The oven will be heated with small electric heaters, which will have enough heating power with the insulation of the foam. A section view of the oven is shown with the aluminum-carbon fiber-aluminum tube inside in figure 5.8.4-1. Once the carbon fiber has cured, the aluminum and PVC tubes will be removed and the tail boom will be ready to install on the aircraft.

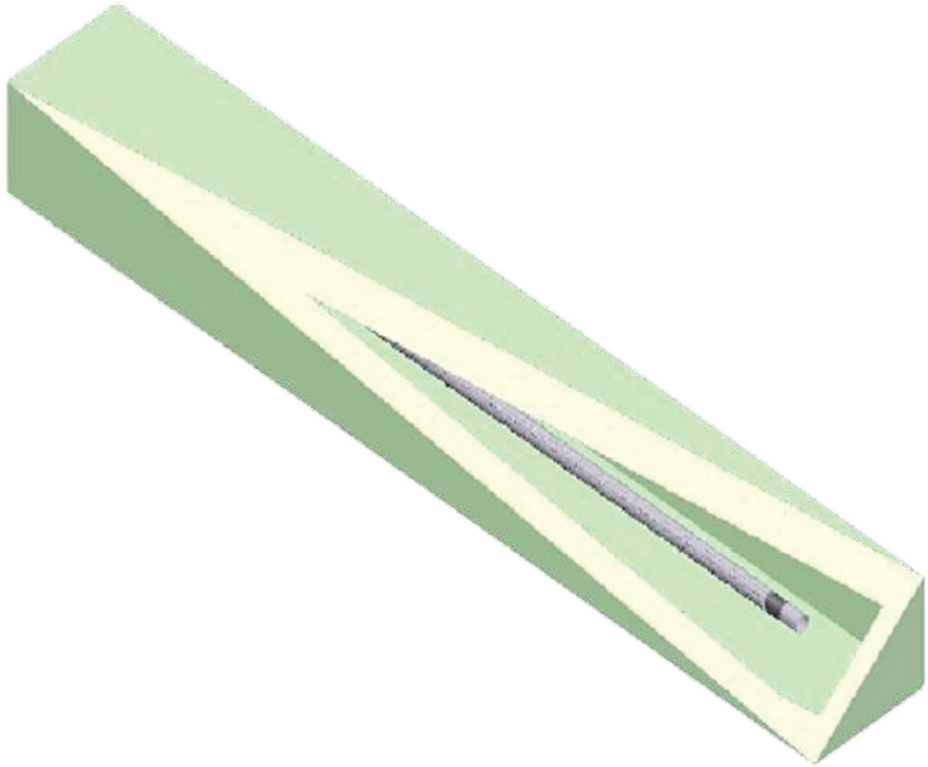

Figure 5.8.4-1. Carbon Fiber Tail Boom Oven with Tube.

5.8.6. Propeller

The 3-D model of the propeller was used to program a CNC mill to cut the propeller out of foam. This propeller can be seen in Figure 5.8-1. The propeller was cut from a block of Expanded Polystyrene (EPS) foam to test the manufacturability of the propeller. The foam cut nicely and produced an accurate representation of the propeller. Currently construction on the prop is continuing, however with a slightly different approach. Negative molds will be made of the propeller by cutting positive molds out of machining foam and using these to create fiberglass panels which will become the negative molds. The propeller will then be cut out of EPS and covered with fiberglass, with carbon fiber reinforcements. This will then be vacuum-bagged using the negative fiberglass molds to preserve the shape of the propeller while it is curing. The blades of the propeller will then have a carbon fiber tube inserted into them at their axis of pitch to connect them to the prop shaft and allow for variable pitch of the propeller. The pitch will be variable via a manual variable pitch mechanism in the full-scale prototype, and an automatic pitch controller in the final competition aircraft.

5.9. Wind Tunnel Testing

Virginia Tech's Open Jet wind tunnel was used to observe airflow over a 3 ft test section of the wing. The test section consisted of 7 balsa/foam ribs spaced 6 inches apart. Clear 0.001 in thick Dura-Lar® was used as a covering. The covering on the outer segments of the test section were slightly loose due to the fact that the outer ribs were not designed to take a horizontal load. These segments were disregarded during testing. The test section seated in the wind tunnel can be seen in figure 5.9-1. The objective of the testing was to ensure that:

1. The flow over the wing stayed attached
2. The Dura-Lar® covering held its shape and stayed taut
3. The leading edge did not deform during aerodynamic loading
4. The spar location induces no pitching moment

Figure 5.9-1. Open Jet Wind Tunnel Test Section.

The test procedure used during this experiment was as follows:

1. Attach wing holders into middle of test section
2. Place wing into wing holders
3. Start wind tunnel motor
4. Slowly increase speed to desired 24.5 mph
5. Use yarn to check flow attachment
6. Allow spar to rotate freely in wing holders

After testing it was concluded that the Dura-Lar® covering was a sufficient covering material. It did not deform or flap while the wind tunnel was running. The yarn showed an attached flow going over the wing, which was as expected. The spar location, however, was found to not be sufficient; a strong pitch down moment was created indicating that the spar would need to be located farther back. Testing of this new spar location is planned for the near future.

5.9.1. Aileron Testing

A three foot test section of the wing containing an aileron was constructed and tested in the Virginia Tech Open Jet Wind Tunnel. The purpose of the aileron test was to determine:

1. How many aileron actuators would be necessary to effectively deflect the aileron
2. What structural reinforcements will allow constant deflection across the aileron
3. Is the selected actuator strong enough to deflect the aileron uniformly

Construction of the aileron test section was preformed as discussed above in the aileron construction section. In the test section, an electronic servo was used for actuation of the aileron. The complete aileron test section can be seen in figure 5.9.1-1.

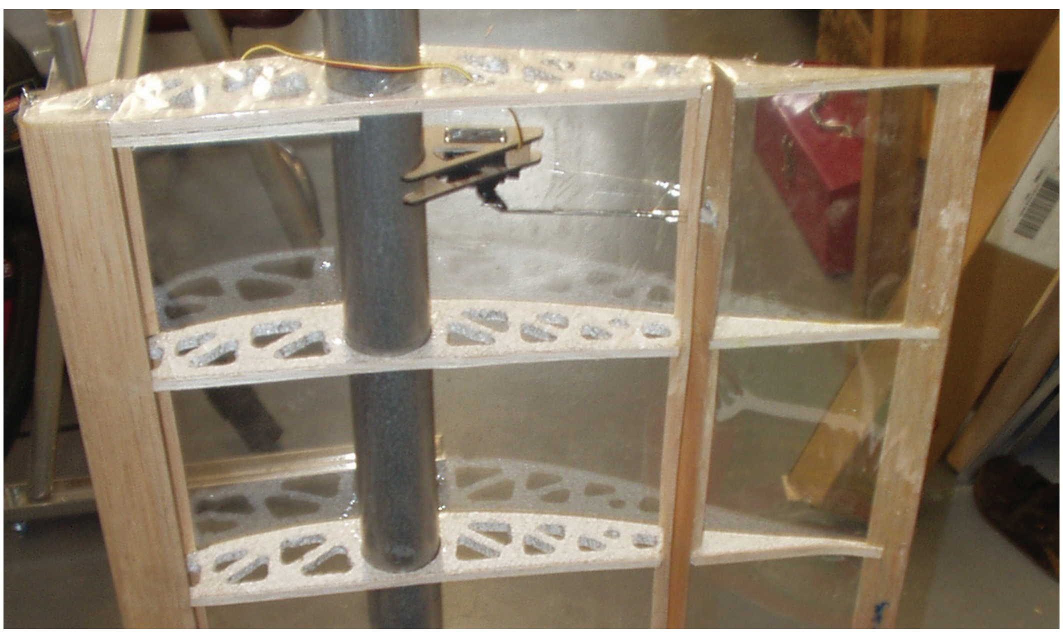

Figure 5.9.1-1. Aileron Test section.

It was predicted that using four actuators on each aileron would provide sufficient deflection. After testing, it was concluded that four actuators spaced evenly throughout the aileron would provide sufficient power and allow even deflection.

5.9.2. Spanwise Flow

To be completed

5.9.3. Torque Testing

Results pending

5.9.4. Parking Lot Testing

A 10 ft section of our wing was constructed with the intent of measuring spanwise deflection to validate our ANSYS models. This wing was constructed out of DAE 11 ribs and a 2.0 in outer diameter aluminum spar. The ribs, leading edge, trailing edge, and covering were attached exactly as they will be done on the final wing. A measuring stick was attached to the tip of the wing so that deflection measurements could be obtained while the wing was moving at flight speed.

Once the wing was constructed, a mounting plate was created to attach the wing to the roof rack of a team member's car. The car and the wing were then driven to a large empty parking lot where a ¼ mile strip of open flat pavement was found. Several tests were then completed with varying speeds and angles of attack. The wing section can be seen attached to the car in figure 5.9.4-1.

Figure 5.9.4-1. Test section attached to car.

After the flight testing was completed, it was found that our camera mount was not secure enough to get reliable deflection measurements. However, it should be noted that, qualitatively, the wing performed very well at all conditions tested. Deflection testing to validate the ANSYS models was performed on an etched tube. This testing can be seen below in Section ###.

5.10. Etched tube Testing

A 1.75 in outer diameter tube was chemically etched down to the desired thickness. This tube was then tested to determine:

1. Tip deflection without covering
2. Tip deflection with covering
3. Uniformity of wall thickness throughout tube

The tip deflection without covering will be measured and compared with the ANSYS model to validate them. The team has been unable to account for the load taken by the covering in ANSYS.

Weighted water bottles were added to the spar every six inches to simulate loading that will be provided by our ribs in flight. A picture of this testing can be seen in figure 5.10-1.

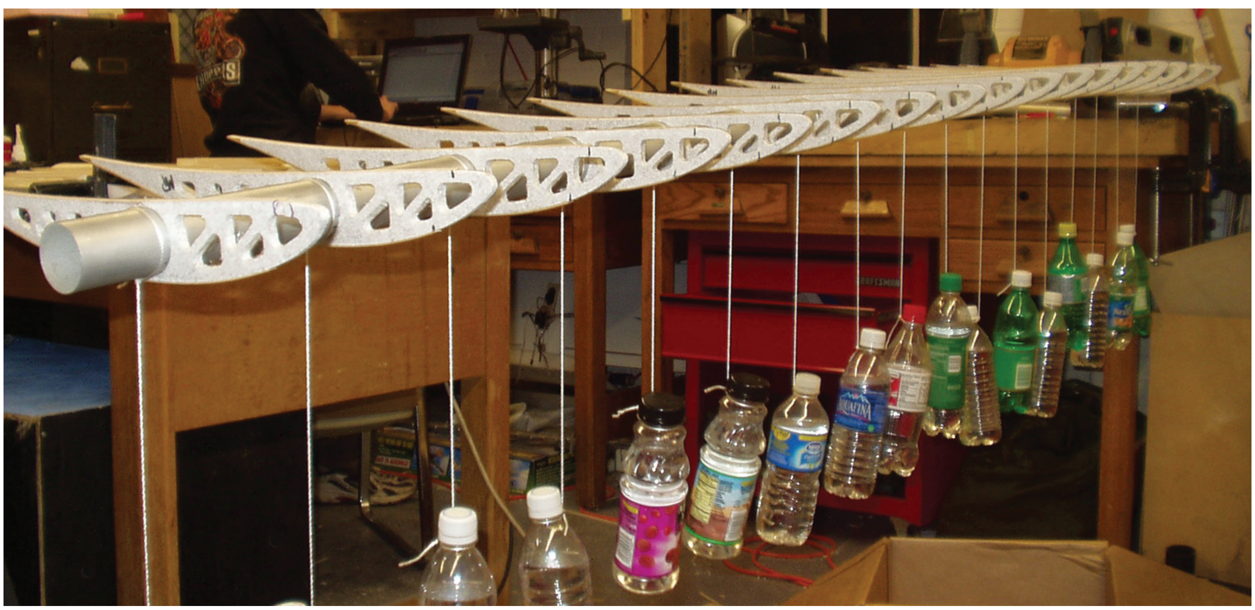

Figure 5.10-1. Deflection of etched tube.

Results TBD.

After the covering testing is done, we will be cutting the tube into smaller sections and checking thickness uniformity.

6. Project Status and Plan for Remaining Semester

Currently, the team stands with a nearly completed full-scale design, flight-test data from several flight-tests of the quarter-scale model, and wind tunnel test data of wing sections. The improvements made to the model have allowed for validation of the control and stability of the aircraft design. This validation led to the continuation of final prototype design as well as the go-ahead to start prototype construction.

6.1. Quarter-scale Model

Based on the performance of the quarter-scale model, more confidence can be placed on moving forward on design of the full-scale prototype. The quarter-scale model demonstrated sufficient elevator, rudder, and aileron authority during flight, as well as confirmed the aerodynamic predictions. It was originally planned to fly a scaled down version of the competition course; however, this objective was partially abandoned due to the size limitation of the flight-test field. Should a larger field be made available in the future, this goal will be reattempted.

After the model withstood multiple hard landings during flight-testing, the team is hesitant to attempt additional flights until a sizeable field is available. However, it is believed that the model has sufficiently demonstrated the aircraft's ability to complete the course per the competition constraints.

6.2. Prototype

The team will continue construction until the anticipated completion date of May 1, 2007. Please see the Gantt chart in section 5.1 for the design and construction schedule. Certain aspects of the aircraft, such as the propeller pitch control mechanism, will be designed while other sections of the aircraft are being constructed. It is anticipated that wing construction will take significantly longer than any other section of the aircraft; therefore, it will be started first. During this stage of construction, other parts of the final design that are not integrally connected with the wing can be finalized.

6.3. Plans for 3rd Year Team

Next year's Virginia Tech Human Powered Aircraft Team will have a working prototype with which to continue testing and refine the competition model design. It is suggested that the competition aircraft be completed by early spring 2007 in order to allow the pilot ample time to practice before competing in the UK late spring of 2008. During this test time, it will be necessary for the team to register for the prize and make arrangements for the trip.

7. Administration Details

7.1. Funding

There are three levels of donations to encourage companies to donate substantially to the project. For each level, the donor would be recognized on the team's website and in any written publication concerning the design and fabrication of the aircraft or progress of the team. For a more substantial donation, the donor's logo would also be displayed on the prototype and final aircraft trailer. The decal would be no smaller than six inches in its largest dimension. For the highest level of donation, the donor's logo would be displayed on the prototype and final aircraft trailer with a decal no smaller than 1 ft in its largest dimension. The three levels are as follows:

- Silver Sponsor ($1-$499.99)
- Gold Sponsor ($500-$999.99)
- Platinum Sponsor ($1000+)

In order to fund construction of the prototype, the team rigorously pursued new sources of funding over the first half of the spring semester. To reach the funding goal of $10,000, the team advertised corporate sponsorship on the HPA web site and contacted aerospace and ocean engineering companies to request donations. Advertisement on the team's web site resulted in one sponsor, Moore Fans, who donated $1000 towards the purchase of the aluminum spars for the prototype. Of the 107 companies contacted to request funding, two have responded with an interest in the project, Peacock Builders and Sonic Tools, Inc. A donation from Sonic Tools is still pending; however, $2200 was donated by Peacock Builders in response to the team's proposal. In addition to the donations made by these companies, the team received materials from TW Metals and B&M Sheet Metals as well as a number of personal donations from family members and friends. In total the team has received $5,672.23 in monetary donations and is about halfway to completing the fundraising goal.

Presently the team has spent $3,004.54 towards construction of the prototype and has $2,270.63 remaining in the account (the Virginia Tech Foundation keeps 7% of all donated funds). In the first half of the semester the team spent approximately $100-$200 per week on construction on the prototype. Since the purchases in the second half of the semester are proving to be larger and more frequent, it is estimated that the team will spend $200-$300 per week during the second half. At this rate, the team will need a new source of funding within the next 5 or 6 weeks. To obtain this funding, the team has begun talking to local Virginia businesses and hopes to reach the fundraising goal by the end of the semester.

7.2. Facilities

Maintenance and reconstruction of the quarter-scale model had been performed mostly in Derek Slaughter's living room. However, given the size of the prototype, a more suitable location had to be found for its construction. After investigating all storage options, the team was able to find space on campus in the Virginia Tech Ware Lab, where it will share a bay with the Design Build Fly Team of Virginia Tech. The team was granted access to the Ware lab as of November 30, 2006, and it is reserved until spring of 2008, thereby providing a space for next year's team to continue the project and prepare for the competition.

7.3. Budget

A definite budget for construction of the prototype has yet to be set. Once optimization of the materials to be used in the prototype is completed, a final budget will be determined. At the moment, it is expected that construction will cost approximately $8,550. The team is hoping to receive some of the materials for the prototype, such as the Mylar®, as a donation. Although not all of the funds will be necessary at the beginning of the construction phase, the majority of the budget will be spent in this phase of the schedule. For instance, a reliable working surface is essential to accurate building of the wing and will require a specially made table, which may cost several hundred dollars. These and other immediate costs will require funding as soon as possible to allow construction to begin. An estimate of the cost of the prototype can be seen in figure 7.3-1 below. Structures with known materials are labeled and priced accordingly; structures with unknown materials are estimated.

Table 7.3-1. Estimate Cost for Prototype Construction.

Part	Material	Cost
Spar	6061-T6 Aluminum tube	$3,000
	Carbon Fiber Tail Spars	$200
Ribs	Styrofoam	$300
	Balsa	$400
Guy Wires	Kevlar©	$50
Skin	Mylar©	$600
Leading Edge	Corrugated Paper	$100
Tail boom	Carbon Fiber	$600
Power Train	6061-T6 Aluminum	$900
Epoxy	Unknown	$400
Cockpit	Carbon Fiber Supports	$800
Etching Solution	Unknown	$200
Lab Equipment		$1,000
Total Cost		$8,550

8. References

1. ANSYS, Inc. ANSYS 10. Avail at http://www.ansys.com/, 2006.

2. "Densities of Various Materials." Marcus Materials Co. http://www.mcelwee.net/html/densities_of_various_materials.html

3. Drela, M. ALV Extended Vortex-Lattice Model. Avail at http://web.mit.edu/drela/Publie/web/avl/,2004.

4. Emory, Chirs; Roadman, Jason; et all. 2005. "The Iron Butterfly: A Human Powered Aircraft for Sport." Virginia Polytechnic Institute and State University. http://www.aoe.vt.edu/~mason/Mason_f/HPAFinalRptSo6.pdf.

5. Foner, Joel. "Weights of Common Materials." Charles River Radio Controllers. http://www.charles-riverrc.org/articles/construction/joelfoner_materialweights.thm Updated January 1998.

6. Goss, James. "Monokote or Ultracote?" Fortune City. http://www.fortunecity.com/meltingpot/palau/4/id167.htm

7. Grosser, Morton. Gossamer Odyssey: The Triumph of Human-Powered Flight. St. Paul, MN: Zenith Press, 2004

8. Hallauer W. L. Jr. and Devenport W. J., 2006, "AOE 3054 Experimental Methods Course" http://www.aoe.vt.edu/~devenpor/aoe3054/manual/expt3/index.html

9. McIntyre, J., 2004. Human Powered Flight Group. The Royal Aeronautical Society http://ourworld.compuserve.com/homepages/j_d_mcintyre/hpag.htm.

10. Mylar Polyester Film Product Information. Dupont Teijin Films. http://www.dupontteijinfilms.com/datasheets/Mylar®/productinfo/properties/h37232-3.pdf

11. Sid Kauffman, Ph.D., SLK Electronics. ElectriCalc. Avail at http://www.slkelectronics.com/

12. The Royal Aeronautical Society, 2004. Human Powered Flight: Rules and Regulations for the Kremer Human-Powered Aircraft for Sport. The Royal Aeronautical Society. http://ourworld.compuserve.com/homepages/j_d_mcintyre/sport.pdf.

13. 2002. Takeoff Speed. http://www.aerospaceweb.org/question/performance/q0088.shtml. Aerospaceweb.org.

14. 2006. Aviation. http://en.wikiquote.org/wiki/Aviation. Wikiquote.

15. 2006. Gossamer Albatross. http://en.wikipedia.org/wiki/Gossamer_Albatross Wikipedia: The Free Encyclopedia.

16. Wilson, David G., Bicycling Science

17. Whitt, Frank R., Bicycling Science: Ergonomics and Mechanics

18. Pavol, Michael J., Owings, Tammy M., Grabiner, Mark D., Body Segment inertial parameter estimation for the general population of older adults. Journal of Biomechanics vol 35 pp. 707-712, 2002.

9. Appendices

Appendix A: Data Tables
Appendix B: Flight-test Reports
Appendix C: Test Flight Summary Sheets
Appendix D: Mission Model Code

Appendix A. Data Tables

Table A-1. Experimental results of wing torsion test.

Without Guy Wires

Weight (oz)	Deflection (in)	Delta (in)	Alpha (degrees)	Torque (oz-in)
0	8.875	-0.0625	-0.596809451	0
4	8.4375	0.375	3.576334375	20
8	8	0.8125	7.711892413	40
16	7.0625	1.75	16.26020471	80
0	8.75	0.0625	0.596809451	0

With Guy Wires

Weight (oz)	Deflection (in)	Delta (in)	Alpha (degrees)	Torque (oz-in)
0	8.75	0	0	0
4	8.75	0	0	20
8	8.5	0.25	2.38594403	40
16	8.125	0.625	5.946863054	80
32	7.375	1.375	12.90740867	160
0	8.75	0	0	0

Table A-2. Calculations for Max L/D

Angle of Attack	CL	CD	L/D	
-2	0.34576	0.02186	15.817	
-1	0.44347	0.02279	19.459	
0	0.54106	0.024	22.5442	
1	0.63849	0.02551	25.029	
2	0.73572	0.02732	26.9297	
3	0.8327	0.02941	28.3135	
4	0.92939	0.03179	29.2353	
5	1.02574	0.03446	29.7661	
6	1.1217	0.03741	29.984	
7	1.21724	0.04063	29.9591	
8	1.31231	0.04413	29.7374	safety factor
9	1.40686	0.04789	29.3769	safety factor
10	1.50086	0.0519	28.9183	stall
11	1.59426	0.05617	28.3828	stall
12	1.68702	0.06067	27.8065	stall
16	2.05083	0.08086	25.3627	stall

Appendix B. Flight-test Reports

HPAG - VT		Model: 1/4 Scale Model	Test:1
Dir:	Doughten	Test Location: Kentland Farms	Date: 10/03/06
Pilot:	Skidmore	Aircraft Weight: 54 oz	Temp: 54 F
Caller:		Bat used: A	Wind: 3 mph NNW
Launch:	Beach	Notes: Fog	
Video:	Slaughter	Barometer: 29.04 in Hg	

Test	Ref No.	Description	Real Time	Flt Time
		Beach practices running launch	8:28	
A	Straight & Level Glide			
	1	Launch	8:30	0:00
	2	Land		0:05
	Notes:	Wing twisted forward => wing joiners bent forward		
B	Straight & Level Powered ½ Throttle			
	1	Launch	8:55	0:00
	2	Land		0:06
	Notes:	Broke motor mount and was reglued with Reid's off-brand CA		
C	Straight & Level Powered Full Throttle			
	1	Launch (from far end of field – wind change)	9:10	0:00
	2	Beach caught a/c in mid-air preventing crash		0:02
D	3/4 Throttle Flight			
	1	Launch	9:13	0:00
	2	Caught in mid-air		0:02
	Notes:	Strong pitch-up during launch moment from thrust line => added down trim => not enough to cover moment		
E	3/4 Throttle flight			
	1	Launch	9:13	0:00
	2	Left Bank (w/ full R. rudder & full R. ail.)		0:04
	3	Land		0:05

HPAG - VT	Model: 1/4 Scale Model	Test: 2
Dir: Doughten	Test Location: Kentland Farms	Date: 10/26/06
Pilot: Skidmore	Aircraft Weight: 54 oz	Temp: 34 F
Caller:	Bat used: A	Wind: calm
Launch: Beach	Power: 100% Throttle = 41 W; 75% Throttle = 27 W; 50% Throttle = 11 W	
Video: Slaughter	Barometer: 29.01 in Hg	

Notes: Overcast, low humidity, moist grass, CG at 0.4 MAC

Test	Ref No.	Description	Real Time	Flt Time
A	Straight & Level Glide			
	1	Launch	8:20	0:00
	2	Land		0:07
	Notes:			
B	Straight & Level Powered Full Throttle			
	1	Launch	8:38	0:00
	2	Control		0:12
	3	Land		0:17
	Notes:	L wing bent, R rear top guy wire snap, fuse/wing joint separated		
C	Coordinated Turn			
	1	Launch (full throttle)	9:05	0:00
	2	R turn – mostly rudder, slight ail.		0:16
	3	Land		0:26
	Notes:	Broken rudder bracket		
D	Coordinated Turn			
	1	Launch (100% throttle)	9:17	0:00
	2	R turn – mostly rudder		0:11
	3	Throttle reduction to 75%		0:14
	4	Land		0:18
	Notes:	Rudder bracket loose, top L wing T.E. deformed		

HPAG - VT		Model: 1/4 Scale Model	Test: 3
Dir:	Doughten	Test Location: Kentland Farms	Date: 11/09/06
Pilot:	Skidmore	Aircraft Weight: 54 oz	Temp: 51.8 F
Caller:		Bat used: A	Wind: 12.7 mph
Launch:	Beach	Power: 100% Throttle = 42 W; 50% Throttle = 16 W	
Video:	Slaughter	Barometer: 29.79 in Hg	

Notes: Foam wheel l.g. added, paperclip hinge on elev.,
CG 1 5/8”. Wing incidence @ root: top = 5 °. Bot = 2 °.

Test	Ref No.	Description	Real Time	Flt Time
A	Glide			
	1	Launch	7:27	0:00
	2	Crash (into Thalia)		0:08
	Notes:	Pilot comment: a/c began to respond at power-off to S&L		
		Broke motor mount => CA w/ lashing to repair		
B	Glide			
	1	Launch	7:56	0:00
	2	Power off		?
	3	Land		0:13
C	360 °. Turn			
	1	Launch	8:00	0:00
	2	Land		0:07
	Notes:	skid plate/landing gear complete break, Pilot: still sensitive in pitch		

HPAG - VT		Model: 1/4 Scale Model	Test: 4
Dir:	Doughten	Test Location: Kentland Farms	Date: 11/14/06
Pilot:	Skidmore	Aircraft Weight: 54 oz	Temp: 44 F
Caller:		Bat used: A	Wind: calm
Launch:	Beach	Notes: Elevator doesn't return to neutral after deflection – check clevis	
Video:	Slaughter	Barometer: 29.90 in Hg	

Test	Ref No.	Description	Real Time	Flt Time
A	Straight & Level Powered then glide			
	1	Launch	8:20	0:00
	2	Rudder surface flutter		0:01
	3	Throttle cut, flutter stopped		0:03
	4	Land		0:07
	Notes:	coord. ail. response, L wing joint Bent, loose rudder connection		
B	Powered 360 °. Turn			
	1	Launch	8:45	0:00
	2	Crash into telephone pole		0:09
C	Powered 360 °. Turn			
	1	Launch	8:55	0:00
	2	180 °. Turn		0:13
	3	90 °. Turn		0:34
	4	Land		0:36
D	Powered 360 °. Turn			
	1	Launch	8:57	0:00
	2	Ail. only 90 °. Turn		0:14
	3	Ail. w/ rudder 90 °. Turn		0:21
	4	~180 °. Turn		0:29
	5	Land		0:41
E	Powered 360 °. Turn			
	1	Launch	9:02	0:00
	2	180 °. Turn w/ rudder and ail.		0:16
	3	Land		0:31
	Notes:	pilot: natural L yaw tendency L top wing tip disconnect, L.G., elev ctrl horn, rudder bracket, clean up pin, re-bend pin		

HPAG - VT		Model: 1/4 Scale Model	Test: 5
Dir:	Doughten	Test Location: Kentland Farms	Date: 11/28/06
Pilot:	Skidmore	Aircraft Weight: 54.18 oz	Temp: 35.2 F
Caller:		Bat used: A	Wind: 7 mph
Launch:	Beach		
Video:	Slaughter	Barometer: 30.36 in Hg	

Test	Ref No.	Description	Real Time	Flt Time
A	360 °. Turns			
	1	Launch	8:25	0:00
	2	All ail. Turn		
	3	Land		
	Notes:	steady flt, no phugoid, broke L.G.		
B	Figure 8			
	1	Launch	8:45	0:00
	2	Unable to turn: attempt w/ both ail. and rudder		
	3	Bank L		
	4	Land		
	Notes:	Broke L.G., motor mount, guy wires, fix pins		

Appendix C. Test Flight Summary Sheets

HPAG Initial Flight-test Plan: Date: 10/03/06 Location: Kentland Farms

1. Pre-flight checklist:
    - __ Attach wings
        - __ Servo connections
        - __ Tape joints
    - __ Attach forward fuselage boom
        - __ Motor/servo connections
    - __ Attach tail surfaces (pinhead facing up on rudder)
    - __ Check strut joints
    - __ CG check

2. Range check radio
3. Field check

4. Glide Test
    - Hand launched
    - S & L flight

5. Straight and level flight – at least ~100ft
    - Hand launched

6. Demonstrate control authority in flight
    - Hand launched
    - Attempt steady roll, yaw – learn handling qualities
    - (Rudder primary control for roll)

7. Perform ~15° banked turn (left or right – choose depending on flight conditions)
    - Hand launched

8. Demonstrate landing in ~11° sideslip WOD conditions
    - Hand launched or complete at finish of previous flight-test

HPAG Initial Flight-test Plan: Date: 10/26/06 Location: Kentland Farms

1. Pre-flight checklist:
    - __ Attach wings
        - __ Servo connections
        - __ Tape joints
    - __ Attach forward fuselage boom
        - __ Motor/servo connections
    - __ Attach tail surfaces (pinhead facing up on rudder)
    - __ Check strut joints
    - __ CG check

2. Range check radio
3. Field check

4. Glide Test
    - Hand launched
    - S & L flight

5. Straight and level flight – at least ~100ft
    - Hand launched

6. Demonstrate control authority in flight
    - Hand launched
    - Attempt steady roll, yaw – learn handling qualities
    - (Rudder primary control for roll)

7. Perform ~15° banked turn (left or right – choose depending on flight conditions)
    - Hand launched

8. Demonstrate landing in ~11° sideslip WOD conditions
    - Hand launched or complete at finish of previous flight-test

HPAG Initial Flight-test Plan: Date: 11/09/06 Location: Kentland Farms

1. Pre-flight checklist:
    __ Attach wings
        __ Servo connections
        __ Tape joints
    __ Attach forward fuselage boom
        __ Motor/servo connections
    __ Attach tail surfaces (pinhead facing up on rudder)
    __ Check strut joints
    __ CG check

2. Range check radio
3. Field check

4. Glide Test
    - Hand launched
    - Powered start (full throttle?)
    - Cut throttle when A/C is 'wings steady,' straight and level
    - Observe glide angle (ensure camera man is in position perpendicular to flight path)

5. Attempt 360° controlled turn
    - Hand launched and powered (full throttle)
    - Apply bank and yaw as necessary to hold turn
        - Recommended turn radii for corresponding bank angles:
        $\varphi = 15°$: Radius = 35 – 40 ft
        $\varphi = 10°$: Radius = 50 – 60 ft
        $\varphi = 5°$: Radius = 95 – 100 ft

6. Attempt controlled turns at various bank angles
    - Hand launched and powered (full throttle)
    - Controlled turns at 15°, 10°, and 5° bank angles excepting what was successfully used for 360° turn (as close as pilot can)
        - Use recommended turn radii listed above
        - Try to keep steady AOA (CL required for these turns requires AOA of almost 7° - consider this an upper limit)
        - During each turn, stall margin will be low (about 0.2) – if A/C stalls, attempt landing
        - *watch for tip stalls

HPAG Initial Flight-test Plan: Date: 11/14/06 Location: Kentland Farms

1. Pre-flight checklist:
   - __ Attach wings
     - __ Servo connections
     - __ Tape joints
   - __ Attach forward fuselage boom
     - __ Motor/servo connections
   - __ Attach tail surfaces (pinhead facing up on rudder)
   - __ Check strut joints
   - __ CG check

2. Range check radio
3. Field check

4. Glide Test
   - Hand launched
   - Powered start (full throttle?)
   - Cut throttle when A/C is 'wings steady,' straight and level
   - Observe glide angle (ensure camera man is in position perpendicular to flight path)

5. Attempt 360° controlled turn
   - Hand launched and powered (full throttle)
   - Apply bank and yaw as necessary to hold turn
     - Recommended turn radii for corresponding bank angles:

     $\varphi = 15°$: Radius = 35 – 40 ft

     $\varphi = 10°$: Radius = 50 – 60 ft

     $\varphi = 5°$: Radius = 95 – 100 ft

6. Attempt controlled turns at various bank angles
   - Hand launched and powered (full throttle)
   - Controlled turns at 15°, 10°, and 5° bank angles excepting what was successfully used for 360° turn (as close as pilot can)
     - Use recommended turn radii listed above
     - Try to keep steady AOA (CL required for these turns requires AOA of almost 7° - consider this an upper limit)
     - During each turn, stall margin will be low (about 0.2) – if A/C stalls, attempt landing
     - *watch for tip stalls

HPAG Initial Flight-test Plan: Date: 11/28/06 Location: Kentland Farms

1. Pre-flight checklist:
    __ Attach wings
        __ Servo connections
        __ Tape joints
    __ Attach forward fuselage boom
        __ Motor/servo connections
    __ Attach tail surfaces (pinhead facing up on rudder)
    __ Check strut joints
    __ CG check

2. Range check radio
3. Field check

5. Attempt 360° controlled turn
    - Hand launched and powered (full throttle)
    - Apply bank and yaw as necessary to hold turn
        - Recommended turn radii for corresponding bank angles:
        $\varphi = 15°$: Radius = 35 – 40 ft
        $\varphi = 10°$: Radius = 50 – 60 ft
        $\varphi = 5°$: Radius = 95 – 100 ft

6. Attempt controlled turns at various bank angles
    - Hand launched and powered (full throttle)
    - Controlled turns at 15°, 10°, and 5° bank angles excepting what was successfully used for 360° turn (as close as pilot can)
        - Use recommended turn radii listed above
        - Try to keep steady AOA (CL required for these turns requires AOA of almost 7° - consider this an upper limit)
        - During each turn, stall margin will be low (about 0.2) – if A/C stalls, attempt landing
        - *watch for tip stalls

7. Attempt controlled turns at various power settings (between 75% and full)

Appendix D. Mission Model Code

```
%Calculates time taken to fly around the course twice (upwind and downwind) as func-
tion of speed and bank angle

%Course and atmospheric geometry
CCW_turn = [30;120;120;30]*pi/180; %course turn angles, rad
CW_turn = [120;120;120]*pi/180;  %Clockwise turn angles
length =[500;500;500]*3.28; %leg lengths, ft
w = 16.4; %wind speed, ft/sec
g = 32.2; %acceleration of gravity, ft/sec^2
q=1/2*.0023*180; %q=1/2*rho*S in slugs/ft, using a rho of .002slugs/ft^3 and a area
of 180ft^2
weight=215;     %weight of 215 pounds (page 46 in report)
cd0=.01;        %report quotes a cd0 of 0.00748 on page 25, using .01 for safety
k=1/(pi*60/1.5*1.18);  %k=1/(pi*AR*e) using an AR of 60/1.5 and an e of 1.18 (pg 27
in report)

% Preallocating cl required and power required
    clreq_cuw1=zeros(6,11);
    powerW_cuw1=zeros(6,11);
    powerE_cuw1=zeros(6,11);
    clreq_cuw2=zeros(6,11);
    powerW_cuw2=zeros(6,11);
    powerE_cuw2=zeros(6,11);
    clreq_dnw=zeros(6,11);
    powerW_dnw=zeros(6,11);
    powerE_dnw=zeros(6,11);
    clreq_CCW=zeros(6,11);
    powerW_CCW=zeros(6,11);
    powerE_CCW=zeros(6,11);
    clreq_upw=zeros(6,11);
    powerW_upw=zeros(6,11);
    powerE_upw=zeros(6,11);
    clreq_cdw1=zeros(6,11);
    powerW_cdw1=zeros(6,11);
    powerE_cdw1=zeros(6,11);
    clreq_cdw2=zeros(6,11);
    powerW_cdw2=zeros(6,11);
    powerE_cdw2=zeros(6,11);
    clreq_CW=zeros(6,11);
    powerW_CW=zeros(6,11);
    powerE_CW=zeros(6,11);
    time=zeros(6,11);
    CW_time=zeros(6,11);
    CCW_time=zeros(6,11);
    v_concat=zeros(1,11);
    phi_concat=zeros(1,6);

%On/off switches for outputs and calculation method
seconds = 0;
labels=0;
indpower=0;%printout the individual power graphs for each leg, versus one for turn
and one for straight legs
clreqplot=0;%print plots of clrequired
```

```
phiindex = 1;
for phi = (15)*pi/180; %bank angle, rad
    vindex = 1;
    for v = (20:30)*(5280/3600); %airspeed in mph, conversion to ft/sec shown


        %FIND GROUNDSPEEDS and TIMES
        %Cross-upwind legs 1 and 2
                %By Law of Cosines, it can be shown that vg.^2 - (2*w*cos(angle))*vg
+(w^2-v^2) = 0
                %where angle is the interior angle between vg and wind vector, inde-
pendent of v.
                %Then, by solve(vg.^2 - (2*w*cos(angle))*vg +(w^2-v^2),vg), we get
                %vg = [ w*cos(angle)+(w^2*cos(angle)^2-w^2+v^2)^(1/2)]
                %      [ w*cos(angle)-(w^2*cos(angle)^2-w^2+v^2)^(1/2)]
                %Of which only the first is the positive root.
            angle =120*pi/180;  %For this leg, interior angle is 120 deg (converted
to radians)
            vg_cuw1 = w*cos(angle)+(w^2*cos(angle)^2-w^2+v^2)^(1/2);
            vg_cuw2 = vg_cuw1;

            cuw1_t = length(1)/vg_cuw1;
            cuw2_t =cuw1_t;

            %The following 3 calcs are currently the same for all legs of
            %the course except for the turns, however, when the effect of
            %the crosswind is factored in later, they will be different due
            %to the increased power required to keep a straight heading in
            %a crosswind.
            n=1;    %load factor of 1 used, which isn't entirely correct due to
crosswind
            clreq_cuw1(phiindex,vindex)=n.*weight./(v.^2.*q); %Calculates cl re-
quired for flight
            [powerW_cuw1(phiindex,vindex),powerE_cuw1(phiindex,vindex)]=powerrequir
ed(v,n,q,weight,cd0,k);

            clreq_cuw2(phiindex,vindex)=clreq_cuw1(phiindex,vindex);
            powerW_cuw2(phiindex,vindex)=powerW_cuw1(phiindex,vindex);
            powerE_cuw2(phiindex,vindex)=powerE_cuw1(phiindex,vindex);

        %Downwind leg
            vg_dnw = v +w;

            dnw_t = length(2)/vg_dnw;

            n=1;    %load factor of 1 used
            clreq_dnw(phiindex,vindex)=n.*weight./(v.^2.*q); %Calculates cl required
for flight
            [powerW_dnw(phiindex,vindex),powerE_dnw(phiindex,vindex)]=powerrequired
(v,n,q,weight,cd0,k);


        %Turn lengths
            %radius
            CCW_R = v.^2/g ./tan(phi);
```

```
            %distances
            CCW_s = CCW_R*CCW_turn;
            %use average speed for turns
            CCW_v_avg = (vg_cuw1+vg_dnw+vg_cuw2)/3;
            %time
            CCW_turn_t = sum(CCW_s)/CCW_v_avg;

            n=1./cos(phi);    %load factor calculated from bank angle for coordi-
nated turn
            clreq_CCW(phiindex,vindex)=n.*weight./(v.^2.*q); %Calculates cl required
for flight
            [powerW_CCW(phiindex,vindex),powerE_CCW(phiindex,vindex)]=powerrequired
(v,n,q,weight,cd0,k);


        %CLOCKWISE
        %Upwind leg
            vg_upw = v-w;
            upw_t = length(2)/vg_upw;

            n=1;    %load factor of 1 used
            clreq_upw(phiindex,vindex)=n.*weight./(v.^2.*q); %Calculates cl required
for flight
            [powerW_upw(phiindex,vindex),powerE_upw(phiindex,vindex)]=powerrequired
(v,n,q,weight,cd0,k);

        %Cross downwind 1 and 2
            %Law of cosines shows that vg^2 - 2*w*cos(angle)*vg + w^2-v^2 = 0, which
solves by >> solve(vg^2 - 2*w*cos(angle)*vg + w^2-v^2, vg)
            %to give vg =
            %[ w*cos(angle)+(w^2*cos(angle)^2-w^2+v^2)^(1/2)]
            %[ w*cos(angle)-(w^2*cos(angle)^2-w^2+v^2)^(1/2)]

            %for both cross downwind legs, angle =60 deg
            angle = 60*pi/180;
            vg_cdw1 = w*cos(angle)+(w^2*cos(angle)^2-w^2+v^2)^(1/2);
            vg_cdw2 = vg_cdw1;

            cdw1_t = length(1)/vg_cdw1;
            cdw2_t = length(3)/vg_cdw2;

            n=1;    %load factor of 1 used, which isn't entirely correct due to
crosswind
            clreq_cdw1(phiindex,vindex)=n.*weight./(v.^2.*q); %Calculates cl re-
quired for flight
            [powerW_cdw1(phiindex,vindex),powerE_cdw1(phiindex,vindex)]=powerrequir
ed(v,n,q,weight,cd0,k);

            clreq_cdw2(phiindex,vindex)=clreq_cdw1(phiindex,vindex);
            powerW_cdw2(phiindex,vindex)=powerW_cdw1(phiindex,vindex);
            powerE_cdw2(phiindex,vindex)=powerE_cdw1(phiindex,vindex);

            %Add in turn time, using average speed
            CW_s = CCW_R*CW_turn;
            CW_v_avg = (vg_upw + vg_cdw1 +vg_cdw2)/3;
            CW_turn_t = sum(CW_s)/CW_v_avg;
```

```
            n=1./cos(phi);    %load factor calculated from bank angle for coordi-
nated turn
            clreq_CW(phiindex,vindex)=n.*weight./(v.^2.*q); %Calculates cl required
for flight
            [powerW_CW(phiindex,vindex),powerE_CW(phiindex,vindex)]=powerrequired(v
,n,q,weight,cd0,k);

        %Sum times
            time(phiindex,vindex) = CCW_turn_t+ cuw1_t+ dnw_t+cuw2_t +  upw_t +
cdw1_t +cdw2_t + CW_turn_t;
            CW_time(phiindex,vindex) = upw_t + cdw1_t +cdw2_t + CW_turn_t;
            CCW_time(phiindex,vindex) = CCW_turn_t+ cuw1_t+ dnw_t+cuw2_t;
            v_concat(vindex) = v;

            vindex = vindex+1;

    end

    v_mph = v_concat*3600/5280;

    %TOTAL COURSE
        if seconds
        figure(1) %Seconds
        plot(v_mph,time(phiindex,:),'-')
        hold on
        end
        figure(2) %Minutes
        plot(v_mph,time(phiindex,:)/60,'-')
        hold on
    %CLOCKWISE
        if seconds
        figure(3) %Seconds
        plot(v_mph,CW_time(phiindex,:),'-')
        hold on
        end
        figure(4) %Minutes
        plot(v_mph,CW_time(phiindex,:)/60,'-')
        hold on
    %COUNTERCLOCKWISE
        if seconds
        figure(5) %Seconds
        plot(v_mph,CCW_time(phiindex,:),'-')
        hold on
        end
        figure(6) %Minutes
        plot(v_mph,CCW_time(phiindex,:)/60,'-')
        hold on
    %Cl and Power required
        if clreqplot
            figure(7)
            plot(v_mph,clreq_dnw(phiindex,:))
            hold on
            figure(8)
            plot(v_mph,clreq_CCW(phiindex,:))
            hold on
```

```
            figure(9)
            plot(v_mph,clreq_CW(phiindex,:))
            hold on
        end
        figure (10)
        plot(v_mph,powerW_dnw(phiindex,:))
        hold on
        figure (11)
        plot(v_mph,powerW_CCW(phiindex,:))
        hold on
        figure (12)
        plot(v_mph,powerW_CW(phiindex,:))
        hold on

    phi_concat(phiindex) = phi;
    phiindex=phiindex+1;
end %end of bank angle loop


%FIGURE ANNOTATIONS AND LABELS
%TOTAL
    if seconds
        figure(1)
        xlabel('Indicated Velocity (mph)')
        ylabel('Time to complete course (sec)')
        title('Time to complete full course vs airspeed')
        grid on
        %add course deadline
        siz_v = size(v_concat);
        plot(v_mph, 7*60*ones(1,siz_v(2)), 'x-')

        if labels
            clear phi
            for phi =phi_concat;
                string = sprintf('=%2.0f',phi*180/pi);
                gtext(['\phi' string])
            end
        end

    end

    figure(2)
    xlabel('Indicated Velocity (mph)')
    ylabel('Time to complete course (min)')
    title('Time to complete full course vs airspeed')
    grid on
    %add course deadline
    siz_v = size(v_concat);
    plot(v_mph, 7*ones(1,siz_v(2)), 'x-')

    if labels
        clear phi
        for phi =phi_concat;
            string = sprintf('=%2.0f',phi*180/pi);
            gtext(['\phi' string])
        end
```

```
    end

%CW
    if seconds
        figure(3)
        xlabel('Indicated Velocity (mph)')
        ylabel('Time to complete course (sec)')
        title('Time to complete CW course vs airspeed')
        grid on

        if labels
            clear phi
            for phi =phi_concat;
                string = sprintf('=%2.0f',phi*180/pi);
                gtext(['\phi' string])
            end
        end
    end

    figure(4)
    xlabel('Indicated Velocity (mph)')
    ylabel('Time to complete course (min)')
    title('Time to complete CW course vs airspeed')
    grid on

    if labels
        clear phi
        for phi =phi_concat;
            string = sprintf('=%2.0f',phi*180/pi);
            gtext(['\phi' string])
        end
    end


%CCW
    if seconds
        figure(5)
        xlabel('Indicated Velocity (mph)')
        ylabel('Time to complete course (sec)')
        title('Time to complete CCW course vs airspeed')
        grid on

        if labels
            clear phi
            for phi =phi_concat;
                string = sprintf('=%2.0f',phi*180/pi);
                gtext(['\phi' string])
            end
        end
    end

    figure(6)
    xlabel('Indicated Velocity (mph)')
    ylabel('Time to complete course (min)')
    title('Time to complete CCW course vs airspeed')
    grid on
```

```
    if labels
        clear phi
        for phi =phi_concat;
            string = sprintf('=%2.0f',phi*180/pi);
            gtext(['\phi' string])
        end
    end


%Cl and Power required
if clreqplot
    figure(7)
    xlabel('Indicated Velocity (mph)')
    ylabel('Cl Required on Downwind Leg')
    title('Cl required on Downwind Leg vs airspeed')
    grid on
%   labels   %ALL BANK ANGLES ARE THE SAME NO NEED FOR LABELS
    figure(8)
    xlabel('Indicated Velocity (mph)')
    ylabel('Cl Required on CCW Turn')
    title('Cl required on CCW Turn vs airspeed')
    grid on
    if labels
        clear phi
        for phi =phi_concat;
            string = sprintf('=%2.0f',phi*180/pi);
            gtext(['\phi' string])
        end
    end
    figure(9)
    xlabel('Indicated Velocity (mph)')
    ylabel('Cl Required on CW Turn')
    title('Cl required on CW Turn vs airspeed')
    grid on
    if labels
        clear phi
        for phi =phi_concat;
            string = sprintf('=%2.0f',phi*180/pi);
            gtext(['\phi' string])
        end
    end
end
    figure (10)
    xlabel('Indicated Velocity (mph)')
    ylabel('Power Required on Downwind Leg (watts)')
    title('Power Required on Downwind Leg vs airspeed')
    grid on
%   labels   %ALL BANK ANGLES ARE THE SAME NO NEED FOR LABELS
    figure (11)
    xlabel('Indicated Velocity (mph)')
    ylabel('Power Required on CCW Turn (watts)')
    title('Power Required on CCW Turn vs airspeed')
    grid on
    if labels
        clear phi
```

```
        for phi =phi_concat;
            string = sprintf('=%2.0f',phi*180/pi);
            gtext(['\phi' string])
        end
    end
    figure (12)
    xlabel('Indicated Velocity (mph)')
    ylabel('Power Required on CW Turn (watts)')
    title('Power Required on CW Turn vs airspeed')
    grid on
    if labels
        clear phi
        for phi =phi_concat;
            string = sprintf('=%2.0f',phi*180/pi);
            gtext(['\phi' string])
        end
    end
```

Human Powered Aircraft Group
at Virginia Tech
presents

The Iron Butterfly

A Human Powered Aircraft for Sport

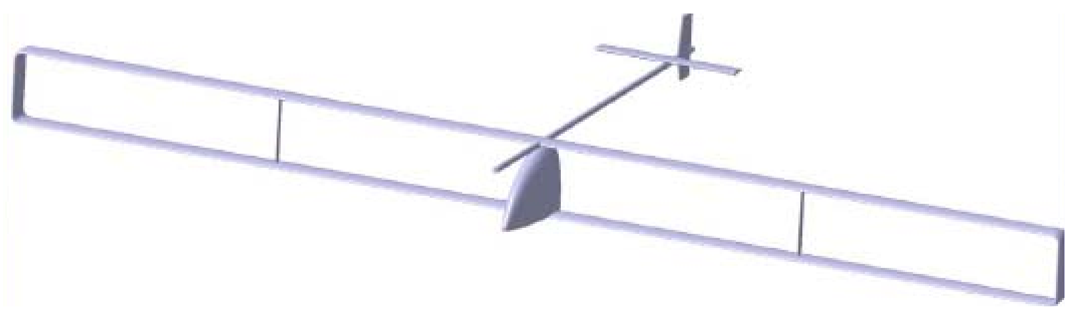

Aerospace and Ocean Engineering Department
Virginia Polytechnic Institute and State University
May 4, 2005

Team Members:

Chris Emory
Imraan Faruque
Matthew Janeway
Blake Jeans
Jason Roadman
Lee Skidmore
Wesley Slemp

Contents

1. Executive Summary

1.1 Conceptual Design

The first phase in the design process was conceptual design. The team thoroughly went over the rules for the Kremer Human Powered Aircraft (HPA) for Sport Prize. A mission analysis was performed to indicate how the airplane would need to perform. A set of design constraints was defined based on the rules, the mission analysis, and the capability of a human propulsion and control system. Given the design constraints, each team member developed a basic concept. The team evaluated the concepts and ranked them in a design matrix based on a number of criteria deemed important for a successful design.

1.2 Aerodynamics

Preliminary aerodynamic analysis began with a comparison between the top two conceptual designs. With a boxplane design coming out on top, airfoils were researched and the best options were selected. The wing area was then selected through a constraint analysis based on the design requirements. The drag of the design was analyzed in detail. The wing and tail surfaces were shaped and configured to give the most functional and lowest drag configuration.

1.3 Structures

The structural analysis began with a comparison between a monoplane and a biplane wing structure. Some simple models were built and tested. When the biplane model proved superior an analytical structural solution was created. Finite element analysis was used to further analyze and refine the structural design. The finite element analysis results were validated using the data from the simple biplane structure model tests. The number of struts on each wing was determined with a trade study considering mostly drag. The gap between the wings was determined through parametric study with the goal of minimizing drag. The materials were selected and the structural configuration was developed based on constraints which were set for the final structural design.

1.4 Stability and Control

Evaluation of stability and control began with defining detailed requirements for the airplane. The longitudinal stability and control characteristics were assessed first, followed by the lateral and directional. An initial control scheme derived from examination of similar aircraft was developed. The control surfaces were sized analytically. The aircraft dihedral was selected through parametric study of a simplified layout using a vortex lattice code. Finally, a more detailed model was developed to preform final verification of compliance with the requirements.

1.5 Human Propulsion

To gain a better understanding of the propulsion system for the airplane, human power production was researched. Learning that the process by which power was being produced for the airplane was about 25% efficient, a cooling system was designed for the cockpit to remove excess heat. A bicycle like drive train was designed to get the power from the pilot's legs to the aircraft's propeller. Research was conducted to determine the best pilot position and a seat was designed to accomodate this position.

1.6 Propeller Design

A propeller was designed using several methods to get very efficient power production at the design conditions. A automatic pitch controller was designed to regulate the propeller pitch to get the optimum performance at various flight conditions.

1.7 R/C Model Development

A quarter scale R/C model was designed to evaluate the dynamic stability and control of the model. The model was Froude scaled so it would behave dynamically similar to the full scale aircraft. The wing wing designed so it would perform like the the full scale wing. The structure was designed overly rigid to remove some aeroelastic effects and built with some artificial deflection so the deflection in flight would be the same for the quarter and full scale. Since the model was Froude scaled, it should behave dynamically similarly; however, the dynamic and control similarity was analyzed for verification. Some simple flight tests were conducted and some fixable problems were encountered.

2. Background and Narrative

The catalyst for most human-powered aircraft (HPA) activity for the past 40 years or so has been the Kremer Prizes offered by the Royal Aeronautical Society. The competitions have dictated the design criteria for most HPAs since the advent of the prize in 1959. The requirement of this first prize was to fly a figure-8 course. The completion of the objectives set out by the different prizes has separated the many failed HPA from the successful ones. The first successful HPA was Paul McCready's Gossamer Condor which won the first Kremer Prize in 1977 a whole 18 years after the prize had been introduced[1]. Many of the early attempts at HPA were based on emulating sailplanes. McCready changed the direction and expanded on the concepts used in hang-gilders to create his successful HPA. The major change in thought then went from trying to add human-power to sailplanes to creating extremely light airplanes.

McCready also won the next Kremer Cross Channel Prize only two years later in 1979[1]. The Gossamer Albatross was the plane his team created to cross the English Channel. Five years later the RAS offered a new prize for a speed aircraft. With a bit of a departure from the previous rules, the speed aircraft rules allowed for ten minutes of energy storage by the pilot just prior to the flight. There were two main competitors for the speed prize, again McCready and now a group of students from MIT. McCready's team designed the Bionic Bat and managed to attempt to fly the course before the MIT team. The attempt was initially declared successful; however, the officials governing the competition decided that McCready's method for proving the batters he used for energy storage only had the pilot's energy stored in them was not sufficient and the attempt was made void. McCready's team then departed from the energy storage method all together and attempted to modify the plane to do the lap in time under human power alone. The MIT group took this opportunity and adapted to the method for proving the batteries to be dead and successfully flew their entry Monarch to win the prize.

There have additionally been several non-Kremer entry successful HPAs. One of the earliest successful designs other than those by McCready was Chrysalis. It was a biplane designed by a group of MIT students in the late '70s. MIT also did a project to recreate the mythical flight of Daedalus from the island of Crete. The prototype for this project, called the Michelob Light Eagle, as well as two Daedalus aircraft, 88 and 89, were constructed. Germany has also had a few successful HPA the Velair 89 as well as the Musculair 1 and 2[2].

The designs of many of the successful HPA have several similar characteristics. Table 2.1 details some of the design points on all of the aircraft mentioned. The first and very important similarity is the pilot seating position. In all but the Condor, the pilot is seated in a recumbent position. This position proves to be much better for power production than the upright position. Another important similarity is the aft tail on all but the two Gossamer aircraft. This is likely for aerodynamic efficiency. With the exception of Chrysalis which was a biplane, all the planes have high and generally straight wings. The reason for high wings is likely prop clearance and possibly structure. One similarity between most the control systems is an all flying tail, many of them with anti-servo tabs. Most the planes have some type of ailerons. The main one that did not was Daedalus. They were cut from Daedalus to remove a small amount of weight and since the mission of Daedalus involved almost no turning they did not really seem necessary. There is a fairly even mixed bag when it comes to tractor or pusher prop configuration. All the MIT planes are tractors while all the other planes are pushers. In the table, the span of the Monarch is bolded because it is not like the others in the fact that it is much smaller. The Monarch had to fly the same course as the current Kremer prize requires where most the other planes with larger spans were for endurance.

The new set of rules for the Kremer Sport Prize contains one major difference from all the previous prizes. It has a minimum wind velocity required during the prize flight. As a result of this

Table 2.1. Comparison Table for previous HPAs

	Gossamer Condor	Gossamer Albatross	Chrysalis	Bionic Bat	Monarch	Daedalus	Velair	Musculair
Span [ft]	95	95	72	?	62	112	76	64
Arrangment	high swept	high swept	biplane	high straight	high straight	high straight	high straight	high straight
Pilot Pos.	upright	recumbent	recumbent	recumbent	recumbent	recumbent	recumbent	recumbent
Tail Config.	forward	forward	aft	aft	aft	aft	aft	aft
Prop Pos.	pusher	pusher	tractor	pusher	tractor	tractor	pusher	pusher
Roll Control	wing warping	wing warping	wing warping	ailerons	ailerons	secondary	rotating tips	aileron

wind requirement the plane will have to have a significantly higher indicated airspeed. The plane will also have to be more docile to be able to deal with the two crosswind legs of the flight. The plane has to have a quick assembly and disassembly and be stored in a trailer of specified maximum size. The speed required due to the wind will likely require a smaller airplane than the previous prizes. The plane will have to be even lower drag and lighter than the previous aircraft. The prize flight will likely require a very well trained athlete capable of producing the higher power that will be needed to attain the required ground speed. The new plane will also need to make tighter turns so it does not have to fly a great bit further than the unreachable minimum of 1500 m. Considering the timed assembly and disassembly the structural and control linkages will have to be as simple as possible. All in all, to win the new prize a next step will have to be taken in the performance level of the airplane.

3. Conceptual Design

3.1 Mission Analysis

This aircraft was designed for the Kremer Sport Prize, whose rules are available from the Human Powered Aircraft Group of the Royal Aeronautical Society[1]. After careful examination of these rules, several key considerations were identified: complete of a 4920 ft long, triangular course in both directions in 7 min or less, cross the start/finish line at a minimum altitude of 16.4 ft, have low initial and repair costs, assemble within 30 min from a 26.4 ft long trailer, and be suitable for small batch or kit production.

A vital component of mission success is the identification of how the course must be flown. The Kremer Sport Competition rules state that the vehicle must fly about a course consisting of markers placed in an equilateral triangle with 1640 ft long sides. This flight must be conducted in both directions with wind speeds not less than 16.4 ft/sec (11.2 mph). See Fig. 3.1. During the flights, the vehicle must cross the start/finish line with a minimum height of 16.4 ft. Both flights must be completed in a total time of 7 min. A 1 hr recovery break is permitted between flights.

The designer is given the freedom to choose the specific path through which the HPA navigates the course and the speed and bank angle at which this must be conducted. This is an important consideration since the shortest path is not necessarily the quickest and may not even be possible. All HPAs to date have had severely limited roll control. To quantitatively identify the constraints that this course imposed on a vehicle, a reasonable, but not optimum, path was chosen through it, as shown in Fig. 3.1. The chosen path is more demanding than the optimum, to ensure a margin of safety with respect to time and performance. A vehicle designed to successfully navigate the chosen path within the specified time should be capable of completing a more optimum path in less time.

This mission can generally be then described as takeoff and climb, the three legs of the triangle,

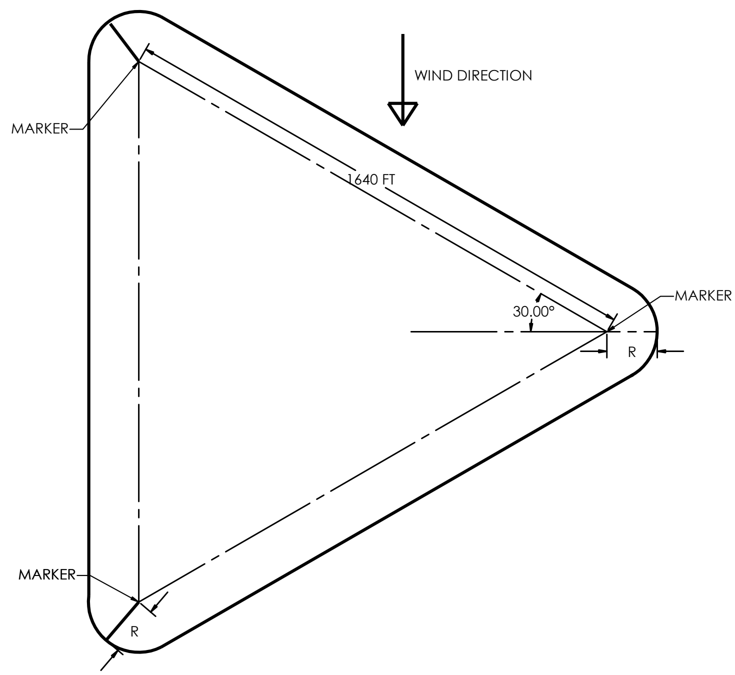

Figure 3.1. Kremer Sport Prize geometry and path.

the turns, and landing. Since the three straight legs and turns are the timed portion of the flight, this was the area of focus during mission analysis. Basic aircraft performance equations were used to model the vehicle's travel about the specified course. The ground speed v_g of an aircraft traveling along the straight legs can be found using the indicated airspeed v, the wind speed w, and the angle relative to the reference line θ. The ground speed can be found by the law of cosines to be:

$$v_g = w\cos(\theta) + \sqrt{w^2\cos^2(\theta) - w^2 + v^2} \tag{3.1}$$

The distance in the turns is a function of the turning radius, which can be found from the bank angle, direction, and flight speed. The turn radius equation is shown in Eq. (3.2), where a turn radius R is specified by the flight velocity v and the bank angle under the influence of gravity g. The average ground speed through these turns was based on the mean value theorem performed on vehicle heading with respect to wind.

$$R = \frac{v^2}{g\tan(\phi)} \tag{3.2}$$

A plot of course time vs. flight speed over a range of bank angles was constructed and is shown in Fig. 3.2. A hashed horizontal line was drawn at 7 min to mark the course deadline. While the time required to complete the course reduces with increasing bank angle, there is a point of diminishing returns and there is little time savings for a bank angle greater than 15 deg. A bank angle this great substantially increases the loads, height, and control moments required for flight. Accordingly, the vehicle was constrained to fly at a velocity of 33ft/s (22.5 mph) and be capable of banking at 15 deg.

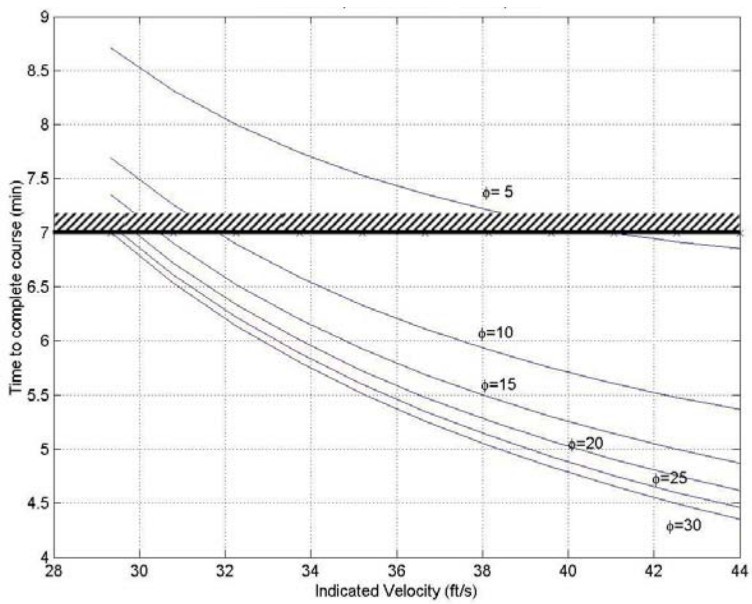

Figure 3.2. Speed, bank angle, and time required to complete course.

The idea behind the sport prize is to make HPAs more practical so that they may be created as a kit and assembled by a hobbyist at relatively low cost. Accordingly, it must be transported in a 26.4 ft maximum length trailer, and subsequently be assembled and ready to fly in less than 30 min. This puts limitations on the size of the aircraft, which must obviously be less than the inside length of the trailer. First, the Code of Virginia was consulted to ensure that a 26.4 ft long trailer was below the legal length limitation in the area in which it would be constructed. Aircraft length and wing panels were restricted to a maximum of 26 ft.

In summary, analysis of the mission creates the following constraints on the human powered airplane: a cruise speed of 33 ft/s or greater, a bank angle capability of 15 deg (in reasonable time), a maximum part length of 26 ft, and a maximum wingspan of 60 ft. Additionally, emphasis is placed on simplicity of construction to allow fast assembly.

3.2 Conceptual Configurations

With the results of the mission analysis and design constraints defined, each team member developed a conceptual design. Each unique viewpoint developed a unique concept configuration. Each configuration focused on different aspects required to complete the mission.

3.2.1 Feathers

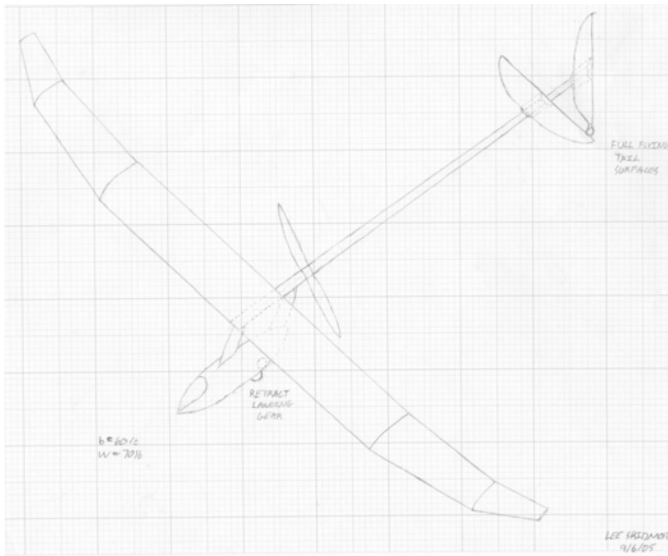

Figure 3.3. Sketch of Feathers concept.

The Feathers concept focuses solely on drag reduction. The wing planform is derived from high-performance sailplane configurations with high aspect ratio wings that reduce span loading and a triple-taper wing to approximate the "aerodynamically ideal" elliptical lift distribution. These two features minimize induced drag. The fuselage is a small pod just large enough to contain the pilot and mechanical components. The small pod has minimal area to reduce friction drag and a streamlined shape to reduce form drag. By mounting the wing on two small pylons, interference drag between the fuselage and the wing is minimized. This approach has been proven effective with world class Radio Controlled (R/C) sailplanes. Continuing to follow R/C sailplane design techniques the tail surfaces are fully flying and mounted to pylons attached to a long boom. The long tail moment arm reduces the required tail area and tail loads, thereby minimizing friction and induced drag. An unusual feature of this concept is the boom-centric propeller. This allows the wing and fuselage to operate in undisturbed air which reduces friction drag. The center wing sees increased air velocity while the tails operate in accelerated flow from the propeller increasing low speed control authority. Conversely, boom-centric propeller is mechanically difficult.

The Feathers concept has potential for very low drag. However, obtaining this low drag requires a large wingspan that is detrimental to turning performance and trailer space utilization. The pod-style fuselage also presents construction challenges and the attachment pylons may not be structurally efficient once landing conditions are considered. Due to trailer length limitations, the long tail boom requires two piece construction adding additional weight and structural complexity. While Feathers is very efficient aerodynamically, structural and practical construction considerations negate these advantages.

3.2.2 Squished Bat

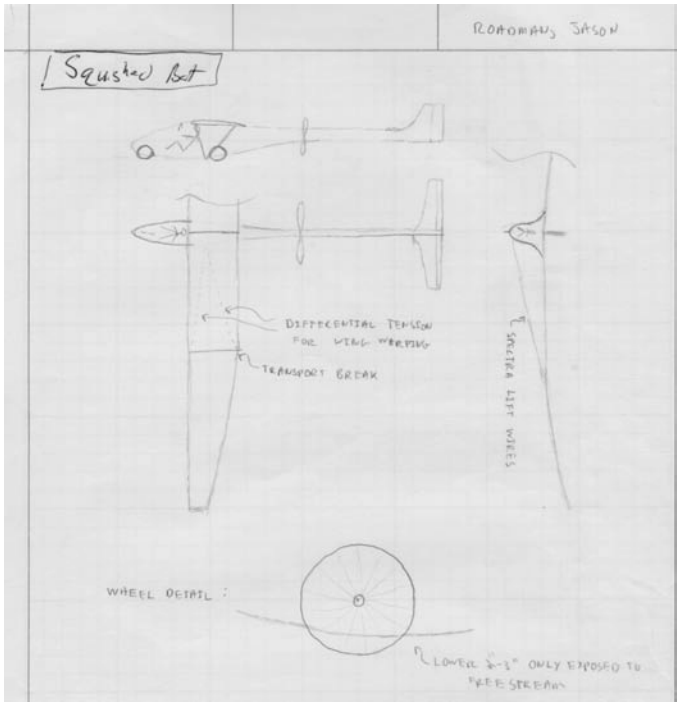

Figure 3.4. Squished Bat Concept sketch.

The Squished Bat concept was investigated in an attempt to build upon the success of Paul MacCready's Bionic Bat. The Bionic Bat was an HPA designed to fly a course similar to the Kremer Sport Prize; however, it utilized electronic power to supplement the pilot. The relatively simple and proven monoplane design was chosen to minimize aircraft drag and maximize overall efficiency. This also simplified aerodynamic and structural analysis.

For this concept, the Bionic Bat design was modified by shrinking the height of the fuselage in an attempt to further reduce its associated drag. The pilot is placed in a recumbent position with the top of his head flush with the top of the wing. Landing gear are placed fore and aft of the pilot, further reducing fuselage height. Placing the pilot in a more reclined position limits frontal area; however, a more upright riding style would allow for visibility.

Additionally, roll control through wing warping could be employed reducing the amount of sideslip and associated drag necessary in a turn. Two flying wires per wing would be used with separate mounting points along the chord. Differential tension in the wires would thereby twist the wings. The added drag from the flying wires is detrimental to performance.

3.2.3 Duck

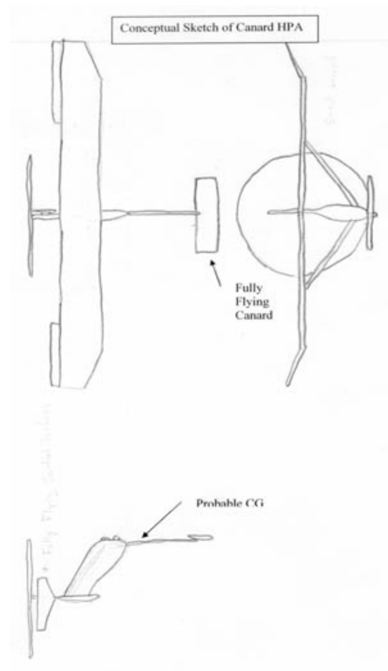

Figure 3.5. Duck.

The Duck concept was developed to be very similar to the Gossamer Condor, the first HPA to win a Kremer Prize[3]. The most distinguishing feature of the Duck was its use of a forward canard to balance and control the airplane. The design uses flying wires to twist the wing and tilt the canard. The tilted canard generates a yaw moment and a secondary roll moment due to roll-yaw coupling. Gossamer Condor's success has proven the control system to be effective. Further, the high wing and canard placement provide the pilot with improved visibility in flight.

The design exhibits poor aerodynamic efficiency due to the required flying wires. The need for flying wires to twist the wing increases the parasite drag. The uniqueness of the roll control scheme complicates control analysis. Stability restricts the wings lifting capabilities. While the Gossamer Condor met its design goals, it flew much slower than required for the Sport Prize.

3.2.4 Bert

The concept called Bert was an attempt to get the most use possible out of every part of the airplane. It had a tandem wing design where the area used for lifting was also used for longitudinal stability and control. The front lifting surface was made larger so it would carry more aerodynamic load to minimize induced drag. The larger front wing was drawn with a high aspect ratio to maximize aerodynamic efficiency. The smaller aft wing held all the controls for pitch and roll so

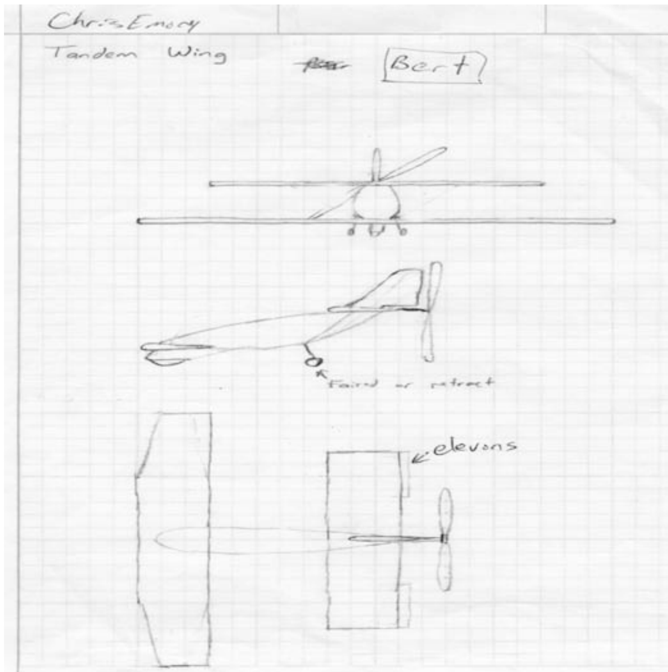

Figure 3.6. Tandem wing concept referred to as "Bert.".

the structure in the larger wing did not have to carry control loads. Roll controls on the smaller wing would have to be larger or deflected more, but would also require less structure due to the shorter moment arm. The fuselage was used to connect the two wings as well as house the pilot. The propeller was placed at the rear of the aircraft because it was the most convenient place, it kept the wings, fuselage, and controls in clean air flow, and it allowed the most propeller clearance.

The Bert concept had aerodynamic advantages because of the non-planar lifting configuration. It also posed the potential for low drag since it did not have a long tail boom and tail surfaces. Since all the load paths were short and direct, it had potential for a very light structure. The highly exposed fuselage would make it very easy to get the pilot inside and give the pilot better visibility. The drawback to the Bert design was that all the advantages would come from a great deal of work and were not guaranteed. The configuration would be complicated and difficult to analyze for aerodynamics and stability. With two separate wings that would need to be broken down to fit into the trailer, assembly was more complicated. Construction and structural analysis would also be difficult with the complex way the fuselage tied into the wings.

3.2.5 Fighting Fish

The fighting fish concept was developed by designing the aircraft around the ideal for the propulsion system. The pilot's position was first established and the rest of the aircraft was shaped around the pilot. The wing was placed above the cockpit to provide good visibility and increase the roll

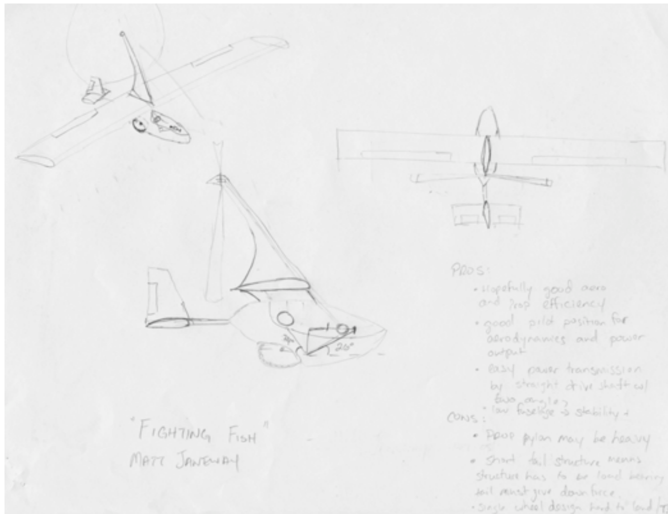

Figure 3.7. Fighting Fish concept sketch.

stiffness of the aircraft in the hope that the pilot need not concentrate extensively on flying while pedaling. Horizontal and vertical tails were placed in their conventional locations for simplicity of analysis. To fit a large propeller above the tail boom and to keep it out of the effects of the fuselage wake, a large propeller boom was designed above the wing. Finally, landing gear was added fore and aft of the pilot's seat to easily support the center of gravity.

Unfortunately, several negative issues become apparent quickly when analyzing this concept. First, the large propeller boom adds a significant amount of unwanted structure and weight. Placing the center of the propeller this high above the centerline of the aircraft also produces a very significant nose down pitching moment. Secondly, placing the propeller in this high position complicates the drive train by forcing two axis-of-rotation angle changes. Other designs only require one axis-of-rotation angle change of 90 deg.

3.2.6 Bipolar

The concept known as Bipolar was a biplane concept inspired by MIT's Chrysalis and resulted from a realization of the decrease in induced drag achieved with a biplane over a monoplane. A large span is desired to create a low drag profile. If an aircraft's span is limited to less than the optimum monoplane span, then a biplane configuration should be considered because it increases the effective aspect ratio. A biplane configuration also reduces the Reynolds number across the wing by reduction of the chord (versus the monoplane) aiding in the reduction of friction drag. This vehicle was envisioned to have full-flying tail surfaces to reduce the size and complexity thus reducing the total weight and assembly time of the surfaces. Struts placed between the wings to reduce the required weight of the spar structure and impose a smaller drag penalty than flying

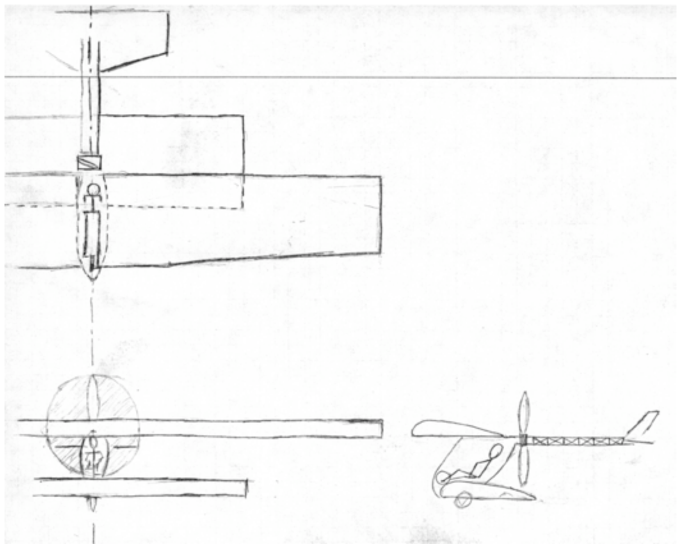

Figure 3.8. Conceptual sketch of Bipolar.

wires. A lightweight carbon-fiber or aluminum tail boom joins the fuselage to the tail.

Additionally, the tractor propeller configuration was selected for three reasons. First, the need for a large diameter prop to maintain efficiency means that the aft-mounted pusher prop would need to be mounted as high as possible, presumably boom-centric. A boom-centric propeller is mechanically complex and can easily be avoided with a tractor propeller. Second, in this configuration the propeller is presented with clean and undisturbed air flow which is required for its efficient operation. The final advantage to a tractor mounted propeller is the ram-air effect afforded to a pilot cooling duct on the fuselage.

There are disadvantages to this design. A biplane has lower induced drag only if the vehicle must have a limited span. At the time this concept was conceived, it was not clear whether the optimum span would be greater than that available with a three-piece monoplane wing span of 60 ft. There is the added task of fabricating two wings, and the fuselage must be stiffened between the wings. Analysis is more complicated leading to a potential for more errors. The lower wing offers less ground clearance and constrains low-altitude bank angles more than a high wing aircraft; however, adding dihedral to the lower wing could help remedy this problem. Finally, the ideal gap (vertical separation between the wings) is infinite, meaning that a taller fuselage is preferred aerodynamically.

3.3 Figure of Merit based Concept Selection

To objectively evaluate the relative capability of the concepts presented, a figure of merit system was used. The Feathers concept selected as the baseline because of its traditional layout. This concept was then given the reference score of zero and all other concepts were benchmarked against it. In each category, a design was assigned a plus one if better than the reference, a minus one if worse, and a zero if there was no real difference. In the case of outstandingly superior performance in a category, a score of two might be assigned, but this was done sparingly. The concepts were rated on the basis of the following factors:

1. Efficiency of structure: This score was based on the subjective interpretation of how well structure (and hence mass) was utilized on the vehicle. Does the structure serve multiple purposes? Are the load paths clearly delineated and in areas of natural reinforcement?
2. Efficiency of aerodynamics: This score was based on how well the concept was expected to perform with respect to both skin friction and induced drag. For example, items with more protruding surfaces such as flying wires received lower scores here.
3. Trailer fitting/ease of assembly: This score reflects the vehicle's ease of assembly. Concepts which integrate extensive cross-bracing and have a high number of parts received lower scores here.
4. Simplicity of construction: As per the Kremer Prize rules the design must be suitable for batch production or assembly from a kit. This category evaluated each concept's ease of construction.
5. Wind tolerance: This was an assessment of the total vertical surface area as well as the ratio of vertical surface area ahead of the concept's aerodynamic center versus the vertical surface area aft of the aerodynamic center.
6. Simplicity of structure: Created to assess the relative complexity of the structure; therefore, the complexity of analyzing each structure. Straightforward concepts receive higher scores here.
7. Simplicity of stability and control: This was a measure of the difficulty in analyzing the stability and control of the design. More traditional design received better scores in this category.
8. Inherent stability: Due to the need for high power output from the pilot, natural stability will be required for ease of piloting. This category assessed the natural stability of the design.
9. Pilot integration: How well does the pilot fit into the design? The ideal concept is one where the natural structure defines a suitable place for the pilot to comfortably sit and pedal. This area also considered the relative ease with which the pilot could be loaded and unloaded (an area that has historically presented difficulty in many HPAs).
10. Propulsive adaptability and efficiency: This area considered the ease with which the drive train could be routed throughout the vehicle, and a propeller mounted. Short, direct drivelines

were preferred for lower weight and losses. Designs scored lower if the design required that the propeller be either a tractor or pusher.

11. Pilot visibility: Kremer Sport Prize rules stipulate that the pilot may not be assisted via radio from the ground. It is essential that the pilot have a good view of the surrounding area and good reference marks such that he or she can quickly ascertain the altitude and attitude of the aircraft to control it.

3.4 Conclusions

Based on the figure of merit evaluation scheme, two concepts were selected for further development: Feathers and Bipolar. Bipolar was clearly the leader in the concept scoring matrix (Table 3.1) and represented what the team believed was the most promising concept. Feathers was retained for continued analysis both for completeness and because the biplane configuration was new to the analysis team. If a more detailed analysis revealed that Bipolar was not as promising as initially thought, Feathers would be ready for continued design.

Evaluation of why the other vehicles were rejected shows little in the way of trends. The fact that the rejected concepts were all given negative scores in the category stability and control simplicity is apparent, as is the superiority of each of those designs in the area of pilot visibility.

The biplane concept emerged as the most viable concept and eventually developed into three concepts. These concepts are a biplane with the same span as the comparable monoplane (60 ft), a biplane that takes advantage of the effective aerodynamic increase in span and reduces its geometric span to 45 ft, and a final derivative concept, a "boxplane". The boxplane concept, or Iron Butterfly as it has come to be known, is essentially a biplane with two winglets that extend the full length of the gap between the wings, forming an endplate at the wingtips. This concept can be seen in Fig. 3.9.

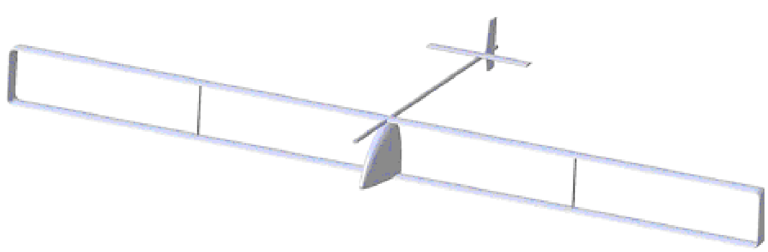

Figure 3.9. Iron Butterfly preferred concept.

While the boxplane concept introduces slightly more complexity, it also presents several advantages over any of the designs already discussed. The endplates have a beneficial induced drag reduction and are structural members that can carry enough load to significantly reduce the weight

Table 3.1. Figure of merit concept comparison relative to Feathers

Concept	Weight	Bipolar		Duck		Stealth		Bert		Fighting Fish	
Efficiency of Structure	5	1	5	-1	-5	-1	-5	1	5	-1	-5
Efficiency of Aerodynamics	5	2	10	-1	-5	1	5	1	5	0	0
Trailer Fitting/Ease of Assembly	5	-1	-5	0	0	-2	-10	-1	-5	-1	-5
Simplicity of Aerodynamics	4	-1	-4	0	0	-1	-4	-1	-4	0	0
Simplicity of Construction	4	0	0	0	0	1	4	-1	-4	-1	-4
Wind Tolerance	4	1	4	-1	-4	-2	-8	0	0	-1	-4
Simplicity of Structure	3	0	0	0	0	0	0	-1	-3	-1	-3
Simplicity of Stability and Control	3	0	0	-1	-3	-2	-6	-2	-6	-1	-3
Inherent Stability	3	-1	-3	-1	-3	-2	-6	1	3	0	0
Pilot Integration	3	-1	-3	0	0	1	3	1	3	2	6
Propulsive Adaptability/Efficiency	2	1	2	-1	-2	-1	-2	-1	-2	2	4
Pilot Visibility	1	-1	-1	1	1	1	1	1	1	1	1
Total			**5**		**-21**		**-28**		**-7**		**-13**

of the spars used. Feathers, Iron Butterfly, and two biplane configurations were passed on to preliminary design.

4. Aerodynamics

4.1 Drag Analysis of Conceptual Designs

With the initial concepts reduced to a monoplane, two biplanes, and a boxplane, an analysis was required to arrive at a final concept. Because of the human power limit, drag becomes the most important attribute to be considered. The drag of the different concepts is largely dependent on the efficiency of the main wings; therefore, the tail moment arms, fuselage, and drag due to propulsion are assumed to be equal for all concepts. This simplified the drag analysis considerably. For analysis purposes, drag was catagorized into three main components: induced, friction and form, and interference.

A series of assumptions was made to conduct a simplified drag analysis. Based on previous HPAs, gross takeoff weight was estimated to be about 215 lb. This allows for a 150 lb pilot and 65 lb for the aircraft. The requirements for good turning performance and trailer limitations constrain the wingspan to 60 ft. To obtain a realistic C_L of about 0.8 for a cruise velocity of 33 ft/s the preliminary wing area was assumed to be 215 ft^2. The actual airfoil to be used is ignored in the preliminary drag analysis but the thickness is still required for an accurate drag analysis and is assumed to be 12%. This thickness allows for adequate structure and from previous airfoil experience was determined to be realistic. Without knowledge of the loading of the wing and the structural requirements the struts were given an arbitrary thickness of 20% and a chord of 5 in and the endplates were given a thickness of 12% and a chord equal to the wing chord.

Also, the horizontal tail volume coefficient was assumed to be 0.5, and the vertical tail volume coefficient was assumed to be 0.035 based on that used on Monarch[2]. To maintain an efficient tail, the aspect ratio of the horizontal and vertical tail was assumed to be 7 and the thickness of the tails was set at 12%. The tail surfaces for each concept were now fully defined and the only configuration dimension still required is the gap for the biplane and boxplane configurations. With the pilot in a recumbent position it was determined that a minimum gap of 54 in was required to fit the pilot and mechanics within the fuselage and so the gap was set to 54 in for both the biplanes and boxplane.

Induced drag is the drag that results from the production of lift. Induced drag is directly proportional to the strength of the wing trailing vortices and any reduction in the vortices will result in a reduction in induced drag. It is due to the reduction of these vortices that the biplane and boxplane configurations are considered. Because a biplane can affect a larger volume of air than a monoplane it is able to impart a smaller average velocity change to the air and therefore has less induced drag than a monoplane. If the gap of a biplane is made infinite then each wing will carry 1/2 the load of the monoplane wing and the trailing vortex will be 1/4 as strong as the monoplane. This means that at infinite gap, the biplane has 1/2 the induced drag of a monoplane. A boxplane is advantageous over a biplane because the end plates affect the strength of the trailing vortex such that it is more efficient than a biplane at smaller gap to span ratios. An effective way of comparing the efficiency biplane and the boxplane to the monoplane is by saying that the gap effectively increases the aspect ratio. Figure 4.1 by Hoerner shows the increased aspect ratio as a function of gap/span ratio and shows the increased efficiency of the boxplane[4].

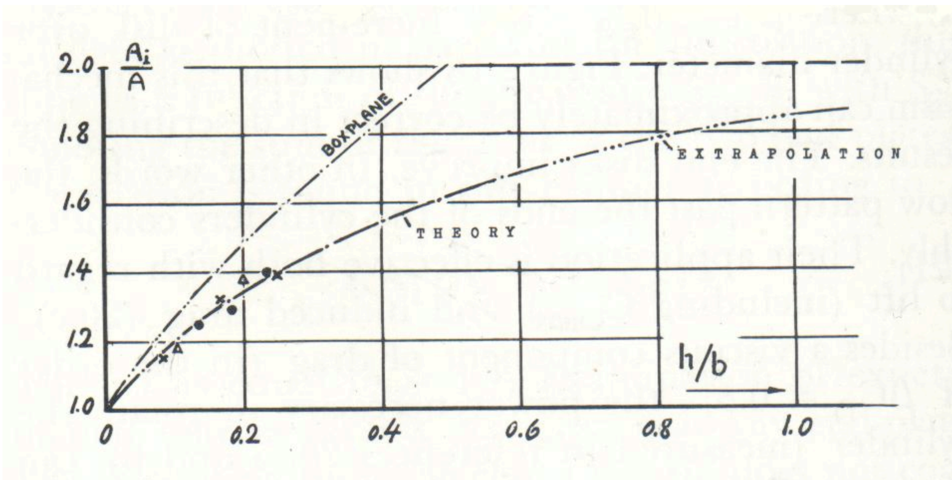

Figure 4.1. Effective Aspect Ratio vs. Gap[4]

The induced drag of a monoplane is given by Eq. (4.1).

$$C_{di} = \frac{C_l^2}{\pi ARe} \tag{4.1}$$

Assuming a realistic value of $e = 0.93$, a quick calculation of the induced drag of the monoplane for the drag analysis was obtained. NACA Report 151 focuses on non-planar lifting surfaces and relates the induced drag of a non-planar wing to a monoplane with Eq. (4.2)[5].

$$C_{di_2} = C_{di_1} - C_l^2/\pi(S_1/b_1^2k_1^2 - S_2/b_2^2k_2^2) \tag{4.2}$$

In Eq. (4.2) the value of $k = A_i/A$ is related to the gap to span ratio by Fig. 4.1[4]. From these relations the induced drag for each of the four final concepts was calculated and tabulated.

Another source of drag is friction and form drag. The airflow over the wing, tails, and struts is assumed to be laminar and so[6]:

$$C_f = 1.328/\sqrt{Re} \tag{4.3}$$

Due to the low Reynolds numbers that this aircraft will be operating at (about 400,000), the assumption of laminar flow is reasonable and only a small portion the wing will experience turbulent flow. The chord of the tails changes slightly according to the area calculated from the tail volume coefficients and the $AR = 7$ assumption and using the form factors found in Hoerner,

$$FF = 1 + 1.2(t/c) + 70(t/c)^4 \tag{4.4}$$

the drag for the tails of each concept is easily calculated. This form factor was also applied to the endplates for the boxplane concept. However, because the struts have a thickness of 20% which is outside the validity range of the form factors used for the wing and tails, a different form factor is used. (Eq. (4.5))

$$FF = 2(c/t)^{0.75} + 2(t/c)^{0.25} + 120(t/c)^{3.25} \tag{4.5}$$

Interference drag is a result of the boundary layer interactions at the junctions of two different components. This drag is a function of both thickness and chord:

$$C_{d_{int}} = 0.8(t/c)^3 - 0.003 \tag{4.6}$$

The interference at the wing-fuse and strut-wing joint was calculated and tabulated. The interference between the tail surfaces and the mounting pylons is neglected as it will remain constant between the concepts and with the use of thin pylons, $t/c \approx 2\%$, this drag can be considered negligible.

Table 4.1 shows the complete tabulation of the preliminary drag calculations. Here it can be seen that classic monoplane configuration is competitive against the biplanes and is ranked second according to total drag. The 60 ft biplane has considerably lower induced drag and wing interference drag than the monoplane. However, due to the smaller wing chord the tail geometry must be modified thus producing higher the drag on the tail compared to the monoplane. Increased tail drag is also present in the boxplane but the increased efficiency of the wing offsets this and the overall drag is lower. The boxplane concept was chosen to be the final concept because of the lower drag.

Table 4.1. Drag-Estimate of Preliminary Design Concepts

Design	Monoplane	45ft Biplane	60ft Biplane	**Boxplane**
Drag, [lb]	4.7	5.8	4.5	**4.2**

4.2 Airfoil Selection

The wing will be operating at an Re of 400,000 as opposed to typical Re in the millions which increases complexity of airfoil selection. Because HPAs operate at extremely low Reynolds number the drag is dominated largely by the control of the separation bubble. If the separation bubble becomes large then the pressure distribution around the bubble will have a component against the direction of flight and cause pressure drag. Because the air within the separation must be mixed into the boundary layer, a large bubble will require a large amount of air to be mixed with large losses in momentum resulting in high drag. To reduce the possibility of an excessive bubble or complete separation, transition from laminar to turbulent flow must occur. The most efficient place for transition to occur for low drag is within the separation bubble itself. The location within the separation bubble that transition occurs requires attention as well. If transition occurs too early then there will be a penalty due to increased turbulent flow. If transition occurs too late then the bubble will grow in size and the pressure and mixing losses previously mentioned will result. The separation bubble must also be located as far aft on the airfoil as possible. There is a limit to this because as the airfoil geometry is changed to move the bubble aft, it creates conditions that will allow the bubble to rapidly move forward or the flow to completely separate at off design conditions. This would result in loss of lift and have drastic consequences on the flight[7].

Due to the stringent requirements of HPA airfoils it is impractical to try to design an airfoil without significant prior knowledge and experience in airfoil design. Researching the airfoils previously used yielded three candidates - NACA 4412, FX76MP, DAE 11 - 31.

The NACA 4412 has been used on several HPAs including the 11th JIBR Championship[1]. While it has proven successful at JIBR, it has the highest drag of the three candidates. The Wortmann FX76MP has been utilized many times and this airfoil was designed by Wortmann specifically for HPA use[8]. The location of the separation bubble has been addressed by Wortmann but at the time this airfoil was developed the aerodynamic community lacked the high power CFD tools that are available to current aerodynamicists. The DAE series were developed by Drela to address the issue of transition. This series has the lowest drag of any of the candidates[7].

In addition, the DAE series has a lower pitching moment that will allow a lower structure weight. The combined lowest C_d and C_m in conjunction with favorable boundary layer behavior at off design conditions results in the DAE series being the final airfoil selection for the Iron Butterfly. This series is comprised of DAE 11, DAE 21, and DAE 31 which have been separately optimized for a specific C_l so that they may be used to obtain the desired span wise lift distribution.

4.3 Wing Area Constraint Analysis

The preliminary selection of wing area was achieved by defining a series of wing constraints in terms of lift coefficient, C_l. A design space was plotted with the defined constraints and wing area chose from within the space. The design space for wing area may be seen in Fig. 4.2.

The first and most obvious constraint is stall, C_{lmax}. Estimates for C_{lmax} were determined from XFOIL[2]. XFOIL is an airfoil analysis program, predicts a 2D $C_{lmax} = 1.58$ and due to 3D

[1]Japan International Birdman Rally
[2]XFOIL is released under GNU General Public License[9]

effects of the airflow the 3D C_{lmax} is set at 1.5. This sets a constraint for minimum wing area of 110 ft^2. Further, a stall margin of 15% C_{lmax} was set for both straight and level flight and turning flight. The next constraint is the C_l that corresponds to the drag bucket limit, where drag becomes excessive if C_l is reduced further. This drag bucket limit imposes a maximum area of 210 ft^2. The final constraint is that the tail chord must be equal or greater than 1 ft. This is merely a structural and ease of building constraint that constrains the wing area through the tail volume coefficients. The maximum lift to drag ratio, L/D_{max} represents a wing area that will result in the best L/D at cruise conditions. Each constraint is indicated in Fig. 4.2 and also on the drag polar in Fig. 4.3.

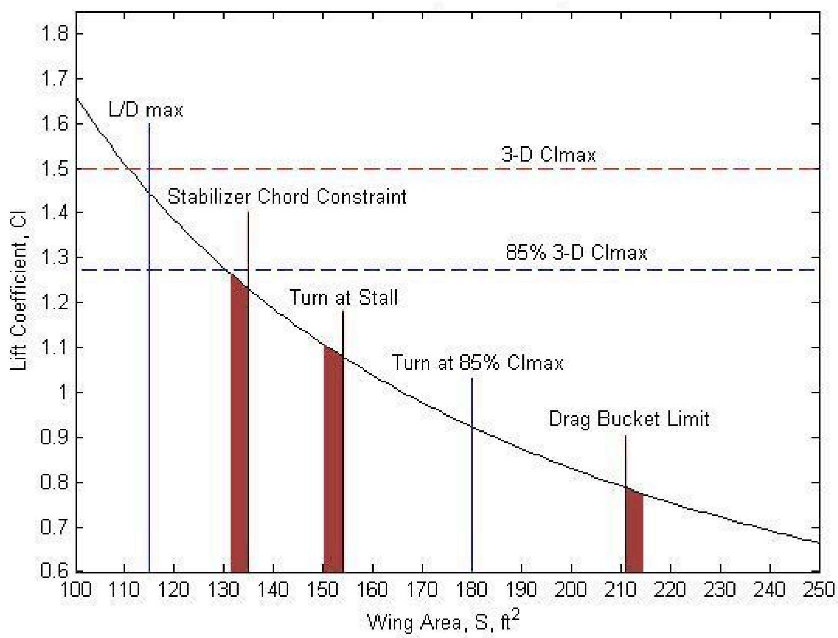

Figure 4.2. Compilation of constraints on wing area

Figure 4.2 indicates that flying at L/D_{max} is not feasible and any area greater than 114 ft^2 will have higher drag. The stabilizer chord constraint is lower than the turn at stall constraint and the required area to fly in a turn at a 15% C_{lmax} stall margin lies in considerably before the drag bucket limit. The lower the wing area the lower the drag. Therefore the stall margin in the turn becomes the lower limit on wing area. The wing area was set at 180 ft^2.

4.4 Friction-F Agreement

To validate the previous drag calculations, a model of the final design was created and analyzed with the program Friction-F. Friction-F will take inputs of length, area, Re, thickness, and percent laminar flow from which it will output a total profile drag coefficient C_{d_0} for the entire aircraft

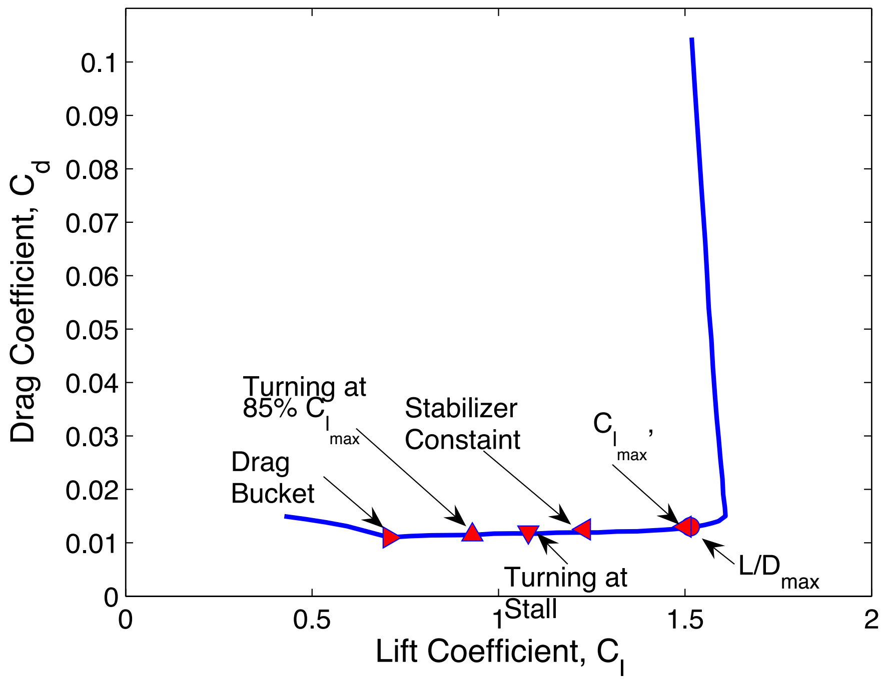

Figure 4.3. Compilation of constraints on wing area indicated on Drag Polar

configuration by calculating skin friction C_F, and the form factor FF, of each component and performing a summation. The model included wings, tails, and struts and comparing the results from Friction-F to the previous results calculated from the Hoerner's drag equations in Section 4.1, a large difference was noticed. This large difference lead to the investigation and validation of both drag analysis's.

Initially the values of C_F were in disagreement, though both analysis's assumed pure laminar flow. The Friction-F code was reviewed and the methodology for C_F compared to the previous drag analysis and it was determined that they were indeed similar and should produce the same results. After much work it was determined that the error was in the Friction-F model resulting in the calculation of C_F for a much greater Re. Once the values for C_F converged, a difference still remained, see Table 4.2.

Table 4.2. Friction-F and Hoerner Drag Analysis Agreement

	C_{dF}	C_{dForm}	C_{d_0}	Drag
Hoerner	0.00603	0.00145	0.00748	2.081
Friction-F	0.00603	0.00140	0.00743	2.068

Here it can be seen that the difference lies in the form factors used to determine drag due to thickness. Drag due to thickness is not a phenomenon that can be derived mathematically such as friction or induced drag. Due to this, there are several different methods for calculating form factors. Friction-F uses the methodology developed at Northrop Grumman and by looking at Fig. 4.4 it can be seen that these are the most optimistic of the different form factors.

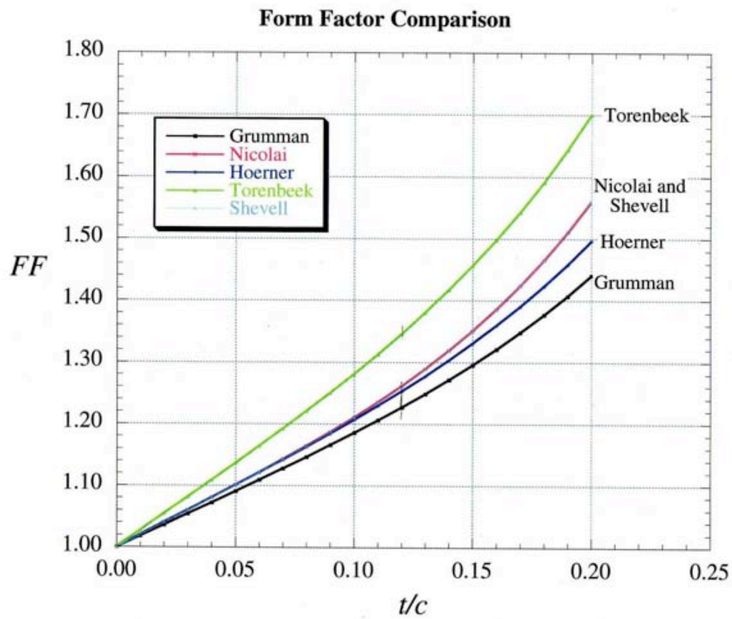

Figure 4.4. Comparisons of form factors developed independently.[10]

Exploring the FF values for individual components it was discovered that the greatest difference lies at high t/c values, great than $t/c = 15\%$, such that the struts had a difference of 3. However, due to the low speeds of HPAs this results in a 0.013 lb difference between designs.

In an effort to minimize the possibility of designing an aircraft with greater drag than the thrust available, the Hoerner form factors were used for final drag analysis though Friction-F remains a useful tool in calculating C_F for flows that both laminar and turbulent.

4.5 Wing Development

The full scale wing twist distribution presented a number of analytical problems. I-Drag[3] is incapable of handling a full geometric model of the wing and therefore is incapable of providing an ideal lift distribution to work to match. To obtain this ideal lift distribution, correlating to minimum drag, AVL[4] was used in an iterative manner to obtain an even downwash angle across the wing. The full scale wing is comprised of a blending of two airfoils, the DAE 11 and the DAE 21. The DAE 21 was designed to provide a lower C_{l_α} than the DAE 11 and was used over the last ten

[3] I-Drag is released as freeware[11]

[4] AVL is released under GNU General Public License[12]

feet of the wing where the local lift coefficient drops. To define twist distribution the wing was decomposed into nine stations. The twist at each station was adjusted until an even downwash was obtained and changes in efficiency per iteration were smaller than 0.5%. The final twist distribution has been tabulated, Table 4.3.

Table 4.3. Tabulated Twist Distribution

Span Location, [ft]	0	2	4	12	20	27.6	28.6	29.5
Top [deg]	1.5	1.5	1.7	1	-0.5	-2.7	-4	-4.6
Bottom [deg]	0	0	1.6	1	-0.5	-2.7	-4	-4.6

The endplates on a boxplane represented a unique design challenge in that their efficiency is highly dependent on their lift distribution. Because I-Drag is incapable of handling a complete geometric model of the airplane including the polyhedral, several simpler models were run and analyzed to identify any trends. These models consisted of straight top and bottom wings that remain parallel and have simple dihedral with angles of 0, 5, 11, and 15 deg. It was seen that increasing dihedral angle only causes the distribution to translate and carry greater loads. However, increasing the dihedral angle had the effect of increasing the loading on the top wing and decreasing the loading on the bottom such that at 15 deg the top wing is carrying almost twice the load of that on the bottom wing. Since this is know to not be the case due to the previous AVL model, the translation effect was considered to be due to complications or errors within the I-Drag program. At 0 deg dihedral the top and bottom wing are loaded equally and the endplate load distribution was used.

Like the wing airfoil, the endplates operate at very low Re and so the low Re airfoil list generated for the main wing from the UIUC LSAT's was reviewed. Due to the low $C_{l_{req}}$ and the symmetric positive to negative loading, only symmetrical airfoils were considered. Due to time constraints the endplates were designed to utilize the NACA 0012. A initial twisting of the endplates, Table 4.4, resulted in an increase in efficiency and reduced the downwash angle at the tips. The final lift distribution and resulting downwash can be seen in the AVL Trefftz Plane plot, Figure 4.5.

Table 4.4. Tabulated Endplate Twist Distribution

Vertical Location, [ft]	-2.5	0	2.5
Twist [deg]	3	0	-3

It can be seen that this wing twist and endplate design results in a very efficient airplane with an induced drag coefficient of 0.011 and a corresponding efficiency of 1.18. With the performance considerations previously discussed this will yield a total target L/D of 20.

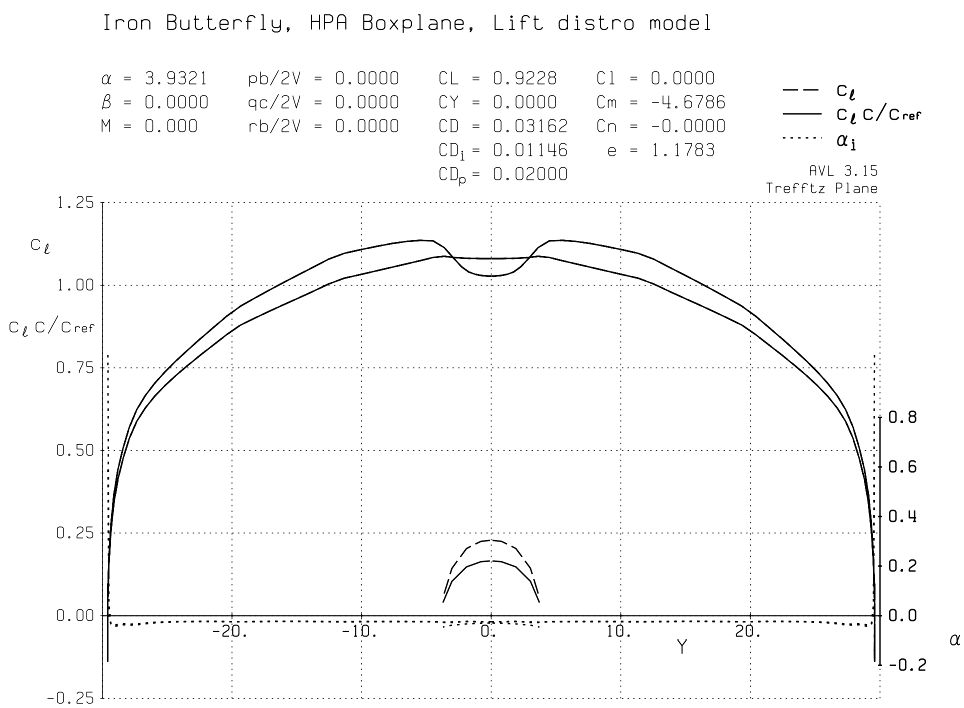

Figure 4.5. AVL Trefftz Plane Plot

4.6 Vertical Tail Planform

A gap of 5 ft and an allowance of 10 deg of rotation at take off required that the tail only extend down 2.14 feet below the tail boom. To maintain efficiency the tail becomes asymmetric about the tail boom so that the lower surface has a low AR and the top surface has a high AR. This asymmetry then requires a definition of the area and loading on each surface. However, when the fin is deflected to produce a moment for a right turn, it produces a rolling moment to the left due to the asymmetry. In addition, the loading of each surface greatly affects the net efficiency of the vertical tail and the more load carried on the bottom surface the greater the induced drag during turning. To further complicate the issue, the greater the rolling moment produced the stronger and heavier the tail boom must be made, which degrades overall flight performance. In addition the rolling moment affects the stability and control of the aircraft. Due to the complexity of this optimization problem and the limited time available, the net tail load was divided evenly between the upper and lower surface with the lower surface comprising 1/4 of the total area required to obtain the desired tail volume coefficient. From this, root and tip chords were adjusted to obtain a tail with an overall AR of 5.6. The tail shape may be seen in the drawing packages in the appendix. This tail produces a rolling moment of 7.8 lbs in a turn and currently appears structurally reasonable. However, future development of the aircraft should include a reassessment of this problem with an optimization including input from structures and stability to obtain the most efficient vertical tail.

5. Structures

At the conclusion of the conceptual design phase, the structural comparisons between a biplane configuration and a monoplane configuration were left to be further quantified. Power required for an aircraft varies with the weight to the 3/2 power whereas it varies linearly with drag[13]. Thus, significant emphasis was placed on producing a lightweight structure, specifically for the spar design. Once the basic configuration was chosen, focus could shift to the development of secondary structures.

5.1 Conceptual Model Testing

Initial attempts to quantify differences between a monoplane and a biplane proved computationally intensive. Instead, models were built of several configurations and compared against one another. Three biplane models were built, two with single struts on each wing and one with two struts on each wing. A cantilevered monoplane structure was also built. The aerodynamic drag from flying wires at the speeds necessary to win the Kremer Sport Prize made them ineffective so they were not used during testing.

All four models used the same amount of load carrying material in their spars. The biplanes used 1/16 in x 1/8 in basswood whereas the monoplane used 1/8 in square stock. Struts were not accounted for in overall aircraft weight and were made stiff enough to support the assumption of them remaining rigid throughout testing. Rough scaling was employed off the best estimate of aircraft configuration at the time of testing. The models were restrained in a loading fixture and simply supported at the tips. Weights were hung from the center structure. A picture of one of the deformed structures can be found in Fig. 5.1.

Figure 5.1. Deformed basswood biplane model during testing

A plot of measured displacements for applied loads can be found in Fig. 5.2. Model testing showed significant stiffness improvements over the monoplane structure with the biplane configurations. Both biplanes with single struts per wing exhibited similar stiffnesses, implying that number of struts was more important than location. The biplane with two struts per wing was also significantly stiffer than those with single struts. Based on the results of the basswood model testing, the biplane configuration was chosen for further investigation.

5.2 Analytical Solution to the Biplane Structure

Upon selection of the biplane aircraft configuration, it was necessary to quantify displacements and stresses in the structure to adequately size spar shapes and components. The frame structural model, shown in Fig. 5.3, was defined encompassing all relevant aircraft configurations. It was assumed that the struts were rigid and that the beams all had equal cross-sections and material properties for initial analysis.

The problem defined above proved to be statically indeterminate and could not be solved directly. Instead, an implicit solution proved necessary using structural displacements. The six spar sections of the frame were modeled as beams allowing extension and bending. Shear was ignored. A set of two differential equations governed the displacement of the beams in this case, Eq. (5.1) for extension and Eq. (5.2) for bending. P_x is defined to be the distributed loading in the vertical direction along the beams[14]. EI_{yy} are beam cross-sectional properties, its flexural stiffness.

$$\frac{d^2 w_i}{dz^2} = 0 \tag{5.1}$$

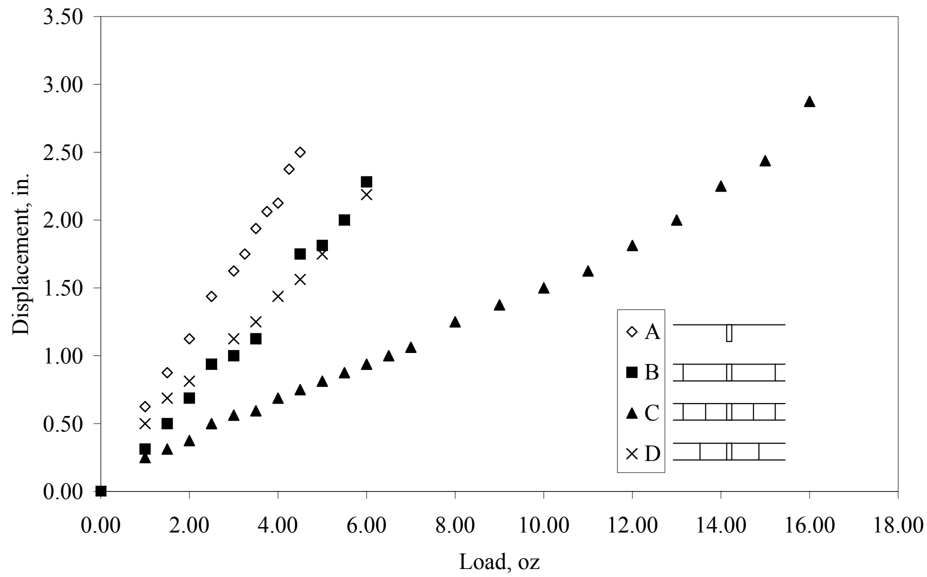

Figure 5.2. Measured displacements for basswood spar models

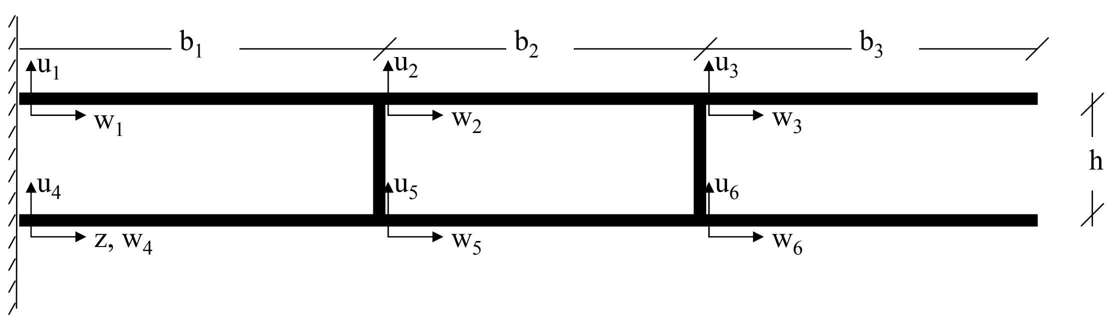

Figure 5.3. Definition of biplane structural components for analytical solution

$$\frac{d^4u_i}{dz^4} = \frac{P_x}{EI_{yy}} \tag{5.2}$$

The problem was solved in terms of the variables b_1, b_2, b_3, h, EI and EA, the beam's extensional stiffness. From there, determination of the displacement and stress distribution for a specific design case was trivial. Additional assumptions included that of a linearly elastic structure with isotropic properties. All beams were composed of the same constant cross-section.

This problem definition provided a system of 36 coupled differential equations with the necessary 36 boundary conditions. Six came from setting the displacement and slope to zero at the root. Twelve came from displacement and slope continuity at the joints. Six from the free end conditions at the tips of beams 3 and 6. The last twelve came from displacement, slope, force, and moment relations across the struts.

MATLAB®[5] was used to solve the system of equations symbolically. Solutions were initially validated by examining the physical correctness of the solution. In other words, for a positive lift configuration did the structure deflect upward? Displacement shapes were compared qualitatively and quantitatively with the basswood models using material properties derived from the cantilevered monoplane case and will be discussed in detail in a later section.

Shear force and bending moment relations for the basswood biplane spar model with two struts per wing for two different loading configurations were developed to explain the non-intuitive displaced shapes observed. Figure 5.4 shows the solution corresponding to a total loading of 7 oz distributed as 4 discrete point loads of 7/4 oz on each wingtip, a specific case tested during the initial investigation. Figure 5.5 shows the solution corresponding to a lift of 7 oz evenly and constantly distributed over each wing.

Local bending moment in the top and bottom spar ranged from negative to positive values, jumping at the location of each strut. This variation leads to the development of the non-intuitively "s" shaped displaced structures. Tensile forces in the lower spar and compressive forces in the upper spar also jumped in value at each strut. These jumps are caused by the transfer of loads between spars due to the rotation of the struts. Examination of the results showed that the sum of the couple generated by the normal forces in the beams and the local bending moments in each individual spar was equal to the bending moment at that point for a similarly loaded cantilevered beam, a necessary condition for equilibrium.

This analysis was not, however, without its drawbacks. Only relatively simple loading situations could be defined mathematically and thus, actual elliptic or asymmetric loading configurations would prove challenging. The struts were assumed to be rigid, although when actually built they would not fully exhibit this property. Adding to the analysis to better model the physical problem proved tedious and time-consuming. Due to these constraints and the intense time line set for design, a more rigorous and expeditious tool was sought.

[5]MATLAB® is a registered trademark of The MathWorks Inc.

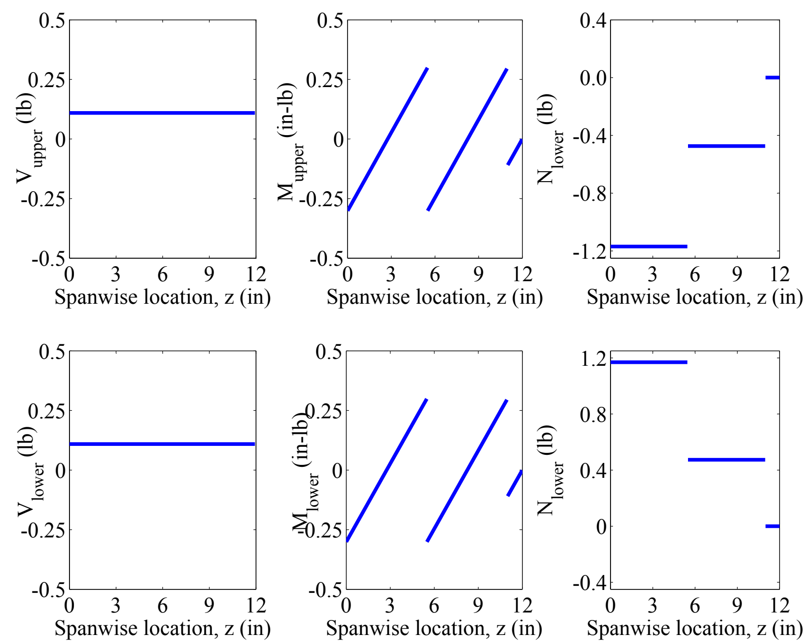

Figure 5.4. Shear force, bending moment, and normal force in 2 strut basswood biplane model with 7 oz lift distributed as tip loads.

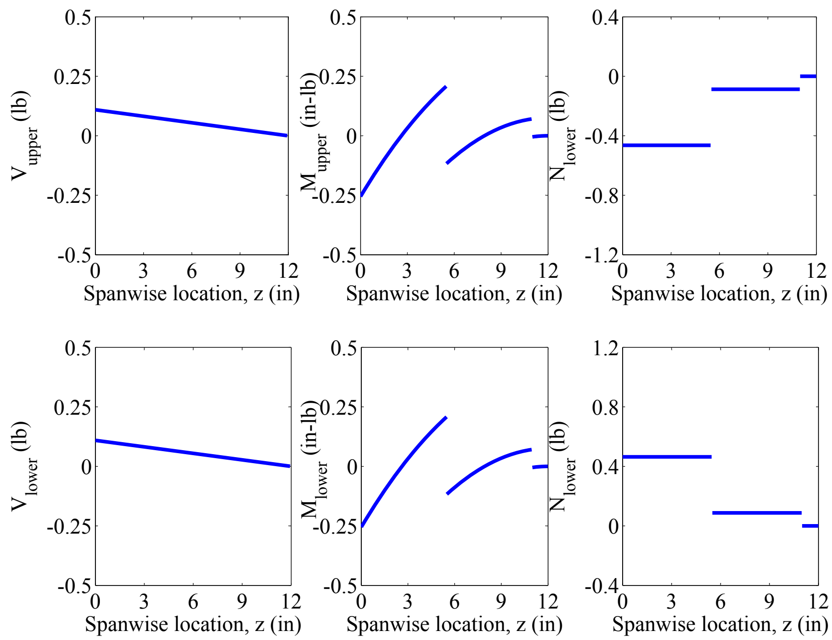

Figure 5.5. Shear force, bending moment, and normal force in 3 strut basswood biplane model with 7 oz lift evenly distributed spanwise.

5.3 ANSYS® Finite Element Models

During the development of the analytical MATLAB® model, ANSYS®[6] FEM software, version 8.0, was made available to the design team. Some experimentation showed that numeric results equal to and surpassing the analytical model could be obtained. The structure was again modeled with linear elastic, isotropic beam elements. Extension, bending, and shear deformations were now included. Each beam from the analytical solution was now broken down into as many as 8 elements. Cross sectional properties and loading could be defined for each element. Thus, using this model tapered spars and more complicated loading configurations were now easily analyzed. However, shear force, bending moment, and normal force diagrams equivalent to Figs. 5.4 and 5.5 are not easily developed, although the capability does exist.

Again, validation was achieved by qualitatively and quantitatively comparing the results of the model against the already-tested basswood biplane spar models. Stresses in the elements could be computed. Nodal displacements were also given in the solution. Comparisons were made only against measured displacements. Shear deflection accounted for less than 0.1% of model displacement, supporting the earlier assumption that shear deformations were negligible. Upon sufficient validation of the modeling technique, ANSYS® was selected as the primary tool for sizing spar components both for the remote control model and the final aircraft.

5.4 Validation of Analysis

Comparisons were made between the basswood biplane spar models tested in early stages of development, the analytical model, and ANSYS® finite element models. Figure 5.6 shows this comparison for the model closest to the actual aircraft geometry, one with two struts per wing. In this case, the load P is equivalent to the lift described earlier. Non-linearities were not accounted for in either the finite element or analytically modeled structure, as exhibited by the straight line curve fits to these solutions. The analytical model slightly over-predicted structural stiffness because the struts were forced to remain rigid. This assumption allowed more of the overall bending moment in the structure to be carried as compressive or tensile forces. Despite the rather weak assumption of modeling the basswood as a linearly, isotropic material, a good fit between the ANSYS® model and the tested basswood models exists.

5.5 Strut Number Analysis

The tradeoff between structural weight and associated drag required a quantitative analysis to determine the best number of struts. For a given amount of spar material, adding struts makes the wing stiffer. Thus, the structural weight of the spars can be reduced by adding struts to achieve the same overall structural stiffness. The finite weight associated with each added strut partially

[6] ANSYS is registered trademark of ANSYS Inc.

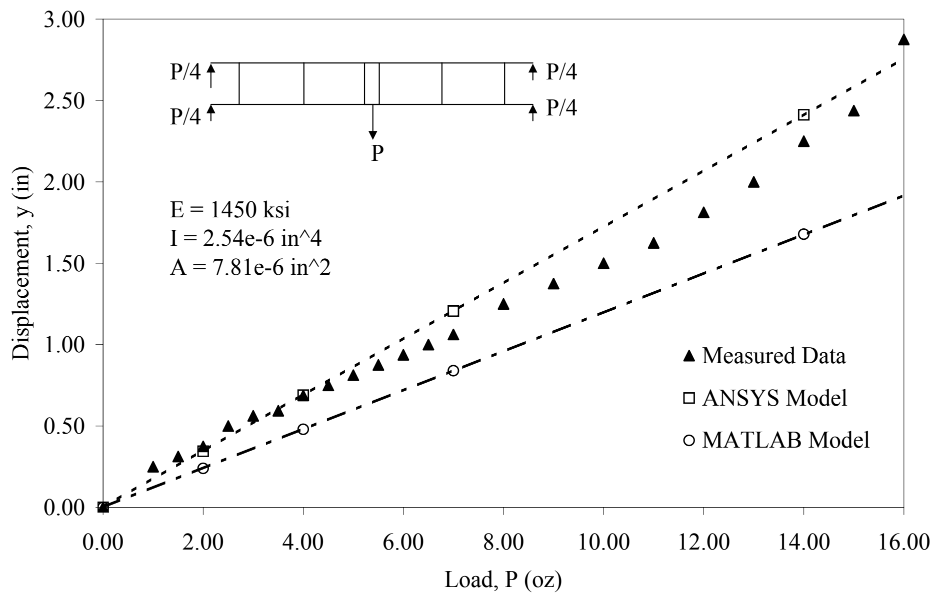

Figure 5.6. Comparison of analytical and ANSYS® finite element models with data

offsets the reduction in spar weight. Even so, any appreciable number of struts per wing added would reduce the overall structural weight.

To quantify the problem and determine the final number of struts to use, several assumptions had to be made. The spar weight was assumed linear with its moment of inertia. Thus, spar weight decrease was directly proportional to a reduction in wing stiffness. Physically this would be equivalent to a case where spar caps are reduced in width to reduce structural stiffness while their height and separation remain unchanged. Added strut weight was assumed proportional to the new spar weight so the strut weight was not a constant value. Thus, the bending rigidity of the struts was kept in line with that of the spars and simple finite element modeling was achievable. Original spar weight was determined as a fraction of the aircraft gross take off weight. Exact values of this ratio were not known, but analysis was completed for the range of 2.5% to 10%.

The analytical process used the unmodified boxplane as the baseline aircraft to which comparisons were made. A number of struts were added to each wing, evenly distributed across the span and the associated reduction in required spar stiffness to maintain reasonable tip displacements was calculated using ANSYS® models. This reduction in stiffness led to an associated reduction in aircraft gross takeoff weight. Each new weight was used to calculate a drag for each strut configuration. As long as drag was reduced, the addition of the strut proved beneficial. Analysis was repeated for several spar weight fractions in the assumed range.

The drag change associated with additional struts comes in two forms. The first is reduced induced drag. By reducing the gross weight of the aircraft, the lift generated is reduced, weakening

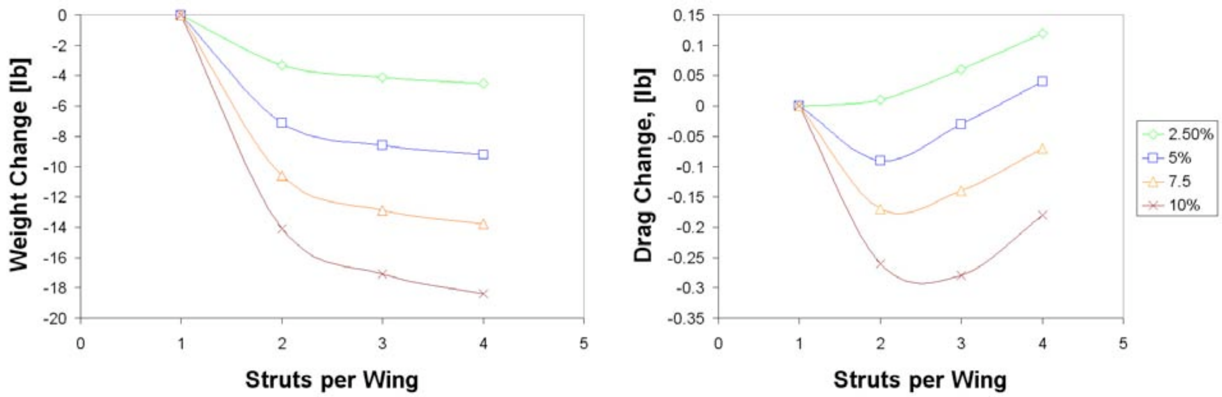

(a) Weight v. Struts. (b) Drag v. Struts.

Figure 5.7. Strut, spar weight, and drag optimization

the trailing vortices and lowering induced drag. The second drag change is parasitic drag due to friction and interference. Each additional strut adds wetted area and two additional junctions where interference drag is present. These two effects increase drag, thus a balance between increased parasitic drag and reduced induced drag must be established. To obtain accurate changes in induced drag I-Drag was utilized. C_{di} values for each strut configuration and the reduction of induced drag was quantified by changing the I-Drag model to reflect changes in C_L. Increased parasitic drag was calculated using Hoerner form factors and under the assumption that 80% of the flow over the strut was laminar. Values of C_F for this mixed flow were obtained from the program Friction-F. Then by calculating the additional interference drag, the total change in parasitic drag per strut could be calculated. Thus, the total change in drag for each strut configuration was found, and can be seen in Fig. 5.7 At the low end of the spar weight fraction, near 2.5%, one or two struts proved most beneficial. At the high end of the range, near 10%, two or three struts proved most beneficial. Thus, a configuration with two struts per wing was chosen for further investigation. All further calculations will be performed on the two strut configuration.

5.6 Gap

Several studies were made to understand the influence of the gap between the two wings on aircraft performance. Considerations included structural weight, total drag which translates to power required, minimum fuselage height and propeller efficiency. Additionally, the aircraft must fit in the trailer and be relatively easy to work on while assembled. It was assumed that structural weight increased with moment of inertia, spars were untapered and loading was constant along the span for initial studies. 2D ANSYS® finite element models with beam elements were used for all structural bending analysis. Although tapered spars and elliptic loading would be designed for eventually, each test case required construction of a separate model and a considerable amount of time. These simpler cases would still show the same trends.

Initially, two extreme cases were examined to further understand how the structure deforms, shown in Fig. 5.8. First, when spar stiffness is much higher than strut stiffness, case a, only minimal stiffening is achieved from the struts, they simply deform until each spar carries the majority of the load. Bending moments are carried mainly in each local spar rather than as tension in the bottom and compression in the top. Displacement is governed by each individual spar stiffness and the displacement curve looks similar to that for a single cantilevered beam. For this case, the stiffening desired from having two wings separated by struts is not achieved.

For case b, when strut stiffness is much higher than spar stiffness, a somewhat non-intuitive “s” displacement is exhibited, much like the conceptual model testing discussed earlier. In this case the struts do not deform, but simply rotate. Bending moments are carried as both local bending moment in each spar along with tension in the bottom spar and compression in the top. As in the discussion of the initial conceptual model testing, the variation between position and negative bending moments between the struts is the main cause for the oddly shaped displacement curve. Stiffening by separating the wings is achieved, however, only to a point. A gap is reached at which further increase no longer increases the overall structural stiffness.

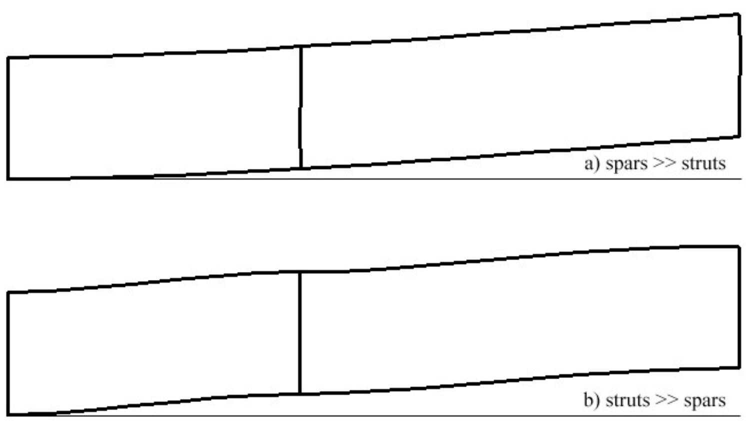

Figure 5.8. Bending for various spar to strut stiffness ratios.

For the final aircraft, however, the strut stiffness and spar stiffness will be on the same order of magnitude. Thus, one final assumption was made in analyzing component weight as a function of gap. The spar and strut stiffness were assumed equal. Models were analyzed with a 1G elliptic load for cruise. Aluminum tubes with outer diameters of 2 in were used for structural members. For each gap, wall thickness was varied to achieve the desired stiffness resulting in a 40 in deflection at the tip, a large but allowable value providing much of the desired dihedral in flight. Knowing the necessary wall thickness, the total weight of struts and spars for each gap could be calculated.

Figure 5.9 shows spar weights as a function of gap. When spar and strut stiffnesses are on the same order of magnitude, significant stiffening is not achieved and structural weight actually increases with gap. Scatter shown in the figure is the result of discretizing the load and sizing the spars to achieve tip displacements less than 40 in but not exactly 40 in. Thus, a curve was fit to the weight versus gap data and used as a better representation of how spar weight varies with gap. This equation is shown on the figure.

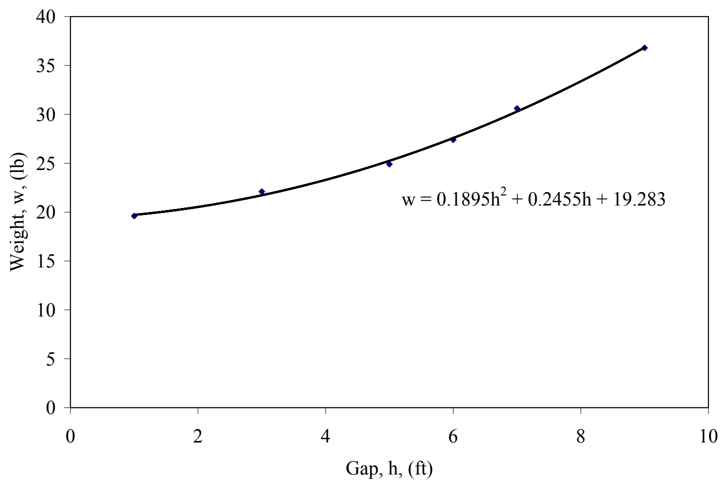

Figure 5.9. Spar weight as a function of gap.

Once structural weight was known as a function of gap, the weight of all other components and pilot were given a constant value of 200 lb for drag analysis. The drag of the wing consists of two main components, induced and friction. The friction drag increases with gap. This was calculated using the Hoerner form factors and with a t/c of 12%. The flow was assumed to be 75% laminar yielding a C_f of 0.00363. Under these assumptions, the friction drag was easily quantified.

Increasing the gap increases the efficiency of the wing and therefore reduces C_{d_i}. However, increasing the gap also requires a heavier spar structure and increases C_{d_i}. To quantify this problem a simple I-Drag model was constructed consisting of straight parallel wings with 11 deg. of dihedral in the center. From this the gap could easily be adjusted accordingly and a quick calculation yielded the corresponding $C_{l_r eq}$ for each case. The C_{d_i} yielded from I-Drag was then used to calculated the total induced drag of that configuration.

The results of each case were tabulated and graphed, Fig. 5.10. Here it can be seen that there is a clear minimum at a gap of 5 ft although that minimum is incredibly shallow. This is 6 in greater than the minimum gap required for pilot placement and is also small enough to allow easy access to both wings from the ground once assembled. The difference between the worst case and best case is only 3.5% but still large enough to make a measurable difference. It is through this structural and aerodynamic analysis that the final gap of 5 ft was chosen as the final gap.

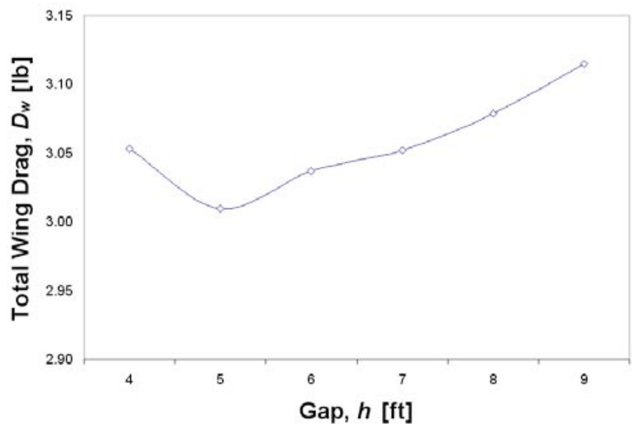

Figure 5.10. Total Wing Drag vs. Gap.

It is worth noting that many simplifying assumptions were made in the analysis of how gap affected aircraft performance. It is suggested that future work study the influence of the ratio of strut stiffness to spar stiffness while including elliptic loading in the analysis earlier. The problem seems to be highly sensitive as a whole and is worth additional investigation. It seems likely that a lighter configuration could be achieved, although the current one will work.

5.7 Constraints for Detailed Structural Analysis

To conduct detailed structural analysis for both the model and the full scale aircraft, several additional constraints were placed on the structure. Wing gap was defined as described above as 60 in. Final deformed shape at cruise was specified from control and stability analysis as a dihedral necessary to turn, discussed in Section 6.3 to be 11 deg of effective dihedral. This deformed shape at cruise was achieved with a combination of built in geometry and structural deformations in flight. Unlike most aircraft, HPAs deform significantly in flight and rigid structures cannot be assumed. However, by allowing the structure to deform significantly, lighter construction can be achieved. Deformation due to wing weight was not accounted for in final deformations.

Instead of the simple dihedral specified, a more efficient and realistic polyhedral was designed for as the structure would bend everywhere along the span, not just at the root. Each wing section was kept to 8 ft in length for the full scale aircraft as most tubes are available with this as a maximum length. To achieve a 60 ft span, the outboard panels were allowed to reach 10 ft in length since loading was significantly less there. Thus, a small 2 ft section could be spliced on without the addition of significant weight. Limiting the full scale sections to 8 ft resulted in 24 in long sections for the R/C model. An excel spreadsheet written by Martin Brungard[15] was used to design a reasonable polyhedral with similar angles at each panel break that would provide the necessary 11 deg of effective polyhedral, shown in Fig. 5.11 for both the R/C model and the full scale aircraft. Y_{max}, was used as the design factor for initial strain based analysis at cruise in ANSYS®. Spars and struts were the only components modeled, stiffening by the skin and other components provided an additional safety factor. Validation of this structure would be done using stress analysis of the structure for more extreme loading situations. Effect of the components own weight was assumed negligible.

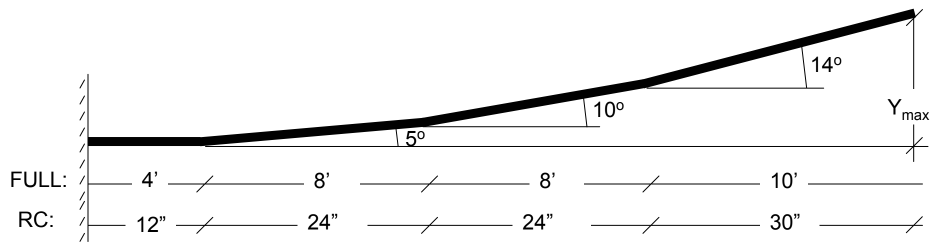

Figure 5.11. Desired polyhedral distribution for adequate turn initiation.

5.8 Material Selection and Structural Layout

Human powered aircraft employ major structural components in layouts very similar to many remote control models, specifically sailplanes. A main spar placed near the airfoil quarter-chord and point of maximum thickness with the possible addition of a trailing spar placed in the rear third of the wing will be used. To connect the two wings, a frame, similar to that on a bicycle will make up most of the fuselage and faired struts will be placed at semi-span and wingtip locations. A single tail boom will extend aft from the main fuselage to which simple, full-flying control surfaces will attach. Both these surfaces and the main wing will use ribs and a stressed skin design to attain the desired aerodynamic shapes. Hinges for the surfaces will utilize the spars themselves and provide relatively simple attachment points. Landing gear will be connected to the main fuselage structure along with the lower wing structure. Basic aircraft shape and these details can be seen in the drawing package in Appendix A2.

Although many human powered aircraft, especially high performance ones, employ composite spars because of their capability of attaining high strength to weight ratios, significant experience is necessary in designing such a spar. Without significant experience composite spars may actually end up being heavier than an associated aluminum spar. Many prototype aircraft have used thin-walled aluminum tubing as spars to great success including Monarch and Chrysalis. Based on this information and the advice of Juan Cruz, the main structural designer of the Daedalus and many other human powered aircraft, aluminum spars were chosen instead of composite for the full scale aircraft spars. The considerable simplification of analysis by choosing an isotropic material was also considered in this decision. Foam ribs with cap strips of wood or composite tape will be utilized as secondary structure. Fairings around the fuselage will attain their shape utilizing balsa or basswood secondary structures covered in the same material as the wings and possibly using thin fiberglass fairings near the nose.

Final material selection for spars, struts, and the tailboom consisted of the various aluminum alloys. These alloys exhibit almost identical stiffnesses, densities and Poisson ratios. The main difference that sets them apart is their yield strength. Stress analysis, discussed below, showed that it was important to use the alloys with the highest yield strength available, the 7075 series. From Beer and Johnston, 7075-T6 aluminum has a modulus of elasticity of 10.4x106 psi, Poisson ratio of 0.3, yield strength of 73 ksi, and a density of 0.101 lb/in^3[16]. All final analysis assumed the material to be isotropic and in its linear elastic regime.

5.9 Skin Material

The skin used on the aircraft is an important choice, as it is a stressed skin and an essential structural part of the aircraft. Previous HPAs have almost exclusively used tensilized Mylar, which is essentially the material in a cassette tape. Tensilized Mylar, or "Tenzar" as it was called when first introduced in magnetic cassette tapes, is a fiber-reinforced bi-axially oriented polyester film with a heat seal layer, either ethylene vinyl acetate or ethylene vinyl acetate.

In the interest of improving on what has already been done, alternatives to tensilized Mylar were explored. The two most relevant parameters to consider were: tensile strength, and weight (or density). These were combined to create a term called, appropriately, specific tensile strength.

A few different skin materials were considered. Since many of the team members had previous experience with R/C skin materials, these were investigated and used to benchmark the other skin materials. Fig. 5.12 shows the dependence of the eventual total skin weight on the skin material used. Of particular note is the high weight of the older fabric coverings, which gave a skin weight of near 12 lbs[7].

The familiar R/C covering materials are in the middle of this region, such as Monokote, Econocote, Microlite, and similar. All of these materials are shown for the thickness in which they are available. Finally, the line of alphanumeric designators at the bottom of the plot is trade names for different varieties of tensilized Mylar in a thickness comparable to the R/C hobby coatings. Mylar is available in a wide variety of thicknesses. From this figure, it becomes obvious why previous

[7]The value plotted for fabric represents only the fabric itself and enough glue to adhere it. In reality, more glue would need to be added to smooth the surface, thus further increasing the weight.

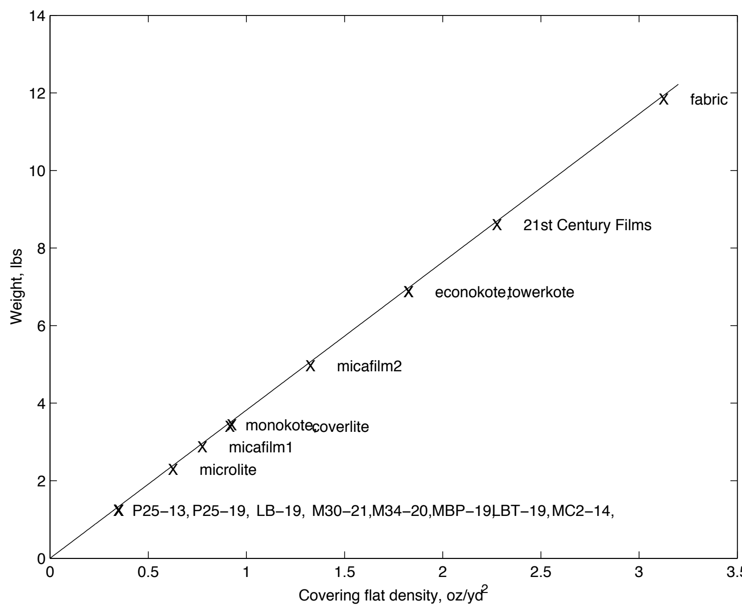

Figure 5.12. Skin weight as function of covering flat density, assumed S_{wet} = 550 ft^2.

HPAs have used tensilized Mylar as a covering material; there is the potential to reduce the skin weight to less than 2 lb, certainly a tremendous weight savings from the fabric covering discussed earlier. For these reasons, tensilized Mylar was selected for the final design.

5.10 Final Structure

Aluminum tubing is available in a variety of diameters and wall thicknesses. (See ref [17], [18], and [19]). Just like for the R/C model spars, only the finite thicknesses available were sized fo3 all components including wing and tail spars, struts and the tailboom.

With the exception of the main wing spar and strut system, all components could be sized analytically without the help of finite element software. Constant cross-section tubes were used in all cases. Both tail spars were sized by placing the entire load the surface was capable of generating at stall at the tip of the spar and calculating the root bending moment. Wall thicknesses were varied to provide a factor of safety of two from yielding. Tip displacements were then checked to be less than 10% of the span. For the elevator spar, an outside diameter of 1 in with 0.020 in thick walls should be used. A single cross section rudder spar would prove excessively heavy. Instead, a "step" taper as in the remote control model will provide a much lighter solution. These cross sections are detailed in the final drawings, but all use a wall thickness of 0.040 in.

Stress sizing of the tailboom provides a very light solution. However, upon investigation of its deflection and slope at the tip it was found that control reversal might occur under full load of the surfaces. Instead, the tailboom was sized with a constant cross-section for a slope of less than 5 deg at the tip under full rudder deflection, the larger of the two surfaces. This tailboom could be made significantly lighter with the use of a tapered boom, however to date no source was known to be available. A 3 in diameter was used to stiffen the boom without the addition of much weight or drag. It is also detailed in the final drawings with a wall thickness of 0.090 in.

A first cut at the spar and strut configuration using an evenly distributed 1G cruise load case with 2 in diameter tubes and 0.030 in thick walls displaced to the desired shape and weighed 32 lbs. However, further stress-based analysis must be used to ensure that the structure is not beyond it's linear elastic regime.

Initial attempts were made to expand the use of ANSYS® for stress analysis as well. However, specifying geometry directly in the program is difficult and tedious. The capability exists to import IGES files and define geometry in that manner. A parametric CAD model of the spar and strut structure in NX 3.0 was defined such that wall thicknesses, gap, and dihedral breaks could be easily updated and re-analyzed. ANSYS® had difficulty developing the geometry from the IGES files, however, mainly due to the large length and very small wall thicknesses.

The team had more experience with stress analysis using NX's in-house analyzer, Structures P.E. Initial meshes and stress distributions were attained using this avenue. A trial case was analyzed with a point-load of 108 lbs at the tip (1G tip load) evenly divided between the top and the bottom in an attempt to merely get some feel for how the stress was distributed throughout the structure. Figure 5.13 shows the overall displacement curve. Different colors denote different values of the octahedral stress. A more instructive view is shown in Fig. 5.14 whereby the stress is seen to be highest near the joint in the struts themselves.

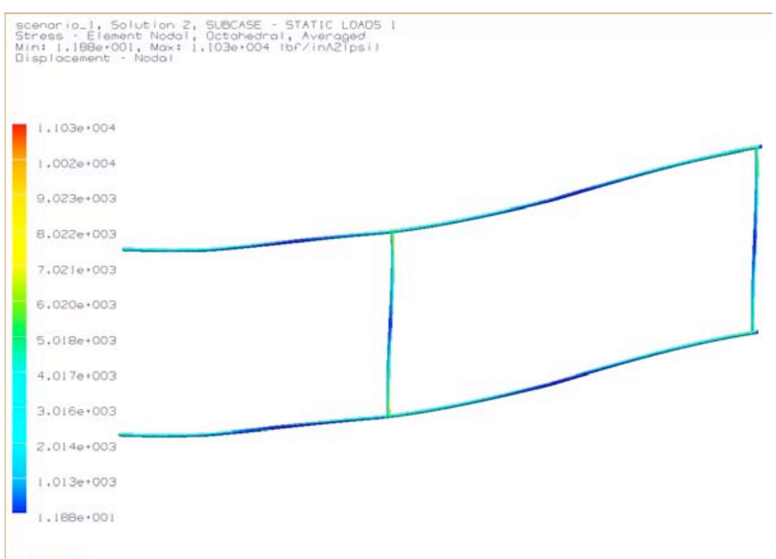

Figure 5.13. Overall stress distribution for a 108 lb point load.

Wall thicknesses were increased near the joint and joiner tubes used to connect the individual tubes at the joints were also modeled now to more accurately represent the stress at the joint. The loading was discretized for an elliptic 2G load case. Difficulty was again found in generating adequately fine meshes due to the large length and small wall thicknesses. This problem was complicated further by the additional loads instead of point loads. Nonetheless, overall octahedral stress distribution from this case is shown in Fig 5.15.

Magnitudes of the stresses between the first test case and the second varied by an order of magnitude. The team is unsure why, although, this leads one to believe that this stress analysis provides merely qualitative results. More experience is necessary to trust the results from finite element stress analysis and use it to size the spars and struts.

Stress results were inconclusive at best and were suspended on the project for three reasons: the difficulty generating an adequate mesh of the desired structure, the team's significant inexperience with finite element methods, and the time constraints in finishing the scale model. It was felt that the team did not possess adequate experience to validate the results from the stress analysis and trust them. Regardless, before final construction of the aircraft significant stress analysis of all major components including wing and tail spars, struts, tailbooms, and fuselage structure should be conducted. Once local stresses are known, buckling analysis should also be conducted. A variety of loading conditions would prove instructive including the 2G pull-up, entering into a turn, a steady-state turn and gust loading. The safety factors necessary for a light enough structure for this project to be feasible are very low and warrant significant analysis before one can entrust pilot safety to the design.

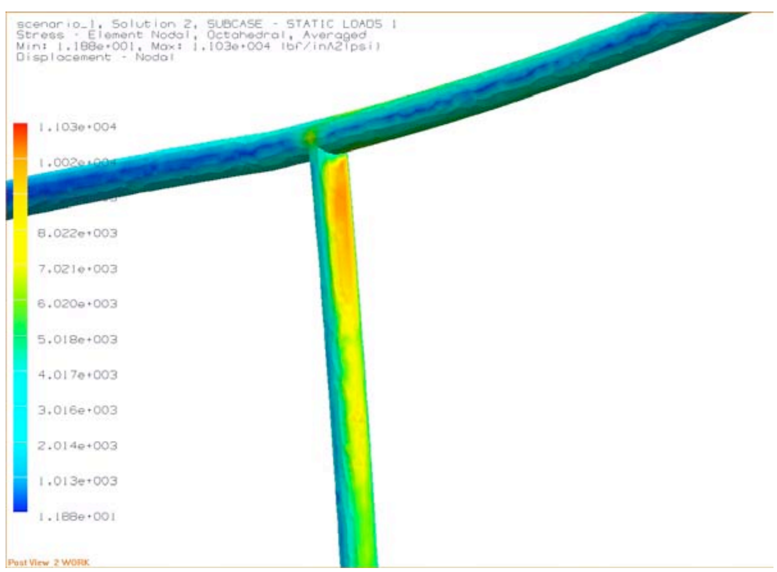

Figure 5.14. Octahedral stress distribution near the mid-span joint.

Due to the preliminary nature of several of the major aircraft components, center of gravity calculations would be rough at best. However, initial analysis shows that as long as the pilot

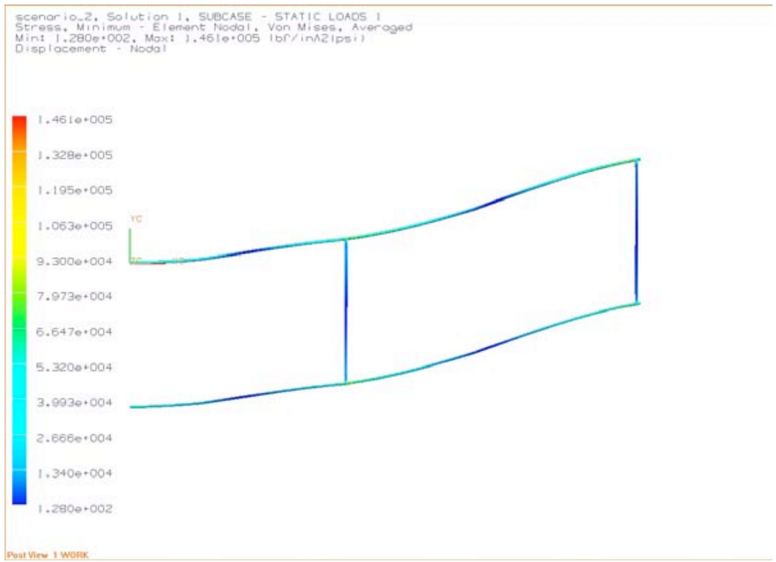

Figure 5.15. Overall octahedral stress distribution for 2G distributed load.

is placed somewhat ahead of the wing aerodynamic center, the aircraft will balance. This exact location should be defined after component sizes are finalized and a more accurate weight statement can be made. A current listing of component weights can be found in Table 5.1. It shows that a 148 lb pilot could still fly the aircraft at the design gross take-off weight of 215 lbs.

Table 5.1. Structural Weight Breakdown

Component	Weight [lb]
Wing spars and struts	25.3
Tailboom	21.7
Rudder Spar	0.16
Elevator Spar	0.80
Wing Ribs and secondary structure	1.56
Tail secondary structure	0.50
Fuselage Frame	5.00
Covering	2.00
Propeller	2.00
Drive Train	3.13
Miscellaneous Hardware	5.00
Pilot	148
	215 lbs

Additional design work could analyze several aspects that may lead to lighter structures. The aforementioned problem of the ratio of strut stiffness to spar stiffness requires more in depth investigation. Also, different strut configurations including non-perpendicular alignments may be useful. If these changes prove beneficial, a wider range of pilot weight may be achievable. At any event, preliminary sizing shows that with a very small safety factor, the aircraft is capable of the desired structural performance and winning the Kremer prize.

6. Stability and Control

6.1 Requirements

The stability and control requirements were determined based on the mission requirements. Because the pilot is both the propulsion and pilot it was determined the airplane must exhibit significant natural static stability. Further the plane must exhibit positive directional stability. The dynamic motion must be either stable or have long periods. The HPA must be capable of turning at a rate sufficiently fast for completion of the course. The design philosophy followed for the aircraft was to carefully examine the mission, set the requirements for longitudinal and directional control power and stability, develop an initial control scheme derived from examination of similar aircraft, analytically surface sizes, select center of gravity location and dihedral from parametric study with a simplified layout using a vortex lattice code. Finally, a more detailed model was developed to preform final verification that the requirements were met.

6.2 Longitudinal Stability

To ensure minimal pilot longitudinal control effort the HPA was designed to exhibit significant longitudinal stability for a range of pilot weight in normal operating conditions. The horizontal tail size and center of gravity location were selected such that longitudinal motion is stable, the pilot has a full range of controllability, and both parasite drag and trim drag remain low.

Table 6.1 contains the horizontal tail volume coefficient for several HPAs. The table indicates most HPAs have a horizontal tail volume coefficient around that typical for sailplanes about $V_H = 0.5$[20].

Aircraft	Horizontal V_H
Monarch B[2]*	0.49
Musculair 1[21]*	0.57
Bionic Bat[21]*	0.41
VELAIR 89[21]*	0.35

Table 6.1. Horizontal tail volume coefficients of representative HPAs. *Note these values were estimated from drawings in the cited text.

Because the pilot is both the propulsion system and pilot, it should not be expected that he maintain a heavy work load due to insufficiently stable aircraft. Thus the aft limit of the center of gravity was selected to be that which guarantees the aircraft be 10% stable. The forward limit was selected to insure the HPA has enough longitudinal control authority by guaranteeing the ability to trim the aircraft in cruise without excessive rudder deflection ($\delta e \leq 8\,\text{deg}$). For a typical aircraft, the tail size may be selected from these constraints and with the known CG travel. HPAs have no real center of gravity variation in flight with the exception of variation due to shift in pilot weight. However, it was desired that the aircraft preform effectively for a range of pilot weights. For this reason a minimum of 5% mean aerodynamic chord or $0.05\bar{c}$ (only about 1 in) allowable shift in CG in both directions was required. Figure 6.1 depicts the design space for horizontal tail volume coefficient and center of gravity location. Both the left and right limits for center of gravity are plotted along with the stablitity limit. The selected tail size is indicated in the figure as well.

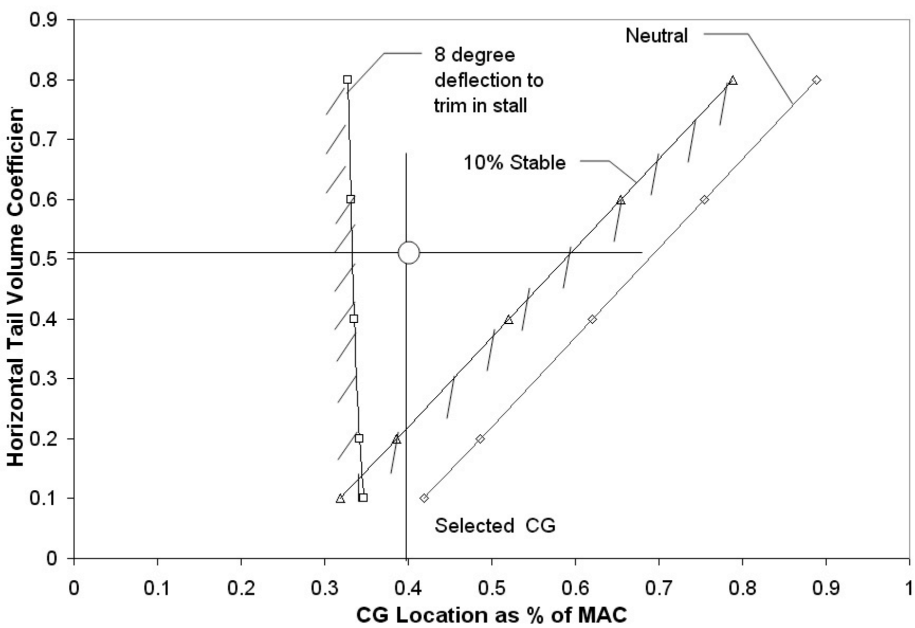

Figure 6.1. Design space for determination of tail volume and center of gravity location

The center of gravity location was selected based on the induced drag on the tail while trimming the aircraft in cruise. The induced drag in cruise was plotted against center of gravity location in Fig. 6.2. The figure indicates a minimum drag for a center of gravity location of about 35% MAC; however, the center of gravity was selected to be at $0.4\bar{c}$ to allow for 5% CG shift and not cross the forward center of gravity limit with a horizontal tail volume coefficient of $V_H = 0.5$.

For monoplanes, the vertical CG location has negligible effect on stability; however, for a biplane with a large gap to chord ratio, the vertical center of gravity location is critical as a large moment may be produced at high angle of attach. This is illustrated through Fig. 6.3. When the center of gravity is located within the lower wing, the lift on the top wing produces a stabilizing moment at

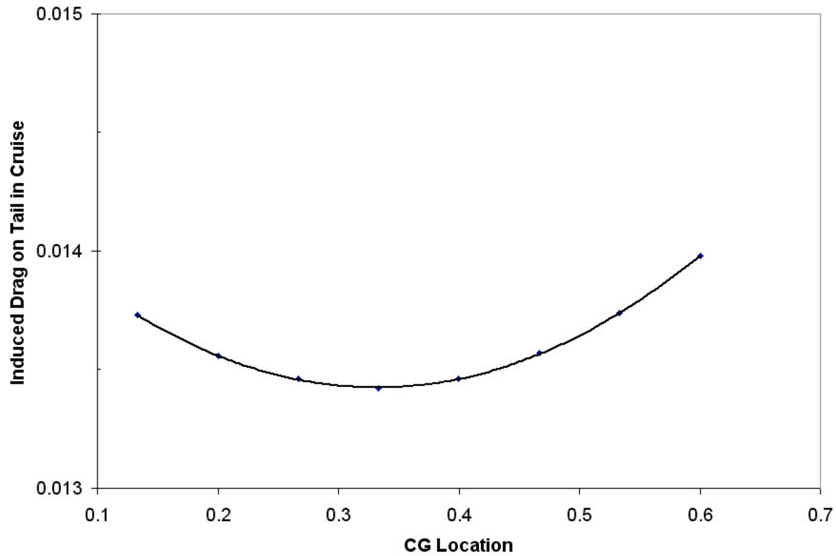

Figure 6.2. Trim drag verses center of gravity location for trim in cruise

high angle of attack. The effects of vertical CG location are seen in Fig. 6.4. The figure illustrates that for a CG located above center, the airplane becomes unstable at positive angle of attack. Similarly, for CG located below center, it becomes unstable at negative angle of attack. Thus a CG located at the middle of the wings was desired.

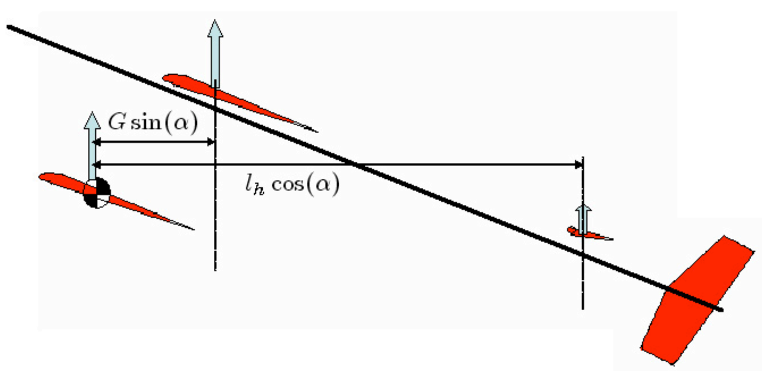

Figure 6.3. Illustration of biplane at high angle of attack depicting effect on stability

6.3 Lateral Stability and Control

The selection of the rudder size, aileron size, and dihedral was performed on the bases of lateral stability and controllability through parametric study.

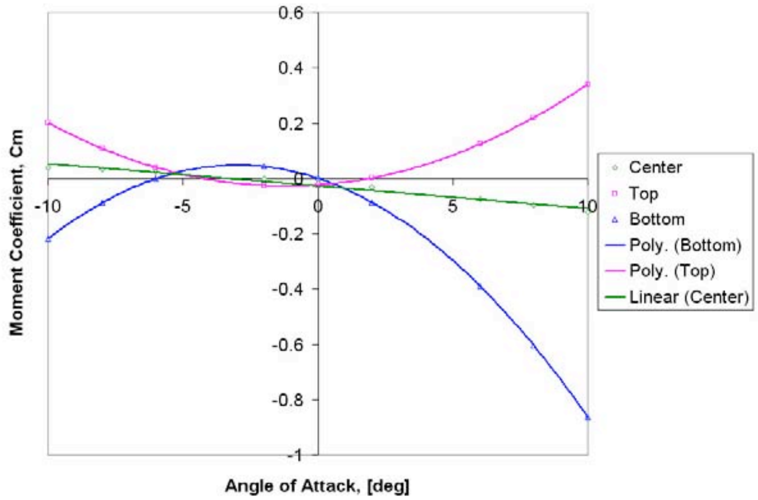

Figure 6.4. Pitch moment with angle of attack for varying center of gravity locations

The role of the vertical tail is to provide directional stability and yaw control. Initial sizing was estimated based on the typical vertical tail volume coefficient. Table 6.2 contains the vertical tail volume coefficient for several HPAs. The table indicates HPAs typically have a vertical tail volume coefficient is about 0.035. This was used as an initial estimate. Formal assessment of directional stability, steady bank, and cross-wind landing were used to specify the tail volume coefficient.

Aircraft	Horizontal V_H
Monarch B[2]*	0.035
VELAIR 89[21]*	0.045
Bionic Bat[21]*	0.030
Musculair 1[21]*	0.02

Table 6.2. Vertical tail volume coefficients of representative HPAs. *Note these values were estimated from drawings in the cited text.

To determine the appropriate tail size a simplified model was created using AVL. The wings were divided into only two panels so that the dihedral could be varied easily without significant remodeling work. Figure 6.5 contains a picture of the simplified model used to analyze the lateral directional control sizes for the aircraft. The smallest rudder tail volume such that the aircraft exhibit significant directionally stability, required less than 5 deg of deflection to land in the most severe cross-wind possible ($\beta = 11.3\,\mathrm{deg}$), and required no more than 9 deg deflection to maintain a banked 15 deg turn was selected. In Fig. 6.6 each of these three constraints are examined. Naturally, increasing the tail size increases directional stability, but it also increases the rudder deflection needed to land in a cross-wind. Further the required deflection to maintain a 15 deg bank angle in a turn is minimized at a tail volume of about 0.06. A tail volume coefficient of 0.05

was selected because it provides good directional stability, requires about 5 deg rudder to land in a cross-wind and nearly minimum rudder deflection in a steady-state turn.

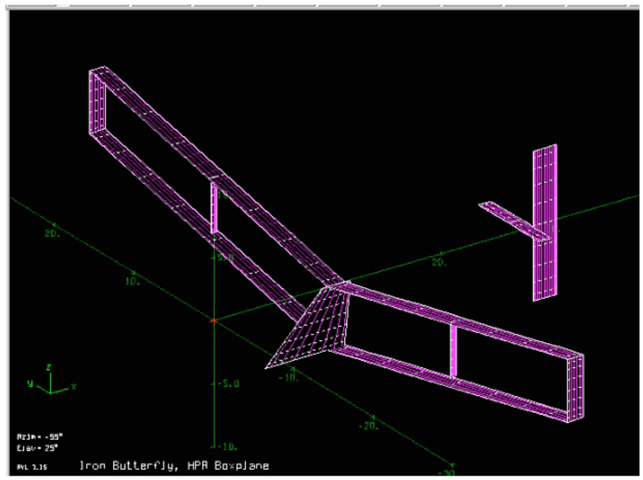

Figure 6.5. AVL model used for lateral control sizing

The wing dihedral was critical for turning. In a steady state turn the rolling moment must sum to zero. Monarch relied on an effective dihedral (C_{l_β}) of about 11 deg to counter the roll due to yaw rate (C_{l_r})[2]. Typically the effective dihedral angle lies between 10 and 13 deg. The design philosophy followed for dihedral angle selection was to use a straight dihedral model to perform parametric study to determine the variation in rudder deflection and slip angle for a coordinated turn with dihedral angle. The results would be confirmed on a more sophisticated polyhedral model with the same effective dihedral. The results are seen in Table 6.3. The results indicate the required slip angle in a coordinated turn decreases while the rudder deflection increases with increasing rudder size. As a trade off a dihedral angle of 11 deg was selected. A realistic polyhedral design was employed to provide an effective dihedral of 11 deg. The polyhedral is described in Fig. 5.11.

Dihedral Angle, Γ	Rudder Deflection, δr	Side Slip, β
10 deg	8.0 deg	5.5 deg
11 deg	8.8 deg	4.6 deg
13 deg	9.6 deg	3.5 deg

Table 6.3. Variation in steady-state coordinated turn deflections with dihedral

6.4 Rolling the Aircraft

The problem of turning HPAs may be related to the large span, low speeds, and extreme light weight. Early attempts to win the Kremer Prize were unsuccessful due to the inability to turn

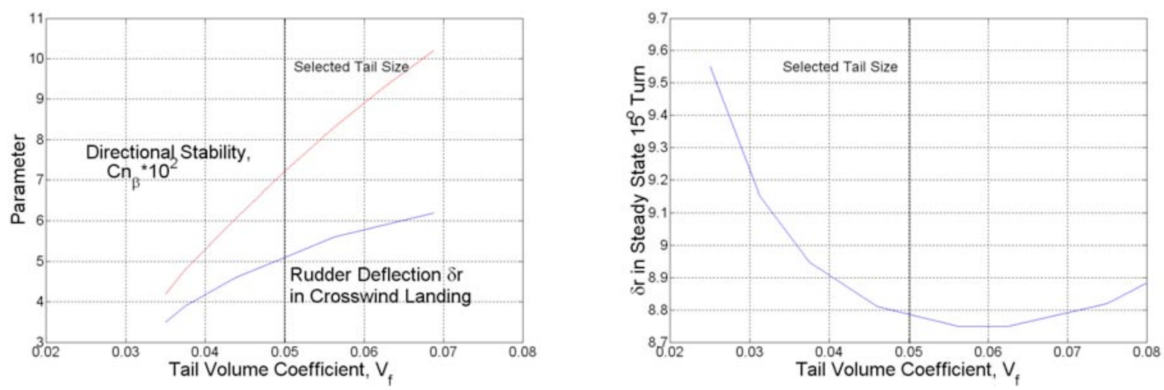

(a) Cross-wind landing and directional stability.

(b) Rudder in steady turn.

Figure 6.6. Vertical tail sizing

rather than the low power available. Initial explanation for the difficulty was attributed to the apparent inertia; however, more recent study has attributed the difficulty to turn to a damping effect rather than inertial[7].

The rolling inertia of an extremely light airplane will contain a component related to the apparent mass. The component results from additional energy needed to accelerate a body of air around the wing of the airplane as well as the airplane itself. For HPAs this effect is substantial. The apparent mass is equivalent to the mass of the circular cylinder of air around the wings. For the Gossamer Condor, the apparent inertia in pitch and roll are 140% and 440% of the actual moments of inertia[7]. Thus conventionally sized surfaces may not be sufficient to accelerate the HPA at the desired rate. Apparent inertia effects must be considered.

The effect of inertia simply restricts the ability to acquire excessive accelerations. There is no restriction making a given roll rate unattainable. This effect alone does not completely describe the rolling difficulties for HPAs. The effects of substantial span and low speeds results in a damping force apposing the rolling motion. A measure of the importance of roll damping may be characterized by the damping time constant defined by Eq. (6.1)[7].

$$\tau_{roll} = \frac{\dot{\phi}}{\ddot{\phi}} \approx \frac{24 I_{roll}}{\rho V b^3 \bar{c} m} \tag{6.1}$$

Where the roll rate is $\dot{\phi}$, the roll inertia is I_{roll}, and m the lift curve slope. If the roll inertia is calculated as purely the inertia of the column of air around each wing, the time constant may be compared to other HPAs in the Table 6.4.

The ineffectiveness of ailerons for primary roll control may be seen by considering a single degree of freedom model in principle coordinates. The equations of motion are:

Table 6.4. Approximation of first order roll time constant for HPAs

HPA	Time Constant τ_{roll}[s]
Condor[7]	0.10
Musculair II[7]	0.05
Iron Butterfly	0.05

$$I_x \dot{p} = L_v v + L_p p + L_r r + \Delta L_c \tag{6.2}$$

Where the control is applied through ΔL_c. In the simplest case when $v = r = 0$ the effect of step aileron deflection is a step deflection of a first order system. Thus the steady state roll rate for a step aileron deflection may be expressed as[20]:

$$p_{ss} = \frac{2VC_{l_{\delta a}}\delta a}{C_{l_p} b} \tag{6.3}$$

Further Eq. (6.3) may be rewritten in terms of the $C_{l_{\delta a}}$ required to achieve a given steady state roll rate. To achieve a roll rate of 10 deg/sec at an aileron deflection of 15 deg, $C_{l_{\delta a}}$ must be at least 0.47. Table 6.5 shows estimates for $C_{l_{\delta a}}$ for different aileron sizes. Note aileron size is defined as the length of aileron from the wing tip and the % chord the aileron occupies. The table indicates that for any realistic aileron size, inherited roll damping prevents turning at the desired roll rate. For this reason, it was determined that ailerons alone would be insufficient and yaw-roll coupling needed to be employed.

Length	% Chord	$C_{l_{\delta a}}$
15	40	0.311
30	40	0.430
15	50	0.351
30	50	0.485
15	60	0.380
30	60	0.520
24	60	0.470

Table 6.5. Ineffectiveness in HPAs to create 10deg/sec roll rate

As Table 6.5 indicates, conventional sized ailerons are insufficient. Over sized ailerons were used in the past on Musculair I, and II[7]. However, as it was seen in Table 6.5 this may still be insufficient. Further problems such as aileron control reversal further complicate the roll problem. For these reasons the Gossamer Condor, Daedalus, and Monarch relied on secondary roll generated through yaw-roll coupling[7]. For the Iron Butterfly, the primary roll control system utilizes yaw-roll coupling through deflection of the rudder. The roll control is supplemented through deflection of ailerons. The ailerons were designed to occupy the outboard 15 ft of the 30 ft semi-span. The

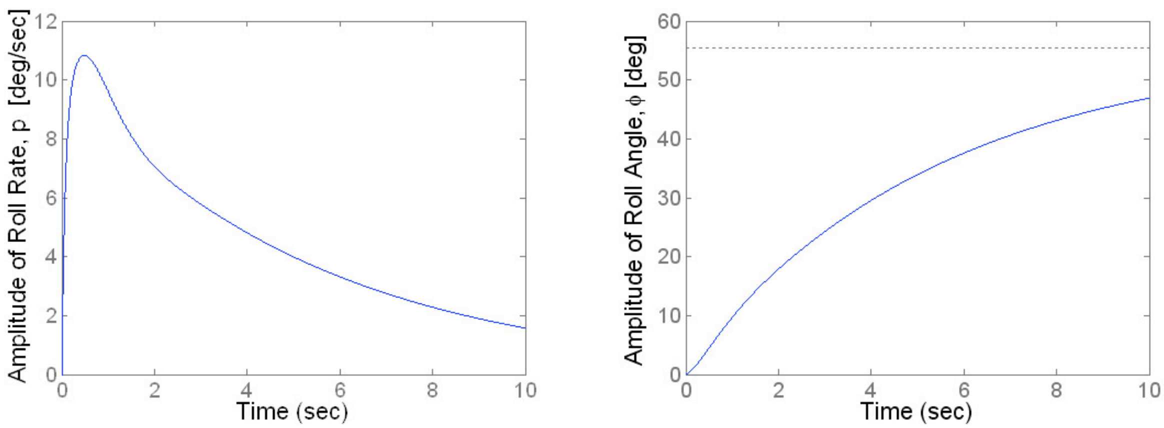

(a) Roll Rate p. (b) Roll Angle ϕ.

Figure 6.7. Response of Iron Butterfly to Aileron-Rudder Step

hinged at the $0.7\bar{c}$ position occupying 30% of the chord.

A six degree-of-freedom(DOF) dynamic model was developed and used to verify the ability to turn with the specified control system. Figure 6.7 indicates the roll response of the aircraft with application of 15 deg aileron deflection and 8 deg rudder deflection. The figure indicates a peak roll rate of about 11 deg/sec occurs and is diminished as time progresses. Also plotted in Fig. 6.7 is the bank angle as a function of time corresponding to the step control deflection. The figure indicates appropriate roll response. The desired 15 deg bank angle is acquired within 1.6 sec.

6.5 Dynamic Stability

Iron Butterfly was required to be dynamically stable in all modes except spiral. The spiral mode was required to be stable or have a time to double amplitude greater than 10 sec. HPAs in general do not exhibit spiral stability; however, the instability grows slow enough that the pilot may maintain control of the aircraft. It was required that the time to double amplitude be no less than 20 sec. Small perturbation theory was used to obtain the longitudinal and lateral directional modes. The eigenvalues for longitudinal motion of both the aircraft and quarter-scale model may be seen in Table 6.6. For a typical aircraft there are two oscillatory longitudinal modes. However, Iron Butterfly experiences a single oscillator mode (Phugoid mode) and then a pair of stable real exponential modes. The first real mode has a time to half amplitude ($t_{1/2}$) of 0.13 sec and the second has $t_{1/2}$ of 0.02. This structure of longitudinal dynamics is typical for HPAs and was felt on Monarch and Chrysalis[2].

The lateral-directional modes were found in a similar fashion. These modes are summarized in Table 6.7. The lateral-directional modes are characterized by a pair of complex eigenvalues representing the dutch-roll mode and two real stable roots. The first stable root represents the highly damped roll mode, the second is the spiral mode. It must be noted that unlike most HPAs the spiral mode is stable; however, it is marginally stable. The spiral mode is characterized by a time to half amplitude of 11.6 sec. The criteria for dynamic stability were met.

Table 6.6. Eigenvalues and time to half amplitude for longitudinal dynamics

Eigenvalue	Time to half [sec]	ζ	ω
-34.7	0.02	-	-
-5.3	0.13	-	-
-0.072 + 0.74i	9.70	0.17	1.05
-0.072 -7.4i	-	-	-

Table 6.7. Eigenvalues and time to half amplitude for lateral-directional dynamics

Mode	Eigenvalue	Time to half [sec]	ζ	ω
Dutch Roll	-4.92+3.51i	0.14	6.04	0.81
-	-4.92-3.51i	-	-	-
Roll	-2.03	0.34	-	-
Spiral	-0.06	11.6	-	-

6.6 Requirement Compliance Assesment

The analysis provided in the preceding section has indicated the concept Iron Butterfly is capable of preforming the requirements set by the mission. The aircraft demonstrates significant longitudinal and lateral-directional stability. The aircraft is capable of preforming a steady state 15 deg banked turn without excessive control deflection or side slip. The aircraft is capable of landing in a severe crosswind situation. The eigenmodes indicate the aircraft will experience good dynamic properties. It must be noted that small perturbation theory was employed to preform the dynamic analysis. However, more complete nonlinear integration to simulate the dynamic response of the aircraft in realistic flight scenarios could prove invaluable. The aims of this design team were to preform such "simulation" through a dynamically similar 1/4 scale model. The details of the dynamic similarity as well as the flight test results are described in Sections 9.5 and 9.6 respectively.

7. Propulsion System

7.1 Human Power Production

Human power is something that has been studied thoroughly throughout the course of history, mostly in the realm of sporting competition. Many vehicles have relied on this most basic means of power production to meet their transportation goals in many different mediums. Upon closer inspection however, human power production is anything but simple. As with any propulsion system, a very basic conservation of energy equation can be written for the propulsion system:

$$E_{rxn} = W + Q \tag{7.1}$$

Here, E_{rxn} signifies the energy available from the burning of fuels from foods with oxygen while W and Q denote mechanical work and excess heat respectively. Maximizing the effective work is an extremely complicated function of many things. It depends on primarily the availability of fuel to burn and oxygen from the bloodstream. The human body, however, has several sources of energy.

The basic fuel for energy producing reactions in muscles is adenosine triphosphate (ATP) which is the high energy form of adenosine diphosphate (ADP). Oversimplifying, the body processes sugars and ADP into ATP mainly in two separate ways before ATP is used in an energy producing reaction which produces ADP and some other interesting byproducts. It is helpful to imagine ATP as ADP + energy + phosphate and to understand that the reaction goes both ways in the body. The highest power output can be obtained through anaerobic metabolism which, burns glucose obtained directly from a starch called glycogen and breaking it down through a reaction called anaerobic glycolysis. This reaction is complicated. It is, however enough for the purposes of this examination to realize that it does not usually involve oxygen and, in the end, it produces 4 ATP molecules and 2 other molecules known as pyruvic acid. However, one ATP molecule must be used to break down more glycogen to continue the process. Pyruvic acid is then converted into lactic acid by an energy-carrying enzyme that needs to get rid of some excess energy so that it may return and process more glucose. It is difficult to define how efficient this process is because as stated above, some energy is passed on to lactic acid which can be used different processes that create ATP. For the purposes of this discussion, it will be assume that the energy passed into lactic acid is lost. Under these assumptions, the process is on the order of 2% efficient. It is also important to note that the amount of glycogen available in the muscles is finite and comparatively low allowing for only a short period of exertion.

At the other end of the exertion spectrum lies aerobic metabolism. Aerobic metabolism relies on the break down of larger molecules like fatty acids and, to a lesser extent, amino acids to release energy. Aerobic metabolism can also use pyruvic acid as a fuel. This process takes place in the mitochondria of “slow-twitch” muscle fibers. Mitochondria are organelles which contain the structure necessary to accept oxygen from the bloodstream. Highly trained athletes have increased mitochondrial density; a term meaning increased surface area (in the form of folds) within the mitochondria themselves allowing for higher oxygen absorption. Some energy in the form of ATP is made directly from the breakdown reactions but most of the energy is carried away through enzyme reactions to be made into ATP elsewhere. Again, drastic oversimplification is employed here, and, using the same glycogen as fuel, 37 ATP molecules are produced by this aerobic metabolism process. This process is on the order of 30% efficient. The only byproducts of this process are carbon dioxide and water which can easily be removed.

A purely aerobic effort in most people, however, does not produce enough power to operate a human powered aircraft. The effort required will be one which combines anaerobic metabolism and aerobic metabolism and makes use of the ability of the body to process lactic acid. Athletes train themselves largely based on a heart rate value that is associated with their lactic acid threshold (LT). This heart rate value is defined as the exertion level at which the mechanisms for processing lactic acid through aerobic metabolism can no longer keep up with its anaerobic production. It is above this heart rate at which lactic acid begins to build up creating a burning sensation. A second heart rate value is used at which the maximum volume of oxygen is processed by the body (VO2max). With training, large gains can be made in raising one's LT, however, VO2max is a quantity which, for the most part, is genetic and not trainable. The effort required here will be one between LT and V02max. Figure 7.1 shows plots for several different groups of people of their power output and oxygen consumption and the time for which they can maintain a cycling effort[22].

Two basic lines are shown. The lower of the two is for an average healthy man. The upper line is for first class athletes whom are most likely professional or elite amateur cyclists. Since there is little direction given by the Kremer prize rules on the subject, the power available will be based on this upper line. There are several important things that can be taken from this plot. It can be seen that in very short intervals where anaerobic metabolism can be used, power output can be very high. Note, however, that this graph uses a logarithmic scale along the x-axis, creating a false sense of sustainability. There is a leveling of the data around 10 min where the maximal sustainable effort level is LT. For the use of this design discussion an average intensity of 400 W will be chosen as sustainable for the duration of a 3.5 to 4 min effort. This is chosen such that slightly increased power demands due to flight conditions such as a headwind are not catastrophic.

A second factor to be optimized is the pedaling frequency. Slower pedaling frequencies are more efficient mechanically because they minimize the excess motion of the legs. However, at low pedaling frequencies, different muscle fibers are recruited than at higher pedaling frequencies. At low pedaling frequencies "Type I" fibers, which work predominately from anaerobic metabolism are recruited, creating a very powerful motion with extremely high energy usage. At higher pedaling frequencies "Type II" fibers, which work predominately with aerobic metabolism are used, produc-

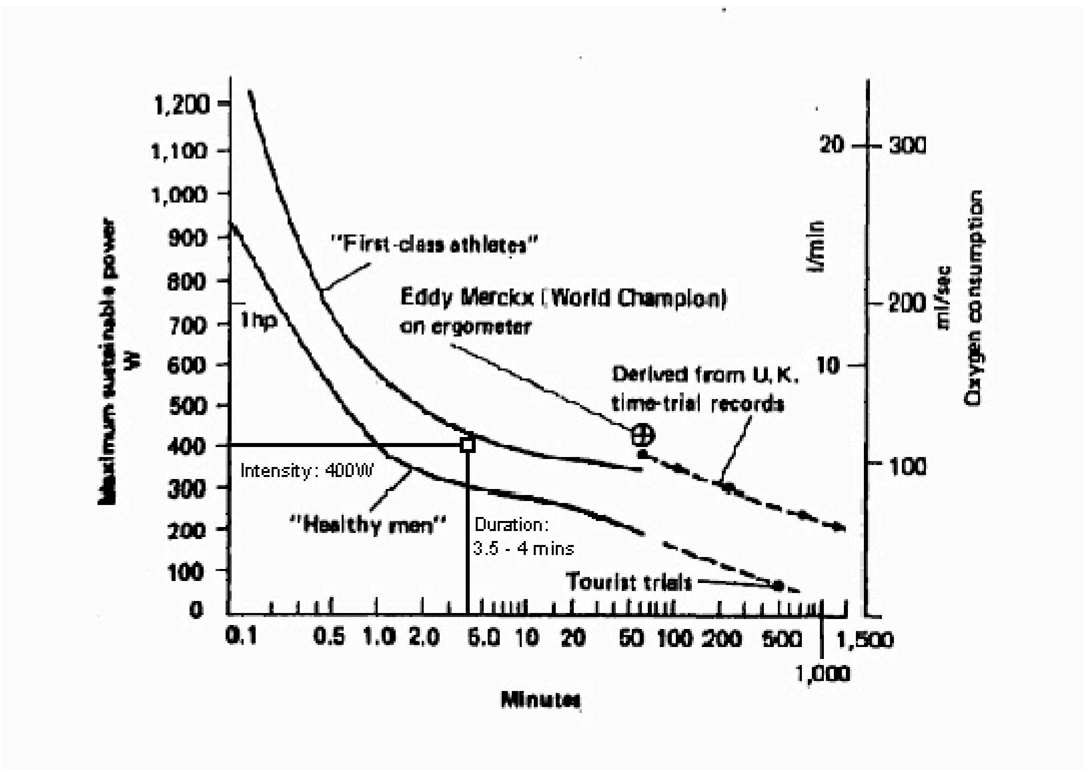

Figure 7.1. Maximum power, oxygen consumption and sustainable time for particular efforts[22].

ing a less powerful and more energy conservative motion. For these reasons, a balance between high and low cadence must be found. Below, in Fig. 7.2 adapted from Ball, the dependency of oxygen consumption on power output and pedaling frequency is shown[23]. It is important to note that the lines representing the experimental data have been artificially extended to reach the design point for this application.

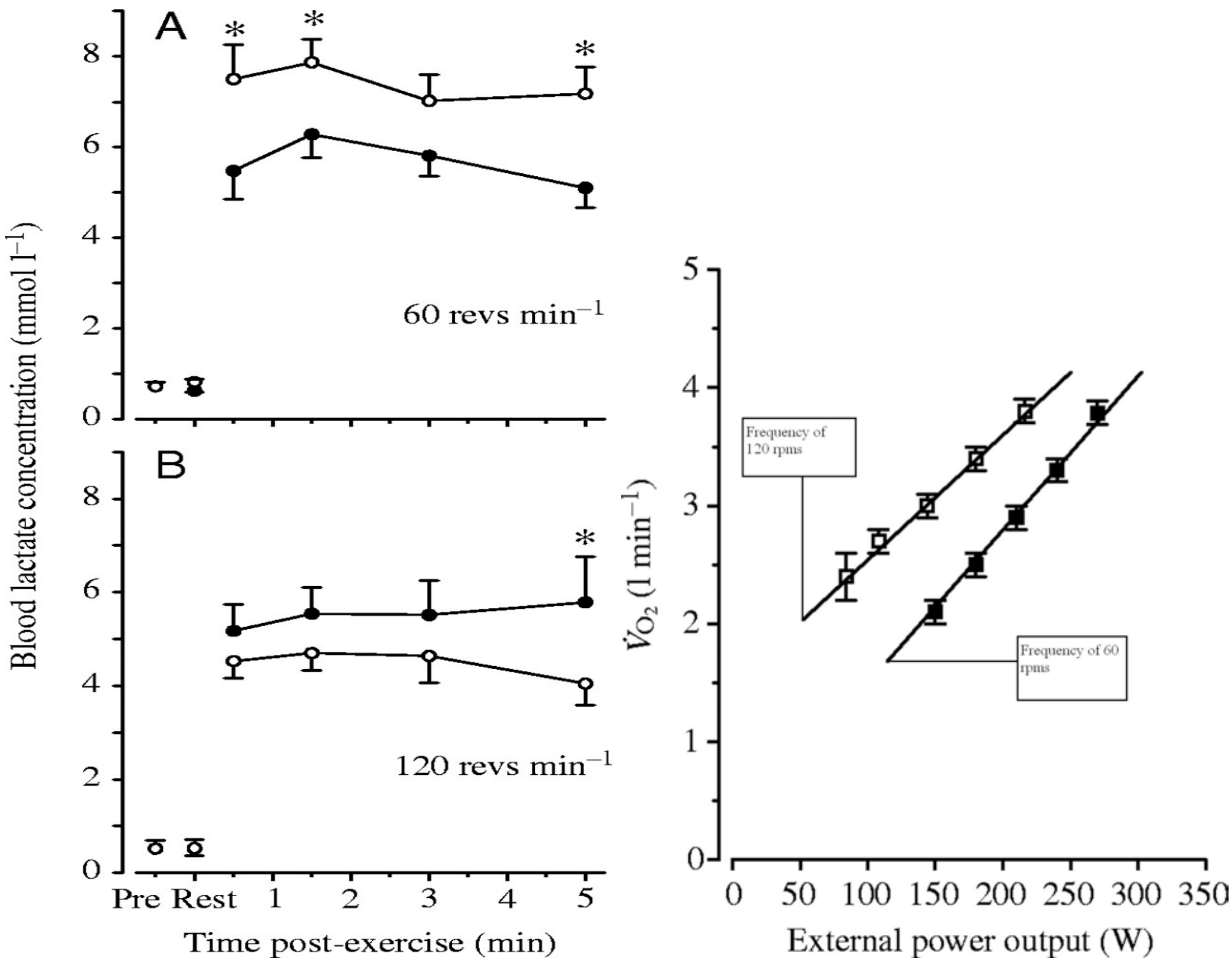

Figure 7.2. Dependency of oxygen consumption on external power output and pedaling frequency as well as the dependency of blood lactate concentration over time on pedaling frequency.[23].

In Fig. 7.2, it can be seen that blood lactate concentration is higher over all the post exercise measurements taken at 60 rpm than at 120 rpm. For the reasons above, a design pedaling frequency of 90 rpm will be used for this application. It appears that at this level there is a good balance of oxygen consumption, mechanical efficiency, and lactate production.

7.2 Cooling

Revisiting the issue of metabolic efficiency, it will be assumed that this effort is far closer to an aerobic effort than an anaerobic one and the overall efficiency of the pilot will be assumed to be 25%. This assumption appears to be a good one due to the fact that in Fig. 7.1 the chosen power output appears much closer in magnitude to the leveling region around the five minutes sustainable time than the maximal efforts around 0.1 min sustainable time. Very simply, a relation between efficiency, available power, and excess heat production can be written.

$$\eta_p = \frac{P}{\dot{Q}} \tag{7.2}$$

This equation shows directly that by picking a desired power output, $P = 400$ W, it will be necessary to dissipate 1600 W of excess heat.

From the above discussion, it is noted that there is a very significant amount of heat to be dissipated in some manner. For the purpose of the design of the cooling system, 2000 W will need to be chosen as an amount of heat that needs to be dissipated to account for variations in exertion level and surrounding temperature. The heat will dissipate in two ways: convection through the skin of the aircraft and a ducting system which will carry cool outside air and exchange it for warmer cockpit air. Eq. 7.3 describes the relationship of heat dissipation.

$$\dot{Q} = \dot{Q}_{conv} + \dot{Q}_{cond} \tag{7.3}$$

First, a general approach to the problem will be outlined. Both the heat flow through the duct and the heat flow through convection depend on the interior cockpit temperature. For the sake of simplicity, the cockpit temperature will be assumed to be constant throughout the interior of the fuselage and time invariant although obviously the interior temperature near the walls of the fuselage will be lower, and it will take time for the air inside the cockpit to heat. Effectively, an equilibrium cockpit temperature is being defined. In the limiting case that there is no duct flow, the cockpit equilibrium temperature will be very high. In this case all the heat is dealt with through convection. In the other limiting case that there is no convection, the duct will be very large and cause a great deal of drag. This is the essence of the trade off. Increasing duct size lowers the cockpit temperature but increases drag. A rigid constraint will be placed at 100^{o}F over which it will be assumed that power production becomes a problem for the pilot.

Looking more in depth at the convection term, several other things affect the amount of heat that can be dissipated in this manner. It is actually a two part problem. The first part in which the heat is passed through the skin is dependent on the surface area of the fuselage, the thermal conductivity of the skin material, k and the temperature gradient $(T_\infty - T_e)$ across the skin materials thickness, t.

Here the subscripts, e and ∞ denote the interior wall temperature and the exterior free stream temperature. Since the air inside the cockpit is assumed at a constant temperature and zero velocity, it can be assumed that the interior wall temperature is equal to the cockpit equilibrium temperature. The second part of the problem involves convection over the outside surface of the cockpit wall.

$$\dot{Q}_{conv} = hA(T_e - T_\infty) \tag{7.4}$$
$$\dot{Q}_{conv} = 0.664(Pr)^{1/3}\sqrt{Re}\tfrac{kA}{L}(T_e - T_\infty) \tag{7.5}$$

Eq. (7.5) from Schetz, applies only to a flat plate in laminar isothermal flow, but relates the heat lost through convection to the Reynolds number and Prandtl number[6]. The Reynolds number at any particular point depends on the length from the beginning of the surface and the local velocity. At this point it becomes necessary to assume a fuselage shape so that a velocity profile may be calculated. The fuselage shape was assumed to be a symmetric NACA 0036 airfoil to calculate the local velocities with a vortex lattice panel method. It is also important to note here that the assumption of a NACA 0036 airfoil likely makes the laminar boundary layer assumption in Eq. (7.5) invalid. However, since this is a purely theoretical fuselage shape and relations similar relations to Eq. (7.5) exist for turbulent boundary layers, only Eq. (7.5) will be applied to simplify the analysis method. At this point a m-file script was written in MATLAB®which performs the following:

1. Reads in velocity and position data along the airfoil surface obtained from a vortex panel method code.
2. Selects an amount of heat to be dissipated by convection.
3. Solves for the interior temperature by:
   - Starting with an exterior wall temperature equal to the surrounding temperature.
   - Breaking up the airfoil into many small flat plates with local velocities as found by the vortex panel method and local Reynolds numbers according to their position along the length of the airfoil surface.
   - Integrating the heat dissipation over the length of the airfoil surface.
   - Increasing the exterior wall temperature if the calculated heat dissipation is less than the selected.
   - Combining Eqs. (7.3) and (7.5) to calculate the interior cockpit temperature.

The equations for the ducted mass flow term are simple to evaluate.

$$\dot{Q}_{duct} = \dot{m}C_p(T_{eq,c} - T_\infty) \tag{7.6}$$

This was then used together with Eq. 7.3 to expand the MATLAB®code to do the following:

4. Calculate the amount of power needed to be dissipated through ducted flow.
5. Calculate the amount of mass flow needed for this ducted heat dissipation.
6. Calculate the amount of drag caused by slowing the free stream duct flow to rest in the cockpit as a worst case scenario.
7. Plot this amount of drag versus cockpit temperature.

The plot of this drag versus cockpit temperature is shown in Fig. 7.3. From the figure the a minimum drag of 0.08 lbs may be expected to result from the duct cooling system.

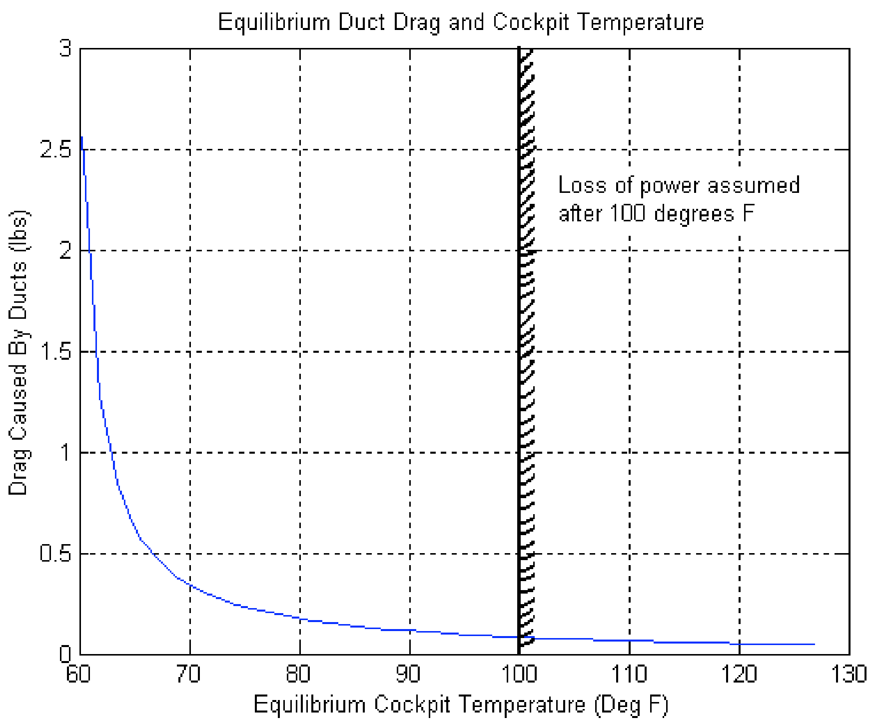

Figure 7.3. Result of MATLAB®code for duct design.

Further iterations of this code will take into account the real shape of the fuselage and boundary layer transition to turbulence. The drag estimate will also be further revised to resemble fully developed flow in a pipe through the cockpit. Still, despite the inaccuracies and assumptions, the trends reflected in the above plot reflect those in actuality and the magnitudes of the drag and cockpit temperature are close to the actual values.

7.3 Drive Train

7.3.1 Concept Development

The drive train of this aircraft has a simple mission. It must produce the highest efficiency with the lowest weight and smallest deflections due to the forces applied to it. For simplicity and historical success reasons, a bicycle-type drive train was chosen. There are several issues which must be resolved to use such a system in a human powered aircraft. First, the axis of rotation of the pedals will be ninety degrees offset from that of the propeller assuming the pilot is facing the same direction as the propeller. Second, the orientation of the pilot in the fuselage must be optimized for maximal power output. Finally, a decision should be made on the structure supporting the pilot and handling the drive train loads. To solve the first constraint, several ideas were considered. The decision matrix below in Table 7.1 details how the decision was made. Here, the figure-of-merits rating scheme of Section 3.3 was employed.

Table 7.1. Drive train decision matrix

Concept	Details	Efficiency	Weight	Resiliency	Total
1	Gear box attached to pedal bearing shaft; Drive shafts connect pedals, propeller	1	-2	1	0
2	Geared roller chain with bevel gear to propeller	0	0	0	0
3	Non-traditional plastic and twistable roller chain twisted 90 degrees	-1	2	0	1

The third option was chosen for its potential for light weight without intolerable losses in resiliency and efficiency. The challenge is to find a sufficiently strong chain which is flexible enough to take the twist. Despite this challenge, this path has been successfully taken in the past by the Gossamer Condor designers. Two promising candidates were selected from the WM Berg company: the “Flex-E-Pitch” line and the “Pow-R-Tow” line of drive chains.

7.3.2 Design Point Definition

At the heart of the drive train problem is the analysis and design of the structure and drive train components. To achieve this goal, it is necessary to assign a design condition on which the loads will be based. For the purposes of this analysis, this design condition will be one in which the pilot is producing the assigned 400 W, but at a cadence of only 45 rpm. This provides for a factor of safety of 2 over normal operating conditions, the 400 W at 90 rpm from Section 7.1). This is a high torque condition as it corresponds to 85 pounds of pressure on the pedals, but one that a normal person is completely capable of producing. It will be important that pilots be aware of this condition and not exceed it. By doing some simple calculations the drive train loads can be calculated. These values are shown in Fig. 7.4.

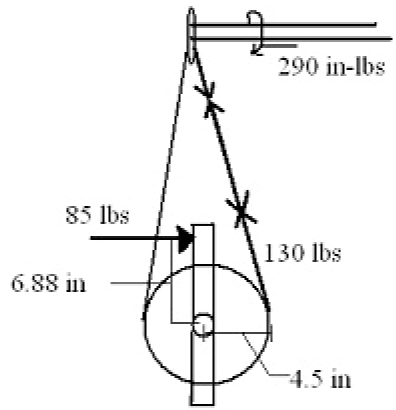

Figure 7.4. Drive train loads and dimensions. The dimensions shown are for standard off the shelf bicycle components (which are usually measured in millimeters).

A gear ratio between the lower chain ring and the upper gear was chosen of 2:1 such that the pilot can pedal at a 90 rpm while the propeller turns at 180 rpm.

7.3.3 Detailed Part Design

To fulfill the light weight requirements of this drive train application, improvements in weight must be made over conventional bicycle components. Bicycle components must be designed for many years of use at relatively high torque to sustain use under much more stringent design conditions than will be required for this application. Since the pilot will be positioned in a recumbent position, it will be impossible for them to put all of their weight on the pedals. Also, the aircraft is meant to fly at a specific power output and will be geared to achieve this output at a specific cadence. The pedal crank arms and pedal bearing axle will therefore be designed to carry these loads with an additional factor of safety of two. To minimize weight and displacement, the "paperclip" crank arm concept shown in Fig. 7.5 below was developed which maximizes the moment of inertia of the cross section to resist bending from pedal force with a minimum amount material.

As can be seen from the design, the part is a hollow shell at the ends and has a large slot in the middle to minimize weight. In further efforts to reduce weight, the pedal crank arms will be produced from a cast magnesium alloy. Magnesium alloy AZ91C was chosen for its extremely high stiffness with very low density when compared with other metals like aluminum and steel. It is known that parts magnesium alloys are not as durable as parts made from aluminum or steel, however this is not a large concern considering the mission of the aircraft.

To design the dimensions of the crank arms, a three dimensional computer (CAD) model of the part was constructed in Unigraphics NX 3.0. The CAD model was then analyzed by Unigraphic's

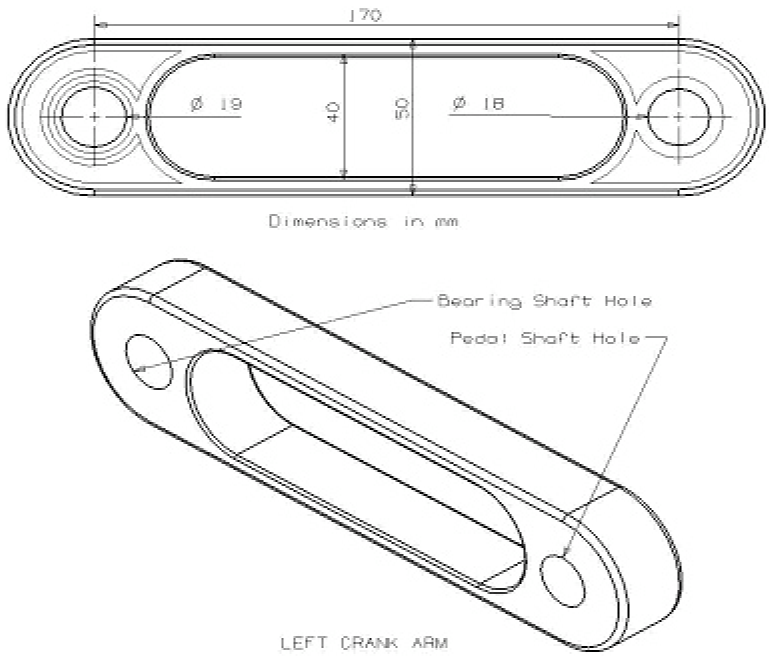

Figure 7.5. Left Pedal Crank Arm.

proprietary finite element structural analysis code, Structures P.E. Brief calculations were done previously to determine a test case load of 85 lbs. Using a fixed constraint applied to the crank bolt hole and point load and moment applied to the pedal shaft hole, it was found that the crank arm would deflect .063 in for a crank arm of length 6.7 in (a standard bicycle crank arm length). It was further found that in this configuration the maximal Von Mises stress was 10600 psi, significantly less than the yield strength of the magnesium alloy (15000 psi). Finally the weight of the part is 6.15 oz., a savings of 1.41 oz. over a popular high end bicycle component. Figure 7.6 shows the finite element model with exaggerated displacements. The different colors denote different values of octahedral stress in the part.

The right crank adds a web feature to which the chain ring will be attached. With the additional web feature, the right crank weighs 6.35 oz. The pedal bearing axle was designed in similar fashion to the crank, using Structures P.E. Figure 7.7 shows the dimensioned shaft below and has a weight of 0.8 oz. It was found that under the design torque of 290 lb-in the shaft twists negligibly and has a maximal stress values that are orders of magnitude less than the yield strength of the chosen aluminum material for this part.

Because the chain ring and gear are thin cast parts which do not require much material, they will be made from aluminum for cost savings over magnesium. The chain ring and gear weigh 4.26 oz. and 2.12 oz. respectively. The final part to be designed is the propeller shaft. This part experiences very low loads. It will be made from extremely thin aluminum tubing with a wall

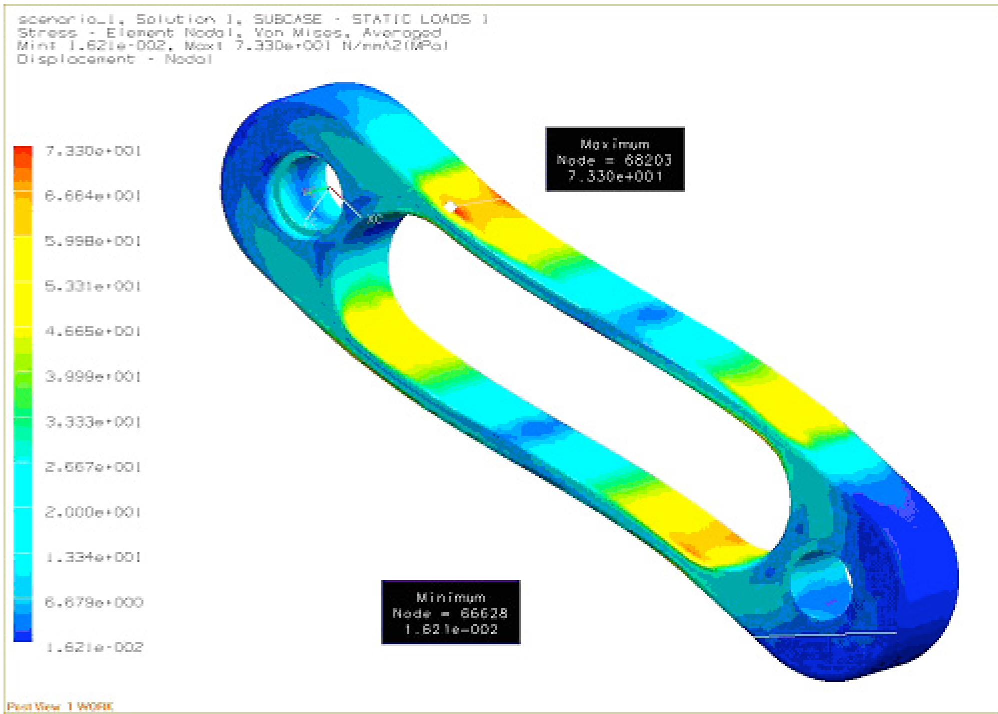

Figure 7.6. Finite element model of crank arm with exaggerated displacements.

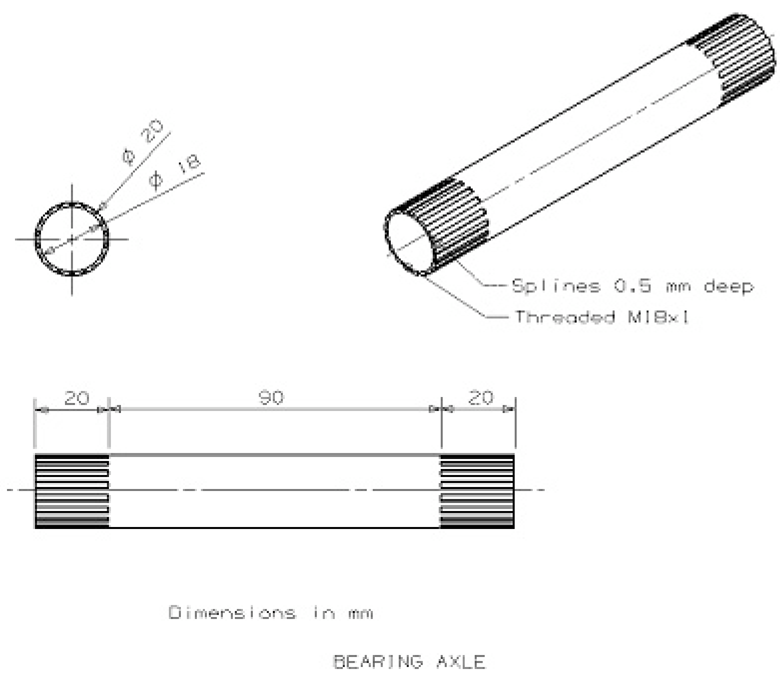

Figure 7.7. CAD of bearing axle shaft.

thickness of 0.04 in. and will weigh 8.75 oz. Table 7.2 details the weights and positions of all the drive train components. The total weight of the drive train is very light at just over 3 pounds.

Table 7.2. Propulsion Weights Table

Part	Material	Weight [oz.]
BB shaft	6061 Al	0.8
BB Bearings	6061 Al	4.24
Left Crank	AZ91C Mg	6.15
Crank Bolts	6061 Al	1.34
Right Crank	AZ91C Mg	6.35
Chain Ring	6061 Al	4.26
CR Bolts	6061 Al	0.13
Gear	6061 Al	2.12
Prop Shaft	6061 Al	8.75
PS Bearings	6061 Al	4.24
Chain		12.32
TOTAL		**50.7**
		3lbs 2.7 oz.

7.4 Pilot Positioning and Seat Design

The issue of positioning the pilot within the fuselage depends on three factors. First and foremost the pilot constitutes a very large fraction of the gross weight of the aircraft and hence needs to sit as close to the aerodynamic center of the wing as possible. Next, the pilot's orientation must be decided. It is important that the pilot be able to see forward to fly the aircraft. Also, for compatibility in training purposes the pilot's orientation must be as close to that of a normal bicycle as possible. The relevant parameters for the similitude of pedaling position are the knee and hip angles at the fully extended position. These angles should be about 175 deg and 90 deg respectively. The 90 degree hip angle requirement sets the angle between the seat back and the line between seat and crank arm axle. The 175 degree knee angle forces the seat to be fore-aft adjustable since no two people are likely to have the same leg length allowing for the same knee angle at a given seat position. Using these constraints, a rough geometric cockpit layout is shown in Fig. 7.8.

The seat position was designed to be adjustable by the use of a two-bolt tube-shaped clamp. The seat frame itself is constructed of very thin bent aluminum tubing and is covered with rip-stop nylon fabric. The assembly drawings of the drive train and fuselage structure, including seat, are shown below in Fig. 7.9 the assembly drawings of the drive train and fuselage structure shown below. The fuselage structure was designed such that members were oriented in the direction of the primary loads on the structure. These loads are predominately vertical, due to the weight of

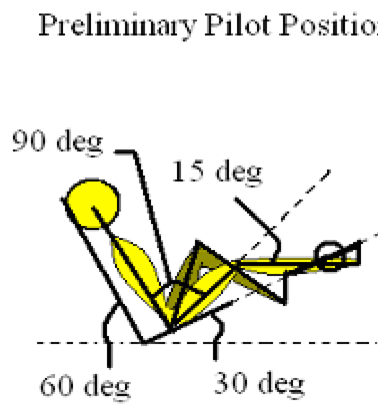

Figure 7.8. Shown are the approximate necessary angles for maximum power production and comfort. These angles will change slightly based on personal preference.

the pilot and lift of the wings, and in the pedal direction due to the pressure applied to the pedals.

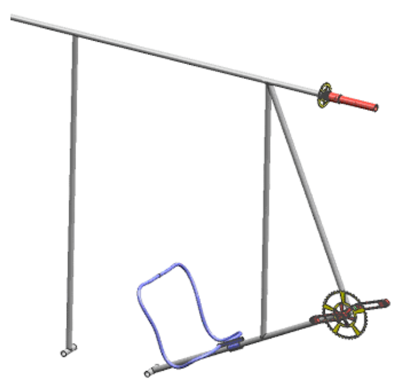

Figure 7.9. Drive Train Assembly.

8. Propeller

In this slow flight regime, a propeller is the most efficient and lightest means of propelling an aircraft and has accordingly been selected for the final design. Given the limited power available and the miniscule power margin of which the aircraft operates, every bit of pilot power must be utilized. However, propellers used on general aviation planes operate on the order of between 75 to 80% efficiency. At the 400W power level, this corresponds to an 80 to 100W power loss simply from the propeller, an unacceptable result. Consequently, the situation required a propeller designed for this specific flight regime with a target efficiency of 90%. The purpose of this prop design was then to maximize the prop efficiency while minimizing its weight. There are three things that are very beneficial in this design, however. The first is that acoustic noise, normally a major design factor, is irrelevant. Second, the low disc loading[8] allows for small angle approximations to be made in the analysis, while the third is the low rpm at which the prop can spin with very little gearing (it actually spins faster than the engine, a rarity in prop design).

8.1 Design Method and Results

Propeller design is primarily a function of diameter, chord, twist, rpm, and airfoil. In general, the larger the propeller diameter, and lower disc loading this causes, the more efficient it is. The first step in any propeller design is to determine how large a prop one can have. This dimension is limited by geometry, Mach number effects at the tip, and weight. Geometrically, the prop is limited to approximately the current gap between wings to allow for ground clearance. This is a radius of 54 in. For most aircraft, tip Mach number effects are the limiting factor on length. However, this turns out to not be a factor, as at this radius and a relatively high rpm of 360, the tip barely approaches Mach 0.15, and flow about it can still be regarded as incompressible. This is due to 360 rpm being very low for a prop design. Finally, weight is a complicated function of geometry and construction details, and optimization for weight is saved for a later exercise.

The first cut prop design procedure can be summarized as follows:

1. Determine maximum size from geometry
2. Choose the number of blades. For a given mass, using fewer blades is generally more efficient, as it allows the maximum radius prop. In the limiting case, using a one-bladed prop would be very efficient, but the weight needed to counterbalance it is significant. For this reason, a two-bladed prop was selected.
3. Use a flat plate airfoil (or maintain a consistent airfoil between designs). The consistent airfoil section will allow one to isolate the effects of twist and chord, and find the ideal case.
4. Choose a reasonable rpm. 180 rpm was selected given the available gearing ratios. This step specifies a propeller advance ratio in cruise of 0.389.
5. Choose a reasonable lift coefficient C_L. Here, $C_L = 0.8$ was used, as L/D_{max} occurs at this C_L for several airfoils that operate at the Reynolds numbers this propeller sees.

With these variables specified, it remains to optimize the twist and chord for minimum induced loss. An analysis technique was proposed earliest by Glauert in 1936, with a combination of momentum theory and blade element theory.[24] This analysis was restricted to lightly loaded propellers. Using Betzs proposed minimum induced loss span, a design procedure can be constructed using graded momentum theory, which was popularized most recently by Eugene Larrabee[25]. This

[8]Disc loading is defined to be the thrust force on the prop divided by the swept area of the prop disc.

method uses the Betz-Prandtl tip loss correction factor. This has the undesirable effect of reducing the analysis to apply only to lightly loaded blades[9] and low advance ratios, but this is sufficient for the entire HPA flight regime. Despite its usual disadvantages, it is a quick way to get a reasonable performance propeller, and a good place to start, and was used in early design iterations.

An improved design method is the use of potential flow formulation. This design approach is not restricted to lightly loaded blades or low advance ratios, for one solves for the entire helically-symmetric potential flow through a streamtube downstream of the propeller. In essence, the heli-coidal vortex sheet that makes up the streamtube can be likened to a rotating rigid screw, whose downstream motion is similar to the apparent motion of a rotating barber pole. This method thus gives a better consideration of the energy imparted to the flow downstream, and the impact on thrust and efficiency. However, these equations must be numerically solved and can become computationally intensive, so the praxis of this theory has historically been a final optimization of a propeller arrived at through another means, and was in the Iron Butterfly design as well. Reference was also made to Adkins' and Liebeck's work regarding the nonlinear prop flow solution with the inclusion of limited downstream viscous effects[26].

Finally, in recognition that many propeller optimizations are conducted to evaluate the cruise thrust and power conditions but that few design methods consider the static case, an in-house MATLAB script was developed to allow for static thrust predictions. This was based on blade element integration of airfoil strip theory along the radius of the blade, and considered only the conditions at a differential section of the blade, ignoring tip vortex effects. All three of the design procedures described above: Larrabees procedure, the potential flow formulation technique, and the blade element method were used in an iterative manner to determine a reasonable propeller geometry. Generally, Larrabees procedure was the starting point, the potential flow formulation used to modify this result, and finally, static thrust conditions were verified using the blade element method. The numerical solution for the potential flow analysis has been automated in FORTRAN under the name XROTOR[27]. This program is maintained by Mark Drela at MIT and was written for a Unix-based machine. It has been used very successfully in the past for HPAs such as MITs Daedalus. The team acquired access to Unix workstations and compiled the routine. In this routine, one is generally concerned with adjusting the span loading of each blade to minimize induced loss. Since one typically designs for a constant C_L throughout the blade, the chord and angle of attack is instead varied to adjust the lift distribution. As such, a plot of CL versus radius is almost meaningless; it is instead much more instructive to plot circulation versus radius. This is done for the prop designed for this airplane in Figure (8.1) along with the local C_L and local efficiency factor η.

Note that the very inboard section does not contribute to the lift. This inner hub radius was neglected in the lift calculations because not only is there often a spinner in this area, any blade

[9]Note the distinction between a lightly loaded disc and lightly loaded blades: a highly loaded disc can have lightly loaded blades simply by increasing the number of blades.

in the area is moving so slowly that its contribution to the lift is negligible, as can be seen by the tendency of the local efficiency η to drive towards zero as the local radius r becomes small. By integration of this local efficiency, one can obtain the total efficiency of the propeller, in this case 89.2%. Note that the circulation plotted has been non-dimensionalized, by the number of blades B, velocity V, and tip radius R. The circulation as a function of radius is well-developed and approaches the lift distribution Betz proposed, which is the propeller equivalent of an elliptic spanload for a wing.

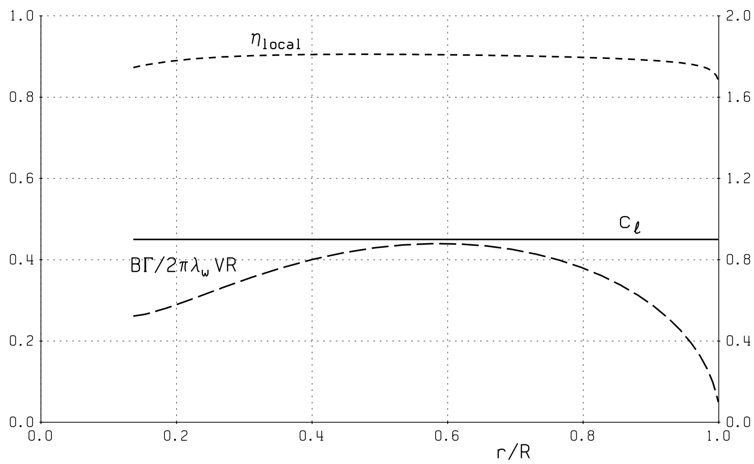

Figure 8.1. Spanwise lift distribution and efficiency for the first propeller blade design.

This is a good place to illustrate the low Mach numbers in which even the prop tip operates.. Again, based on this, it is emphasized that the incompressible approximation is very good here. Finally, note that C_L has been maintained constant at 0.9 along the blade. This was done for convenience, as it will allow one single airfoil to be used for the entire section of the blade. This saves both analysis and production time. Typically, one would specify the C_L at which L/D_{max} occurs for the specific airfoil used. The airfoil used here is the flat plate solution for simplicity, but does provide acceptable results.

8.2 Redesign

8.2.1 Motivation

Airfoil selection to further increase the performance of this propeller had begun, and identified the DAE-series airfoils for use on this propeller, when a final drag buildup for the aircraft was available. With this new information, it became clear that the prop had been optimized for a power output (380W) that was higher than the actual power required for level cruise at the aforementioned V_{cruise} = 33 ft/s. Simple application of the power Eq. (8.1)shows that even after a margin of safety was

#bld= 2	R m = 1.372	$\sigma_{3/4}$ = 0.0540	β_{twist}= 62.070	
Vm/s= 10.060	V/ΩR= 0.3891	P_C = 0.094	C_P = 0.0671	η_{ideal}= 0.9795
h km= 0.000	J = 1.2224	T_C = 0.086	C_T = 0.0502	η = 0.9149
T kN= 0.0314	P kW= 0.3449	RPM = 180.0	β_{tip} = 27.581	

Table 8.1. Performance characteristics of the rediesigned propeller

applied to a high drag estimate of $D = 7$ lbs, (pessimistic estimates are closer to 6.5 lbs), the power required P_{req} is significantly less than this.

$$P_{req} = DV_{cruise} = (7lb)(33ft/s) = 313W \tag{8.1}$$

8.2.2 Results

The same iterative design technique was followed for the new propeller, but the results showed slight efficiency improvement associated with the lower disc loading. The lift distribution and efficiency are shown for the redesigned blade in Fig. (8.2). This gives rise to the propeller performance characteristics summarized in Table (8.1). Although this blade shows a calculated efficiency of 91.49%, real world performance will be reduced, primarily due to the inboard shift of lift and the resulting large amount of twist specificed near the root of the blade. This is visually striking in Fig. (8.3).

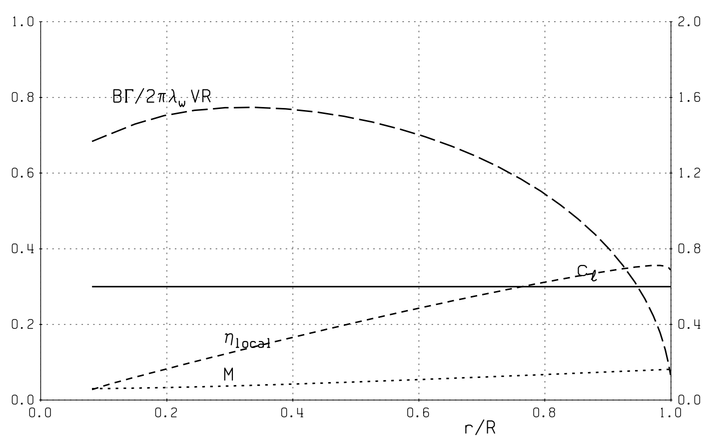

Figure 8.2. Spanwise lift distribution and efficiency for the redesigned propeller blade.

8.2.3 Off-Design Performance

Off-design point calculations were also performed, mainly for the takeoff case (thrust requirements during landing are somewhat relaxed relative to the other mission phases). To illustrate different

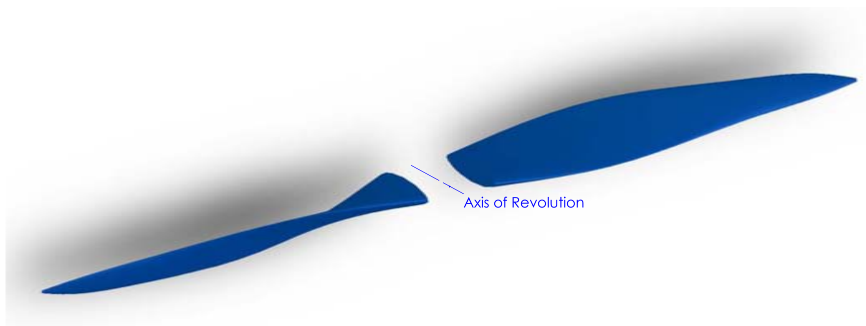

Figure 8.3. 3D CAD model of blades.

operating conditions, we introduce an advance ratio J and a power coefficient C_P as defined in (8.2) and (8.3), where where n is the rotation rate of the prop in rev/s, D is the diameter of the prop in ft, P is power delivered to the prop, ρ is air density, ω the prop angular rotation rate, and R the radius of the prop. A plot of efficiency contour lines and best blade angle contour lines versus these two parameters can be found in Fig. (8.4) and will form the basis for a prop pitch control strategy.

$$J = \frac{V}{nD} \tag{8.2}$$

$$C_P = \frac{P}{\pi \rho \omega^3 R^5} \tag{8.3}$$

8.3 Pitch Controller

8.3.1 Motivation and Constraints

John Langford, co-designer of the MIT Light Eagle human powered airplane, made the statement that the use of "automatic propeller pitch regulation was crucial" to the success of their design[28], a sentiment that we find repeated in other texts. In fact, MIT's Daedalus HPA project experimented with implementation of both a longitudinal and a lateral/directional autopilot to reduce pilot workload[29]. Without a pitch regulator, the propeller is not operating in the most efficient design area, and can waste considerable power, depending on the flight regime. Constraints on this controller were that it had to take two inputs (the freestream velocity and the prop speed), generate one output (blade angle), be lightweight (precluding the use of a traditional computer), and be easily adjusted for multiple users.

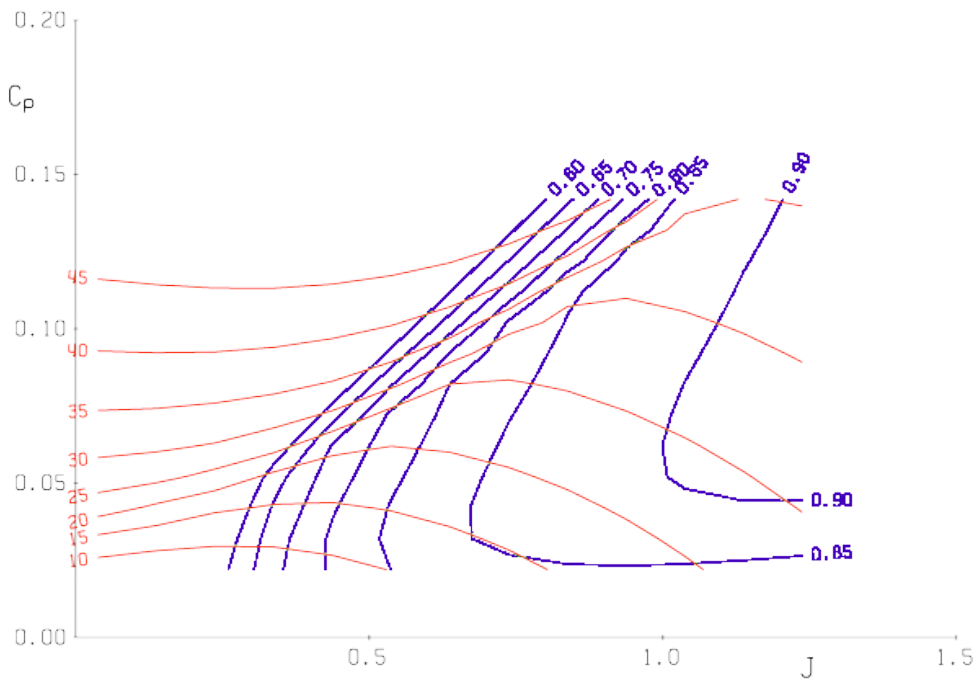

Figure 8.4. Off-design point operating calculations.

8.3.2 Controller Architecture

Accordingly, a two-input, single-output, prop pitch regulation controller was devised as shown in Fig. 8.5. In this controller, measurements are made of the freestream velocity V_M and the prop rotation rate. Measurement noise is assumed high frequency, so these signals are then passed through low pass filters to remove this noise and find the true velocity V and rotation rate.

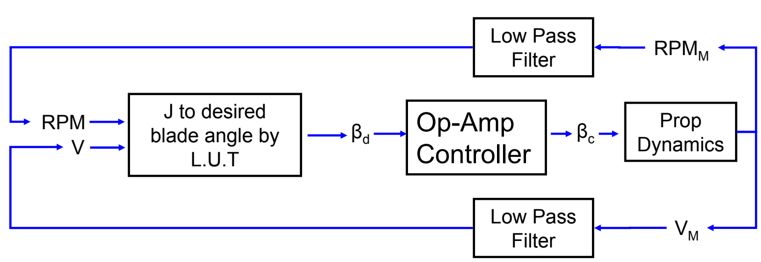

Figure 8.5. Pitch regulation schematic.

The freestream velocity and angular rotation rate can be nondimensionalized via the advance ratio J defined earlier in Eq. (8.2). A look-up-table (LUT) has been generated from efficiency plots such as the one shown in Fig. 8.4. In the pitch controller, this resides on a PIC microcontroller that calculates the advance ratio corresponding to the prop rotation rate and the airspeed, and outputs a desired blade angle β_d, in the form of an analog voltage.

The desired blade angle is then passed to a traditional proportional-integral-derivative (PID) controller. For weight concerns, this has not been implemented on a digital platform, but is made of discrete components including operational amplifiers, resistors (both adjustable and fixed) and capacitors. The circuit used has been adapted from that shown in Fig. 8.6[30] by the addition of variable resistors to allow for customized user settings. The transfer function $H(s)$ for this compensator is shown in Eq. (8.4)[30], where R_i and C_j are specific resistances as identified in Fig. 8.6.

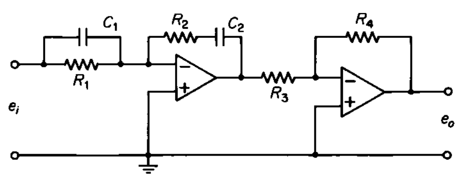

Figure 8.6. Operational amplifier controller.

$$H(s) = \frac{R_4}{R_3}\frac{R_2}{R_1}\frac{R_1C_1s+1}{R_2C_2s+1} \tag{8.4}$$

The output of this stage is the commanded blade angle β_c, which is passed to the servo controlling blade pitch. This servo does add some dynamics to the overall prop dynamics, but the aeroelastic interactions between blade flex and prop angle were outside the scope of this design and probably pretty small. Instead, experimental identification of the PID gains will be used from which the open-loop dynamics for the entire architecture can be found. Tuning of PID gains is a straightforward procedure, for which manuals are available, which is in contrast to aeroelastic research and nonlinear control theory, both of which are topics of current research.

The construction of the controller out of discrete components places it at approximately 30g in weight, not including batteries.

9. R/C Model Development

9.1 Motivation and Purpose

The team had originally planned to construct a full scale prototype of the aircraft; however, too many questions about the design remained and more work than the team thought possible was ahead to finish the prototype by graduation. The team still desired to construct something to prove the design would work and to work out kinks in the design so that a working full scale could built by a future team. The best option seemed to be to build a quarter scale model of the airplane. The model could validate many of the analysis methods used to create full scale design. It could also answer questions on stability and control that were very difficult to analyze. The model was intended to help refine and improve the full scale design.

9.2 Scaling of the Model

9.2.1 Geometric and Dynamic Scaling

In order for the model to be of real engineering value, it had to be scaled properly. The approach described in NASA's "Similitude Requirements and Scaling Relationships as Applied to Model Testing" was used[31]. The report detailed methods of scaling designs for similarity. For the R/C model to fly dynamically similar to the full scale design, it had to be scaled by Froude number shown in Eq. 9.1. First the model had to be geometrically similar essentially meaning that all the dimensions had to be divided by the scaling factor. A table was included in the NASA report that gave the equations for similarity between properties of the model and full scale design based on the Froude scaling method. A quarter-scale model was chosen because it was most feasible to build adhering to the scaling laws. A 1/5 scale model was very stringent on wait and 1/3 scale model seemed too large. Table 9.1 shows the full scale dimensions versus the model dimensions. It may be noted that the wing thickness is not exactly scaled to one-quarter the thickness of the Iron Butterfly. This is because the Froude scaling does not guarantee that the airfoil will exhibit the same behavior. It is the job of the designer to find an airfoil that will perform on the model similarly to the airfoil on the full scale design.

$$Fr = \frac{V^2}{gl} \tag{9.1}$$

The effects of a property not scaled as described was not found in public literature. The equations were manipulated with the help of Bob Parks, an engineer experienced with model scaling. For example, through manipulation of the governing equations the effect of the weight on behavior in cruise can be found. If the model came in at twice the weight it is supposed to, then the speed it flies would have to be increased by approximately 41%. This can be seen in the example below:

$$C_L = \frac{2W}{\rho V^2 S} \tag{9.2}$$

$$V_1 = \sqrt{\frac{2W}{\rho S C_L}} \tag{9.3}$$

$$V_2 = \sqrt{2} V_1 \tag{9.4}$$

In order for the model to exhibit cruise dynamics similar to the full scale, the velocity would have to increase by the square root of 2 for twice the Froude scaled weight. If another parameter were the target, like turning radius, a similar analysis would have to be performed.

Parameter	Full Scale	Model
Wing Span [ft]	60	15
Wing Chord [ft]	1.5	0.375
Wing Thickness [in]	2.25	0.3294
Wing Gap [ft]	5	1.25
Wing Area [ft^2]	2160	11.25
Gap [ft]	5	1.25
Strut Chord [ft]	0.75	0.188
Stab arm [ft]	15.82	3.95
Stab span [ft]	7.64	1.91
Horiz. Area [ft^2]	99.96	0.52
Stab chord [ft]	1.09	0.27
Stab thickness [ft]	0.13	0.52
fin arm [ft]	18.12	4.53
fin span [ft]	11.95	2.99
Vert Area [ft^2]	245.28	1.28
fin chord [ft]	1.71	0.48
fin thickness [ft]	0.21	1.28
Speed [ft/s]	33.00	16.5
Weight [lb]	215	3.36

Table 9.1. Model v. Full Scale Dimensions

9.2.2 Power and Thrust for the Quarter-Scale Model

The scaling report did not mention anything on how to scale the power or thrust. Instead of trying to create a scaling method, the quarter scale power required was calculated. Using conservative drag estimates, the power required to maintain the cruise velocity in a 15 deg bank came out to only 3.8 W. From R/C experience, this value seemed very low. As a safety factor the propulsive efficiency was set to 0.5, a low value for electric R/C propulsion systems. With this power requirement in mind, hobby electric motors were researched. The smallest AXI outrunner motor available (AXI is pretty much the best motor for the power regime) was quoted as producing approximately 18W of power. This provided approximately 10 W of excess power in a 15 deg banked turn at scaled cruise speed.

These results were still looked on with some skepticism. To ease this doubt and to characterize the electric propulsion system, a wind tunnel test was conducted. The propulsion system was run by a Medusa Research test rig and mounted on a load cell feeding thrust data to the Medusa data logger. The data logger also recorded battery voltage and amperage. A series of tests were run from zero throttle to full throttle over a series of wind tunnel speeds covering the full range possible model velocities.

9.3 Model Aerodynamics

The power limitations of the full scale aircraft are not present in the design of the scale model so airfoil selection includes factors other than minimal drag. Therefore the largest consideration in model airfoil selection was performance similitude to the full scale, requiring matching of C_{l_α} between the full scale airfoil and the selected model airfoil. However, before this final agreement was considered, several smaller considerations such as stall margin and ease of construction.

The model will cruise at a velocity of approximately 16.5 ft/s and with a chord of only 4.5 in placing the Reynolds number in the realm of 40,000. This range of Re is considered very low and presents a new set of aerodynamic problems separate from the full scale. However, these problems have already been addressed by many aerodynamicists and studied extensively at the University of Illinois Urbana-Champaign by Dr. Selig, Dr. Gush, and Dr. Tehrani. This study involved the experimental analysis of a large list of low Re airfoils. The results of this study have been published through SoarTech Aero Publications with the complete list of the airfoils studied and associated Re published online[32]. By reviewing this list, several candidates were selected that were applicable to the Re range of the model.

With a list of candidates, several selection criteria were established: C_{lmax}, stall margin (change in AOA to stall), thickness, and ease of building. The model must fly at equal values of C_L so that the flight dynamics of the full scale aircraft are scaled. An analysis of each airfoil was performed using X-Foil to obtain lift and drag polars. From these polars and the C_{lmax} requirement, several candidates were eliminated. Because a model must be flown off visual indicators only, it becomes much harder to fly close to stall and so a larger difference between cruise AOA and stall AOA is required. This reduced the possible candidates to the Verbitski BE-50, the Morris GM15, and the Eppler 387. Looking at Table 9.2, it can be seen that the E387 has a small stall margin, but a large C_{lmax} keeping it a possible candidate. However, further X-Foil analysis revealed that at cruise conditions the separation bubble is unstable and rapid boundary layer changes result in sudden increases in drag and possible flow separation. This would have large consequences on the flight dynamics of the model eliminating the E387. This left the BE-50 and GM-15 for further consideration.

The model wings will be constructed from ribs and spars with a stress skin covering. This construction technique requires that the airfoil be thick enough to allow an adequate main spar and a trailing edge that can be accurately built without warping. Warping of the TE or the wing itself will have a detrimental effect on performance and reduce the correlation between model dynamics and full scale dynamics. The full scale aircraft will implement ailerons and thus so will the model. Ailerons require an airfoil that will allow room for hinging and control linkages. The Morris GM-15 has both the highest stall margin and highest C_{lmax}, but a thin TE. The fineness of the GM-15 TE does not allow room for the mechanics needed for the ailerons and will also present problems in constructing a warp free TE eliminating the GM-15.

Table 9.2. Comparisons of model airfoil candidates.

Candidate Designation	Clmax	AOA at Clmax	AOA at $C_l = 0.92$	Stall Margin [deg]	t/c	Camber	LE Radius	TE angle
A18 Archer	1.23	8.5	5.5	3	0.728	0.0384	0.0061	9.9
BE 50 Verbitski	1.32	10.5	4.5	6	0.0732	0.0395	0.006	5.85
E387 Eppler	1.27	10.5	8	2.5	0.09077	0.0378	0.0084	3.5
GM15 Morris	1.33	9.5	5.2	4.3	0.0674	0.0476	0.0046	20.9
MA409 Achterburg	1.15	8.5	5.5	3	0.0669	0.0333	0.0043	9.43
MB253515 Bame	NA	NA	NA	NA	0.1496	0.0241	0.0078	18.2
NACA 64A010 Champine	NA	NA	NA	NA	0.1	0	0.0068	12.58
SD8020 Selig-Donovan	NA	NA	NA	NA	0.101	0	0.006	7.8

With all the other candidates now eliminated it is necessary to asses the agreement between C_{l_α} of the full scale DAE series and the BE-50. X-Foil was again utilized to produce lift polars for the BE-50. By plotting the lift polar of the DAE 11 and the BE-50, Fig. 9.1, it can be seen that at the design cruise C_l there is good agreement in C_{l_α} that is required for similar flight characteristics.

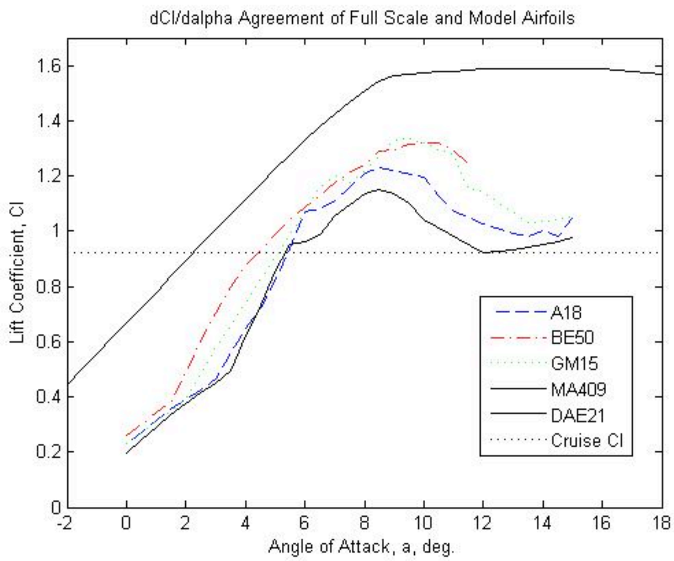

Figure 9.1. Comparison of lift curve slopes for model candidate airfoils to the DAE-11.

The BE-50 has several advantages over the other candidates both in terms of construction and aerodynamically. The airfoil is sufficiently thick for structure and ailerons. Additionally, the top of the airfoil has a large flat section that will allow the wing to be constructed inverted so each rib can be accurately aligned. Aerodynamically, the BE-50 has the lowest drag of the candidates and operates at its minimum drag during cruise in addition to comparable C_{l_α} with the full scale airfoil. This translates to reduced pilot effort to maintain constant cruise speed and reduces sensitivity to small throttle changes. For these reasons, the Verbitski BE-50 was chosen as the airfoil for the model.

9.3.1 Wing Development

With a final airfoil selected for use, the next step in the development of the wing design was defining the twist distribution to provide the most efficient lift distribution. I-Drag was used to compose an initial analytical model of the aircraft configuration, including flight conditions and develop a preliminary twist distribution. I-Drag was used to calculate the minimum induced drag and associated lift distribution for a simplified configuration. Though I-Drag was incapable of providing a final optimum lift distribution, it was useful in the endplate design to be discussed later.

The initial estimate for lift distribution from I-Drag was used to create a more complete AVL model with nine locations per half span, per wing, where the local twist is defined. The initial model was created by analyzing the I-Drag predicted distribution for inflection points and regions of linearity in $\frac{dC_l}{d_y}$. At this stage in wing development the end plates are aligned with the free stream and have zero twist. The AVL model was then run, under straight and level flight conditions, to calculate the lift distribution and associated downwash distribution. An iterative approach was then taken of adjusting the twist at the defined stations to load or unload the local section of the wing until a constant downwash was obtained. The twist was adjusted until the calculated wing efficiency was only showing a 0.5% change and then the model wing twist distribution was considered complete. The twist distributation is tabulated in Table 9.3

Table 9.3. Tabulated Model Twist Distribution

Span Location, [ft]	0	0.5	1	3	4	5	5.9	6.6	7.2
Top [deg]	-1	-0.7	0.2	1.4	0.5	0.2	-0.7	-2	-3.5
Bottom [deg]	2	2	2	1.7	0.5	0.5	-.7	-2	-3.5

Like the wing airfoil, the endplates operate at very low *Re* and so the low *Re* airfoil list generated for the main wing from the UIUC LSAT's was reviewed. Due to the low $C_{l_{req}}$ and the symmetric positive to negative loading, only symmetrical airfoils were considered. This left the NACA 64A10 and the SD8020 as the only candidates. The SD8020 was then chosen as the final candidate due to having lower drag. With the airfoil chosen and the desired loading known, the twist distribution was created by defining 5 stations over the endplate. The twist at each station was easily calculated with the use of an X-Foil calculated lift polar, Table 9.4. The twist was then added to the previous AVL model to complete the model wing design. Fig. 9.2

Table 9.4. Tabulated Model Endplate Twist Distribution

Vertical Location, [ft]	-1	-0.32	0	0.32	1
Twist, [deg]	3	2.4	0	-2.4	-3

9.3.2 Tail Design

The design of the model horizontal and vertical tail required a symmetrical airfoil capable of operating at very low Reynolds number. Once again the realm of small R/C gliders was explored to find a suitable airfoil. After reviewing several candidates the HT08 was selected. This airfoil was created by Mark Drela specifically for the purpose of full flying tail surfaces for low Re applications. This airfoil was designed to eliminate the 'dead band' common to full flying surfaces. This dead band is an area of unresponsiveness when deflection angles are low and can be problematic, particularly at low flight speeds. In addition the HT08 exhibits excellent drag qualities in that it has a low

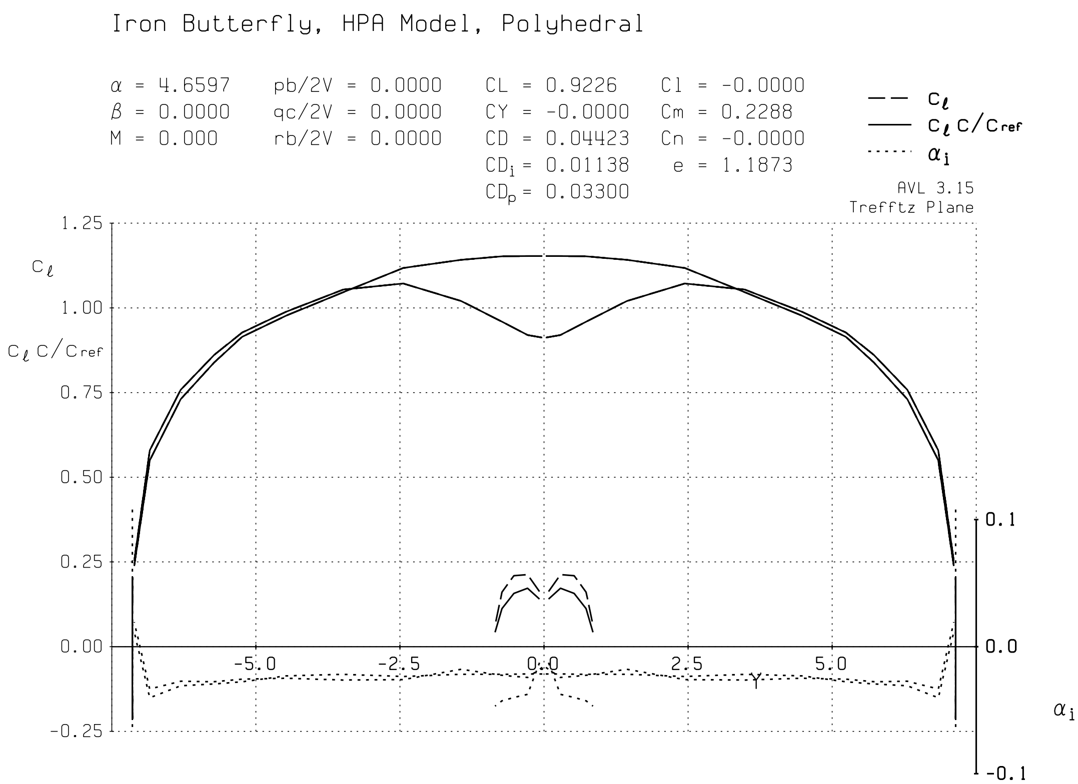

Figure 9.2. AVL Trefftz Plane Plot of 1/4 Model

profile drag, due to a t/c of 5%, low induced drag with a large bucket at the Re regime it will be operating.

With the airfoil chosen the next step was to size the tails. Here there were three main constraints that needed addressed. First was a span limit on the vertical tail to allow 8 deg. of rotation on take off. This limited the span to 37.6 in but was reduced to 36 in to allow construction with off the shelf material lengths. The next constraint was the aerodynamic constraint of limiting the tip Re to 25,000. This keeps the airfoil operating within its design specifications and minimizes unwanted aerodynamic effects from extremely low Re flow. Additionally there was a structural constraint requiring a minimum tip thickness of 0.125 inch. This is both to satisfy strength issues and thicknesses less than 0.125 inch becomes very difficult to accurately construct. With these constraints the following table was generated, Figure 9.5.

	AR	Root Chord	Tip Chord	Tip Re	Tip Thick.	Span
Horizontal	6	4.5	2.5	23,500	0.125	20.8
	6	**4.0**	**3.0**	**28,300**	**0.150**	**20.8**
	6	3.5	3.5	33,000	0.175	20.8
	7	4.0	2.5	23,500	0.125	22.4
	7	3.5	3.0	28,300	0.150	22.4
Vertical	6	8.5	3.5	33,000	0.175	36.0
	6	8.0	4.0	37,676	0.200	36.0
	6	**7.5**	**4.5**	**42,400**	**0.225**	**36.0**
	6	7.0	5.0	47,100	0.250	36.0

Table 9.5. Selection Analysis of Model Tail Size

Because only two geometric configuration of the horizontal tail can be eliminated with the defined constraints it became important to address considerations as well as constraints. The largest consideration is that the lift distribution of the tail is controlled by LE taper and not twist. It was for this reason that the horizontal tail was chosen to have a root chord of 4.0 in, tip chord of 3.0 in and a span of 20.8 in. The rudder was chosen to have a root chord of 7.5 in and tip chord of 4.5 in. With the model tail sizes finalized, the aerodynamic design of the model is complete and performance analysis can begin.

9.3.3 Performance Expectations

The performance of the model is dependant on two main things, the efficiency of the wing and cleanliness of the construction, i.e. minimal protrusions into the free stream. The efficiency of the wing can be accurately estimated with the use of AVL but the parasitic drag due to various protrusions is much harder to quantify without detailed wind tunnel tests and requires the performance of the final model to be defined in terms of an envelope as opposed to a single design point.

The induced drag of the wing, with non-lifting endplates, is reported by AVL to be C_{di} =

0.01165. The addition of the twisted endplates increases C_{di} to a value of 0.01138 to yield a 2.4% decrease in induced drag. This is a small change and a poorly constructed joint between the wing and the endplate could easily negate the decrease in induced drag so great care was required in building a clean junction. However, if flight test time allows for the testing of the model with the endplates removed, i.e. biplane configuration, the reported C_{di} is 0.01181. This means that the twisted endplate configuration should have 3.8% decrease in drag over the biplane and should be a large enough difference to be measurable with glide tests.

At this point only induced drag has been discussed but parasitic drag plays a very large role in the ultimate performance of the airplane. Assuming all hinging and control surface actuation is done internally so that the airplane is completely smooth, assuming all flow is laminar, and including interference effects at junctions, a base drag coefficient, C_{d_0} of 0.0213 is obtained. However, these assumptions are not completely valid in that the airplane will not be completely free of obtrusions to the free stream and there will be regions of flow that are completely turbulent. Using Friction-F to obtain C_f values for partially turbulent flow and using the Hoerner form factors a higher, and more expected, value of $C_{d_0} = 0.0327$ is obtained. Taking the added drag of control rods, horns, etc. into consideration, C_{d_0} is estimated at 0.376, allowing for a 15% increase in parasitic drag. This is significantly higher than the completely clean and laminar case but is felt to be much more plausible and is used to avoid over estimations or potential problems due to having too little power.

Unfortunately there is little that can be done to back-calculate induced and parasitic drag separately from total drag when performing the simple flight testing that is scheduled. One of the simplest ways to determine drag characteristics of an airplane is a simple power off glide test. The glide angle is directly related to the L/D through $\cot(\theta) = L/D$. Because the glide angle is easy to measure, L/D is the major performance parameter being tested. The completely clean, laminar, twisted endplate design has a L/D of 28. This represents the upper limit of the performance. Accounting for turbulence and free stream disruptions, yields an L/D of 19, representing the lower limit. This is clearly a large range, however, if the effectiveness of the twisted endplate is ignored and the C_{di} of the plain boxplane is used and still allowing for a 10% increase in the turbulent C_{d_0} from protrusions gives an L/D of 19.5. This will be the projected.

9.4 Structures

An ANSYS finite element model with material properties from the basswood model testing was used to size the spars for the remote control model combined with those from MATWEB. An average value of 1450 ksi for the modulus of elasticity and 0.3 for Poisson's ratio were used. The need for maximum bending rigidity led to a spar design with caps instead of a constant rectangular cross-section located at the point of maximum thickness in the wing, shown in Fig. 9.3. Cap thickness was limited by rib considerations. A certain percentage of material is necessary to connect the leading edge of the rib to the trailing edge together. Only finite thicknesses of hardwood and balsa are produced by manufacturers. A standard thickness of 3/32 in provided adequate rib connection material and still provide significant material as far away from the neutral axis as possible for bending rigidity. Thus, only the spar cap width needed to be varied to attain the necessary bending rigidity. Only standard size widths, 1/32 in increments, were considered because of material availability. Struts were built out of wrapped carbon tubes available from www.graphitestore.com[33]. Due to time constraints, model gap was matched to provide the same gap to span ratio as Chrysallis[21]. This set the gap to 25 in.

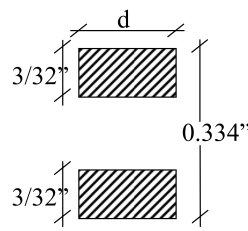

Figure 9.3. Spar cap sizing for remote control model structure.

Displacement-based analysis was used to size all spar caps for the model. For the wing, the distributed elliptic load specificed from aerodynamics was used at cruise conditions. Reasonable tip deflection was picked to be 5% of semi-span, requiring a 3 deg break built in at each panel to achieve the desired model polyhedral at cruise. This tip deflection was specified because it was known to be stiffer than necessary but able to produce a light enough wing. It was desired to reduce the aeroelastic tendancies of the model through stiffer components than what actually would be exhibited on the final aircraft. Aeroelastic testing was left as an exercise for another model. Final model spars were tapered from root to tip in finite sections. Each panel had constant cross-section spars for ease of construction and material availability. However, this "step" taper still provided a much lighter structure than constant cross section along the entire span. Each panel spar width, d, was varied along with strut wall thicknesses to get even deflections at each panel break so that final wing deflection at cruise matched the designed cruise state, mentioned in Section 5.7. Additional considerations were given to overal structural weight, sizing, and wing stiffness. Each panels cross-sectional spar dimensions are specified in the detailed drawings in the appendix.

A simpler sizing method was used for tail surface spars as they could easily be modeled as cantilevered beams. For a significant safety factor, the full lift at stall was applied as a tip load. Cross-sections were sized to keep tip deflections under 10%. The rudder used the same spar cap design as the wing, however the elevator used a rectangular cross-section since it was significantly thinner. Details for these spar cross-sections are also shown in the model detailed drawing in the appendix.

Figure 9.4. Cross-sectional layout of rudder rib, wing similar.

Figure 9.4 shows a cross section of the built-up method used for wing and rudder construction. Due to the elevator's size, the similar built-up method was not feasible. It was sanded out of balsa wood with a hardwood spar inset. Most secondary components were sized based on their general fit and available sizes. Often one thickness was too large, the next smaller size just right, and the next smallest way too small. For example, for wing ribs with a 4.5 in chord, 3/32 in was excessively large and heavy, 1/16 in provided adequate gluing surface and stiffness, and 1/32 in way too brittle and flimsy. Rib spacing was chosen to be 1.5 in, 3/8 of the chord, a good ballpark while still providing adequate aerodynamic shape. A more detailed cross-sectional layout is shown in the detailed model drawing in the appendix. Upon construction, it was found that this method for tail sizing significantly over-designed them. Tail sections could have been made lighter. However, their robust nature will make them more resilient during model testing although their weight aft will make balancing more difficult.

A detailed mass budget can be seen in Table 9.6. Component locations were taken using a datum 4 in in front of the nose, lined up with the tailboom shown in Fig. 9.5. All components were assumed to be point masses at their respective locations and center of gravity was calculated using simple moment balances. Current horizontal center of gravity is located at the desired $0.40\bar{c}$ and vertical center of gravity is right at the center of the two wings.

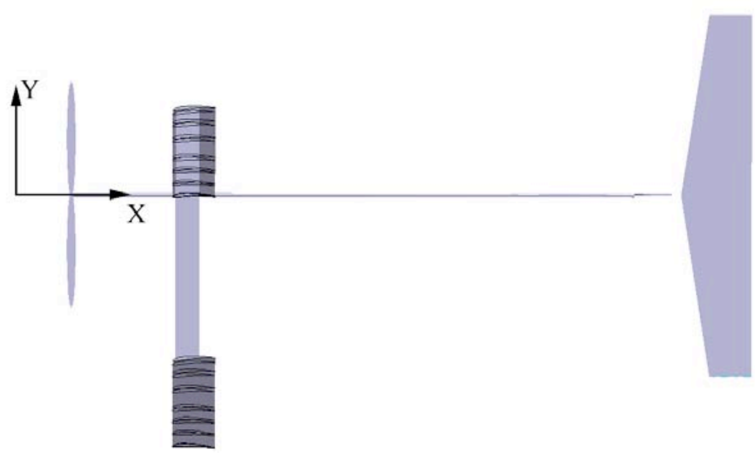

Figure 9.5. Coordinate system used for mass budget and CG calculations.

Table 9.6. Model Weight Breakdown

Component	Weight [oz]	X-Moment Arm [in]	Y-Moment Arm [in]
Wings w/o struts	23.94	22.6	-15.0
Struts - GraphiteStore AE001815	3.52	22.6	-12.5
Rear Angled Strut	0.41	31.7	-12.5
Tailboom - CST T585-40STD	2.22	31.0	0.0
Vertical Tail	2.50	77.2	0.0
Horizontal Tail	1.27	71.2	-2.4
Fuselage	4.00	17.5	-12.0
Landing Gear	1.50	22.6	-25.0
Motor - AXI 2204/54	0.86	4.0	0.0
Prop	0.26	4.0	0.0
Speed Control - CC Phoenix 25	0.59	8.0	-1.0
Batteries - Thunder Power TP1320-2S	2.05	12.0	-2.0
Receiver	0.94	13.0	-24.0
Aileron Servos - HS 55 x 2	0.54	22.6	-20.0
Rudder Servo - HS 81	0.52	16.6	-23.0
Elevator Servo - HS 81	0.52	16.6	-23.0
Nose Ballast	4.06	5.0	0.0
Fuselage Ballast	4.06	10.1	-25.0

9.5 Dynamic/Control Similarity

The 1/4 scale model was designed to preform dynamically similar to the full scale aircraft to test the non-standard control scheme. The static margin, elevator to trim in stall, control deflections, and time to bank are summarized in Table 9.7. The table indicates that there is little difference in the longitudinal characteristic as well as the control parameters. The model should behave similarly in longitudinal control, coordination of a turn, and banking.

	Iron Butterfly	Scaled Model
Static Margin	0.17	0.14
Trim in Stall δ_e [deg]	4.8	6.0
Turning δ_a [deg]	11.1	10.8
Turning δ_r [deg]	7.5	7.9
Turning β [deg]	3.3	8.3
Time to bank [sec]	1.6	1.1

Table 9.7. Comparison of stability and control of design and scaled model.

Tables 9.8 and 9.9 depicts a comparison between the longitudinal and lateral-directional dynamic modes of the model with those of the full scale aircraft. The tables indicate that the dynamic modes of the model are quite similar to the aircraft itself. The longitudinal modes share the form and are comparable in time to half amplitude, frequency, and damping. Further, the lateral-directional dutch roll and spiral modes are fairly similar as well. The roll mode is significantly different. The time to half-amplitude occurs at about 1/10 of the time it would for the aircraft itself. Overall the scaling was successful, making the model dynamically similar to the Iron Butterfly.

Aircraft	Eigenvalue	Time to half [sec]	ζ	ω
Iron Butterfly	-34.7	0.02	-	-
	-5.3	0.13	-	-
	-0.072 + 0.74i	9.70	0.17	1.05
	-0.072 -7.4i	-	-	-
Scale Model	-10.1	0.07	-	-
	-4.0	0.17	-	-
	-0.17 + 1.0i	4.0	0.096	0.75
	-0.17 - 1.0i	-	-	-

Table 9.8. Eigenvalues and time to half amplitude for longitudinal dynamics

Aircraft	Mode	Eigenvalue	Time to half [sec]	ζ	ω
Iron Butterfly	Dutch Roll	-4.92+3.51i	0.14	6.04	0.81
	-	-4.92-3.51i	-	-	-
	Roll	-2.03	0.34	-	-
	Spiral	-0.06	11.6	-	-
Scale Model	Dutch Roll	-4.65+2.39i	0.15	5.23	0.89
	-	-4.65-2.39i	-	-	-
	Roll	-26.4	0.03	-	-
	Spiral	-0.089	7.84	-	-

Table 9.9. Eigenvalues and time to half amplitude for lateral-directional dynamics

9.6 Flight Testing Results

Just after sunrise on April 30, 2006, the Iron Butterfly quarter scaled model made eight flight attempts. In the first couple flights, the rudder was determined ineffective due to excessive flexibility in The tailboom in conjuction with the pull-pull control system. As a quick fix, guide wires attached the aft end of the tail boom to the inner wing struts, and the rudder was locked in a slight negative(left) deflection as an eyeball estimate to counter propeller torque. The plane was found to be very directionally stable. In most of the flights after the rudder was locked, the plane was observed to turn left regardless of the aileron input given by the pilot. This was attributed to two possible causes: the locked left rudder was overpowering the aileron input and the wing had become twisted during one of the landings. Furthermore, aeroelastic twisting of the flexible wing in flight indicated that any effectiveness of the ailerons would probably result in excitation of the twisting aeroelastic mode and not impose a rolling moment for the aircraft. Over the eight flight tests, the pilot indicated that the elevator was very powerful and he needed very little input to obtain substantial response. The elevator was designed to require only 8 deg deflection to trim in stall, and therefore it is not unexpected to obtain good elevator authority. However, some of the effect may be due to the fact that the model was balanced slightly above the center of the wings which could cause it to be unstable at large positive angles of attack. For details see the discussion in Section 6.2 and Fig. 6.4. The pilot also noted that there was a very small pitch up margin to stall which was expected.

10. Conclusions

Currently the team stands with a nearly completed full scale design and a quarter scale model that could provide some very valuable flight test data with slight modifications. With stiffening the tail boom and rudder control linkage, the quarter scale model could be ready to provide some good drag and L/D data and will be able to validate the lateral and directional control. Next year's Virginia Tech Human Powered Aircraft Team can complete the model testing and then refine and change the current full scale design to construct a slower and lower powered full scale prototype. With this practice prototype, the team will be able to conduct flight testing to validate the design methodologies used and refine the full scale design. It will also offer a training platform for the competition pilot. A third team will then be charged with building a competition aircraft and winning the Kremer Sport Prize.

A1 Acknowledgement

The Human Powered Aircraft Group at Virginia Tech would like to thank the support of the Aerospace and Ocean Engineering Department faculty for support of the project. We extend special thanks to: the SGA for funding the development of our quarter-scale prototype; Dr. William Mason for significant guidance; Bob Parks, John Langford, Juan Cruz volunteering their extensive HPA knowledge; and students within the Architecture Department.

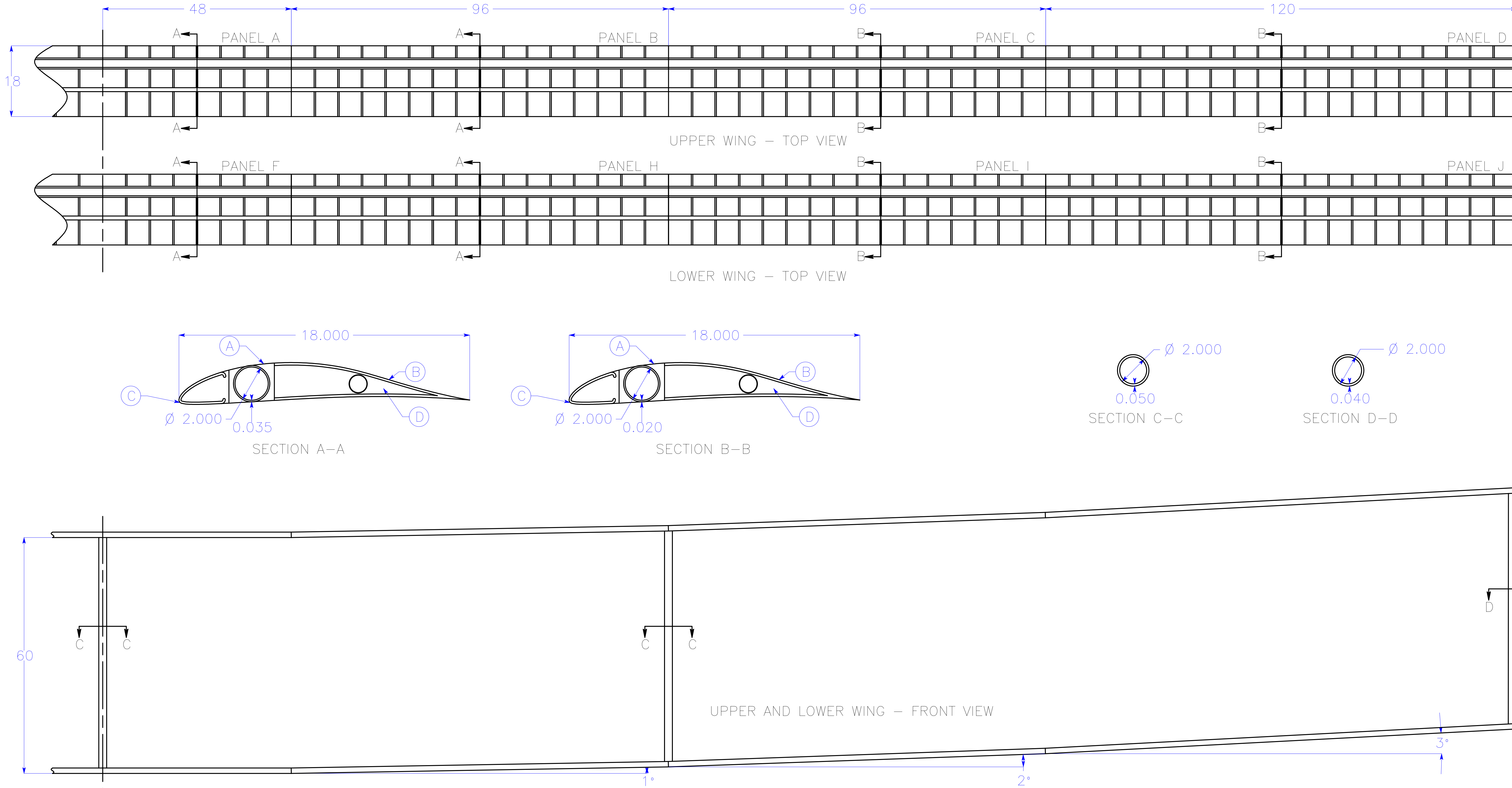

NOTES:
1) ALL SECTION VIEWS 1:6 SCALE
2) ALL OTHER VIEWS 1:24 SCALE
3) WINGS FLATTENED IN TOP VIEW
4) UPPER WING HAS SAME POLYHEDRAL AS LOWER WING
5) CARBON STRUTS FAIRED WITH HOTWIRE FOAM SECTIONS
6) PLANE SPAR AT POINT OF MAX THICKNESS

BALLOONS:
A) 1/64'' PLY
B) 1/8'' BALSA CAP STRIPS
C) HOTWIRED BEADED FOAM LEADING EDGE
D) FOAM RIBS

IRON BUTTERFLY FULL SCALE AIRCRAFT	
	DRAWN BY: BLAKE JEANS
	CHKD BY: LEE SKIDMORE
	CHKD BY: JASON ROADMAN
PG 1/2	APPRVD BY: CHRIS EMORY

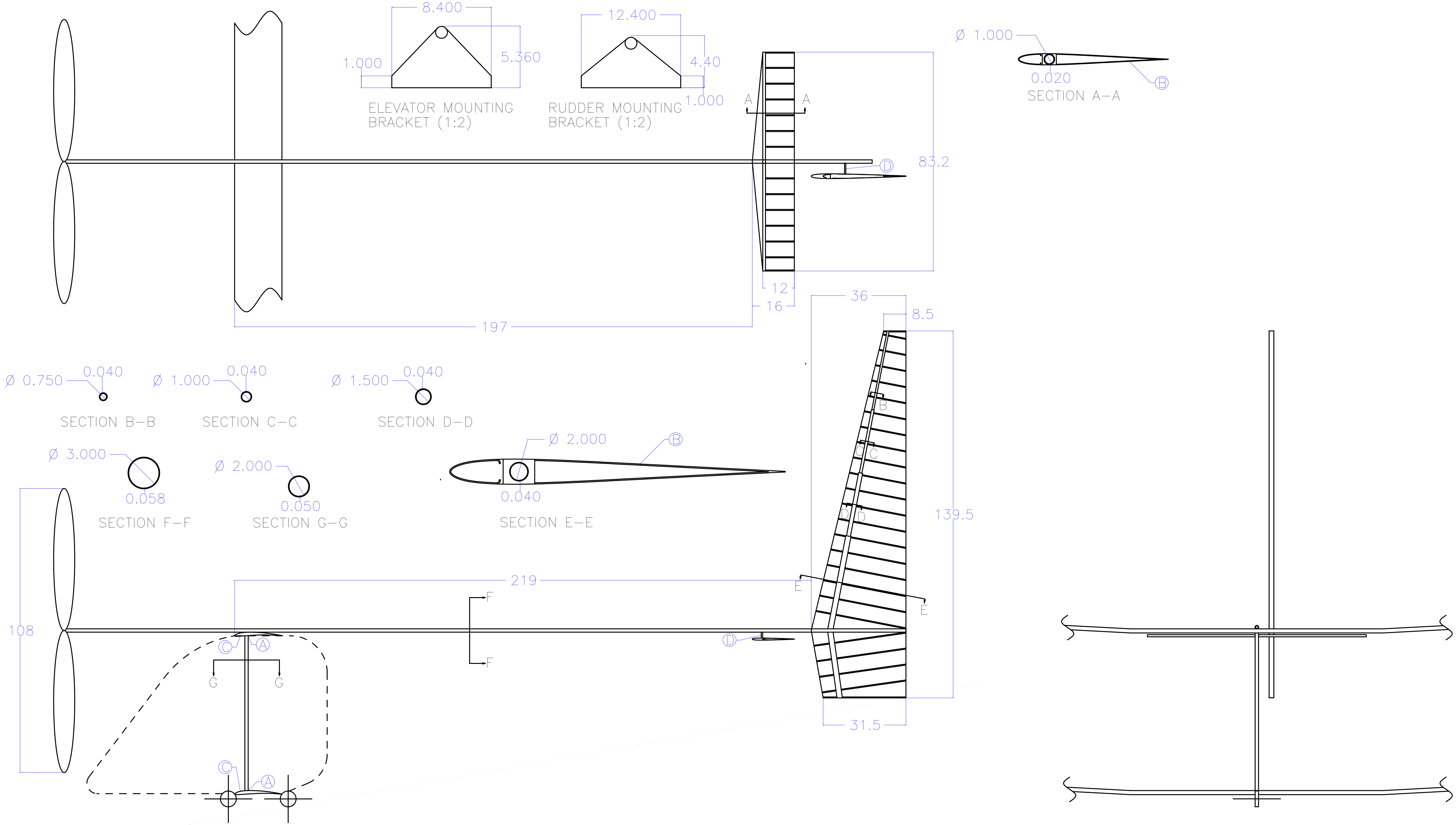

NOTES:
1) ALL SECTION VIEWS 1:9
2) TAIL SCRAPE ANGLE = 10 DEG

BALLOONS:
A) KEVLAR LASHING
B) HT14 AIRFOIL
C) 5 DEG INCIDENCE
D) SURFACES HINGED AT 23% CHORD

	IRON BUTTERFLY FULL SCALE AIRCRAFT	
SCALE: 1:36	PG 2/2	DRAWN BY: BLAKE JEANS

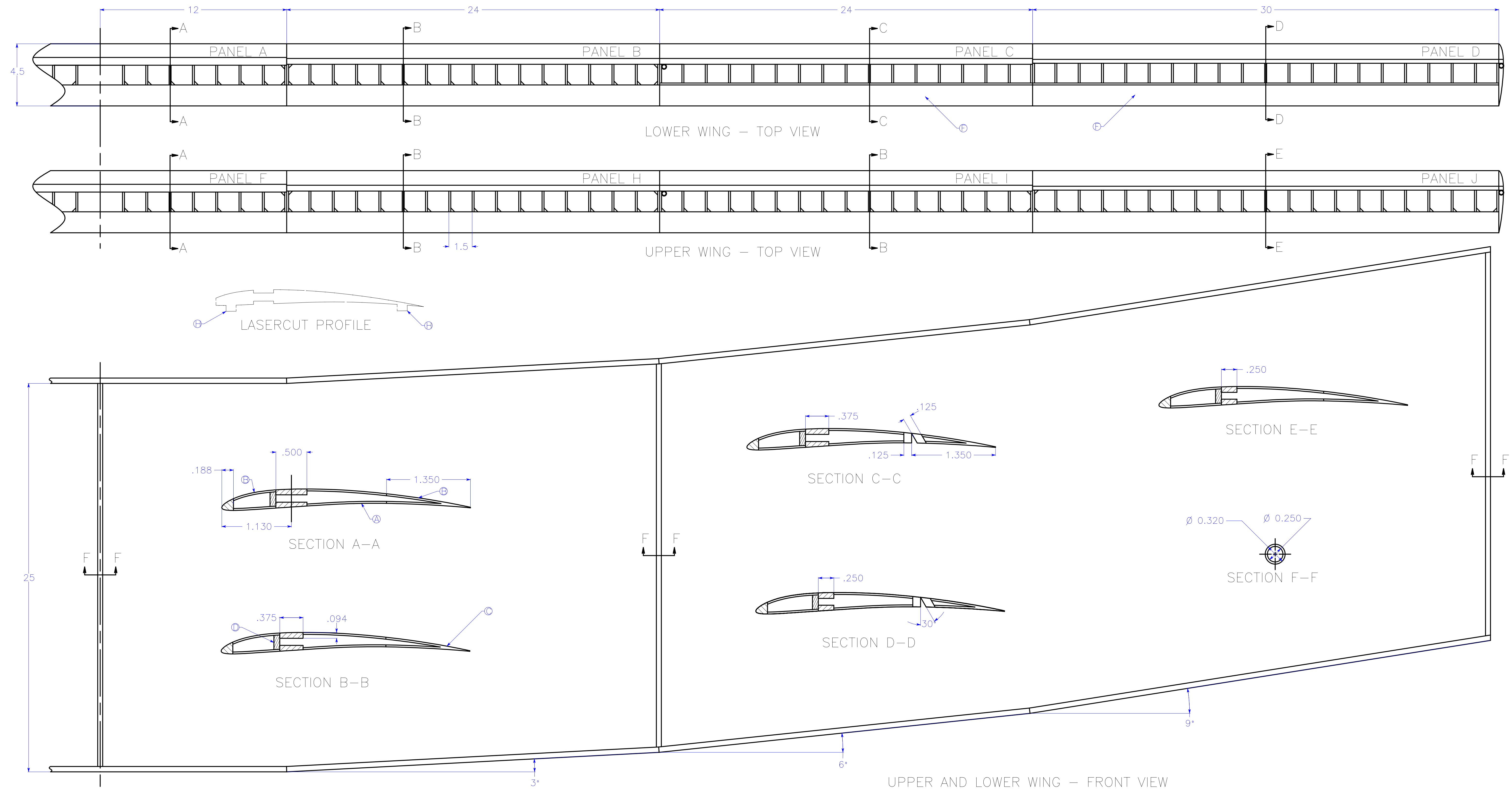

NOTES:
1) ALL SECTION VIEWS 1:1.5 SCALE
2) ALL OTHER VIEW 1:6 SCALE
3) WINGS FLATTENED IN TOP VIEW
4) UPPER WING HAS SAME POLYHEDRAL AS LOWER WING
5) CARBON STRUTS FAIRED WITH HOTWIRE FOAM SECTIONS

BALLOONS:
A) 1/32'' CAP STRIP (1/8'' WIDE)
B) 1/32'' SHEETING
C) MODIFIED BE50 AIRFOIL
D) 3/32'' VERTICAL GRAIN SHEAR WEB
E) ROLL-WRAPPED CARBON TUBE
F) AILERON
G) KEVLAR LASHING
H) ALIGNMENT TAB

IRON BUTTERFLY 1/4 SCALE RC MODEL	
	DRAWN BY: BLAKE JEANS
	CHKD BY: LEE SKIDMORE
	CHKD BY: JASON ROADMAN
PG 1/2	APPRVD BY: CHRIS EMORY

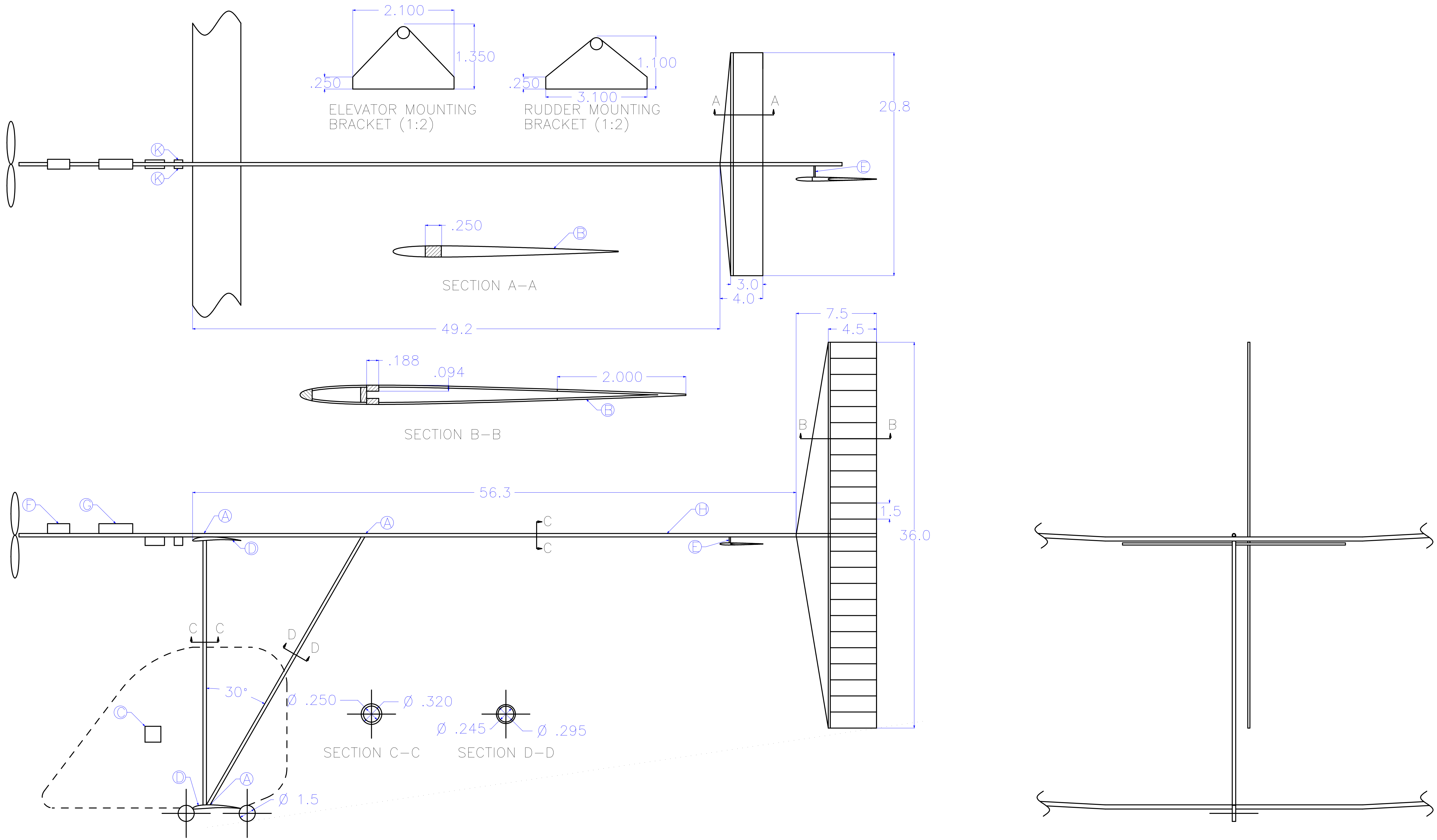

NOTES:
1) ALL SECTION VIEWS 1:1.5
2) TAIL SCRAPE ANGLE = 8 degrees

BALLOONS:
A) KEVLAR LASHING
B) HT08 AIRFOIL
C) ADJUST BALLAST FOR 3.36LB GTOW & CG
D) 5 DEG INCIDENCE
E) SURFACES HINGED AT 23% CHORD

PARTS LIST:
F) CASTLE CREATIONS PHOENIX 25 ESC
G) THUNDER POWER TP1320-25 LI-PO BATTERY
H) GST-T585-40STD TAPERED CARBON TUBE
J) AXI 2204/54 MOTOR
K) HS-81 SERVO

	IRON BUTTERFLY 1/4 SCALE RC MODEL	
SCALE: 1:9	PG 2/2	DRAWN BY: BLAKE JEANS

References

[1] J. McIntyre. The Royal Aeronautical Society, Human Powered Flight Group. Avail at http://ourworld.compuserve.com/homepages/j_d_mcintyre/hpag.HTM.

[2] J.S. Langford. "A Human Powered Speed Aircraft Using Electrical Energy Storage". Master's thesis, Massachusetts Institute of Technology, 1984.

[3] J.D. Burke. "The Gossamer Condor and Albatross: A Case Study in Aircraft Design". *American Institute of Aeronautics and Astronautics Professional Study Series*, (AV-R-80/540), 1989.

[4] Hoerner S.F. *Fluid-Dynamic Drag; Practical Information on Aerodynamic Drag and Hydrodynamic Resistance*. Midland Park, 1965.

[5] M.M. Munk. "General Biplane Theory". NACA Report 151, National Advisory Committee for Aeronautics.

[6] J.A. Schetz. *Boundary Layer Analysis*. Prentice Hall, Upper Saddle River, NJ, 1993.

[7] M. Drela. "Aerodynamics of Human-Powered Flight". *Annual Review of Fluid Mechanics*, (22):93–110, 1990.

[8] "Nihon University Aero Student Group: Airfoil Database". Avail at http://www.nasg.com/afdb/show-airfoil-e.phtml?id=1180, 2005.

[9] Drela, M. "XFOIL Subsonic Airfoil Development System". Avail at http://raphael.mit.edu/xfoil/, 2000.

[10] Mason W. "Form Factor Comparison" Generated by request. Virginia Polytechnic Institute and State University.

[11] J. Grasmeyer. "I-Drag". Three FORTRAN programs avail at: http://www.aoe.vt.edu/ mason/Mason_f/MRsoft.html#idrag.

[12] Drela, M. "AVL Extended Vortex-Lattice Model". Avail at http://web.mit.edu/drela/Public/web/avl/, 2004.

[13] J.S. Langford. "The Daedalus Project: A Summary of Lessons Learned". *American Institute of Aeronautics and Astronautics, Inc.* Aurora Flight Sciences Corp.

[14] M.J. Patil. "AOE 3024 Thin-Walled Structures". Structual Ref., Virginia Polytechnic Institute and State University.

[15] M. Brungard. Effective Dihedral Calculator Tool. mabrungard@hotmail.com, avail at: http://www.charlesriverrc.org/articles/design/eda1.xls.

[16] P.F. Beer, E.R. Johnston, and J.T. DeWolf. *Mechanics of Materials*. McGraw Hill, New York, 3rd edition, 2001.

[17] Argyle industries, inc. source for aluminum extrusions avail. at http://www.argylein.com/, 2005.

[18] Aluminumwerk, unne-usa, inc. source for aluminum avail. at http://www.aluminiumwerk.com/, 2005.

[19] Tennessee metal services. source for aluminum avail. at http://www.eaglealloys.com/, 2005.

[20] D. P. Raymer. *Aircraft Design: A Conceptual Approach*. American Institute of Aeronautics and Astronautics, Inc., New York, 3rd edition, 1999.

[21] J.D. McIntyre. HPAG Information CD,. Royal Aeronautical Society.

[22] F.R. Whitt and D.G. Wilson. *Bicycling Science*. MIT Press, Cambridge, 1982.

[23] D. Ball, R.A. Ferguson, and A.J. Sargeant. "Effect of Muscle Temperature on Rate of Oxygen Uptake During Exercise in Humans at different Contraction Frequencies". *The Journal of Experimental Biology*, 205:981–987, 2002.

[24] H. Glauert. *Airplane Propellers*. Springer Verlag, Gloucester, MA, 1935.

[25] E. Eugene Larrabee. Practical Design of Minimum Induced Loss Propellers. *Society of Automotive Engineers Technical Paper Series*, April 1979.

[26] C.N. Adkins and R.H. Liebeck. Design of Optimum Propellers. *American Institute of Aeronautics and Astronautics 21st Aerospace Sciences Meeting,*.

[27] M Drela. X-Rotor Propeller Design Program. Massachusetts Institute of Technology.

[28] J. Langford. Interview on Sept 11. Aurora Flight Sciences, 2005.

[29] S.L. Sullivan R.B.and Finberg. The Flight Control System for the Daedalus Human Powered Aircraft. *American Institute of Aeronautics and Astronautics*, (89-3593), 1989.

[30] K. Ogata. *Modern Control Engineering*. Prentice Hall, Upper Saddle River, NJ, 4th edition, 2002.

[31] C. H. Wolowicz. "Similitude Requirements and Scaling Relationships as Applied to Model Testing". (1435), 1979.

[32] M. Selig, P. Gush, and K. Tehrani. "UIUC Low Speed Airfoil Tests". University of Illinois at Urbana-Champaign, http://www.ae.uiuc.edu/m-selig/uiuc_lsat.html, 2005.

[33] GraphiteStore.com. http://www.graphitestore.com.

[34] J.R. Cruz. "Weight Analysis of the Daedalus Human Powered Aircraft". Massachusetts Institute of Technology.

[35] J.R. Cruz and M. Drela. "Structural Design Conditions for Human Powered Aircraft". Massachusetts Institute of Technology.

[36] M. Drela. "Method for Simultaneous Wing Aerodynamic and Structural Load Prediction". *Journal of Aircraft*, 27(8):692–699, 1990.

[37] M. Drela. "Method for Simultaneous Wing Aerodynamic and Structural Load Prediction". *American Institute of Aeronautics and Astronautics, Inc.*, (89-2166), 1989.

[38] M. Drela. "Low Reynolds Number Airfoil Design for the MIT Deadalus Prototype". Massachusetts Institute of Technology.

[39] B. Etkin and Reid L.D. *Dynamics of Flight: Stability and Control*. John Wiley & Sons, Inc., Danvers, 3rd edition, 1996.

[40] E. B. Kasari. Flight Mechanics. In *Overview: Aircraft Design and Development*, 1973. Presented to Department of Navy Naval Air Systems Command by Virginia Polytechnic Institute and State University.

[41] I. Kroo. "Nonplaner Wing Concepts for Increased Aircraft Efficiency". Standford University, 2005.

[42] C. B. Millikan. "An Extended Theory of Thin Airfoils and it's Application to the Biplane Problem". NACA Report 362, California Institute of Technology.

[43] B.N. Pamadi. *Performance, Stability, Dynamics, and Control of Airplanes*. American Institute of Aeronautics and Astronautics, Inc., Reston, 2nd edition, 2004.

[44] E. Schoberl. "The Musculair 1 & 2 Human Powered Aircraft and Their Optimization". *The Technical Journal of IHPVA*, 1986. http://www.ihpva.org/HParchive/PDF/16-v5n2-1986.pdf.

[45] T. Shalon. "Design and Sizing of the MIT Daedalus Prototype". *American Institute of Aeronautics and Astronautics, Inc.*, (87).

[46] T. Smith. "Skycylce Design". URL translated with Google Translate http://kidachi.kazuhi.to/hpa/links.html.